Jakob Neumayer, BSc

Equilibrium and transport properties of single-layer graphene nanoribbons

MASTER THESIS

for obtaining the academic degree
Diplom-Ingenieur

Master Programme of
Technical Physics

Graz University of Technology

Supervisors:

Univ.-Prof. Dipl.-Phys. Dr.rer.nat. Wolfang von der Linden
Univ.-Prof. Dr.rer.nat. Enrico Arrigoni
Institute of Theoretical and Computational Physics

Graz, January 2014

... to Sabrina and my dear parents

Deutsche Fassung:
Beschluss der Curricula-Kommission für Bachelor-, Master- und Diplomstudien vom 10.11.2008
Genehmigung des Senates am 1.12.2008

EIDESSTATTLICHE ERKLÄRUNG

Ich erkläre an Eides statt, dass ich die vorliegende Arbeit selbstständig verfasst, andere als die angegebenen Quellen/Hilfsmittel nicht benutzt, und die den benutzten Quellen wörtlich und inhaltlich entnommenen Stellen als solche kenntlich gemacht habe.

Graz, am ……. ……..
(Unterschrift)

Englische Fassung:

STATUTORY DECLARATION

I declare that I have authored this thesis independently, that I have not used other than the declared sources / resources, and that I have explicitly marked all material which has been quoted either literally or by content from the used sources.

……. ……..
date (signature)

Abstract

Graphene nanoribbons (GNRs) exhibit a variety of fascinating properties on account of the particular honeycomb lattice and the chemical properties of elementary carbon, in combination with quantum size effects due to the GNR's finite width. It is the main objective of the present thesis to gain deeper insight into the equilibrium and transport properties of GNRs, with the arising differences between zig-zag and armchair edge orientations as one of the key aspects. The focus is also on a suitable inclusion of electron-electron interactions to point out distinctions against the idealistic non-interacting picture. Therefore, the two-dimensional Hubbard model for GNRs within the framework of Cluster Perturbation Theory (CPT) is the model of choice, due to its effective and accessible way of including electron-electron interactions into the calculations. Disorder, phonons and lattice relaxations are neglected, for reasons of simplicity.

The energy-momentum dispersion relation and the electronic Density of States (DOS) of various GNR geometries are analyzed in the equilibrium situation to allow for a comprehensive interpretation of the arising physical characteristics. A comparison between narrow and broad GNRs is performed to point out occurring quantum size effects.

Electronic transport investigations of infinitely long GNRs are performed within the Wannier-Stark model, where a homogeneous electrical field is applied along the overall structure to drive a current to flow. Dissipation is represented in a simplified way by coupled voltage probes (artificial fermion bath chains) instead of an explicit consideration of phonons, to prevent an occurrence of Bloch oscillations (BOs) within the infinite geometries. Appearing Wannier-Stark resonances in the steady-state current characteristics of the GNRs demand for a comprehensive understanding of the physical transport processes within the Wannier-Stark model, which is gained by a non-equilibrium investigation of an infinite tight-binding (TB) chain.

Kurzfassung

Graphen weist eine Vielzahl außergewöhnlicher physikalischer Effekte auf. Grund dafür sind die spezielle hexagonale Struktur des Atomgitters und die chemischen Eigenschaften des elementaren Kohlenstoffs. Bei der Betrachtung von Bändern aus Graphen mit Breiten im Bereich von einigen Nanometern (Graphen-Nanobänder) treten zusätzlich Größenquantisierungseffekte auf. Ziel dieser Arbeit ist eine detaillierte Untersuchung solcher Graphen-Nanobänder bezüglich ihrer elektronischen Gleichgewichts- und Transporteigenschaften, wobei ein Hauptaugenmerk auf den Unterschieden zwischen Armchair- und Zigzag-Bändern liegt. Ein weiterer wichtiger Aspekt ist eine geeignete Einbeziehung von Elektron-Elektron-Wechselwirkungen in die physikalischen Betrachtungen, um Abweichungen vom idealen nicht-wechselwirkenden Fall aufzuzeigen. Das zweidimensionale Hubbard-Modell für Graphen bildet, in Kombination mit einer Erweiterung der Störungstheorie auf atomare Cluster (CPT), das Modellsystem für die Untersuchungen der Graphen-Nanobänder, wodurch Elektron-Elektron-Wechselwirkungen auf effektive Weise in die Berechnung miteinbezogen werden können. Störungen des atomaren Gitters durch Defekte, Phononen oder Gitterrelaxationen werden vernachlässigt, damit die Effekte von verschiedenen Randstrukturen und Elektron-Elektron-Wechselwirkungen bestmöglich analysiert werden können.

Um eine umfassende Beschreibung des physikalischen Gleichgewichtsverhaltens von Graphen-Nanobändern zu ermöglichen, werden die Dispersionsrelation und die elektronische Zustandsdichte (DOS) für verschiedene Geometrien berechnet, wobei breite und schmale Bänder betrachtet werden, um eine anschauliche Beschreibung der auftretenden Größenquantisierungseffekte zu ermöglichen.

Der elektronische Transport durch unendlich lange Graphen-Nanobänder wird anhand des Wannier-Stark-Modells untersucht, in welchem ein stationärer Stromfluss durch Anlegen eines homogenen elektrischen Feldes hervorgerufen wird. Da es in unendlich langen Modellen zur Ausbildung von Bloch-Oszillationen kommt, wird aufgrund der vernachlässigten Phononen ein vereinfachter Ansatz zur Beschreibung der Energiedissipation im atomaren Gitter verwendet, worin fermionische Teilchenketten künstlich an das physikalische System angekoppelt werden und die Funktion von Energiebädern übernehmen. Die Erkenntnisse der Betrachtung einer unendlichen eindimensionalen Kette im Tight-Binding-Modell ermöglichen schlussendlich ein umfassendes Verständnis der Wannier-Stark-Resonanzen, welche in den stationären Stromverläufen der Graphen-Nanobänder auftreten.

Acknowledgements

THANK YOU, mom and dad! You are the most loving, caring and supporting parents I could ever imagine.

THANK YOU, Prof. Wolfgang von der Linden! Your shown motivation, interest and support in supervising me was incredible. Having a sympathetic ear for my countless questions to you at every time of the year, was a tremendous assistance for my entire work.

THANK YOU, Prof. Enrico Arrigoni, for being my co-supervisor! Your ideas and concepts for approaching occurring problems were unvaluable important.

THANK YOU, Martin, for all the time you spent in introducing me to the methods commonly used at our institute, especially in my early days! Your unlimited readiness to invest your time in discussing my problems provided a great deal of help.

THANK YOU, Anja, Lilia, Antonius, Christoph, Faruk, Georg, Manuel, Markus, Max, Robert, Simon and Werner! It was a pleasure working, discussing and staying with you during my work at our institute.

THANK YOU, Sabrina! Your love, patience and empathy encouraged me in countless situations during the last year. Your extraordinary cheerfulness especially in the late hours of our days were invaluable relieving.

Table of Contents

List of Figures

Glossary

AC-W4	armchair graphene nanoribbon with a width of 4 carbon atoms
AC-W5	armchair graphene nanoribbon with a width of 5 carbon atoms
AC-W30	armchair graphene nanoribbon with a width of 30 carbon atoms
BO	Bloch oscillation
BZ	Brillouin zone
C	carbon
CNT	carbon nanotube
CPT	Cluster Perturbation Theory
cRPA	constrained random phase approximation
DC	direct current
DOS	electronic density of states
ED	Exact Diagonalization
e.g.	exempli gratia (english: for example)
etc.	et cetera (english: and other things)
GNR	graphene nanoribbon
i.e.	id est (english: that is to say)
LDOS	local electronic density of states
KNEGF	Keldysh non-equilibrium Green's functions
MFT	Mean Field Theory
QMC	Quantum Monte Carlo
RGT	Renormalization Group Theory
TB	tight-binding
ZZ-W3	zig-zag graphene nanoribbon with a width of 3 carbon atoms
ZZ-W4	zig-zag graphene nanoribbon with a width of 4 carbon atoms
ZZ-W5	zig-zag graphene nanoribbon with a width of 5 carbon atoms
ZZ-W30	zig-zag graphene nanoribbon with a width of 30 carbon atoms
2d	two-dimensional

1 Introduction

Since *Novoselov et al.* reported their experimental discovery of the two-dimensional material graphene in 2004 [1], tremendous efforts in scientific research on this material have been taken. More than 8000 articles on graphene were reported between the years 2005 and 2011 [2]. Graphene's unique ballistic transport properties even at submicron distances may be taken as one explanation for that. Due to this vast research activities, publishing a comprehensive review article in a reasonable extent is all but impossible. General reviews focusing on transport in gated graphene [2], device applications [3], graphene's mechanical properties [4] [5], etc. are on hand though, presenting fundamental background for subsequent specific research activities.

More than 10 years before the experimental synthesis of graphene the research activities in the field of carbon (C) had undergone a rapid development too, when quasi-one-dimensional semiconducting carbon nanotubes (CNT) - first fabricated in 1991 [6] - were in the focus of numerous scientists [7]. Continuously breaking-up the carbon-carbon bonds along the tube axis leads to a flat two-dimensional carbon geometry called graphene nanoribbon (GNR). In literature this process is often referred to as *longitudinal unzipping of CNTs to form GNRs* [8]. Figure 2.2 in Chapter 2 shows a schematic outline of the method. Since any experimentally fabricated material has naturally finite physical dimensions, every prepared graphene sample is indeed a GNR. This fact accounts for the necessity of theoretical investigations on GNRs, which have drawn the attention of the carbon research community to themselves in the last years.

The edge orientation of the GNRs has a strong influence on the equilibrium and non-equilibrium transport properties of GNRs [2] [9] (for details on the different edge orientations see Chapter 2). GNRs with armchair edges can either be metallic or semiconducting, depending on the ribbon width. In contrast to that, GNRs with zig-zag edges possess localized edge states and thus always exhibit a metallic system [9]. This subsequently leads to major differences in the energy spectrum, in the electronic density of states (DOS) or in the development of magnetic edge states [10] [11]. Focusing on non-equilibrium properties of GNRs the characteristics of the electronic conductance of GNRs is similarly depending on the edge orientation [12]. The effect of edge reconstruction on quantum transport in graphene nanoribbons was studied most recently, as well as the impact of electron-electron interactions in the extended Hückel model [13].

Although the amount of scientific reviews about GNRs is immense, there exist only few taking into considerations electron interactions. Ever since E. Schrödinger proclaimed his famous equation about the time-evolution of quantum states in 1926 [14], it is known that electron-electron interactions are the most difficult to describe. Furthermore, the whole interacting quantum many-body problem is not exactly solvable without considering appropriate simplifications or considering specific limiting cases. One standard and well-known diagrammatic technique of solving interacting many-body problem is weak-coupling perturbation theory, which treats the limiting case of small electron-electron interactions [64]. However, in this work a more recent approach was chosen, which captures short-range dynamical correlations within strongly correlated models. By applying a proper cluster tiling to the graphene geometries under investigation within the one-band Hubbard model, the electron-electron interactions can be taken into account in an effective way using Cluster

Perturbation Theory (CPT) - a cluster extension of strong-coupling perturbation theory.
Generally, the present work consists of two major parts, the investigation of electronic equilibrium *and* electronic transport properties in various graphene geometries. After a short summary of the physical and chemical properties of graphene and GNRs respectively in Chapter 2, the equilibrium properties of various GNR geometries with different edge orientations are investigated in Chapter 3. This first major part includes a treatment of the applied numerical methods as well as a presentation of all the gained results. In Chapter 4 non-equilibrium electronic transport calculations are presented. This second major part of the work describes the numerical methods adopted in this work as well as all obtained results. The role of voltage probes - semi-infinite tight-binding (TB) chains mimicking dissipation mechanisms - is discussed in Sec. 4.2, while the electronic transport through an infinite TB chain is in the focus of Sec. 4.3. Finally, the electronic transport properties of GNRs are under investigation in Sec. 4.4.

2 Physicochemical properties of graphene and graphene nanoribbons

Elementary carbon is found in the two well-known different structural modifications diamond and graphite. While the diamond structure features extraordinary strong covalent bondings between all C atoms, graphite is characterized by a layered structure composed of stacked honeycomb lattice layers. A single honeycomb lattice layer separated from the remaining layers is called graphene. The elementary electronic properties of graphene described in this chapter are to a large extent based on a comprehensive review about the electronic properties of graphene by *Castro Neto et al. (2009)* [15].

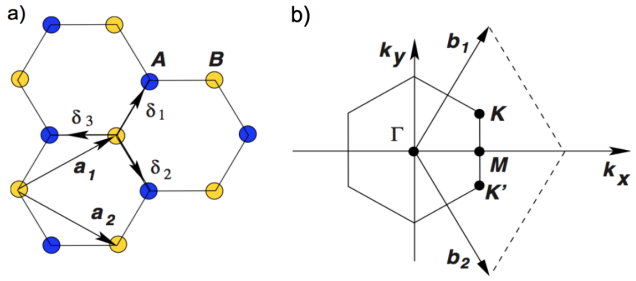

Figure 2.1: (a) Hexagonal structure of graphene's honeycomb real lattice. The two centered rectangular (rhombic) sublattices are indicated by blue (sublattice A) and yellow (sublattice B) dots. The real lattice vectors a_1 and a_2 are plotted in addition, as well as the three equivalent basis vectors $\delta_{1,2,3}$. (b) Corresponding first Brillouin zone with the reciprocal lattice vectors b_1 and b_2. K and K' mark the reciprocal points where the Dirac cones are located [15]

.

In single-layer graphene C atoms are arranged in a honeycomb lattice (see Fig. 2.1a). The hexagonal structure arises from two centered rectangular (rhombic) sublattices, which are indicated as sublattice A and sublattice B. Practically, a two-atoms basis δ_i is chosen and repeated on every lattice point of either sublattice A or B. Considering the graphene lattice in Fig. 2.1a, there are three equivalent choices of this basis

$$\boldsymbol{\delta}_{1,2} = \frac{a}{\sqrt{3}} \left\{ \begin{pmatrix} 0 \\ 0 \end{pmatrix}, \begin{pmatrix} \frac{1}{2} \\ \pm\frac{\sqrt{3}}{2} \end{pmatrix} \right\} \quad \text{or} \quad \boldsymbol{\delta}_3 = \frac{a}{\sqrt{3}} \left\{ \begin{pmatrix} 0 \\ 0 \end{pmatrix}, \begin{pmatrix} -1 \\ 0 \end{pmatrix} \right\} \tag{2.1}$$

where $\frac{a}{\sqrt{3}} \approx 1.42$ Å is the C-C distance in graphene, which follows from the experimentally found lattice constant $a = 2.46 \pm 0.02$ Å [16]. Bold symbols mark vectors and matrices throughout the whole work. In Eq.(2.1) a can be understood as the lattice constant of the sublattices, which are

spanned by the following real lattice vectors

$$\boldsymbol{a}_1 = \frac{a}{\sqrt{3}} \begin{pmatrix} \frac{3}{2} \\ \frac{\sqrt{3}}{2} \end{pmatrix} \qquad \boldsymbol{a}_2 = \frac{a}{\sqrt{3}} \begin{pmatrix} \frac{3}{2} \\ -\frac{\sqrt{3}}{2} \end{pmatrix} \tag{2.2}$$

as indicated in Fig. 2.1a.
The corresponding reciprocal lattice vectors are given by

$$\boldsymbol{b}_1 = \frac{4\pi}{3a} \begin{pmatrix} \frac{\sqrt{3}}{2} \\ \frac{3}{2} \end{pmatrix} \qquad \boldsymbol{b}_2 = \frac{4\pi}{3a} \begin{pmatrix} \frac{\sqrt{3}}{2} \\ -\frac{3}{2} \end{pmatrix} \tag{2.3}$$

which are indicated in Fig. 2.1b, alongside important points in reciprocal space (Γ, $\boldsymbol{M}$, $\boldsymbol{K}$ and $\boldsymbol{K}'$). These points will become significantly important in Chapter 3 where the energy-momentum characteristics of graphene and GNRs will be calculated. Especially the corners of the first Brillouin zone $\boldsymbol{K}$ and $\boldsymbol{K}'$, where the so-called *Dirac cones* will occur in the energy-momentum dispersion relation. The nomenclature *Dirac cones* is chosen, because these two points mainly account for the relativistic behaviour of the charge carriers in graphene, which have an effective speed equal to the speed of light. This electronic transport characteristic is essentially described by Dirac's (relativistic) equation, leading to the nomenclature *Dirac cones* in further consequence [17]. The Dirac cones are located at the following positions in momentum (reciprocal) space

$$\boldsymbol{K} = \frac{4\pi}{3a} \begin{pmatrix} \frac{\sqrt{3}}{2} \\ \frac{1}{2} \end{pmatrix} \qquad \boldsymbol{K}' = \frac{4\pi}{3a} \begin{pmatrix} \frac{\sqrt{3}}{2} \\ -\frac{1}{2} \end{pmatrix} \tag{2.4}$$

For a quantum mechanical description of graphene the *hopping energy* t describes the hopping between nearest-neighbour carbon sites. A comparable value

$$t \approx 2.8\ eV \tag{2.5}$$

is found in many references [15] [2] [18].
The exceptional characteristics of graphene basically originate from the physical and chemical properties of the lattice building element carbon. Carbon is an element of the 14^{th} group of the periodic table of elements. Hence it features a special electron configuration with a half filled L-shell, i.e. four outer electrons (two in the 2s-shell and two in the 2p-shell). This configuration gives rise to a great variety of possible chemical bondings, the greatest of all chemical elements on earth. In the particular case of graphene the C atoms are sp^2 hybridized. Due to this fact, GNRs (CNTs) exhibit a semiconducting *or* metallic behaviour depending on their width or diameter as well as on the shape of the edges (the rolling angle) of the graphene sheets.

Experimental fabrication of GNRs by means of mechanical exfoliation was reported in 2004 for the first time [1], as stated above. Several other methods of production like synthesis [19], lithographic patterning [20] [21] or chemically splitting of graphite by oxidation and/or heating [22] [23] have been announced since then. As explained above CNTs are basically graphene sheets, which are rolled at a specific and discrete angle. Due to this fact a further possibility for the fabrication of GNRs is longitudinal unzipping of CNTs [8]. The procedure is schematically outlined in Fig. 2.2.

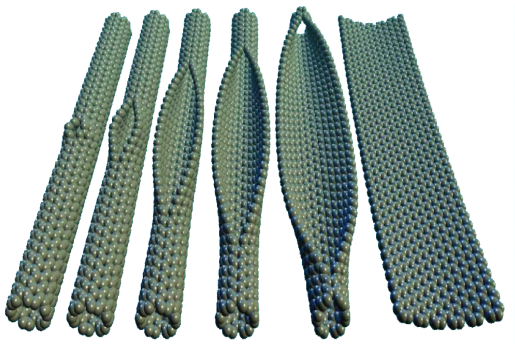

Figure 2.2: Schematical outline of the longitudinal unzipping of a CNT to form a GNR (adapted from Ref. [8]).

This directly leads to the role of edge orientations in determining electronic properties of GNRs. There are basically three different kinds of edge orientations of GNRs, namely *zig-zag*, *armchair* and *chiral* (see Fig. 2.3). While the latter is studied on rare occasions in practical experiments, the fabrication of armchair and zig-zag GNRs has been reported several times, as written above.

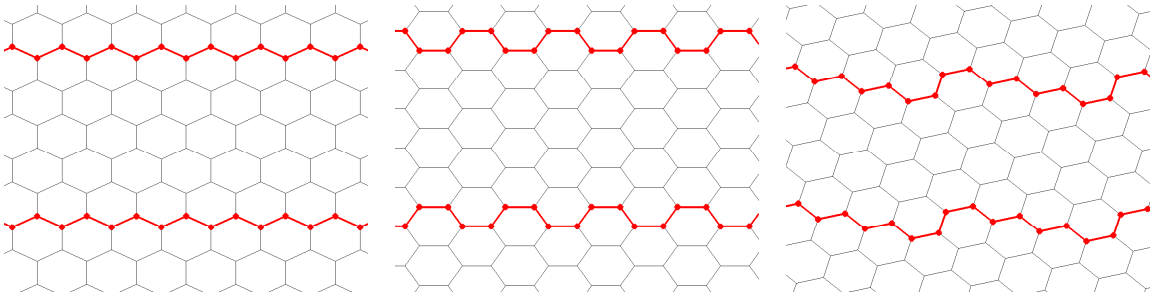

Figure 2.3: Honeycomb lattice of graphene with the three different edge orientations of GNRs indicated in red: (a) zig-zag GNR, (b) armchair GNR, (c) chiral GNR.

As shown in Fig. 2.3a zig-zag GNRs have zig-zag edges along the longitudinal (horizontal) axis, while armchair GNRs conversely possess armchair edges along the longitudinal axis (see Fig. 2.3b). This classification assumes the longitudinal axis to be considerably longer than the transversal. Focusing on the electronic properties, a significant difference between zig-zag and armchair GNRs arises. Zig-zag GNRs of any possible width are predicted to always behave like a metal, whereas the width of armchair GNRs determines wether the system behaves semiconducting or metallic [24]. An armchair ribbon is metallic if the number of C atoms along the transversal axis (i.e the ribbon width) N = 3M - 1, where M is an integer [25].
An interesting discrepancy in terminology arises between GNRs and CNTs. Rolling up a GNR with zig-zag edges yields an armchair CNT and vice versa. This clarifies why a zig-zag GNR and an armchair CNT behave in a similar way and *not* a zig-zag GNR and a zig-zag CNT.

3 Equilibrium properties of graphene nanoribbons

In this chapter the focus is on electronic properties of graphene and GNRs in equilibrium. Here *equilibrium* means that there are no external fields or non-static potentials applied. In addition the samples are considered to be *clean*, which means that no lattice defects are taken into consideration. Furthermore, naturally-occurring phonons are neglected in the overall work. From an experimental point of view, the consequences of these neglects on the characteristics of the investigated materials can be rather determinative, since lattice defects and especially acoustic phonons undoubtedly affect physical properties like e.g. the electronic conductivity. However, in this work the focus is mainly on the effects of electron-electron interactions on the equilibrium and transport properties of GNRs, which justifies the simplifications taken into account in a way.
Nothing but the bare atomic structure of graphene and GNRs is investigated in context of the one-band Hubbard model, which can be seen as an improvement of the simple TB approach. Instead of a typical numerical approach like Exact Diagonalization (ED) or Quantum Monte Carlo (QMC), which both are limited to periodic systems with no more than about 20 sites (ED) or 100 sites (QMC), an appropriate quantum cluster approach, called Cluster Perturbation Theory (CPT) is used. CPT is basically a cluster extension of strong-coupling perturbation theory [26]. In this approach finite clusters of a small number of sites are solved exactly. In a further step these clusters are connected to or embedded in a larger lattice, with dimensions up to infinity. There exist several possibilities for this connection or embedding, which will be explained in the following sections. A major benefit of using the Hubbard model within the framework of CPT is the comparatively simple way of including electron-electron interactions, represented by the on-site repulsion U in the Hubbard model. Because of the rather small size of the used clusters, it is possible to solve them numerically with these Hubbard interactions considered. After the final connection or embedding of the clusters to a larger lattice, a numerically treatable fully interacting model of the investigated graphene geometry is established. It has to be noted here that the basic one-band Hubbard model only takes into account short-range interactions. While this is no longer an issue in metals, where electrons act collectively to screen electric fields and therefore effectively short range the strong long-range Coulomb interactions between the electrons [27], the situation differs in the case of graphene. It will be shown in Sec. 3.2 that pristine graphene is neither a metal nor an insulator and therefore cannot screen the long-range Coulomb interaction in the usual (metallic) way. It has been shown that the Dirac cones in pristine graphene are reshaped by long-range electron-electron interactions [27]. However, in case of GNRs the effect of long-range interactions is expected to be rather weak due to their strict metallic *or* semiconducting physical behaviour, which justifies the use of the Hubbard model again.
The final purpose of this chapter is to calculate equilibrium quantities of graphene and GNRs. First of all the spectral function $A(\mathbf{k}, \omega)$, which provides the energy-momentum (ω-$\mathbf{k}$) spectrum of the considered atomic structure, is obtained. Furthermore, the particular energy gaps $\Delta(U)$ can be calculated from the spectral function, which are of significant importance, since the gaps are expected to increase with increasing interaction U [11]. The local electronic density of states (LDOS) on every

site as well as the overall DOS can also be calculated rather easy within this formalism. Both are of great interest, since there are significant differences expected in the DOS of zig-zag GNRs and of armchair GNRs [25] [28] [29]. But that is not all, also the LDOS is expected to feature rather different results for zig-zag and armchair ribbons, since zig-zag GNRs are expected to possess localized states along the zig-zag edges, in contrast to armchair GNRs, where no localized states are predicted [30]

This chapter is organized as follows: In Section 3.1 detailed information about the used numerical methods is provided. The role of Green's functions in the field of many-body problems and their relation to experimental observables is discussed, subsequently followed by a detailed description of the CPT approach, including the necessary ED methods, namely the Lanzcos and the Band-Lanzcos algorithms. The application of the numerical methods to simple infinitely extended 2d graphene for obtaining equilibrium properties, like the DOS e.g., is presented in Section 3.2. Finally, in Section 3.3 - 3.5 the results for the equilibrium properties of GNRs with different geometries are discussed and compared to each other, with the major difference between a zig-zag and an armchair edge orientation shown in conclusion.

3.1 Numerical methods

The calculation scheme for the equilibrium properties of GNRs remains basically unchanged when different geometries are considered. Interactions are also tunable by simply changing the interaction parameter U. For U = 0 the non-interacting case is modeled, which can be checked analytically. The general applied calculation scheme is outlined in this section. All parameters depending on the exact considered geometry are treated in a general way in this part. References to the sections where these parameters are specified according to the particular GNR structure are added.

Most of the considered GNR geometries were investigated entirely using MATLAB [31] as numerical computing environment. For larger cluster sizes (8 and 10 sites) a C++ code was used in addition.

3.1.1 The role of Green's functions

Understanding experimentally observable quantities of physical systems is the ultimate objective of the quantum mechanical description of many-particle systems. The general calculation scheme for equilibrium properties in different graphene geometries is explained in detail in the following sections. First of all it is valuable to give thought about quantities which can be evaluated conveniently on the one hand and characterize the experimentally accessible observables of a physical system on the other hand. One approach of learning about physical systems is measuring its response to external probes. The results of measurements of these kind can be expressed conveniently in terms of Green's functions.

In consequence of the major importance of this approach - using Green's functions to describe characteristics in physical systems - for the present work, an illustrating example is given [32]: It should be noted first that all variables except the time variable are suppressed. An experiment is

considered, in which a system is exposed to some perturbation of an external applied field $\boldsymbol{F}(t)$ and its response to it is measured. The response is expected to depend linearly on the applied field, assuming a weak enough field. In this schematical scenario the associated response function (or Green's Function) would be some kind of "proportionality factor". This can be described basically by three equations

$$H_{tot} = H - F(t)O, \tag{3.1}$$

$$\langle O(t)\rangle = \langle O\rangle + \int_{-\infty}^{\infty} \chi(t-t')F(t')dt', \tag{3.2}$$

$$\chi(t-t') = -i\left\langle \left[O(t), O(t')\right]\Theta(t-t')\right\rangle \tag{3.3}$$

where H (H_{tot}) is the Hamiltonian of the unperturbed (perturbed) system and O denotes any kind of measuring operator (note that in this work operators are *not* denoted by a hat, as it is common in a variety of other scientific works). The response of the system to the external field F is given by $\langle O(t)\rangle$, with the angle brackets indicating an expectation value:

$$\langle O\rangle = \frac{tr\ \left(O\ e^{-\beta H}\right)}{tr\ \left(e^{-\beta H}\right)} \tag{3.4}$$

where β represents the inverse temperature, i.e. $\beta = (k_B T)^{-1}$. In this context $\langle O\rangle$ is the expectation value of the unperturbed system, which often vanishes. $\chi(t-t')$ finally represents a *retarded* response function. A retarded property is only non-zero for $t > t'$, which corresponds to the principle of causality. Keeping this definition in mind is crucial for a comprehensive understanding of the present work. The function $\chi(t-t')$ is referred to as correlation function or Green's function. The electrical conductivity σ for example can be related to a retarded current-current correlation function, i.e. the operators O in Eq.(3.1) - (3.3) are represented by current operators. The retarded Green's function of a system can thus be seen as the quantity of interest to calculate, for reasons of comparing many-body theory to experiments.

Many-body real-time Green's function

As a starting point of the following derivation of the retarded Green's function, the many-body (n-particle) real-time time-ordered Green's function is chosen, which is defined by the following expression [33]

$$G^{(n)}\left(\alpha_1 t_1, ..., \alpha_n t_n | \alpha_1{}' t_1', ..., \alpha_n{}' t_n'\right) = (-i)^n \left\langle T\left[c_{\alpha_1}^{(H)}(t_1) ... c_{\alpha_n}^{(H)}(t_n)\ c_{\alpha_n'}^{(H)^\dagger}(t_n') ... c_{\alpha_1'}^{(H)^\dagger}(t_1')\right]\right\rangle. \tag{3.5}$$

Here α_i describes a possible state (position, spin, ...) within the system, while $c_{\alpha_i}^{(H)}(t)$ and $c_{\alpha_i}^{(H)^\dagger}(t)$ denote annihilation and creation operator in the Heisenberg representation

$$O^{(H)}(t) = e^{iHt}\ O\ e^{-iHt}, \tag{3.6}$$

respectively. The angle brackets again indicate an expectation value, while $T[...]$ denotes a time-

ordered product. The corresponding operator T is called time-ordering operator and defined by

$$T\left[O_{\alpha_1}(t_1)O_{\alpha_2}(t_2)\ldots O_{\alpha_n}(t_n)\right] = \zeta^P O_{\alpha_{P_1}}(t_{P_1})O_{\alpha_{P_2}}(t_{P_2})\ldots O_{\alpha_{P_n}}(t_{P_n}) \tag{3.7}$$

where

$$\zeta = \begin{cases} -1, & \text{for Fermions} \\ +1, & \text{for Bosons} \end{cases} \tag{3.8}$$

and P represents the time-ordered permutation of $1, 2, \ldots n$, i.e. the chronological arrangement of the times with the latest to left:

$$t_{P_1} > t_{P_2} > \cdots > t_{P_n}. \tag{3.9}$$

The choice of a suitable thermodynamic ensemble will be considered now, before continuing the treatment of Green's functions.
There are, in general, two different thermodynamic ensembles which may be used for numerical purposes, namely the canonical and grand canonical ensemble [32], The expectation value (defined in Eq.(3.4)) represents a thermal and quantum average in both of them. In a canonical ensemble only the number of particles N in a system is fixed and the system can only exchange energy with the reservoir, which is rather inappropriate for the description of the systems investigated in the present work. In contrast, the grand canonical ensemble allows also for an exchange of particles between the system and the reservoir. Due to this fact the *chemical potential* μ has to be introduced, which determines the average number of particles within the system. This corresponds to a transformation of the Hamiltonian

$$H \to H - \mu N. \tag{3.10}$$

For reasons of a clear arrangement the Hamiltonian will still be written as H in the following, but shall be understood as $H - \mu N$.

Applying the definition of the expectation value in Eq.(3.4) to the general definition of the n-particle real-time Green's function in Eq. (3.5) yields

$$G^{(n)}\left(\alpha_1 t_1, \ldots, \alpha_n t_n | \alpha_1{}' t_1{}', \ldots, \alpha_n{}' t_n{}'\right) = \frac{(-i)^n}{Z} Tr\left(e^{-\beta H} T\left[c_{\alpha_1}^{(H)}(t_1)\ldots c_{\alpha_n}^{(H)}(t_n)\; c_{\alpha_n'}^{(H)\dagger}(t_n')\ldots c_{\alpha_1'}^{(H)\dagger}(t_1')\right]\right) \tag{3.11}$$

where H is the grand canonical Hamiltonian defined in Eq.(3.10) and $Z = Tr\left(e^{-\beta H}\right)$ is the grand canonical partition function. This expression can be simplified and unified conveniently by replacing the creation and annihilation operators with the corresponding field operators $\Psi(x, t)$, i.e. representing them in second quantization [33]:

$$\Psi(x,t) = e^{iHt}\,\Psi(x)\,e^{-iHt} \mathrel{\hat{=}} e^{iHt}\,c_{\alpha_i}\,e^{-iHt} \tag{3.12}$$

where the same transformation applies for the creation operator $c_{\alpha_i}^\dagger$. Writing these operators in the second quantization representation also solves the problem of simultaneously appearing real *and* imaginary times, where the imaginary times appeared in the argument of the exponential functions of the creation and annihilation operator, respectively. Since the grand canonical ensemble is now chosen as the appropriate thermodynamical ensemble it is convenient to denote the expectation

value by angle brackets again. Together with the second quantization representation of the operators this yields

$$G^{(n)}\left(x_1 t_1, \ldots, x_n t_n | x_1{}' t_1{}', \ldots, x_n{}' t_n{}'\right) = (-i)^n \left\langle T\left[\Psi(x_1, t_1) \ldots \Psi(x_n, t_n) \Psi^\dagger(x_n{}', t_n{}') \ldots \Psi^\dagger(x_1{}', t_1{}')\right]\right\rangle . \tag{3.13}$$

It should be noted here that any internal degree of freedom, like the spin e.g., formerly included in the label α is now implicitly included in x.

Another possibility to deal with appearing real *and* imaginary times in the expression of the n-particle Green's function is to define a *thermal or imaginary-time Green's function*

$$\mathcal{G}^{(n)}\left(x_1 \tau_1, \ldots, x_n \tau_n | x_1{}' \tau_1{}', \ldots, x_n{}' \tau_n{}'\right) = \left\langle T\left[\Psi(x_1, \tau_1) \ldots \Psi(x_n, \tau_n) \Psi^\dagger(x_n{}', \tau_n{}') \ldots \Psi^\dagger(x_1{}', \tau_1{}')\right]\right\rangle \tag{3.14}$$

where field operators $\Psi(x, \tau) = e^{H\tau}\, \Psi\, e^{-H\tau}$ in the imaginary-time Heisenberg representation are used.

In contrast to the thermal Green's function, the *zero-temperature Green's function* can be obtained from Eq.(3.13) by taking the ground state expectation value:

$$G^{(n)}\left(x_1 t_1, \ldots, x_n t_n | x_1{}' t_1{}', \ldots, x_n{}' t_n{}'\right) = (-i)^n \left\langle \psi_0 \middle| T\left[\Psi(x_1, t_1) \ldots \Psi(x_n, t_n) \Psi^\dagger(x_n{}', t_n{}') \ldots \Psi^\dagger(x_1{}', t_1{}')\right] \middle| \psi_0 \right\rangle . \tag{3.15}$$

Note the different notations for finite and zero-temperature Green's functions, namely by $\mathcal{G}$ and G. Comparing Eq.(3.14) to Eq.(3.15) yields that apart from the use of real and imaginary times, respectively, the two Green's functions are only distinguished by the prefactor $(-i)^n$ and the denotations of the expectation value brackets. In case of the thermal Green's function it denotes a thermal trace, in contrast to a ground state expectation value in case of the zero-temperature Green's function.

The role of Green's functions as functions representing a response of a system to an external field was stated above. How can the thermal and zero-temperature Green's functions be interpreted in particular as response functions? Physically, the derived expressions for the Green's function at finite (Eq.(3.14)) and zero-temperature (Eq.(3.15)) describe the response of a quantum system to a perturbation created by the injection of particles at some space-time points $\{x_1 t_1\} \ldots \{x_n t_n\}$ and the simultaneous elimination of particles at $\{x_1{}' t_1{}'\} \ldots \{x_n{}' t_n{}'\}$. The injection and elimination processes are described by the field operators $\Psi^\dagger$ and Ψ corresponding to the second quantization representation of creation and annihilation operator. The applicability of the derived expressions for finite *and* infinite systems, with no requirement of translation invariance, should also be noted.

Single-praticle Green's function

Since in the present work most obtained physical quantities can be described by *one-particle (single-particle) Green's functions*, several auxiliary definitions will be introduced in the following [33]. Furthermore, the notation of the zero-temperature Green's function G will be used, although all auxiliary definitions can also be adopted to thermal Green's functions $\mathcal{G}$ simply by using an imaginary-time τ instead of a real-time t and omitting the complex prefactor. First, a compact notation of the n-particle Green's function will be introduced, where the space-time points $\{x_n t_n\}$ are replaced by the

shorthand notation n:

$$G^{(n)}\left(1,\ldots,n|1',\ldots,n'\right) := G^{(n)}\left(x_1t_1,\ldots,x_nt_n|x_1{}'t_1{}',\ldots,x_n{}'t_n{}'\right). \tag{3.16}$$

In this notation, the single-particle (n = 1) Green's function becomes a handy expression

$$G^{(1)}\left(1|1'\right) := (-i)\left\langle T\left[\Psi(1)\Psi^{\dagger}(1')\right]\right\rangle \tag{3.17}$$

where the superscript $^{(1)}$, indicating the single-particle Green's function, will be neglected in the following. There remain only two different time orders in single-particle Green's functions, namely $t_1 > t_1{}'$ or $t_1{}' > t_1$. These two time orders can be distinguished by the definition

$$G^{(1)}\left(1|1'\right) \equiv \theta(t_1 - t_1{}')G^{>}(1|1') + \theta(t_1{}' - t_1)G^{<}(1|1') \tag{3.18}$$

where the *"greater"* Green's Function

$$G^{>}(1|1') = -i\left\langle\Psi(1)\Psi^{\dagger}(1')\right\rangle \tag{3.19}$$

and the *"lesser"* Green's Function

$$G^{<}(1|1') = -i\zeta\left\langle\Psi^{\dagger}(1')\Psi(1)\right\rangle \tag{3.20}$$

have been defined, with ζ denoting 1 for Bosons and -1 for Fermions according to Eq.(3.8). They can be further combined to define the *"retarded"* Green's Function

$$\begin{aligned} G^{R}(1|1') &= \left(G^{>}(1|1') - G^{<}(1|1')\right)\theta(t_1 - t_1{}') \\ &= -i\left\langle\left[\Psi(1)\Psi^{\dagger}(1')\right]_{-\zeta}\right\rangle\theta(t_1 - t_1{}') \end{aligned} \tag{3.21}$$

and the *"advanced"* Green's Function

$$\begin{aligned} G^{A}(1|1') &= \left(G^{<}(1|1') - G^{>}(1|1')\right)\theta(t_1{}' - t_1) \\ &= i\left\langle\left[\Psi(1)\Psi^{\dagger}(1')\right]_{-\zeta}\right\rangle\theta(t_1{}' - t_1) \end{aligned} \tag{3.22}$$

where $[A,B]_{+} \equiv \{A,B\}$ is the anti-commutator, which is used for Fermions, and $[A,B]_{-} \equiv [A,B]$ is the ordinary commutator, used in the case of Bosons. According to the physical interpretation of a *retarded* property already discussed above, it should be noted here that the retarded Green's function G^R is only non-zero for $t_1 > t_1{}'$. On the contrary, the advanced Green's function G^A yields a non-zero value only for $t_1{}' > t_1$.

The Lehmann representation

Green's functions provide an opportunity to make theoretical considerations of many-body problems comparable to experiments. A point has been reached now where it is of major interest *how* the single-particle Green's function can be obtained in fact. In order to achieve a proper calcula-

tion scheme the zero-temperature Green's function is expressed in its spectral representation [34]. Considering the definition of the zero-temperature Green's function in Eq.(3.15) for $n = 1$ (single-particle), the spectral representation can be obtained by inserting a completeness relation, i.e. a complete set of eigenstates of the Hamiltonian $\sum_n |\psi_n >< \psi_n|$, between the field operators:

$$\begin{aligned} G(xt|x't') &= -i\sum_n \theta(t-t') \left\langle \psi_0 \left|\Psi(x,t)\right| \psi_n^{N+1}\right\rangle \left\langle \psi_n^{N+1} \left|\Psi^\dagger(x',t')\right| \psi_0\right\rangle \\ &- i\zeta \sum_n \theta(t'-t) \left\langle \psi_0 \left|\Psi^\dagger(x',t')\right| \psi_n^{N-1}\right\rangle \left\langle \psi_n^{N-1} \left|\Psi(x,t)\right| \psi_0\right\rangle \end{aligned} \tag{3.23}$$

where the time-ordering operator T was replaced according to Eq.(3.18). It is important to note that the two sums are over *different* sets of eigenstates. In the first sum only states ψ_n^{N+1} with $N+1$ particles are considered, while in the second sum there appear only eigenstates ψ_n^{N-1} in the space with one electron less $(N-1)$. The ground state ψ_0 is considered to be a N-particle state in this picture.

The action of the field operators Ψ on the eigenstates $\psi_n^{N\pm1}$ has to be discussed in detail, because it is crucial for the further derivation. Ignoring the complex prefactor and the step-function as a start, the first line of Eq. (3.23) basically reads

$$\begin{aligned} \ldots &= \sum_n \left\langle \psi_0 \left|\Psi(x,t)\right| \psi_n^{N+1}\right\rangle \left\langle \psi_n^{N+1} \left|\Psi^\dagger(x',t')\right| \psi_0\right\rangle \\ &= \sum_n \left\langle \psi_0 \left| e^{iHt} c_\alpha e^{-iHt}\right| \psi_n^{N+1}\right\rangle \left\langle \psi_n^{N+1} \left| e^{iHt'} c_{\alpha'}^\dagger e^{-iHt'}\right| \psi_0\right\rangle \end{aligned} \tag{3.24}$$

where the definition of the field operators (see Eq.(3.12)) was substituted in the second line. This expression can be further developed by using the spectral representation for functions of the Hamiltonian $f(H) = \sum_n f(E_n)|E_n >< E_n|$ [35], which leads to

$$\begin{aligned} &= \sum_n \left\langle \psi_0 \left| e^{iE_0 t} c_\alpha e^{-iE_n^{N+1} t}\right| \psi_n^{N+1}\right\rangle \left\langle \psi_n^{N+1} \left| e^{iE_n^{N+1} t'} c_{\alpha'}^\dagger e^{-iE_0 t'}\right| \psi_0\right\rangle \\ &= \sum_n e^{i(E_0 - E_n^{N+1})(t-t')} \left\langle \psi_0 \left|c_\alpha\right| \psi_n^{N+1}\right\rangle \left\langle \psi_n^{N+1} \left| c_{\alpha'}^\dagger\right| \psi_0\right\rangle . \end{aligned} \tag{3.25}$$

Following exactly the same steps for the second line of Eq. (3.23) results in an expression for the single-particle zero-temperature Green's function

$$\begin{aligned} G(\alpha t|\alpha' t') &= -i\sum_n \theta(t-t') e^{i(E_0 - E_n^{N+1})(t-t')} \left\langle \psi_0 \left|c_\alpha\right| \psi_n^{N+1}\right\rangle \left\langle \psi_n^{N+1} \left| c_{\alpha'}^\dagger\right| \psi_0\right\rangle \\ &- i\zeta \sum_m \theta(t'-t) e^{i(E_0 - E_m^{N-1})(t'-t)} \left\langle \psi_0 \left| c_{\alpha'}^\dagger\right| \psi_m^{N-1}\right\rangle \left\langle \psi_m^{N-1} \left|c_\alpha\right| \psi_0\right\rangle \end{aligned} \tag{3.26}$$

that can be evaluated if the eigenvalue problem of the Hamiltonian $H|\psi_n >= E|\psi_n >$ is completely solvable, i.e. the ground state and all eigenstates with the corresponding eigenenergies are obtainable.

As the explicit time-dependency often is of rather little interest compared to an explicit frequency dependency (when obtaining energy-momentum relations e.g.) a Fourier transform can be applied

according to [33]

$$\begin{aligned} G(\alpha,\alpha';\omega) &= \int_{-\infty}^{\infty} dt\; e^{i\omega t}\; G(\alpha t|\alpha' t') \\ &= -i\sum_n \left\langle \psi_0 \left| c_\alpha \right| \psi_n^{N+1} \right\rangle \left\langle \psi_n^{N+1} \left| c_{\alpha'}^\dagger \right| \psi_0 \right\rangle \int_{-\infty}^{\infty} dt\; \theta(t) e^{i(\omega+E_0-E_n^{N+1})t} \\ &- i\zeta \sum_m \left\langle \psi_0 \left| c_{\alpha'}^\dagger \right| \psi_m^{N-1} \right\rangle \left\langle \psi_m^{N-1} \left| c_\alpha \right| \psi_0 \right\rangle \int_{-\infty}^{\infty} dt\; \theta(t) e^{i(\omega-E_0+E_m^{N-1})t} \\ &= -i\sum_n \left\langle \psi_0 \left| c_\alpha \right| \psi_n^{N+1} \right\rangle \left\langle \psi_n^{N+1} \left| c_{\alpha'}^\dagger \right| \psi_0 \right\rangle \int_{0}^{\infty} dt\; e^{i(\omega+E_0-E_n^{N+1})t} \\ &- i\zeta \sum_m \left\langle \psi_0 \left| c_{\alpha'}^\dagger \right| \psi_m^{N-1} \right\rangle \left\langle \psi_m^{N-1} \left| c_\alpha \right| \psi_0 \right\rangle \int_{0}^{\infty} dt\; e^{i(\omega-E_0+E_m^{N-1})t} \end{aligned} \tag{3.27}$$

where a substitution $(t - t') \rightarrow t$ and $(t' - t) \rightarrow t$ has been performed in the second and third line, respectively. Since the frequency-dependent Green's function should be evaluable for every ω, it must be provided that the integrals in Eq.(3.27) converge at all times. This is ensured by a transformation

$$\omega \rightarrow \omega + i\eta \tag{3.28}$$

with $\eta = 0^+$ a positive infinitesimal. This transformation leads to the final result

$$\begin{aligned} G(\alpha,\alpha';\omega) &= -i\sum_n \left\langle \psi_0 \left| c_\alpha \right| \psi_n^{N+1} \right\rangle \left\langle \psi_n^{N+1} \left| c_{\alpha'}^\dagger \right| \psi_0 \right\rangle \int_{0}^{\infty} dt\; e^{i(\omega+E_0-E_n^{N+1}+i\eta)t} \\ &- i\zeta \sum_m \left\langle \psi_0 \left| c_{\alpha'}^\dagger \right| \psi_m^{N-1} \right\rangle \left\langle \psi_m^{N-1} \left| c_\alpha \right| \psi_0 \right\rangle \int_{0}^{\infty} dt\; e^{i(\omega-E_0+E_m^{N-1}+i\eta)t} \\ &= \sum_n \left\langle \psi_0 \left| c_\alpha \right| \psi_n^{N+1} \right\rangle \frac{1}{\omega + E_0 - E_n^{N+1} + i\eta} \left\langle \psi_n^{N+1} \left| c_{\alpha'}^\dagger \right| \psi_0 \right\rangle \\ &+ \zeta \sum_m \left\langle \psi_0 \left| c_{\alpha'}^\dagger \right| \psi_m^{N-1} \right\rangle \frac{1}{\omega - E_0 + E_m^{N-1} + i\eta} \left\langle \psi_m^{N-1} \left| c_\alpha \right| \psi_0 \right\rangle \end{aligned} \tag{3.29}$$

which is referred to as *Lehmann representation of the single-particle Green's function* at zero temperature in literature [32] [33] [34].

A convenient way for calculating the Green's function of a whole physical system in this representation, fully utilizing the advantages of the CPT approach will be presented in the next section. With the single-particle Green's function at hand the calculation of the important equilibrium properties $A(\omega, \boldsymbol{k})$ and $\rho(\omega)$, namely the spectral function and the DOS, respectively, is a rather easy task, which will be also treated in this context. For the calculation of non-equilibrium electronic transport properties within the CPT approach another important Green's function is needed, namely the Keldysh Green's function in the Keldysh formalism of non-equilibrium Green's functions (KNEGF). This formalism is explained in detail in Chapter 4.

3.1.2 Cluster Perturbation Theory

CPT is a quantum many-body cluster method in which clusters of rather small sizes are solved exactly and subsequently connected to or embedded in a larger lattice with dimensions up to infinity. What follows directly from the characteristics of this method is that only short-range correlations up to the dimensions of the cluster are considered. Correlations between sites further apart than the cluster size are neglected. In the end CPT delivers the single-particle Green's function, which is used for calculating further properties (e.g. the DOS) in a subsequent step. Although discussed in detail later, it is important to note here that CPT is *exact* in the non-interacting limit.
In this section the derivation of the CPT formalism's central equation is discussed first. Afterwards the general calculation scheme for the equilibrium properties of various GNR geometries within the CPT approach, mainly based on the lecture notes of *Sénéchal (2008)* [36], is explained in detail. Some details are also taken from *Negele and Orland (1998)* [33].
CPT is the simplest of all quantum cluster methods. It was introduced in 2000 by *Sénéchal et al.* [37] (though similar earlier approaches exist [38]). In the CPT approach we are considering the one-band Hubbard model on a real lattice λ. The positions of the sites are denoted by $\boldsymbol{r}$ and $\boldsymbol{r'}$ respecticely. Within the notation of second quantization, where $c^\dagger$ (c) and n are the well-known creation (annihilation) and number operator, this leads to the following lattice Hamiltonian:

$$\boldsymbol{H} = \sum_{\boldsymbol{r},\boldsymbol{r'},\sigma} t_{\boldsymbol{r}\boldsymbol{r'}} c^\dagger_{\boldsymbol{r}\sigma} c_{\boldsymbol{r'}\sigma} + U \sum_{\boldsymbol{r}} n_{\boldsymbol{r}\uparrow} n_{\boldsymbol{r}\downarrow} - \sum_{\boldsymbol{r}} (\mu - \epsilon_{\boldsymbol{r}})\, n_{\boldsymbol{r}} \tag{3.30}$$

Here the matrix $t_{\boldsymbol{r}\boldsymbol{r'}}$ describes the hopping processes between lattice sites $\boldsymbol{r}$ and $\boldsymbol{r'}$, U represents the repulsive on-site Coulomb interaction and $\epsilon_{\boldsymbol{r}}$ can be seen as an on-site energy at the lattice site $\boldsymbol{r}$, while μ denotes the chemical potential. As we are in an one-band model, the index σ denotes only the spin state in here. This implies that $c^\dagger_{\boldsymbol{r}\sigma}$ creates an electron with spin σ at the site $\boldsymbol{r}$, while $c_{\boldsymbol{r'}\sigma}$ annihilates an electron with spin σ at the site $\boldsymbol{r'}$. Position and spin are often combined in so-called Wannier orbitals [39].

Cluster tiling

With the lattice Hamiltonian $\boldsymbol{H}$ in hand, a proper cluster tiling of the lattice λ is to be chosen next. Therefore the original lattice λ is divided into identical clusters, containing a number of L sites. This leads to the introduction of a superlattice Λ, with superlattice points denoted by $\boldsymbol{r}^\Lambda$. The positions of the sites within the chosen cluster are labelled by $\boldsymbol{R}$. By combining a superlattice vector $\boldsymbol{r}^\Lambda$ with a cluster-site vector $\boldsymbol{R}$ every single site of the original lattice λ can be expressed by

$$\boldsymbol{r} = \boldsymbol{r}^\Lambda + \boldsymbol{R} \tag{3.31}$$

Fig. 3.1 shows a simple cluster tiling of a two-dimensional (2d) lattice into 4-site clusters and the corresponding lattice, superlattice and cluster-site vectors.

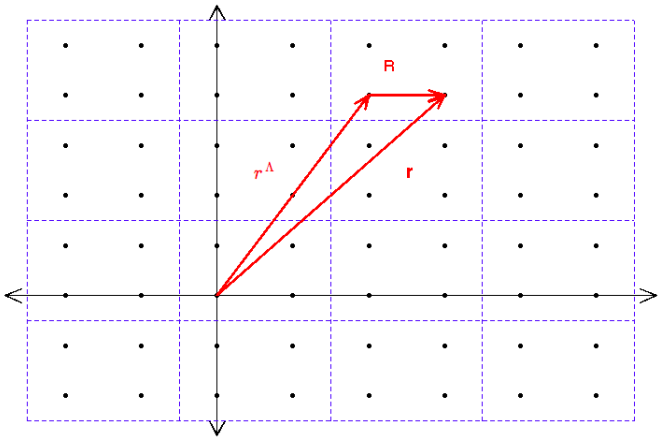

Figure 3.1: Cluster tiling of a 2d lattice into 4-site Clusters with the corresponding lattice vector $\boldsymbol{r}$, superlattice vector $\boldsymbol{r}^\Lambda$ and cluster-site vector $\boldsymbol{R}$.

The chosen cluster tiling allows for a splitting of the lattice Hamiltonian $\boldsymbol{H}$ according to

$$\boldsymbol{H} = \boldsymbol{H}_0 + \boldsymbol{V} \tag{3.32}$$

where $\boldsymbol{H}_0$ is the Hamiltonian of a single cluster, containing the intra-cluster hopping terms (i.e. hoppings strictly inside the cluster) and V containing the inter-cluster hopping terms, which were crossed out of the total lattice Hamiltonian $\boldsymbol{H}$ to attain the cluster Hamiltonian $\boldsymbol{H}_0$. $\boldsymbol{V}$ can be seen as a perturbation of the single cluster by the residual lattice here. In second quantization the inter-cluster hopping matrix is given by

$$\boldsymbol{V} = \sum_{\boldsymbol{r}^\Lambda, \boldsymbol{r}^{\Lambda'}} \sum_{a,b} T_{a,b}^{\boldsymbol{r}^\Lambda, \boldsymbol{r}^{\Lambda'}} \, c^\dagger_{\boldsymbol{r}^\Lambda, a} \, c_{\boldsymbol{r}^{\Lambda'}, b} \tag{3.33}$$

where the hopping matrix $T_{a,b}^{\boldsymbol{r}^\Lambda, \boldsymbol{r}^{\Lambda'}}$ only contains non-zero elements for *inter*-cluster hoppings, i.e. hopping processes between two different clusters. The selected notation here implies that the hopping matrix describes hopping processes between the sites a and b within the two clusters $\boldsymbol{r}^\Lambda$ and $\boldsymbol{r}^{\Lambda'}$, respecticely, while $c^\dagger_{\boldsymbol{r}^\Lambda, a}$ creates an electron at site a in cluster $\boldsymbol{r}^\Lambda$.

The effect of an applied cluster tiling to the total lattice Hamiltonian is schematically shown below, for a non-interacting (i.e. $U = 0$) tight-binding chain in one dimension, assuming equal on-site energies $\epsilon_r = \epsilon$ at every site (a cluster size $L = 3$ is chosen in this example) :

$$\boldsymbol{H}_{tot} \rightarrow \boldsymbol{H}_0 + \boldsymbol{V} = \begin{pmatrix} \ddots & & & & & & \\ & \epsilon-\mu & t & 0 & 0 & 0 & 0 \\ & t & \epsilon-\mu & t & 0 & 0 & 0 \\ & 0 & t & \epsilon-\mu & 0 & 0 & 0 \\ & 0 & 0 & 0 & \epsilon-\mu & t & 0 \\ & 0 & 0 & 0 & t & \epsilon-\mu & t \\ & 0 & 0 & 0 & 0 & t & \epsilon-\mu \\ & & & & & & \ddots \end{pmatrix} + \begin{pmatrix} \ddots & t & & & & & \\ t & 0 & 0 & 0 & 0 & 0 & 0 \\ & 0 & 0 & 0 & 0 & 0 & 0 \\ & 0 & 0 & 0 & t & 0 & 0 \\ & 0 & 0 & t & 0 & 0 & 0 \\ & 0 & 0 & 0 & 0 & 0 & 0 \\ & 0 & 0 & 0 & 0 & 0 & 0 \\ & & & & & t & \ddots \end{pmatrix} \tag{3.34}$$

where the Hamiltonians of the isolated (3×3)-clusters are highlighted in red, while the inter-cluster hopping matrices V are marked blue. The impact of this Hamiltonian splitting on the calculation of the single-particle Green's function is discussed in the following.

Central expression of the CPT approach

As mentioned in the previous section, the single-particle Green's function G of the entire lattice is needed to obtain the spectral function $A(\mathbf{k}, \omega)$. It is important in this context to point out that a slightly different notation will be used in following sections, but not before the completion of all derivations in this chapter, for reasons of comprehensibility. In this notation the single-particle Green's function in frequency space will read

$$G_{\boldsymbol{r}^{\Lambda},a,\boldsymbol{r}^{\Lambda'},b}(\omega) = \left\langle\!\!\left\langle c_{\boldsymbol{r}^{\Lambda},a}; c^{\dagger}_{\boldsymbol{r}^{\Lambda'},b} \right\rangle\!\!\right\rangle_{\omega} \tag{3.35}$$

where the inner angle brackets denote the two distinguishable orders of the creation and annihilation operator $c_{\boldsymbol{r}^{\Lambda},a} c^{\dagger}_{\boldsymbol{r}^{\Lambda'},b}$ and $c^{\dagger}_{\boldsymbol{r}^{\Lambda'},b} c_{\boldsymbol{r}^{\Lambda},a}$ (compare Eq.(3.18)), while the outer angle brackets represent the ground state expectation value, as in Eq.(3.15). The index notation is chosen in this way, because it has to be distinguished now in which clusters the particles are created/annihilated *and* on which sites inside the respective clusters. The former is denoted by $\boldsymbol{r}^{\Lambda}$ and $\boldsymbol{r}^{\Lambda'}$, while the latter is represented by a and b. This notation is used because it is handy on the one hand and it points out the real meaning of the single-particle Green's function in the CPT approach on the other hand, which is in fact the response of the system to the annihilation and instantaneously followed creation of a particle. One could also call this a *particle-hopping process*, where in the present work only hopping processes between neighbouring sites are considered. Therefore, the matrix elements $t_{\boldsymbol{r}\boldsymbol{r}'}$, defined as the elements of the hopping-matrix in Eq.(3.30) can only be non-zero for $\boldsymbol{r}$ and $\boldsymbol{r}'$ representing neighbouring sites.
If the clusters are decoupled, i.e. the inter-cluster hopping part $\boldsymbol{V}$ defined in Eq.(3.33) is equal to zero, the Green's function of the whole lattice γ can be written as

$$G_{\boldsymbol{r}^{\Lambda},a,\boldsymbol{r}^{\Lambda'},b}(\omega) = \delta_{\boldsymbol{r}^{\Lambda},\boldsymbol{r}^{\Lambda'}} G^{0}_{\boldsymbol{r}^{\Lambda},a,b}(\omega). \tag{3.36}$$

Obviously the Green's function is diagonal in the cluster indices in this case. $G^{0}_{\boldsymbol{r}^{\Lambda},a,b}$ denotes the Green's function of the isolated cluster, also referred to as *cluster Green's function* in the following, which can be obtained by ED for small enough cluster sizes. A detailed description of the ED approaches is provided in Subsection 3.1.3.

Applying strong-coupling perturbation theory to the problem defined by Eq.(3.32), with the expression for $\boldsymbol{V}$ in Eq.(3.33) treated as perturbation, leads to the central equation of the CPT formalism

$$\boldsymbol{G}^{-1}(\omega) = \boldsymbol{G}_{0}^{-1}(\omega) - \boldsymbol{T} \tag{3.37}$$

where $\boldsymbol{G}$ is the matrix of the lattice Green's function and $\boldsymbol{G}_0$ the matrix of the exact cluster Green's Function, while $\boldsymbol{T}$ describes the inter-cluster hopping terms, as defined in Eq.(3.33). The central equation is the lowest-order result of a cluster extension of strong-coupling perturbation theory. A

detailed derivation is provided in the appendix of Ref. [40].
It is important to point out here that the size of the matrices $\boldsymbol{G}$, $\boldsymbol{G}_0$ and $\boldsymbol{T}$ is defined by the tensor product $\lambda \otimes B$, where λ denotes the lattice points and B the band and spin states. Due to translational invariances and spin symmetry the size of the matrices can often be reduced dramatically to $\Lambda \otimes \frac{B}{2}$, where Λ stands for the lattice points of one single cluster. As in this formalism only an one-band Hubbard model is considered, B indicates only different spin states. For the further discussion the spin index B will be ignored, because the systems investigated in the present work are spin-symmetric at most times, but one should keep its existence in mind.

The derivation of CPT's central expression can also be performed in terms of a self-energy formulation [36] [38] [40]:
Recalling Dyson's equation [41] the fully interacting exact Green's function of the isolated cluster can also be written in terms of a self-energy $\boldsymbol{\Sigma}$:

$$\boldsymbol{G}_0{}^{-1}(\omega) = \boldsymbol{G}_0^{n.i.\,-1}(\omega) - \boldsymbol{\Sigma}^0(\omega) \tag{3.38}$$

with the cluster self-energy $\boldsymbol{\Sigma}^0$ and $\boldsymbol{G}_0^{n.i.}$ the non-interacting (U = 0) Green's function of the cluster

$$\boldsymbol{G}_0^{n.i.\,-1}(\omega) = \omega - \boldsymbol{T}^0. \tag{3.39}$$

Substituting the expression for the non-interacting cluster Green's function into Eq.(3.38) yields

$$\boldsymbol{G}_0{}^{-1}(\omega) = \omega - \boldsymbol{T}^0 - \boldsymbol{\Sigma}^0(\omega). \tag{3.40}$$

Similar to Eq.(3.39) the non-interacting Green's function of the entire lattice can be expressed as

$$\boldsymbol{G}^{n.i.\,-1}(\omega) = \omega - \boldsymbol{T}^{tot} = \omega - \left(\boldsymbol{T} + \boldsymbol{T}^0\right) \tag{3.41}$$

where $\boldsymbol{T}^{tot} = \boldsymbol{T} + \boldsymbol{T}^0$ is a matrix containing all hopping parameters of the entire system, i.e. the inter-cluster hopping terms in $\boldsymbol{T}$ and the intra-cluster hopping terms $\boldsymbol{T}_0$, which are only describing particle hopping process inside an isolated cluster. Combining Eq.(3.41) and Eq.(3.40) to cancel out the term $\omega - \boldsymbol{T}^0$ results in

$$\boldsymbol{G}_0{}^{-1}(\omega) = \boldsymbol{G}^{n.i.\,-1}(\omega) + \boldsymbol{T} - \boldsymbol{\Sigma}^0(\omega). \tag{3.42}$$

Finally, another Dyson equation is set up for the whole system:

$$\boldsymbol{G}^{-1}(\omega) = \boldsymbol{G}^{n.i.\,-1}(\omega) - \boldsymbol{\Sigma}(\omega) \tag{3.43}$$

where $\boldsymbol{\Sigma}$ now is the whole systems self-energy. By substituting the expression for the non-interacting Green's function, which can be obtained by rearranging Eq.(3.42), into Eq.(3.43), the final expression can be achieved:

$$\boldsymbol{G}^{-1}(\omega) = \boldsymbol{G}_0{}^{-1}(\omega) - \boldsymbol{T} - \left(\boldsymbol{\Sigma}(\omega) - \boldsymbol{\Sigma}^0(\omega)\right) \tag{3.44}$$

which is equal to CPTs central equation (see Eq.(3.37)) if and only if $\boldsymbol{\Sigma}(\omega) = \boldsymbol{\Sigma}^0(\omega)$.

In conclusion this means that the CPT method is equivalent to an approximation of the self-energy

of the entire system by the cluster self-energy. For this reason the central equation of the CPT formalism can also be expressed as

$$\boldsymbol{G}^{-1}(\omega) = \boldsymbol{G}^{n.i.\,-1}(\omega) - \boldsymbol{\Sigma}^{0}(\omega). \tag{3.45}$$

Main characteristics of the CPT formalism

According to CPTs central equation being the lowest-order result of strong-coupling perturbation theory (see Eq.(3.37)), but being also derivable in terms of proper self-energies (see Eq.(3.45)), the following main characteristics of the CPT formalism can be noted:

- Although CPT is an approximation procedure, there exist three important limiting cases in which it becomes exact:

  1. in the $U \to 0$ limit (although strong-coupling perturbation theory is used for the derivation), because the self-energy term Σ in Eq.(3.45) disappears in this non-interacting case

  2. in the so-called strong-coupling limit $t/U \to 0$, where t describes the hoppings between neighbouring C atoms. This becomes clear when the case $t \to 0$ is considered, which describes the simple atomic problem. Moreover the perturbation in the derivation of the central equation of CPT is basically the hopping parameter t (see Eq.(3.33)), so it has to be exact for $t \to 0$.

  3. in the limit of an infinite cluster size, because this would recover the exact solution of the whole considered lattice (where it depends on the particular system's size and parameters wether such a situation is approachable or not).

- CPT finally delivers an approximate single-particle Green's function for arbitrary wavevectors in the strong-coupling regime.

- Broken-symmetry states cannot be investigated using CPT. This is a major disadvantage of this approach. For the description of broken-symmetry states an extension of CPT, e.g. Variational Cluster Approach (VCA) or Cluster/Cellular Dynamical Mean Field Theory (CDMFT), can be applied.

CPT for translational invariant systems

Most of the considered systems in the present work feature a translational invariance in at least one dimension. The investigation of translational invariant systems within the scope of CPT deserves further treatment, since the division into clusters, executed in association with the CPT formalism, obviously breaks the translational symmetry of the systems lattice. Considering the superlattice Λ

generated in consequence of the applied cluster tiling in contrast, translational invariance is partly regained. However, the Brillouin zone BZ^{Λ} is reduced, in comparison to the original Brillouin zone BZ^{λ} of the whole lattice, according to [36]

$$\boldsymbol{k}^{\lambda} = \boldsymbol{K} + \boldsymbol{k}^{\Lambda} \tag{3.46}$$

where $\boldsymbol{k}^{\lambda}$ ($\boldsymbol{k}^{\Lambda}$) denotes any wavevector of the original (reduced superlattice) Brillouin Zone BZ^{λ} (BZ^{Λ}), while $\boldsymbol{K}$ belongs both to the original BZ^{λ} and to the reciprocal superlattice. Eq.(3.46) can be interpreted descriptively as follows: The whole BZ^{λ}, containing L^{λ} possible k-states, gets divided into $L^{C} = L^{\lambda}/\, L^{\Lambda}$ reduced Brillouin zones BZ^{Λ}, due to the applied cluster tiling. In this context L^{Λ} is the number of k-states in BZ^{Λ}, while L^{C} denotes the number of clusters in the superlattice Λ. The wavevectors $\boldsymbol{K}$ in this picture can be seen as the vectors pointing from the origin of the reciprocal lattice to all the BZ^{Λ} in the original BZ^{λ}.

Due to the recovered translational invariance in the superlattice Λ, the hopping matrix $T_{a,b}^{\boldsymbol{r}^{\Lambda},\boldsymbol{r}^{\Lambda'}}$ and the Green's function $G_{\boldsymbol{r}^{\Lambda},a,\boldsymbol{r}^{\Lambda'},b}(\omega)$ in CPTs central equation (see Eq.(3.37)) can be expressed in terms of $\boldsymbol{k}^{\Lambda}$. Starting out with the hopping matrix, Eq.(3.33) is re-considered, but written in a different way [40]

$$\begin{aligned} \boldsymbol{V} &= \sum_{\boldsymbol{r}^{\Lambda},\boldsymbol{r}^{\Lambda'}} \sum_{a,b} T_{a,b}^{\boldsymbol{r}^{\Lambda},\boldsymbol{r}^{\Lambda'}}\, c^{\dagger}_{\boldsymbol{r}^{\Lambda},a}\, c_{\boldsymbol{r}^{\Lambda'},b} = \sum_{\boldsymbol{r}^{\Lambda},\Delta} \sum_{a,b} T_{a,b}^{\boldsymbol{r}^{\Lambda},\boldsymbol{r}^{\Lambda}+\Delta} c^{\dagger}_{\boldsymbol{r}^{\Lambda},a}\, c_{\boldsymbol{r}^{\Lambda}+\Delta,b} \\ &= \sum_{\boldsymbol{r}^{\Lambda},\Delta} \sum_{a,b} T_{a,b}(\Delta) c^{\dagger}_{\boldsymbol{r}^{\Lambda},a}\, c_{\boldsymbol{r}^{\Lambda},b} \end{aligned} \tag{3.47}$$

where the translational invariance of the hopping matrix with respect to the superlattice Λ was used in the second line. It should be noted that the displacement term Δ in these expressions has to be given in units of the superlattice spacing and not of the original lattice λ, because $\boldsymbol{V}$ only describes hopping processes between *different* clusters of the superlattice Λ.
The creation and annihilation operators can be represented through Fourier transforms with respect to the superlattice wavevectors $\boldsymbol{k}^{\Lambda}$ [36]

$$c^{\dagger}_{\boldsymbol{r}^{\Lambda},a} = \frac{1}{\sqrt{L^{C}}} \sum_{\boldsymbol{k}^{\Lambda}} e^{i\boldsymbol{k}^{\Lambda}\boldsymbol{r}^{\Lambda}} c^{\dagger}_{\boldsymbol{k}^{\Lambda},a} \tag{3.48}$$

$$c_{\boldsymbol{r}^{\Lambda}+\Delta,b} = \frac{1}{\sqrt{L^{C}}} \sum_{\boldsymbol{k}^{\Lambda}} e^{-i\boldsymbol{k}^{\Lambda}(\boldsymbol{r}^{\Lambda}+\Delta)} c_{\boldsymbol{k}^{\Lambda},b}. \tag{3.49}$$

Applying these transformations to Eq.(3.47) after some trivial analysis results in

$$\boldsymbol{V} = \sum_{\boldsymbol{k}^{\Lambda}} \sum_{a,b} \underbrace{\left[\sum_{\Delta} T_{a,b}(\Delta) e^{-i\Delta\boldsymbol{k}^{\Lambda}} \right]}_{T_{a,b}(\boldsymbol{k}^{\Lambda})} c^{\dagger}_{\boldsymbol{k}^{\Lambda},a} c_{\boldsymbol{k}^{\Lambda},b}. \tag{3.50}$$

where $T_{a,b}(\boldsymbol{k}^{\Lambda})$ denotes the Fourier-transformed of the inter-cluster hopping terms. Finally, with this transformation of the inter-cluster hopping term $\boldsymbol{V}$ into the space of the reciprocal vectors $\boldsymbol{k}^{\Lambda}$ of the superlattices reduced BZ^{Λ}, the central equation of the CPT formalism for translational invariant

systems can be written as

$$G^{-1}_{a,b}(\omega, \boldsymbol{k}^{\Lambda}) = G^{-1}_{0_{a,b}}(\omega) - T_{a,b}(\boldsymbol{k}^{\Lambda}). \tag{3.51}$$

Comparing the gained expression with the general form of CPT's central equation (see Eq.(3.37)) it can be noticed that all quantities in the above equation still contain the cluster-indices *a* and *b*. This mixed representation (quantum numbers *a* and *b* denote sites within a *cluster*, while $\boldsymbol{k}^{\Lambda}$ denotes *superlattice* momentum vectors) is chosen, because there is one final step remaining, in the derivation of a fully momentum-dependent Green's function. It is referred to as *periodization* [42]. To express the desired fully momentum-dependent Green's function in a suitable form, another Fourier transform has to be applied - this time within the cluster:

$$\begin{aligned} G(\omega, \boldsymbol{k}^{\Lambda} + \boldsymbol{K}, \boldsymbol{k}^{\Lambda} + \boldsymbol{K}') &= \frac{1}{L} \sum_{\boldsymbol{R}_a, \boldsymbol{R}_b} e^{i(\boldsymbol{k}^{\Lambda}+\boldsymbol{K})\boldsymbol{R}_a} e^{-i(\boldsymbol{k}^{\Lambda}+\boldsymbol{K}')\boldsymbol{R}_b} G_{a,b}(\omega, \boldsymbol{k}^{\Lambda}) \\ &= \frac{1}{L} \sum_{\boldsymbol{R}_a, \boldsymbol{R}_b} e^{i\boldsymbol{k}^{\Lambda}(\boldsymbol{R}_a - \boldsymbol{R}_b)} e^{i(\boldsymbol{K}\boldsymbol{R}_a - \boldsymbol{K}'\boldsymbol{R}_b)} G_{a,b}(\omega, \boldsymbol{k}^{\Lambda}) \end{aligned} \tag{3.52}$$

where *L* is the cluster size and $\boldsymbol{R}_a$ and $\boldsymbol{R}_b$ are the corresponding position vectors of the quantum numbers *a* and *b* within the cluster, respectively, according to Eq.(3.31). The obtained Green's function would depend on *two* wavevectors $\boldsymbol{K}$ ($\boldsymbol{K'}$) and $\boldsymbol{k}^{\Lambda}$, which is certainly not correct for a periodic lattice, since these two different wavevectors were established only due to the artificial cluster tiling (see Eq.(3.46)). As mentioned above, this discrepancy can be circumvented with an appropriate periodization, which delivers the full Green's function only depending on the wavevector $\boldsymbol{k}^{\Lambda} + \boldsymbol{K}$ and on the indices of the physical unit cell. It deserves particular mention that the below Green's function only depends on $\boldsymbol{k}^{\Lambda}$ due to the periodicity of the reciprocal lattice.
Now, within CPT the Green's function is equal in each cluster, so there is no restriction in the value for $\boldsymbol{K}$ and $\boldsymbol{K} = 0$ can be chosen. As the non-diagonal elements $\boldsymbol{K} \neq \boldsymbol{K}'$ of the above expression are rather non-physical, as outlined above, $\boldsymbol{K} = \boldsymbol{K}'$ can be taken as a reasonable assumption. This delivers the important final result

$$G(\omega, \boldsymbol{k}) = \frac{1}{L} \sum_{\boldsymbol{R}_a, \boldsymbol{R}_b} e^{i\boldsymbol{k}(\boldsymbol{R}_a - \boldsymbol{R}_b)} G_{a,b}(\omega, \boldsymbol{k}) \tag{3.53}$$

where the superscript $^{(\Lambda)}$ restricting the reciprocal vectors to BZ^{Λ} was neglected (as it will also be the case in the following). The sums in Eq.(3.52) and Eq.(3.53) run over all possible pairs $\{\boldsymbol{R}_a, \boldsymbol{R}_b\}$ of translational equivalent sites in the cluster. It is worth noting here that also a periodization in terms of the self-energy $\boldsymbol{\Sigma}$ would have been possible; however, it has been shown that at least in the case of opening Mott gaps as a consequence of repulsive on-site interactions, periodizing the Green's function delivers better results [36].

A generalized expression for physical unit cells containing more than one atom can be written as [43]

$$G_{\alpha\beta}(\omega, \boldsymbol{k}) = \frac{L_{u.c.}}{L} \sum_{\boldsymbol{R}_a \in \alpha} \sum_{\boldsymbol{R}_b \in \beta} e^{ik^{\Lambda}(\boldsymbol{R}_a - \boldsymbol{R}_b)} G_{a,b}(\omega, \boldsymbol{k}) \tag{3.54}$$

where $L_{u.c.}$ is the size of the physical unit cell, while α (β) again denotes all the translational equiva-

lent sites within the cluster.

The infinite graphene lattice tiled in clusters with a size $L = 6$ is considered for example. One hexagon of the honeycomb lattice is taken as a cluster. The geometry and the labeling of the cluster sites is shown in Fig.3.2c in Section 3.2, where the equilibrium properties of pristine graphene are investigated. As for that chosen cluster tiling the cluster sites $i = \{1, 3, 5\}$ are translationally equivalent, as well as the sites $j = \{2, 4, 6\}$, the sums run over the following pairs

$$\begin{aligned}\{\boldsymbol{R}_a, \boldsymbol{R}_b\} = \{&1;1\},\{3;1\},\{5;1\},\{2;2\},\{4;2\},\{6;2\},\\ &\{1;3\},\{3;3\},\{5;3\},\{2;4\},\{4;4\},\{6;4\},\\ &\{1;5\},\{3;5\},\{5;5\},\{2;6\},\{4;6\},\{6;6\}\ .\end{aligned}$$

It should be noted already at this point that the clusters chosen for the semi-infinite GNR-geometries considered in Section 3.3 - 3.5 *do not* feature *any* translational invariant sites.

Eq.(3.51), Eq.(3.50), and Eq.(3.53) are the three key elements for the calculation of single-particle Green's functions within the CPT approach. The calculation of some important equilibrium properties, obtainable from the single-particle Green's function derived in this section, is presented in the next section. It should be remembered in this context that one is restricted to the calculation of *single*-particle Green's functions within the CPT formalism.

Quantities obtained by CPT

The derivation of some important equilibrium properties is the goal of this section. To calculate the important spectral function $A(\omega, \boldsymbol{k})$, also mentioned above, the Lehmann representation of the single-particle Green's function in Eq.(3.29) is considered again:

$$\begin{aligned}G^0_{\mu\nu}(\omega) &= \sum_n \left\langle \psi_0 \left| c_\mu \right| \psi_n^{N+1} \right\rangle \frac{1}{\omega + E_0 - E_n^{N+1} + i\eta} \left\langle \psi_n^{N+1} \left| c_\nu^\dagger \right| \psi_0 \right\rangle \\ &+ \zeta \sum_m \left\langle \psi_0 \left| c_\nu^\dagger \right| \psi_m^{N-1} \right\rangle \frac{1}{\omega - E_0 + E_m^{N-1} + i\eta} \left\langle \psi_m^{N-1} \left| c_\mu \right| \psi_0 \right\rangle \end{aligned} \tag{3.55}$$

(recall the compound indices μ, ν standing for cluster site and spin at once). What follows is the derivation of a computing scheme for the single-particle Green's function using so-called *Q-Matrices*. The basics for the Q-Matrix formalism are outlined here in detail [36], because they will be of major importance also in the following sections considering ED.

Q-Matrix formalism for exact cluster Green's function

Introducing the notation

$$Q^{(e)}_{\mu n} = \left\langle \psi_0 \left| c_\mu \right| \psi_n^{N+1} \right\rangle \qquad\qquad Q^{(h)}_{\nu n} = \left\langle \psi_0 \left| c_\nu^\dagger \right| \psi_n^{N-1} \right\rangle$$

$$\omega_n^{(e)} = E_n^{N+1} - E_0 > 0 \qquad\qquad \omega_m^{(h)} = -E_n^{N-1} + E_0 < 0$$

where the superscripts $^{(e)}$ and $^{(h)}$ (short hand for *electron part* and *hole part*) label the Q-Matrix for the $(N+1)$ - and $(N-1)$ - particle state, respectively, allows for writing Eq.(3.55) as

$$G^0_{\mu\nu}(\omega) = \sum_n \frac{Q^{(e)}_{\mu n} Q^{(e)*}_{\nu n}}{\omega - \omega^{(e)}_n} + \sum_m \frac{Q^{(h)}_{\mu m} Q^{(h)*}_{\nu m}}{\omega - \omega^{(h)}_m} \tag{3.56}$$

where ω stands for $\omega + i\eta$. The size of the $Q^{(e)}_{\mu n}$-matrix is $2L$ x $N^{(e)}$, where $N^{(e)}$ is a number counting all the states $\left|\psi_n^{N+1}\right\rangle$ giving a non-zero contribution to the sum above and L is the size of the cluster. Similar to that, $Q^{(h)}_{\nu m}$ represents a $2L$ x $N^{(h)}$ matrix, where the same definition as above applies to $N^{(h)}$. The expression for the cluster Green's function can be further compressed by writing $Q^{(e)}_{\mu n}$ and $Q^{(h)}_{\nu m}$ as one matrix and $\omega^{(e)}_n$ and $\omega^{(h)}_m$ as one vector, respectively, like

$$\boldsymbol{Q} = \begin{bmatrix} \boldsymbol{Q}^{(e)} \\ \boldsymbol{Q}^{(h)} \end{bmatrix} \qquad\qquad \boldsymbol{\omega} = \begin{bmatrix} \boldsymbol{\omega}^{(e)} & \boldsymbol{\omega}^{(h)} \end{bmatrix} \tag{3.57}$$

where the resulting matrix and vector sizes, respectively, are

$$\boldsymbol{Q} = [2L \times N] \qquad\qquad \boldsymbol{\omega} = [N]$$

with $N = N^{(e)} + N^{(h)}$. Eq.(3.57) together with the above definitions basically defines the Q-Matrix formalism. To put this formalism into words, the matrix element $Q_{\mu r}$ can be interpreted as the (N-particle) ground state expectation value of the annihilation (creation) operator applied to the μ-th site of the r-th eigenstate of the systems Hamiltonian, where $r = \{1 \ldots r_n\}$ describes eigenstates with $N+1$ particles, while the remaining indices r_{n+1}, r_{n+2}, ... label eigenstates with $N-1$ particles. The superscripts $^{(e)}$ and $^{(h)}$ can be interpreted in this context as labels of the *"plus one electron (e)"*-states and the *"plus one hole (h)"*-states, respectively.
Using these new definitions, the cluster Green's function can be written as

$$G^0_{\mu\nu}(\omega) = \sum_r \frac{Q_{\mu r} Q^*_{\nu r}}{\omega - \omega_r} \tag{3.58}$$

which can be further transformed to a compact matrix product form

$$\boldsymbol{G}^0(\omega) = \boldsymbol{Q}\boldsymbol{g}(\omega)\boldsymbol{Q}^\dagger \tag{3.59}$$

where the diagonal matrix $\Gamma_{rs} = \delta_{rs}\omega_r$ has been introduced to write the denominator of Eq.(3.58) in its matrix representation

$$\boldsymbol{g}(\omega) = \frac{1}{\omega - \Gamma}. \tag{3.60}$$

Q-Matrix formalism for Green's function of translational invariant systems

The derived expression in Eq.(3.59) represents the exact cluster Green's function in a very general way. Now, this expression can be further used to bring the central equation of the CPT formalism for *translational invariant* systems into the most suitable form for its calculation. A rearranged form of Eq.(3.51) is the starting point of the following derivation [43] [44]

$$\begin{aligned} \boldsymbol{G}(\omega,\boldsymbol{k}) &= \left(\mathbb{1}-\boldsymbol{G}^0(\omega)\boldsymbol{T}(\boldsymbol{k})\right)^{(-1)}\boldsymbol{G}^0(\omega) \\ &= \left(\mathbb{1}-\boldsymbol{Q}\boldsymbol{g}(\omega)\boldsymbol{Q}^\dagger T(\boldsymbol{k})\right)^{(-1)}\boldsymbol{Q}\boldsymbol{g}(\omega)\boldsymbol{Q}^\dagger \end{aligned} \tag{3.61}$$

where the Q-Matrix representation of the cluster Green's function (see Eq.(3.59)) was was used in the second line. Applying a taylor expansion of the fraction, according to

$$\frac{1}{1-x} = 1 + x + ...$$

yields

$$\begin{aligned} \boldsymbol{G}(\omega,\boldsymbol{k}) &= \left(\mathbb{1}+\boldsymbol{Q}\boldsymbol{g}(\omega)\boldsymbol{Q}^\dagger T(\boldsymbol{k})+...\right)\boldsymbol{Q}\boldsymbol{g}(\omega)\boldsymbol{Q}^\dagger \\ &= \left(\boldsymbol{Q}\boldsymbol{g}(\omega)+\boldsymbol{Q}\boldsymbol{g}(\omega)\boldsymbol{Q}^\dagger T(\boldsymbol{k})\boldsymbol{Q}\boldsymbol{g}(\omega)+...\right)\boldsymbol{Q}^\dagger \\ &= \boldsymbol{Q}\boldsymbol{g}(\omega)\left(\mathbb{1}+\boldsymbol{Q}^\dagger T(\boldsymbol{k})\boldsymbol{Q}\boldsymbol{g}(\omega)+...\right)\boldsymbol{Q}^\dagger \\ &= \boldsymbol{Q}\frac{1}{\boldsymbol{g}^{-1}(\omega)-\boldsymbol{Q}^\dagger T(\boldsymbol{k})\boldsymbol{Q}}\boldsymbol{Q}^\dagger \end{aligned} \tag{3.62}$$

where some elementary analysis has been performed in the second and third line, while in the last line the terms of the taylor expansion has been recollected. Now, Eq.(3.60) can be used again to further simplify the expression, like

$$\begin{aligned} \boldsymbol{G}(\omega,\boldsymbol{k}) &= \boldsymbol{Q}\frac{1}{\omega-\Gamma-\boldsymbol{Q}^\dagger T(\boldsymbol{k})\boldsymbol{Q}}\boldsymbol{Q}^\dagger \\ &= \boldsymbol{Q}\frac{1}{\omega-\boldsymbol{M}(\boldsymbol{k})}\boldsymbol{Q}^\dagger \end{aligned} \tag{3.63}$$

where the matrix

$$\begin{aligned} \boldsymbol{M}(\boldsymbol{k}) &= \Gamma-\boldsymbol{Q}^\dagger T(\boldsymbol{k})\boldsymbol{Q} \\ [N\times N] &= [N\times N]-[N\times L][L\times L][L\times N] \end{aligned} \tag{3.64}$$

has been introduced. The second line indicates the matrix dimensions, with N defined below Eq.(3.57) and L denoting the cluster size. It is important to note here that the above expression for the CPT Green's function of the whole lattice is still equivalent to CPTs central equation. Furthermore, the energy dependency (ω) appears nicely separated from the wavevector dependency ($\boldsymbol{k}$). Considering Eq.(3.63) again, it is obvious that the poles of the central part $[\omega-\boldsymbol{M}(\boldsymbol{k})]^{-1}$ will also

appear in the resulting Green's function. To find the energy values of these poles is an easy task, since they are exactly the eigenvalues of the introduced $N \times N$ matrix $\boldsymbol{M}(\boldsymbol{k})$. By diagonalizing this matrix in a final step, according to

$$\boldsymbol{U}(\boldsymbol{k})\boldsymbol{M}(\boldsymbol{k})\boldsymbol{U}^{\dagger}(\boldsymbol{k}) = \widetilde{\Gamma}(\boldsymbol{k}) \tag{3.65}$$

where $\widetilde{\Gamma}(\boldsymbol{k})$ is a diagonal matrix containing the $\boldsymbol{k}$-dependent excitation energies of the whole physical system and $\boldsymbol{U}(\boldsymbol{k})$ the unitary transformation matrix, the central fraction appearing in Eq.(3.63) can be rewritten as

$$\frac{1}{\omega - \boldsymbol{M}(\boldsymbol{k})} = \boldsymbol{U}(\boldsymbol{k})\frac{1}{\omega - \widetilde{\Gamma}(\boldsymbol{k})}\boldsymbol{U}^{\dagger}(\boldsymbol{k}). \tag{3.66}$$

This leads to a compact expression for the Green's function of a system with translational invariance:

$$\begin{aligned} \boldsymbol{G}(\omega, \boldsymbol{k}) &= \boldsymbol{Q}\frac{1}{\omega - \boldsymbol{M}(\boldsymbol{k})}\boldsymbol{Q}^{\dagger} = \boldsymbol{Q}\boldsymbol{U}(\boldsymbol{k})\frac{1}{\omega - \widetilde{\Gamma}(\boldsymbol{k})}\boldsymbol{U}^{\dagger}(\boldsymbol{k})\boldsymbol{Q}^{\dagger} \\ &= \widetilde{\boldsymbol{Q}}(\boldsymbol{k})\frac{1}{\omega - \widetilde{\Gamma}(\boldsymbol{k})}\widetilde{\boldsymbol{Q}}^{\dagger}(\boldsymbol{k}). \end{aligned} \tag{3.67}$$

It has to be noted that the derived expression for the CPT Green's function of the entire lattice is of the same form as the expression derived for the cluster Green's function in Eq.(3.59), where only the diagonal matrix Γ was replaced by $\widetilde{\Gamma}(\boldsymbol{k})$ (see Eq.(3.65)) and the Q-Matrices were unitary transformed by $\widetilde{\boldsymbol{Q}}(\boldsymbol{k}) = \boldsymbol{Q}\boldsymbol{U}(\boldsymbol{k})$. The $\boldsymbol{k}$-dependent quantities $\widetilde{\boldsymbol{Q}}$ and $\widetilde{\Gamma}$ can be seen as the equivalents to $\boldsymbol{Q}$ and Γ defined in Eq.(3.57) and Eq.(3.60) in the derivation of the expression for the cluster Green's function within the Q-Matrices formalism, respectively.
Because of these similar Lehmann structures for $\boldsymbol{G}^0(\omega)$ and $\boldsymbol{G}(\omega, \boldsymbol{k})$, some equivalent properties can be obtained. The final expressions for the full CPT Green's function and the cluster Green's functions have poles only on the real axis and the residues are positive [36]. This guarantees on the one hand that the corresponding spectral function $A(\omega, \boldsymbol{k})$ (see below) is strictly positive. On the other hand $\boldsymbol{Q}\boldsymbol{Q}^{\dagger} = 1$ ($\widetilde{\boldsymbol{Q}}\widetilde{\boldsymbol{Q}}^{\dagger} = 1$) can be shown, which ensures that the spectral function is normalized. Due to the non-hermitian structure of $\boldsymbol{Q}$ ($\widetilde{\boldsymbol{Q}}$) this relation does not hold for the conjugated product, i.e. $\boldsymbol{Q}^{\dagger}\boldsymbol{Q} \neq 1$ ($\widetilde{\boldsymbol{Q}}^{\dagger}\widetilde{\boldsymbol{Q}} \neq 1$).

Calculation scheme for obtaining the lattice Green's function using CPT

Before the focus is finally laid on the calculation of the spectral function and the DOS in equilibrium, a *calculation scheme* for obtaining the lattice Green's function of a physical system with translational invariances is outlined:

1. Applying an appropriate cluster tiling with small enough cluster sizes, to make them exactly solvable in further consequence (see Fig.3.1)

2. Solving the clusters exactly, i.e.:

   a) Setting-up the cluster Hamiltonian within the 2d Hubbard model as defined in Eq.(3.30)

b) Solving the eigenvalue problem of the cluster Hamiltonian using a particular *cluster solver*, e.g. the ED method (which is described in the following Subsection 3.1.3)

c) Calculating the corresponding Q-Matrices defined in Eq.(3.56)

d) Obtaining the single-particle cluster Green's function using the Lehmann representation in Eq.(3.59)

3. Setting-up the inter-cluster hopping matrix $\boldsymbol{T}(\boldsymbol{k})$ in consistence with the chosen cluster tiling, according to Eq.(3.50)

4. Obtaining the single-particle Green's function of the whole considered physical system, now using the Lehmann represenation in Eq.(3.67), preliminarily evaluating the expressions is Eq.(3.64) and Eq.(3.65).

5. Periodizing the obtained Green's function to consider also translational invariances occurring inside the cluster, according to Eq.(3.54).

The spectral function

The single-particle spectral function of a physical system, mentioned repeatedly above, is eventually discussed now. It is defined by [32]

$$A(\omega, \boldsymbol{k}) = -\frac{1}{\pi}\Im\left\{G^R(\omega, \boldsymbol{k})\right\} \tag{3.68}$$

where $G^R(\omega, \boldsymbol{k})$ is the retarded component of the lattice Green's function defined in Eq.(3.21), which can be obtained with the ω-transformation introduced in Eq.(3.28), where it is crucial here that $\eta = 0^+$ is a *positive* infinitesimal to get the retarded component.
To interpret this definition, the expression for the retarded Green's function from Eq.(3.67) is used to write

$$A(\omega, \boldsymbol{k}) = -\frac{1}{\pi}\Im\left\{\widetilde{\boldsymbol{Q}}(\boldsymbol{k})\frac{1}{\omega - \widetilde{\Gamma}(\boldsymbol{k})}\widetilde{\boldsymbol{Q}}^\dagger(\boldsymbol{k})\right\}. \tag{3.69}$$

Furthermore, the identity

$$\Im\left\{\frac{1}{x + i\eta}\right\} = -\frac{\eta}{x^2 + \eta^2} \underset{\eta\to 0}{=} -\pi\delta(x) \tag{3.70}$$

with $x \in \Re$, can be used to rewrite the above expression for the spectral function as

$$A(\omega, \boldsymbol{k}) = \widetilde{\boldsymbol{Q}}(\boldsymbol{k})\delta\left[\omega - \omega_r(\boldsymbol{k})\right]\widetilde{\boldsymbol{Q}}^\dagger(\boldsymbol{k}) \tag{3.71}$$

since $\widetilde{\boldsymbol{Q}}(\boldsymbol{k})$, $\widetilde{\Gamma}(\boldsymbol{k}) \in \Re$. The $\boldsymbol{k}$-dependent excitation energies of the overall system were denoted as $\omega_r(\boldsymbol{k})$ in this context.
The obtained expression can be interpreted as follows: The spectral function $A(\omega, \boldsymbol{k})$ is a three-dimensional function with delta-peaks in the z-direction, at every excitation energy of the system $\omega_r(\boldsymbol{k})$. Moreover, by regarding a *top view* of this three-dimensional function, i.e. looking at the ω-

$\boldsymbol{k}$-plane from above, the important *energy-momentum dispersion relation* $\omega(\boldsymbol{k})$ or $E(\boldsymbol{k})$ is obtained. The energy-momentum dispersion relation is a very important equilibrium property of a physical system, since it provides the viewer with *all* energy bands corresponding to the first BZ. The number of energy bands $L_{e.b.}$ in the first BZ is determined by the following rule [45]:
The size of the physical unit cell, which is the smallest possible unit (i.e. which contains the smallest number of atoms) that can be found and used to built up the lattice, determines how many energy bands there are expected to be found in the energy-momentum dispersion relation. If $L_{u.c.}$ is the number of atoms in the physical unit cell, then the number of energy bands

$$L_{e.b.} = L_{u.c.}. \tag{3.72}$$

This rule will be important to remember in Sec.3.2 - 3.5, where the energy-momentum dispersion relation $\omega(\boldsymbol{k})$ is calculated for pristine 2d graphene, as well as for several different GNR structures, because the size of the physical unit cell is proportional to the GNRs width. Therefore, the number of bands in the dispersion relation of GNRs is expected to grow with increasing width.
Considering the mathematical form of Eq.(3.71), it becomes clear now that the spectral function has to be positive for all possible values of ω and $\boldsymbol{k}$, since the Q-Matrices are strictly positive by definition (see above Eq.(3.56)).

The single-particle energy gap

Another interesting equilibrium quantity is the single-particle energy gap Δ, which is obtainable directly from the energy-momentum dispersion relation by taking the difference between the smallest positive and the largest negative energy-value

$$\Delta = \min\left\{ E(\boldsymbol{k})|_{E>0} \right\} - \max\left\{ E(\boldsymbol{k})|_{E<0} \right\}. \tag{3.73}$$

An analogous formula for the single-particle energy gap is obtainable by re-considering Eq.(3.65), where $\widetilde{\Gamma}(\boldsymbol{k})$ was defined as a diagonal matrix containing the $\boldsymbol{k}$-dependent excitation energies of the whole physical system. With this quantity at hand, the single-particle energy gap can be calculated also by

$$\Delta = \min\left\{ \omega_r(\boldsymbol{k})|_{\omega_r>0} \right\} - \max\left\{ \omega_r(\boldsymbol{k})|_{\omega_r<0} \right\} \tag{3.74}$$

where $\omega_r(\boldsymbol{k})$ denotes the $\boldsymbol{k}$-dependent excitation energies of the overall system, as defined above. This second expression is convenient, since the $\omega_r(\boldsymbol{k})$-values were already introduced and used in the derivation of the compact expression for the total lattice Green's function $\boldsymbol{G}(\omega, \boldsymbol{k})$ (see Eq.(3.67)). Therefore, the spectral function *do not have to be calculated* in order to obtain the energy gap Δ (though most of the time both quantities will be calculated, to get a comprehensive picture of the possible energy-states in the system).

The (local) electronic density-of-states

When investigating a systems non-equilibrium properties, knowledge about the electrons' possible energy-states within the system is crucial for a comprehensive understanding. This knowledge is provided by the DOS and/ or LDOS of a system, where the former delivers the possible energy states within the total lattice (system), while the latter provides information about the possible energy states at a specific site in the lattice (or cluster).

Commonly, the DOS is defined as

$$\rho(\omega) = \frac{1}{N_{1^{st}BZ}} \sum_{\boldsymbol{k}} A(\omega, \boldsymbol{k}) \tag{3.75}$$

where $N_{1^{st}BZ}$ denotes the number of possible $\boldsymbol{k}$-states in the first BZ of the lattice. Taking into account the definition of the spectral function $A(\omega, \boldsymbol{k})$ in Eq.(3.68), the expression can be transformed into a form solely depending on the retarded Green's function:

$$\rho(\omega) = -\frac{1}{\pi N_{1^{st}BZ}} \sum_{\boldsymbol{k}} \Im \left\{ tr \left[G^R(\omega, \boldsymbol{k}) \right] \right\} \tag{3.76}$$

where $tr\{\}$ denotes the trace of an operator or matrix O according to

$$tr\{O\} := \sum_{i,j} O_{ij}\delta_{ij} = \sum_{i} O_{ii} \tag{3.77}$$

with the matrix element O_{ij}.

The obtained formula can also be used to calculate the LDOS at a specific site i by simply taking the $i-th$ diagonal component of $G^R(\omega, \boldsymbol{k})$:

$$\rho_i(\omega) = -\frac{1}{\pi N_{1^{st}BZ}} \sum_{\boldsymbol{k}} \Im \left\{ G^R_{ii}(\omega, \boldsymbol{k}) \right\}. \tag{3.78}$$

The DOS (LDOS) as well as the energy-momentum dispersion relation and the corresponding energy gap will be calculated for pristine 2d graphene and several GNR geometries in Sec.3.2 - 3.5. Before this sections are presented, the ED methods used in the present work for solving the clusters introduced by the CPT formalism are outlined and explained in the next subsection.

3.1.3 Exact Diagonalization

As already mentioned above, the size of the clusters used within the CPT formalism is chosen small enough to allow for an *exact solution* of the corresponding eigenvalue problem. An exact solution in this special case includes the exact calculation of the clusters ground state and, furthermore, the calculation of the exact cluster Green's function. It was described in the previous subsection that in order to calculate the cluster Green's function exactly, the solution of the eigenvalue problem (i.e.

Schrödingers equation for a quantum many-body system)

$$\boldsymbol{H}\,|\psi_n\rangle = E_n\,|\psi_n\rangle \tag{3.79}$$

is required, including the ground state $|\psi_0\rangle$ with the corresponding ground state E_0, as well as *some* of the eigenstates $|\psi_n\rangle$ with their respective eigenenergies E_n. The word *some* is crucial to understand in this context: Numerical ED *does absolutely not mean* to calculate all eigenstates (eigenvalues) of the considered Hamiltonian. Since the expenditure of time for a full diagonalization of a (hermitian) Hamilton matrix is on the order of $O(D^3)$ [46], where D denotes the dimension of the systems Hilbert space, which can quickly reach an order of $O(10^5)$ for fairly simple systems, and the necessary memory requirement is on the order of $O(D^2)$, completely solving the eigenvalue problem is far beyond the scope of state-of-the art numerics and computers. Fortunately, it is however not necessary to do so since physically, the ground state together with the low lying excited states are the most relevant for determining the systems physical behaviour in most cases. Due to the iterative characteristics of the particular applied methods (explained in detail in the following), the contribution of eigenstates with large corresponding eigenenergies is rather small.
A detailed explanation of how much memory is actually needed for specific systems is not given here, but can be found in Ref. [46]. One really important fact should be pointed out, though: The dimension D of the Hilbert space grows exponentially with the size of the investigated system [47]. Therefore, it is crucial wether the chosen clusters have a size $L = 6$ or $L = 8$. In exactly these two cases a major difference in the appliable ED methods arises, namely the difference between *full solvers* and *sparse solvers*.
Full solvers usually have to save the total Hamiltonian matrix, which indeed requires a large amount of memory ($O(D^2)$) on the one hand, but delivers the full spectrum of eigenvalues with corresponding eigenstates on the other hand. The general upper limit in the number of sites for an application of an ED method, is reached at about $L = 25$ sites [40].
A lot of applications feature an extremely sparse Hamilton matrix $\boldsymbol{H}$ (i.e. $\boldsymbol{H}$ contains only a few non-zero elements). Due to this fact, it is appropriate to use a certain sparse form for the storing of the Hamiltonian matrix, where the memory effort for a Hamiltonian matrix in sparse form only scales like $O(D)$. The corresponding ED methods are called *sparse solvers*.

It should be mentioned here that the solution of the eigenvalue problem is required not only in the case where the single-particle Green's function has to be calculated. Moreover, it is *the* precondition for the evaluation of any observables or correlation functions in many-body physics.

So, what is the basic idea behind ED? The basic ingredient of every ED method is a coding of an exact representation of the Hamiltonian action on arbitrary state vectors [36], where it was already discussed that this coding does not necessarily suppose an explicit construction of the Hamiltonian matrix. Afterwards, the ground state is obtained in a quasi-exact way by an iterative method, subsequently followed by the calculation of any correlation or Green's function by similar means. Two important ED methods are described in the following subsections, where the *Lanczos algorithm* [48] makes the start in Sec. 3.1.3.1, followed by a generalization of this procedure, namely the *Band Lanczos algorithm* [49] in Sec. 3.1.3.2.

3.1.3.1 The Lanczos algorithm

Before the basic principle of the Lanczos algorithm is outlined, a few words should be said about the *coding of the basis states*. In general a basis state with $n_{i\uparrow}$ ($n_{i\downarrow}$) spin-up (spin-down) particles at site i may be expressed in terms of creation operators as

$$\left(c_{1\uparrow}^{\dagger}\right)^{n_{1\uparrow}} ... \left(c_{L\uparrow}^{\dagger}\right)^{n_{L\uparrow}} \left(c_{1\downarrow}^{\dagger}\right)^{n_{1\downarrow}} ... \left(c_{L\downarrow}^{\dagger}\right)^{n_{L\downarrow}} |0\rangle \tag{3.80}$$

where the chosen arrangement of the creation operators is not unique, i.e. it is a matter of convention. To save memory, basis states are numerically represented as a single number, which is an integer number representation of a binary number containing a 1 at occupied orbitals (i.e. site-index and spin), e.g.

$$n_{bin} = |0000110101010\rangle \rightarrow n_{int} = 426.$$

To reconstruct the physical situation defined by Eq. (3.80), the order in which the creation operators are applied has to be known. Detailed explanations on an actual coding scheme and the corresponding way of setting up the Hamiltonian numerically effective can be found in Refs. [36] [46].

Once the Hamiltonian is set up in a chosen basis matrix representation H, wether full or sparse, the Lanczos method [48] can be applied. In general the Lanczos algorithm is an iterative projection method, which in the end provides the ground state of a matrix too large to be fully diagonalized.
The basic idea is to construct an approximately invariant subspace of H, i.e. building a projection $\mathcal{H}$ onto the so-called Krylov subspace

$$\mathcal{H} = span\left\{|\phi_0\rangle, H|\phi_0\rangle, H^2|\phi_0\rangle, ..., H^M|\phi_0\rangle\right\}, \qquad M < N-1 \tag{3.81}$$

where $|\phi_0\rangle$ is a random start vector and N is the dimension of the Hamilton matrix. In general, a subspace $\mathcal{G}$ is called *invariant*, if

$$|\phi\rangle \in \mathcal{G} \Rightarrow H|\phi\rangle \in \mathcal{G}$$

for every element $|\phi\rangle$ of the subspace [40]. After M iterations an approximation for the ($N \times N$) - matrix H can be obtained by projecting it to the Krylov subspace $\mathcal{H}$ defined above, which can be performed by the following transformation

$$\widetilde{H} \approx G^T H G \tag{3.82}$$

where G is a ($N \times M$) - matrix, containing the basis vectors of the constructed Krylov-space $|\phi_0\rangle$, $H|\phi_0\rangle, ..., H^M|\phi_0\rangle$ as columns. This is in direct accordance to an expansion of the Krylov-space by one more element, yielding

$$\left\{H|\phi_0\rangle, H^2|\phi_0\rangle, ..., H^M|\phi_0\rangle, H^{M+1}|\phi_0\rangle\right\}.$$

The approximation of the Hamilton matrix H in Eq.(3.82) is justified in the case, where one is *only* interested in the *extreme* eigenvalues of H, with their corresponding eigenvectors. In fact, this approximation scheme is applicable on all accounts, when the interested quantity is the Hamiltonians

ground state, as proofed in the following:

Considering a large value for M, the following convergence behaviour can be found, by writing the random start vector $|\phi_0\rangle$ in the eigenbasis of H [40]:

$$\begin{aligned} H^M |\phi_0\rangle &= H^M \sum_{j=0}^{N} c_j |\psi_j\rangle \\ &= \sum_{j=0}^{N} c_j \epsilon_j^M |\psi_j\rangle \\ &= c_0 \epsilon_0^M \left(|\psi_0\rangle + \sum_{j=0}^{N} \frac{c_j}{c_0} \left(\frac{\epsilon_j}{\epsilon_0} \right)^M |\psi_j\rangle \right) \end{aligned} \tag{3.83}$$

where the eigenvalues ϵ_j and eigenvectors $|\psi_j\rangle$ of H were introduced, and in the second line the spectral theorem was used. Assuming $|\epsilon_0| > |\epsilon_j|$ for $j > 0$, the second part in the brackets of the gained equation vanishes, leaving the final result

$$H^M |\phi_0\rangle \approx c_0 \epsilon_0^M |\psi_0\rangle \tag{3.84}$$

for large values of M. The discovered behaviour can be interpreted as follows: The last element of the constructed Krylov-space in Eq.(3.81) $H^M |\phi_0\rangle$ is proportional to the eigenvector $|\psi_0\rangle$ of H, belonging to the *largest* eigenvalue. The proportional constant is determined by the largest eigenvalue ϵ_0^M of the M-times multiple H^M of the Hamilton matrix, which means that the ground state energy ϵ_0 can be obtained in this manner.

The practical implementation of the Lanczos algorithm, including all the individual steps, is outlined in the following. As already explained above, the starting point of the iteration is a random state vector $|\phi_0\rangle$. It has to be noted here that it is not completely arbitrarily to choose, since it is of major importance that the start vector has a non-zero overlap with the ground state. The reason for this will be clear in an instant. In general, there is no information of the ground state available. In this case, choosing an initial state with randomly chosen coefficients most of the times serves its purpose.
Next, the introduced Krylov-space has to be spanned by an iterative application of H, according to Eq.(3.81). The generating states of the Krylov-space are not mutually orthogonal. In order to generate a sequence of orthogonal vectors, the following recursion rule is used [36]:

$$\begin{aligned} |\phi_{n+1}\rangle &= H |\phi_n\rangle - a_n |\phi_n\rangle - b_n^2 |\phi_{n-1}\rangle \\ a_n &= \frac{\langle \phi_n | H |\phi_n\rangle}{\langle \phi_n | \phi_n\rangle} \\ b_n &= \frac{\langle \phi_n | \phi_n\rangle}{\langle \phi_{n-1} | \phi_{n-1}\rangle} \end{aligned} \tag{3.85}$$

with the initial conditions set to $b_0 = 0$, $|\phi_{n-1}\rangle = 0$. The vector $|\phi_n\rangle$ corresponds to the n^{th} element of the constructed Krylov-space. It can be shown easily (e.g. by using an inductive method of proof) that the generated set of vectors is orthogonal.
Using this generated set of vectors in a normalized form, the Hamilton matrix H in the Krylov basis

$|\phi_n\rangle$ has the tridiagonal form

$$\widetilde{H} = \begin{pmatrix} a_0 & b_1 & 0 & 0 & ... & 0 \\ b_1 & a_1 & b_2 & 0 & ... & 0 \\ 0 & b_2 & a_2 & b_3 & ... & 0 \\ 0 & 0 & b_3 & a_3 & ... & 0 \\ \vdots & \vdots & \vdots & \vdots & \ddots & \vdots \\ 0 & 0 & 0 & 0 & ... & a_N \end{pmatrix}. \tag{3.86}$$

Since there exist fast standard methods dedicated to solve the eigenvalue problem of tridiagonal matrices, obtaining the ground state of H in the Krylov basis is a rather easy task. As already mentioned above, this ground state energy of $\widetilde{H}$ in the Krylov basis converges to the desired ground state energy ϵ_0 of H in the original basis when the number of iterations M becomes large enough.
The last remaining thing to do is transforming the gained ground state eigenvector $\left|\widetilde{\psi_0}\right\rangle$ of $\widetilde{H}$ back into the original basis, to obtain the ground state eigenvector $|\psi_0\rangle$ of H. According to the transformation rule used to approximate H by $\widetilde{H}$ (see Eq.(3.82)), the ground state $|\psi_0\rangle$ of the original Hamilton matrix can be caluculated by

$$|\psi_0\rangle = G\left|\widetilde{\psi_0}\right\rangle \tag{3.87}$$

where G again contains the basis vectors $|\phi_n\rangle$ of the Krylov space as columns.

The Lanczos algorithm is a powerful and efficient procedure for obtaining the ground state energy and vector of a large Hamiltonian not fully diagonalizable anymore. There is a convergence criterion, though, which determines how much time is needed to be spent to reach convergency. As long as the ground state energy ϵ_0 is well separated from the next eigenenergy ϵ_1, convergence is reached fast. The algorithm is slowed down continuously as $|\epsilon_0 - \epsilon_1|$ gets smaller.
The Lanczos algorithm is used in the present work to obtain the ground state properties (ϵ_0 and ψ_0) of particular Hamiltonians. To calculate the single-particle Green's function of the investigated physical systems, the algorithm explained in detail in this subsection needs to be further developed, ending up in a continued-fraction representation of the frequency dependent Green's function [36]. The described procedure is not explained in detail here, since it is not used in the present work. However, there exists an extended version of the Lanczos algorithm that on the one hand works a good piece faster than the Lanczos method introduced here, and on the other hand provides the Green's function in the convenient Lehmann representation. An introduction to this *Band* Lanczos algorithm is presented in the next subsection.

3.1.3.2 The Band Lanczos algorithm

The procedure introduced in this subsection is an alternative to the Lanczos algorithm and can be used to calculate the single-particle Green's function defined in Eq.(3.18). Conveniently, it will provide the Green's function in the Lehmann representation, introduced in Sec. 3.1.1.
Essentially the Band Lanczos algorithm is a generalization of the Lanczos method where the introduced Krylov space is not only spanned by the multiple action of Hamilton operators on *one state*, but on *many*. What follows is a schematic outline of the basics of the Band Lanczos algorithm.

Further information about the details is provided in Ref. [49].

As spin generally is conserved in the basic Hubbard model, the explanation of the Band Lanczos method can be restricted to up-spin electrons, resulting in a $L \times L$ single-particle Green's function, where L is the number of cluster sites. Considering also down-spin electrons would result in a $2L \times 2L$ block diagonal matrix representation of the Green's function. Anyways, in the picture of up-spin electrons only, the start vector consists of the L states

$$|\phi_\mu\rangle = c_\mu^\dagger |\psi_0\rangle \quad \text{with } \mu = 1 \dots L. \tag{3.88}$$

It is important to point out that in contrast to the normal Lanczos method, the start vector for the Band Lanczos algorithm *is not chosen randomly* here. Moreover, it is specifically demanded that the start vector consists of states with $N+1$ particles, where N denotes the number of particles in the ground state $|\psi_0\rangle$, formerly obtained with the Lanczos algorithm. The reason for this specific choice becomes clear, when recalling the definition of the Q-Matrices introduced in the derivation of a compact expression for Green's functions in Lehmann representation (see Eq.(3.56) and above in Sec. 3.1.2):
Since the Band Lanczos algorithm is a method providing the excited states $|\psi_n\rangle$ of the Hamilton matrix H, this choice for the start vector is obviously taken to obtain the $(N+1)$ particle excited states $\left|\psi_n^{N+1}\right\rangle$, which finally lead to the electron part of the Q-Matrix

$$Q_{\mu n}^{(e)} = \left\langle \psi_0 \left| c_\mu \right| \psi_n^{N+1} \right\rangle .$$

In the same way the hole part of the Q-Matrix can be obtained with the Band Lanczos method by taking the L $(N-1)$ particle states $|\phi_\mu\rangle = c_\mu |\psi_0\rangle$ $(\mu = 1 \dots L)$ as a start vector. This can be summarized in the following way

$$\text{start vector: } \left\{ |\phi_1\rangle = c_1^\dagger |\psi_0\rangle , |\phi_2\rangle = c_2^\dagger |\psi_0\rangle , \dots , |\phi_L\rangle = c_L^\dagger |\psi_0\rangle \right\} \xrightarrow{\textit{BandLanczos}} Q_{\mu n}^{(e)}$$
$$\text{start vector: } \left\{ |\phi_1\rangle = c_1 |\psi_0\rangle , |\phi_2\rangle = c_2 |\psi_0\rangle , \dots , |\phi_L\rangle = c_L |\psi_0\rangle \right\} \xrightarrow{\textit{BandLanczos}} Q_{\mu n}^{(h)}$$

which leads to the final statement that the Band Lanczos algorithm can be used for obtaining the frequency dependent cluster Green's function using the Q-Matrix formalism (see Eq.(3.67)). The diagonal matrix $\widetilde{\Gamma}(\boldsymbol{k})$ containing the excitation energies of H corresponding to the $(N+1)$ and $(N-1)$ states, which is needed for the evaluation of Eq.(3.67), is also provided within the Band Lanczos algorithm, as shown below.

Next, the individual steps of the Band Lanczos algorithm are schematically outlined:
First, the Krylov space is constructed with the discussed start vector $\{|\phi_1\rangle , |\phi_2\rangle , \dots , |\phi_L\rangle\}$

$$\mathcal{H} = \textit{span} \left\{ |\phi_1\rangle , |\phi_2\rangle , \dots , |\phi_L\rangle , H' \ |\phi_1\rangle , H' |\phi_2\rangle , \dots , H' |\phi_L\rangle , \dots , \right.$$
$$\left. (H')^M |\phi_1\rangle , (H')^M |\phi_2\rangle , \dots , (H')^M |\phi_L\rangle \right\} , \qquad M < N-1 \tag{3.89}$$

where H' denotes all parts of the Hamiltonian acting on the up-spin electrons. The notation H' is

used in this case because of the already discussed restriction to up-spin electrons due to the spin-symmetry of the Hubbard model, which leads to decoupled up and down spins. The constructed space is also referred to as *block Krylov space*, since a *block* of states is used as start vector.

Similar to the Lanczos algorithm (see Eq.(3.85)), an orthonormal Lanczos basis $\{|M\rangle\}$ has to be constructed again by successive application of H' and subsequent orthonormalization. The use of $L > 1$ states as start vector causes some major differences in the iteration scheme of the Band Lanczos algorithm, compared to the standard Lanczos algorithm, introduced in the previous section. For the Lanczos method, the appearance of a Krylov vector $H^k |\phi_0\rangle$ that is linearly dependent on the previous Krylov vectors, results in a termination of the algorithm after k iterations. This is reasonably natural, because in the described case all eigenvalues of the tridiagonal matrix $\widetilde{H}$ are also eigenvalues of H, and a further expansion of the Krylov space would not yield better results [49]. The Krylov space is said to be *exhausted*.
Focusing on the Band Lanczos algorithm now, an occurring linearly dependent Krylov vector does not mean that the block Krylov space is exhausted. Therefore, the iteration is not terminated at this point. However, the linearly dependent vector does not contain any new information, and should be removed in further consequence. Furthermore, all the following H-multiples of the linearly dependent vector has to be removed. The removal and detection of these linearly dependent vector is called *deflation*. The process of deflation is illustrated schematically in the following example. Further details can be taken from Ref. [49].

Assuming a Krylov vector $H' |\phi_1\rangle$ has been generated that can be written as a linear combination of the start vector states $\{|\phi_1\rangle, |\phi_2\rangle, ..., |\phi_L\rangle\}$ would in other words mean that it is linearly dependent on the Krylov vectors left of $H' |\phi_1\rangle$. Naturally, all H-multiples of $H' |\phi_1\rangle$ will be linearly dependent on their lefthand-side Krylov vectors in consequence. In the given case *deflation* means that all vectors $H^k |\phi_1\rangle$ $k \geq 1$ would need to be deleted. These would result in the following deflated Krylov space

$$\mathcal{H}^{deflated} = \left\{|\phi_1\rangle, |\phi_2\rangle, ..., |\phi_L\rangle, H' |\phi_2\rangle, ..., H' |\phi_L\rangle, ..., \left(H'\right)^M |\phi_2\rangle, ..., \left(H'\right)^M |\phi_L\rangle\right\}, \qquad M < N-1.$$

The termination condition for the Band Lanczos algorithm is the occurrence of L deflations, since it can be shown that in this case the Lanczos vectors span an H-invariant subspace, indicating that all eigenvalues $\widetilde{\epsilon}$ of $\widetilde{H}$ are also eigenvalues of H. These eigenvalues $\widetilde{\epsilon}$ can be written along the diagonal of a matrix to construct the diagonal matrix $\widetilde{\Gamma}(\boldsymbol{k})$ in further consequence.

The calculation of the particular $(N+1)$ particle Q-Matrix $Q^{(e)}_{\mu n}$ (and the $(N-1)$ particle Q-Matrix $Q^{(h)}_{\mu n}$, respectively) is an easy task now, since it can be approximated by the projection $\widetilde{Q}_{\mu n}$ of the states $|\phi_\mu\rangle$ (contained in the start vector) on the eigenstates of $\widetilde{H}$

$$Q^{(e,h)}_{\mu n} \approx \widetilde{Q}^{(e,h)}_{\mu n} = \left\langle \widetilde{\psi}^{(e,h)}_n \right| \phi_\mu \rangle \tag{3.90}$$

with $\left|\widetilde{\psi}^{(e,h)}_n\right\rangle$ denoting the n^{th} eigenvector of $\widetilde{H}^{(e,h)}$, where the particular $\widetilde{H}^{(e,h)}$ was constructed with $(N+1, N-1)$ particle states in the start vector.
The single-particle Green's function is obtained, finally, according to Eq.(3.67). In the present work

the Band Lanczos algorithm is used to provide the Q-Matrices as basic ingredients for the calculation of the cluster Green's functions of particular Hamiltonians.

3.2 Pristine graphene

The presentation of the equilibrium properties of different graphene geometries evaluated in this work is the main objective of the current chapter. First of all an infinitely extended single layer of graphene is considered in this section. The results will serve as a reference solution for the GNRs and should be reached by stretching and broadening the geometries of GNRs to infinity.

3.2.1 Lattice geometry

Graphene is composed of two centered rectangular (rhombic) sublattices (see Chapter 2). A segment of the infinite graphene lattice λ is shown in Fig. 3.2a. The two sublattices are marked by the red and blue dots. For the construction of the whole lattice a basis $\boldsymbol{b}_{graphene}$ and two lattice vectors $\boldsymbol{r}_1$ and $\boldsymbol{r}_2$ (sketched as brown arrows in Fig. 3.2a) are needed:

$$\boldsymbol{b}_{graphene} = \frac{a}{\sqrt{3}} \left\{ \begin{pmatrix} 0 \\ 0 \end{pmatrix}, \begin{pmatrix} \frac{1}{2} \\ -\frac{\sqrt{3}}{2} \end{pmatrix} \right\}; \qquad \boldsymbol{r}_1 = \frac{a}{\sqrt{3}} \begin{pmatrix} \frac{3}{2} \\ \frac{\sqrt{3}}{2} \end{pmatrix}; \qquad \boldsymbol{r}_2 = \frac{a}{\sqrt{3}} \begin{pmatrix} \frac{3}{2} \\ -\frac{\sqrt{3}}{2} \end{pmatrix} \tag{3.91}$$

where a is the lattice constant of graphene, introduced in Chapter 2. It has to be noted here that in order to avoid complications with readability the notation of lattice and superlattice vectors has been slightly changed, compared to Section 3.1. While in the mentioned section distinction between lattice and superlattice vectors was achieved by superscripts $^{(\lambda)}$ and $^{(\Lambda)}$, lower and upper case letters are used in the following to denote lattice and superlattice vectors ($\boldsymbol{r}$ and $\boldsymbol{R}$ e.g.).

With the entire graphene lattice at hand, a proper cluster tiling remains to be chosen. In this work the infinite graphene lattice is treated with a six-site cluster approach, represented by the green lines in Fig. 3.2b. This leads to a superlattice Λ, spanned by two superlattice vectors $\boldsymbol{R}_1$ and $\boldsymbol{R}_2$ (sketched as brown arrows in Fig. 3.2b), which are given by

$$\boldsymbol{R}_1 = \frac{a}{\sqrt{3}} \begin{pmatrix} \frac{3}{2} \\ \frac{3\sqrt{3}}{2} \end{pmatrix}; \qquad \boldsymbol{R}_2 = \frac{a}{\sqrt{3}} \begin{pmatrix} \frac{3}{2} \\ \frac{-3\sqrt{3}}{2} \end{pmatrix}. \tag{3.92}$$

and the six-site cluster viewed in detail in Fig. 3.2c.

The six C atoms within the cluster are located at the following positions

$$\begin{aligned} \boldsymbol{c}_1 &= \begin{pmatrix} 0 \\ 0 \end{pmatrix}; \quad \boldsymbol{c}_2 = \tfrac{a}{\sqrt{3}} \begin{pmatrix} \frac{1}{2} \\ -\frac{\sqrt{3}}{2} \end{pmatrix}; \quad \boldsymbol{c}_3 = \tfrac{a}{\sqrt{3}} \begin{pmatrix} \frac{3}{2} \\ -\frac{\sqrt{3}}{2} \end{pmatrix} \\ \boldsymbol{c}_4 &= \tfrac{a}{\sqrt{3}} \begin{pmatrix} 2 \\ 0 \end{pmatrix}; \quad \boldsymbol{c}_5 = \tfrac{a}{\sqrt{3}} \begin{pmatrix} \frac{3}{2} \\ \frac{\sqrt{3}}{2} \end{pmatrix}; \quad \boldsymbol{c}_6 = \tfrac{a}{\sqrt{3}} \begin{pmatrix} \frac{1}{2} \\ \frac{\sqrt{3}}{2} \end{pmatrix} \end{aligned} \tag{3.93}$$

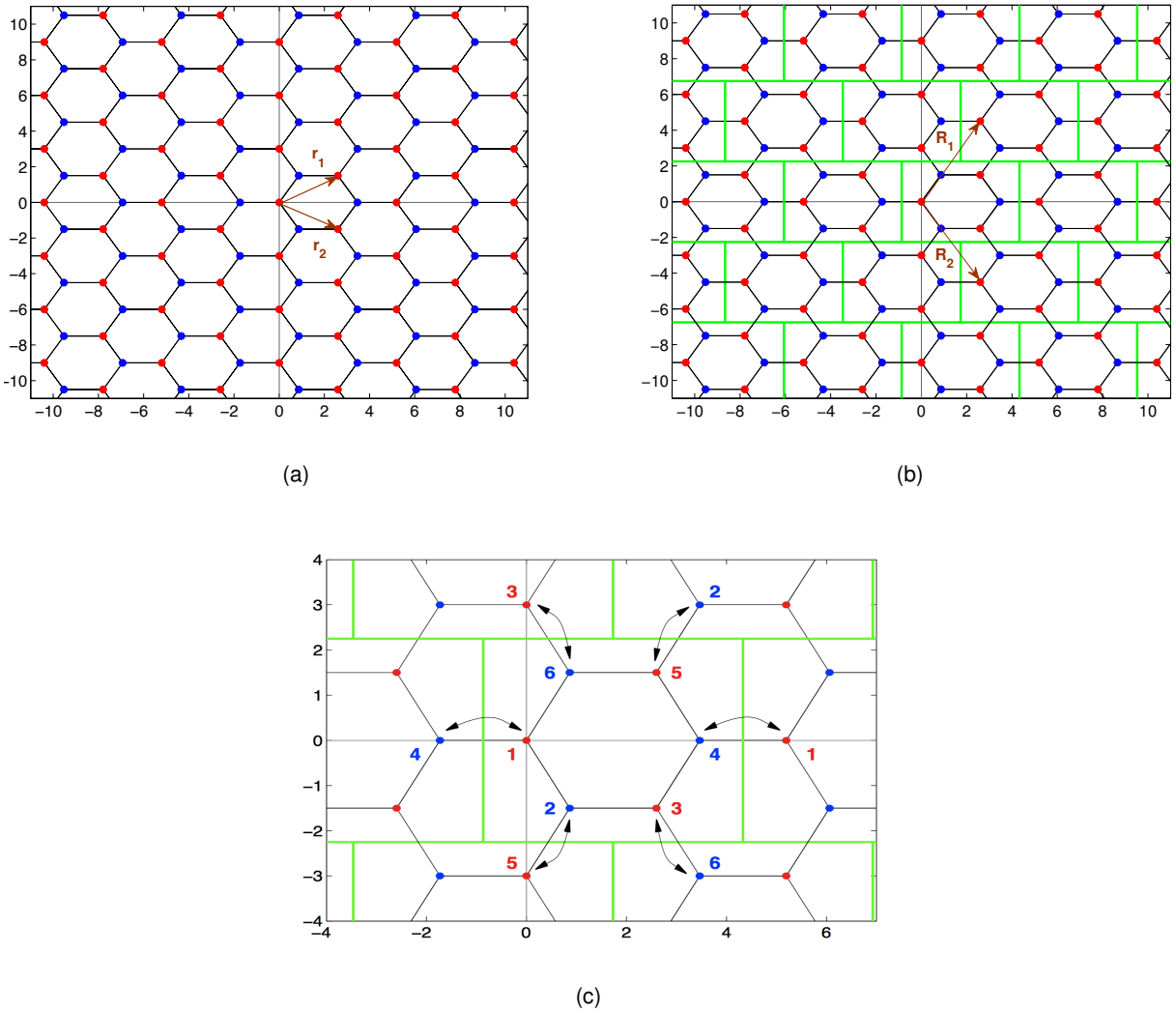

(a) (b)

(c)

Figure 3.2: (a) Real-space lattice of prisitine single-layer graphene. The red and blue dots mark the two different centered rectangular (rhombic) sublattices that span the graphene lattice. The lattice vectors $\boldsymbol{r}_1$ and $\boldsymbol{r}_2$ are represented by the brown arrows. (b) Cluster tiling of the graphene lattice. Here, a six-site cluster approach was used. The corresponding superlattice vectors $\boldsymbol{R}_1$ and $\boldsymbol{R}_2$ are represented by the brown arrows. (c) Detailed view of one six-site cluster. The numbers label the six cluster-sites, while the double-headed arrows indicate the possible inter-cluster hoppings.

When investigating the energy-momentum dispersion relation of a material, the first BZ has to be defined. It is important here to notice that the superlattice Λ introduced by the applied cluster tiling also effects the first BZ of the investigated graphene lattice γ, since it implicitly defines a reciprocal superlattice, with a corresponding superlattice BZ^{Λ} (introduced in Eq.(3.46)). The reciprocal superlattice vectors are given by

$$\boldsymbol{K}_1 = \frac{4\pi}{3a}\begin{pmatrix}\frac{\sqrt{3}}{2}\\ \frac{3}{2}\end{pmatrix}; \qquad \boldsymbol{K}_2 = \frac{4\pi}{3a}\begin{pmatrix}\frac{\sqrt{3}}{2}\\ -\frac{3}{2}\end{pmatrix}. \tag{3.94}$$

The corresponding superlattice BZ^{Λ} is displayed in Fig. 3.3, where the most important points in reciprocal space Γ, $\boldsymbol{M}$ and $\boldsymbol{K}$, located at

$$\Gamma = \begin{pmatrix}0\\0\end{pmatrix}; \qquad \boldsymbol{M} = \frac{4\pi}{3a}\begin{pmatrix}\frac{\sqrt{3}}{2}\\0\end{pmatrix}; \qquad \boldsymbol{K} = \frac{4\pi}{3a}\begin{pmatrix}\frac{\sqrt{3}}{2}\\ \frac{1}{2}\end{pmatrix} \tag{3.95}$$

are labeled.

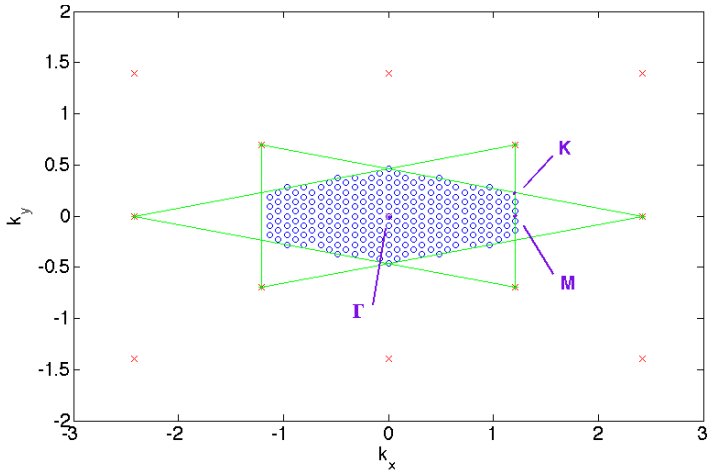

Figure 3.3: First BZ of the superlattice Λ, introduced by the six-site cluster tiling of the infinite graphene lattice. The most remarkable points Γ, M and K are indicated, where the K-point corresponds to the important Dirac point.

To calculate the retarded component of the total lattice single-particle Green's function $\boldsymbol{G}^R(\omega)$ using Eq.(3.37) the Green's function of the cluster $\boldsymbol{G}_0^R(\omega)$ is needed. As explained in the previous section, the cluster Green's function was obtained using the Band Lanczos algorithm, where the ground state quantities are obtained before with the standard Lanczos algorithm. The only input parameter entering the calculations is the Hamilton matrix H of the 2d Hubbard model, defined in Eq.(3.30), where the intra-cluster hoppings in the six-site cluster need to be defined. The investigated graphene lattice features an equivalent hopping integral t_{ij} for all six bonds in the cluster ring:

$$t_{12} = t_{23} = t_{34} = t_{45} = t_{56} = t_{61} = t_{21} = t_{32} = t_{43} = t_{54} = t_{65} = t_{16} = t \tag{3.96}$$

Besides the cluster Green's function $\boldsymbol{G}_0^R(\omega)$, the hopping matrix $T(\boldsymbol{k})$ between the clusters is needed as well for the evaluation of Eq.(3.37). In the detailed view of the six-site cluster in Figure 3.2c the

inter-cluster hoppings, which determine the matrix elements of the hopping matrix T(**k**) according to Eq.(3.50), are plotted as black double-headed arrows. This leads to the following hopping matrix:

$$T^{6s}(\boldsymbol{k}) = t \begin{pmatrix} 0 & 0 & 0 & e^{-i\boldsymbol{k}(\boldsymbol{R}_1+\boldsymbol{R}_2)} & 0 & 0 \\ 0 & 0 & 0 & 0 & e^{-i\boldsymbol{k}\boldsymbol{R}_1} & 0 \\ 0 & 0 & 0 & 0 & 0 & e^{-i\boldsymbol{k}\boldsymbol{R}_2} \\ e^{i\boldsymbol{k}(\boldsymbol{R}_1+\boldsymbol{R}_2)} & 0 & 0 & 0 & 0 & 0 \\ 0 & e^{i\boldsymbol{k}\boldsymbol{R}_1} & 0 & 0 & 0 & 0 \\ 0 & 0 & e^{i\boldsymbol{k}\boldsymbol{R}_2} & 0 & 0 & 0 \end{pmatrix}. \tag{3.97}$$

As in the chosen cluster tiling there occur some equivalent sites ($\alpha = \{1,3,5\}$ corresponding to sublattice A, $\beta = \{2,4,6\}$ corresponding to sublattice B respectively) a periodization of the calculated Green's function is necessary, according to Eq.(3.54)

$$G_{\alpha\beta}(\omega,\boldsymbol{k}) = \frac{L_{u.c.}}{L} \sum_{\boldsymbol{R}_a\in\alpha} \sum_{\boldsymbol{R}_b\in\beta} e^{i\boldsymbol{k}(\boldsymbol{R}_a-\boldsymbol{R}_b)} G_{a,b}(\omega,\boldsymbol{k}) = \frac{2}{6} \sum_{\boldsymbol{R}_a\in\{1,3,5\}} \sum_{\boldsymbol{R}_b\in\{2,4,6\}} e^{i\boldsymbol{k}(\boldsymbol{R}_a-\boldsymbol{R}_b)} G_{a,b}(\omega,\boldsymbol{k}) \tag{3.98}$$

where $G_{a,b}(\omega,\boldsymbol{k})$ is the total lattice Green's function obtained by using the *Q*-matrix formulation of CPTs central equation (see Eq.(3.67)). The equilibrium properties introduced in Sec. 3.1.2 were evaluated for the pristine graphene lattice. The results are presented in the following subsections for different values of the on-site interaction *U*.

3.2.2 Spectral function

The spectral function $A(\boldsymbol{k},\omega)$ was calculated according to Eq.(3.68) for different values of the on-site interaction *U*. The projection of the resulting three-dimensional graph on the energy-momentum ω-$\boldsymbol{k}$ plane (also often referred to as *E*-$\boldsymbol{k}$ plane) was plotted then, in order to achieve the desired energy-momentum dispersion relation $\omega(\boldsymbol{k})$. The resulting $\omega(\boldsymbol{k})$ curves for $U/t = \{0.0, 0.5, 1.0, 1.5, 2.0, 2.5, 3.0, 3.3, 4.0, 5.0\}$ are plotted in Fig. 3.4.

Considering the non-interacting $U = 0$ case in Fig. 3.4a first, the probably most remarkable feature of the pristine infinite graphene lattice can be observed at the *K*-points of the first BZ, namely the occurrence of a linear dispersion relation. A corresponding three-dimensional representation of the plots in Fig. 3.4 would show a formation of Dirac *cones* as described in Chapter 2. In the following the occurrence of a linear dispersion relation will also be referred to as the formation of Dirac cones, since in three dimensions both describe exactly the same feature. The existence of *two* energy bands in the first BZ of graphene can be observed, in accordance to the number of two C atoms in the unit cell (see Eq.(3.72) for the particular rule).

Turning to the interacting $U \neq 0$ cases now, it can be clearly seen that the linear dispersion relation gradually vanishes with increasing *U* - the striking feature of Dirac cones is lost. Additionally, the

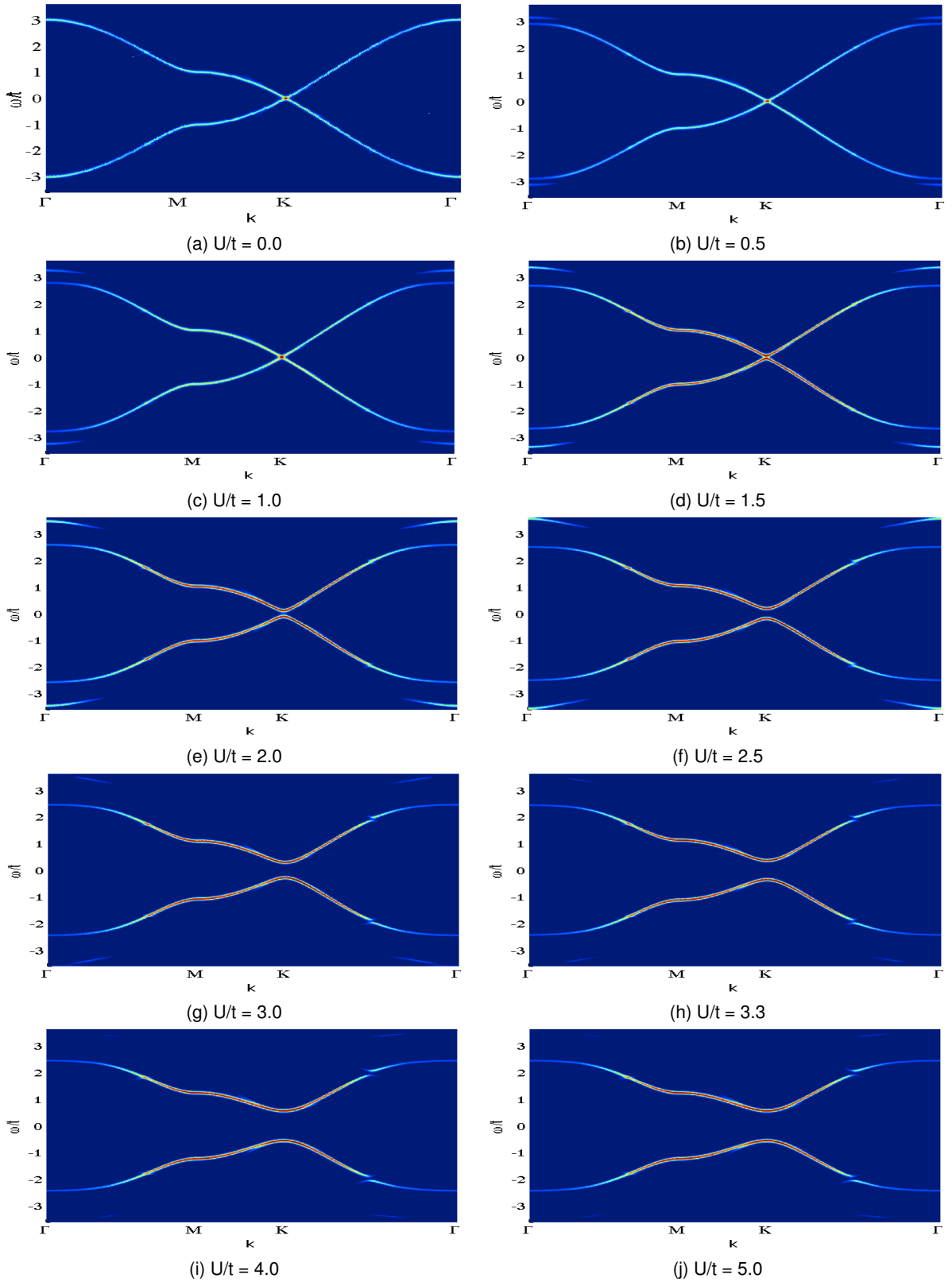

(a) U/t = 0.0 (b) U/t = 0.5

(c) U/t = 1.0 (d) U/t = 1.5

(e) U/t = 2.0 (f) U/t = 2.5

(g) U/t = 3.0 (h) U/t = 3.3

(i) U/t = 4.0 (j) U/t = 5.0

Figure 3.4: Energy-momentum dispersion relation $\omega(\boldsymbol{k})$ of pristine graphene for different on-site interactions $U/t = \{0.0, 0.5, 1.0, 1.5, 2.0, 2.5, 3.0, 3.3, 4.0, 5.0\}$, where the interaction strength (value of U) is labeled below each subplot. The energy ω is plotted in terms of the hopping integral t: $\omega = \omega/t$. The on-site interaction $U = 9.3eV \approx 3.3t$, which was found for graphene using a constrained random phase approximation (cRPA) [50], was used in subplot (h).

opening of an energy gap at a critical value of

$$U_{crit} \approx 1.4t \tag{3.99}$$

is discovered, turning the graphene lattice from the semi-metallic behaviour of the non-interacting graphene lattice in Fig. 3.4a to a semiconducting one for large values of U. Note that the value of U_{crit} can only be given approximately due to the finite broadening of the energy bands. It deserves particular mention here that a previous work on this topic reported an overestimation of the energy gap in the infinitely extended graphene lattice within the CPT formalism compared to QMC calculations [43]. One should remember this for the investigation of the (L)DOS of GNRs in the following sections.

The enhancement of the energy gap $\Delta(U)$ with increasing on-site interaction U can be observed in Fig. 3.5, where the energy gap was calculated according to Eq.(3.74). The critical interaction value U_{crit}, which is the on-site interaction value U where the energy gap Δ exceeds the value of the broadening η (see Eq.(3.28)) for the first time, is observable and indicated as well.

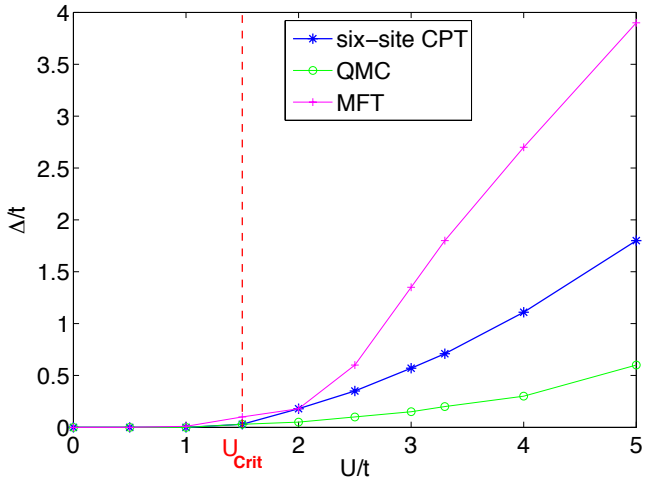

Figure 3.5: Energy gap $\Delta(U)$ of pristine graphene as a function of the on-site interaction U, calculated according to Eq.(3.74). The critical value U_{crit} where the energy gap opens up is indicated. The gained values are compared to data obtained by QMC and mean field theory (MFT) [11].

The obtained values of the energy gap Δ in pristine graphene as a function of the on-site interaction U are compared to data from QMC and MFT calculations [11] in Fig. 3.5. It appears that the CPT method overestimates the energy gap compared to the QMC results, but still delivers better results than the MFT method.

For an on-site interaction $U = 9.3eV \approx 3.3t$, which was reported for graphene by constrained random phase approximation (cRPA) [50], the energy gap has already reached a value of

$$\Delta|_{U=U_{graphene}} \approx 0.71t \approx 2.0\ eV \tag{3.100}$$

obviously characterizing graphene as a direct band gap semiconductor.

In the non-interacting case ($U = 0$), the energy-momentum dispersion relation $\omega(\boldsymbol{k})$ is also obtainable by Fourier transforming the whole problem into wavevector $\boldsymbol{k}$-space, which is possible due to the translational invariance of the whole non-interacting lattice. The analytical solution for $\omega(\boldsymbol{k})$ is given by [45]

$$\omega(\boldsymbol{k}) = \epsilon \pm t\sqrt{1 + 4cos\left(\frac{\sqrt{3}k_x a}{2}\right)cos\left(\frac{k_y a}{2}\right) + 4cos^2\left(\frac{k_y a}{2}\right)} \tag{3.101}$$

where a is the graphene lattice constant. It is plotted in Fig. 3.6 in order to prove the equivalence to the numerical solution of the non-interacting case in Fig. 3.4a.

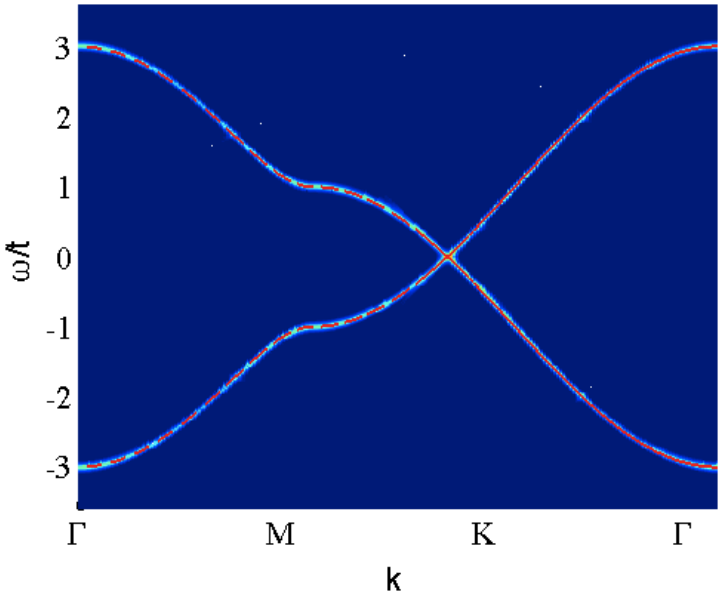

Figure 3.6: Energy-momentum dispersion relation $\omega(\boldsymbol{k})$ of the infinitely extended graphene lattice in the non-interacting $U = 0$ case (corresponds to Fig. 3.4a). The analytical solution given in Eq.(3.101) is plotted in addtion (red dashed line) to show the equivalence to the non-interacting many-body problem. The on-site energy ϵ was chosen to be zero.

3.2.3 (Local) electronic density of states

Summing up all the possible energy states in the first BZ leads to the DOS $\rho(\omega)$, which provides additional information about a systems equilibrium (and/ or non-equilibrium) behaviour. The DOS is calculated according to Eq.(3.76) and is again plotted for different on-site interaction values $U/t = \{0.0, 0.5, 1.0, 1.5, 2.0, 2.5, 3.0, 3.3, 4.0, 5.0\}$, which is shown in Fig. 3.7 and Fig. 3.8, where two figures were used in this case to allow for a detailed inspection of the obtained curves. Additionally, the LDOS of *site 1* and *site 2* (calculated according to Eq.(3.78)) are presented in the top two figures of every subplot, because these two sites are the only translationally inequivalent sites in the graphene lattice, as already explained above. Nevertheless, due to the infinite extent of the lattice in both dimensions, the LDOS is expected to be equal on both sites. Exactly this behaviour is observed, when looking precisely on the LDOS curves in Fig. 3.7 and Fig. 3.8. It has to be noted here that all presented data is *broadened* due to the introduced finite imaginary part of the frequency ω (see Eq.(3.28)).

The emergence of an energy gap for on-site interactions $U > U_{crit}$ can be observed again by investigating the DOS plots. The first appearance of an energy gap was found for $U = 1.5t$ in Fig. 3.7d, corresponding to a zero DOS around $\omega = 0$. Since the critical value was found to be $U_{crit} \approx 1.4t$, the energy gap in Fig. 3.7d is rather small and therefore hard to observe, due to the finite broadening of the energy bands. However, for $U = 2.0t$ in Fig. 3.7e the energy gap can be observed clearly.

A further investigation of the pristine graphene lattice is not topic of the present work. As already stated above, the task of the results gained in this section is to serve as the limiting case for the GNRs, considered in the next sections. By increasing the width W of a particular GNR type (regardless if zig-zag or armchair) up to infinity, the limiting case of the infinitely extended graphene lattice presented in this section should be regained.

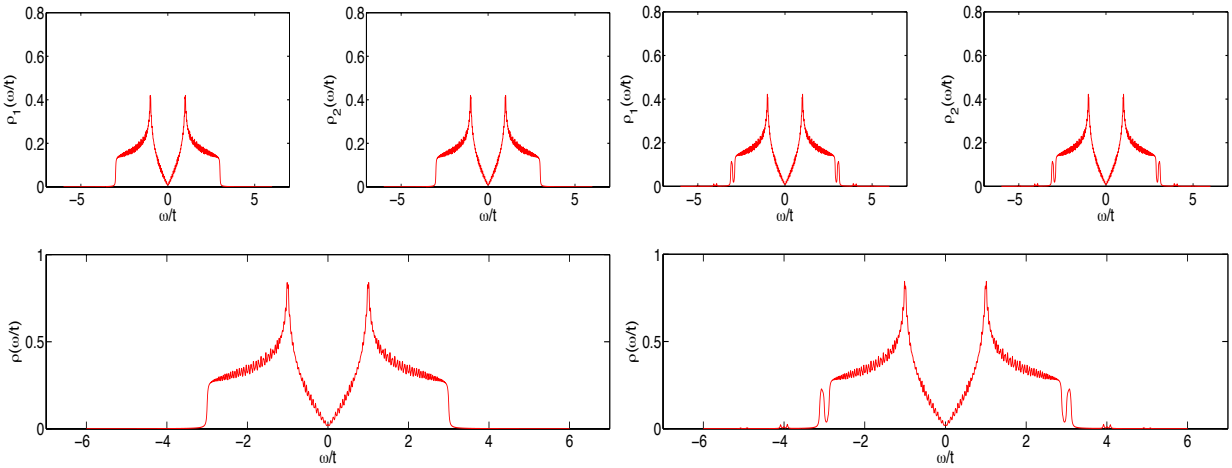

(a) U/t = 0.0

(b) U/t = 0.5

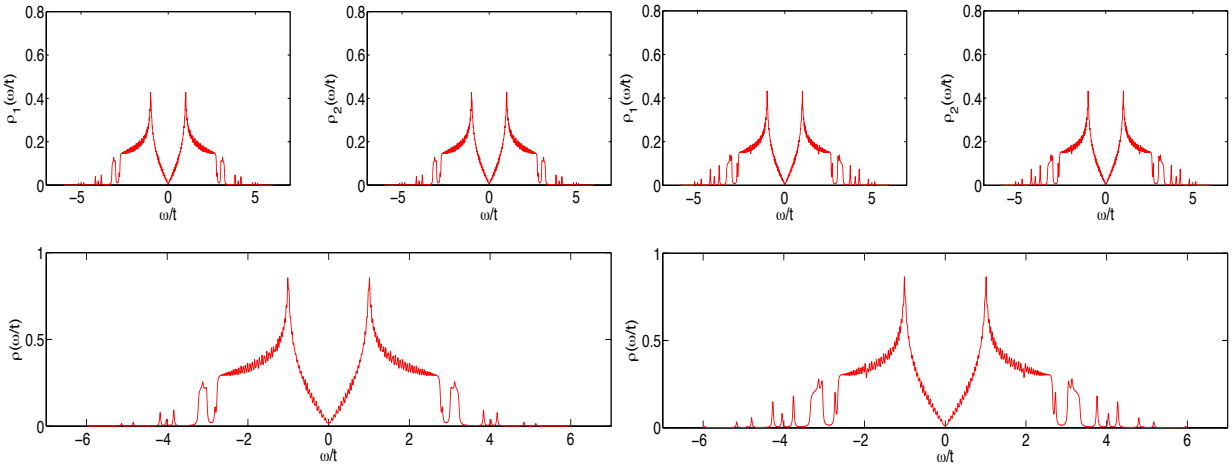

(c) U/t = 1.0

(d) U/t = 1.5

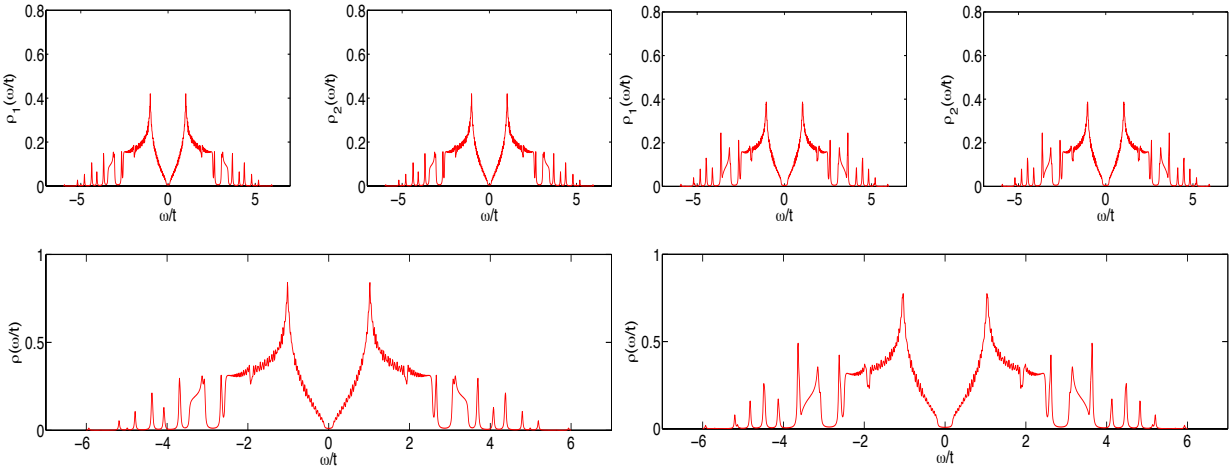

(e) U/t = 2.0

(f) U/t = 2.5

Figure 3.7: DOS $\rho(\omega)$ in the pristine graphene lattice for different on-site interactions $U/t = \{0.0, 0.5, 1.0, 1.5, 2.0, 2.5\}$, where the interaction strength (value of U) is labeled below each subplot. Additionally the LDOS at the two translationally inequivalent cluster sites 1 and 2 is presented in the two top figures of each subplot.

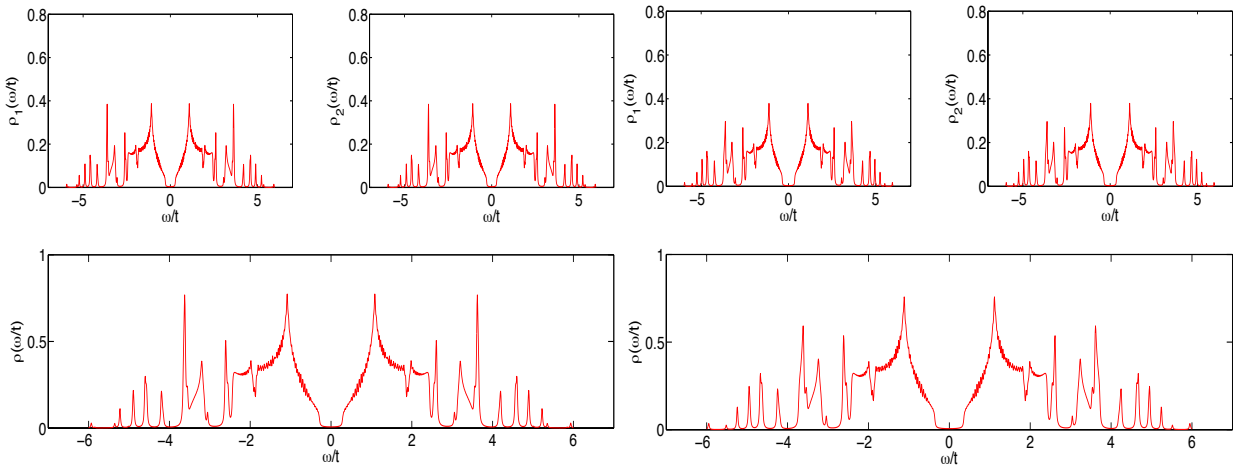

(a) U/t = 3.0

(b) U/t = 3.3

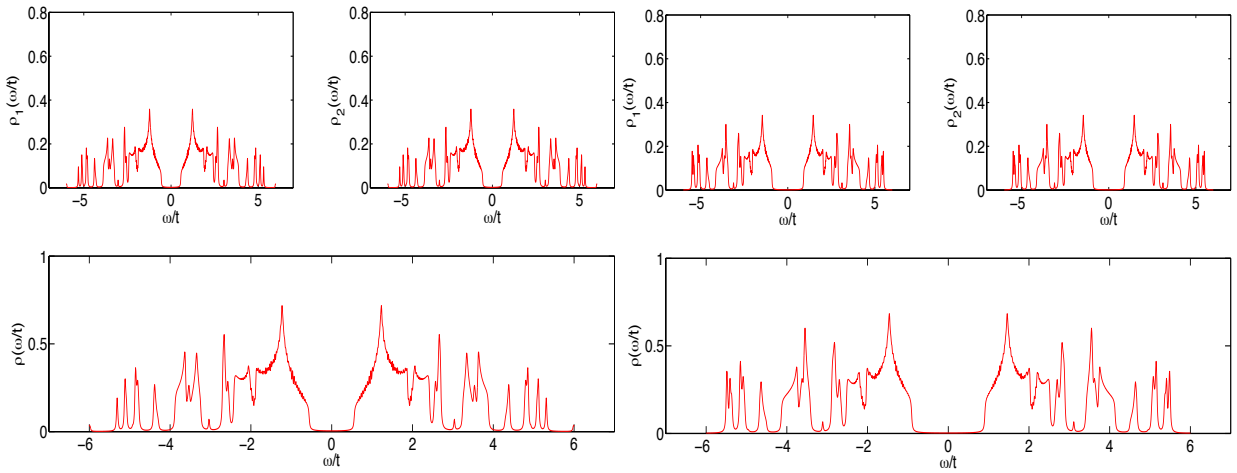

(c) U/t = 4.0

(d) U/t = 5.0

Figure 3.8: Same as Fig. 3.7, but for $U/t = \{3.0, 3.3, 4.0, 5.0\}$. The on-site interaction $U = 9.3eV \approx 3.3t$, which was found for graphene using cRPA [50], was used in subplot (h).

3.3 Zig-zag graphene nanoribbons with a width of three, four and five carbon atoms

After the investigation of the pristine graphene lattice in the previous section, the focus is on 2d graphene structures with one finite physical dimension now, namely the GNR geometries introduced in Chapter 2. Starting out with the zig-zag edge geometry (see also Fig. 2.3a), an investigation of the lattice geometries of the treated structures is performed first. A presentation of the gained results for the equilibrium properties, i.e the spectral function $A(\omega, \boldsymbol{k})$, the energy gap $\Delta_{ZZ}(U)$ and the (L)DOS $\rho(\omega)$, as well as an interpretation of the results in terms of an explanation of the discovered physical behaviours, is what subsequently follows.

3.3.1 Lattice geometry

Zig-zag GNRs with 3, 4 and 5 C atoms along the width W are investigated in this section, where a $W = N$ ribbon is denoted *ZZ-WN* in the following. The geometry of the three investigated zig-zag GNRs is shown in Fig. 3.9a (ZZ-W3), Fig. 3.9c (ZZ-W4) and Fig. 3.9e (ZZ-W5), where the two sublattices of graphene are marked by the red and blue dots again.
While the construction of the infinite 2d graphene lattice required a two-atom basis $\boldsymbol{b}_{graphene}$ and two lattice vectors $\boldsymbol{r}_1$ and $\boldsymbol{r}_2$ (see Eq.(3.91)), the size of the physical unit cell has to be expanded here according to

$$L_{u.c.}^{graphene} = 2 \quad \rightarrow \quad L_{u.c.}^{GNR} = 2W \tag{3.102}$$

due to the fact that for the zig-zag GNR geometries the translational invariance is reduced to the longitudinal dimension.
Due to this reduction from a 2d translational invariance in the case of pristine graphene to an one-dimensional translational invariance in the case of zig-zag GNRs, only *one* lattice vector is needed to span the whole GNR lattice. It is given by

$$\boldsymbol{r} = a \begin{pmatrix} 1 \\ 0 \end{pmatrix} \tag{3.103}$$

where a is again the lattice constant of graphene, introduced in Chapter 2. The direct correspondence of the lattice vector $\boldsymbol{r}$ to the lattice constant a can also be seen clearly, regarding Fig. 3.9. Moreover, since the cluster chosen for the application of the CPT method coincides exactly with the physical unit cell, the arising superlattice vector $\boldsymbol{R}$ also equals the lattice vector $\boldsymbol{r}$:

$$\boldsymbol{R} = \boldsymbol{r} = a \begin{pmatrix} 1 \\ 0 \end{pmatrix} \tag{3.104}$$

As can be seen in Fig. 3.9 the above statements apply to all of the investigated zig-zag GNR geometries. The resulting cluster tilings are represented by the green lines in Fig. 3.9a (ZZ-W3),

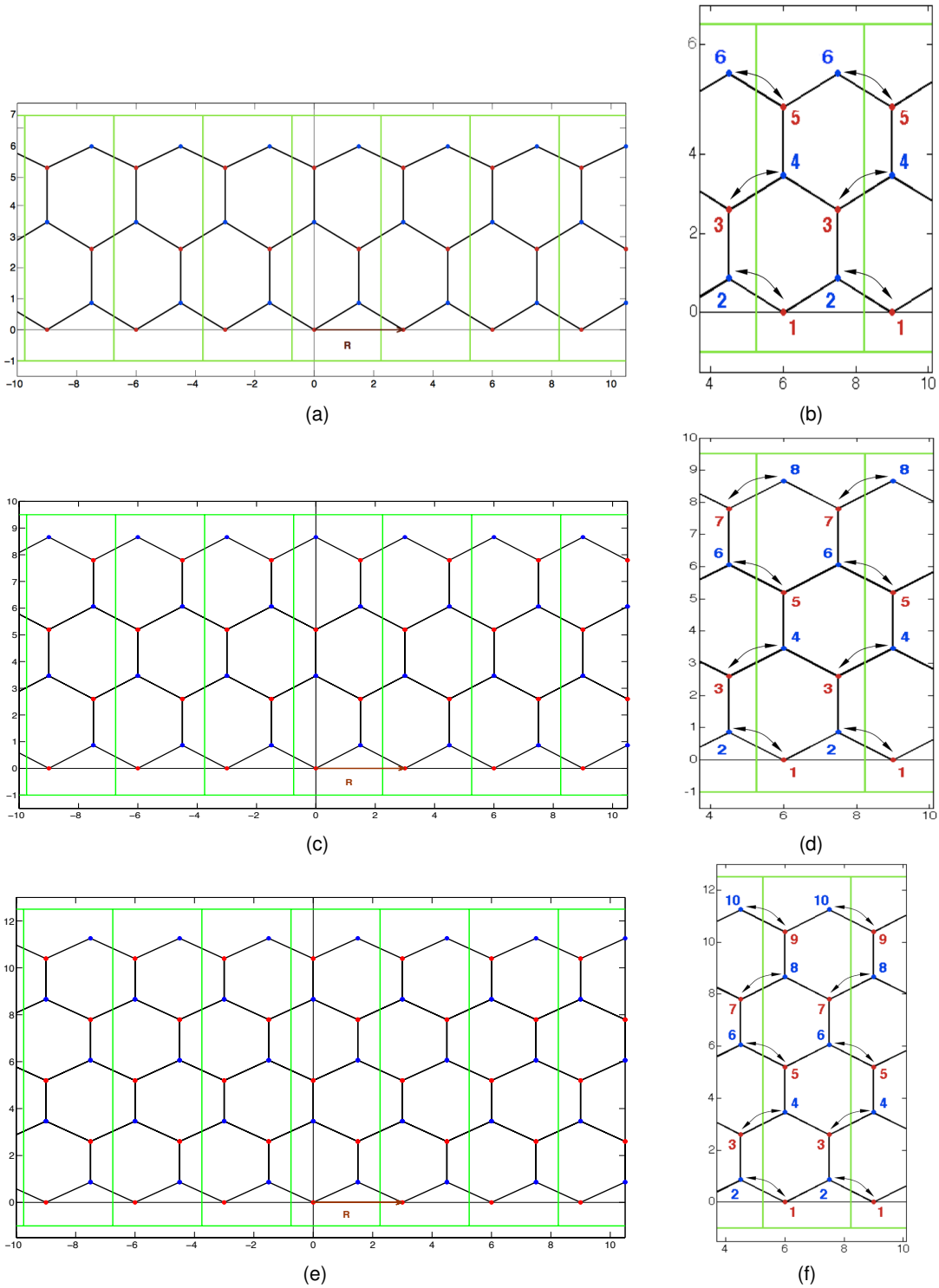

Figure 3.9: Geometry of the real-space lattice λ and the applied cluster tiling for a ZZ-W3 GNR (a), ZZ-W4 GNR (c) and ZZ-W5 GNR (e). The red and blue dots mark the C atoms corresponding to the two different sublattices of the infinite graphene lattice. The lattice vector $\boldsymbol{r}$ and the superlattice vector $\boldsymbol{R}$ (both equal to the lattice constant a) are represented by the brown arrow. (b), (d) and (f): Detailed view of the corresponding $2W$-site clusters. The numbers label the $2W$ cluster sites, while the double-headed arrows indicate the possible inter-cluster hoppings.

Fig. 3.9c (ZZ-W4) and Fig. 3.9e (ZZ-W5). The corresponding superlattice vectors $\boldsymbol{R}$ are sketched as brown arrows. A detailed view of the used clusters, with all the possible inter-cluster hoppings indicated by black double-headed arrows, is presented in Fig. 3.9b (ZZ-W3), Fig. 3.9d (ZZ-W4) and Fig. 3.9f (ZZ-W5)

The $2W$ C atoms within the clusters are located at the following positions

$$\begin{aligned} \boldsymbol{c}_1 &= \begin{pmatrix} 0 \\ 0 \end{pmatrix}; \quad \boldsymbol{c}_2 = \frac{a}{\sqrt{3}} \begin{pmatrix} \frac{\sqrt{3}}{2} \\ \frac{1}{2} \end{pmatrix}; \quad \boldsymbol{c}_3 = \frac{a}{\sqrt{3}} \begin{pmatrix} \frac{\sqrt{3}}{2} \\ \frac{3}{2} \end{pmatrix}; \quad \boldsymbol{c}_4 = \frac{a}{\sqrt{3}} \begin{pmatrix} 0 \\ 2 \end{pmatrix}; \quad \boldsymbol{c}_5 = \frac{a}{\sqrt{3}} \begin{pmatrix} 0 \\ 3 \end{pmatrix} \\ \boldsymbol{c}_6 &= \frac{a}{\sqrt{3}} \begin{pmatrix} \frac{\sqrt{3}}{2} \\ \frac{7}{2} \end{pmatrix}; \quad \boldsymbol{c}_7 = \frac{a}{\sqrt{3}} \begin{pmatrix} \frac{\sqrt{3}}{2} \\ \frac{9}{2} \end{pmatrix}; \quad \boldsymbol{c}_8 = \frac{a}{\sqrt{3}} \begin{pmatrix} 0 \\ 3 \end{pmatrix}; \quad \boldsymbol{c}_9 = \frac{a}{\sqrt{3}} \begin{pmatrix} 0 \\ 6 \end{pmatrix}; \quad \boldsymbol{c}_{10} = \frac{a}{\sqrt{3}} \begin{pmatrix} \frac{\sqrt{3}}{2} \\ \frac{13}{2} \end{pmatrix} \end{aligned} \tag{3.105}$$

where due to the chosen cluster-tiling and site-labeling these particular positions apply to the ZZ-W3 GNR (site 1-6), ZZ-W4 GNR (site 1-8) and the ZZ-W5 GNR (site 1-10) in the same way.

Before the energy-momentum dispersion relation of the investigated zig-zag GNRs can be investigated, the first BZ has to be defined. Similar to the case of an infinitely extended graphene layer, the superlattice Λ introduced by the applied cluster tiling also effects the first BZ of the GNR lattices, since it implicitly defines a reciprocal superlattice, with a corresponding superlattice BZ^{Λ} (introduced in Eq.(3.46)). As the translational invariance is reduced to one dimension in the case of GNRs, there remains only one reciprocal superlattice vector, given by

$$\boldsymbol{K} = \frac{2\pi}{a} \begin{pmatrix} 1 \\ 0 \end{pmatrix}. \tag{3.106}$$

Therefore, the corresponding superlattice BZ^{Λ} is also only one-dimensional. Obviously, the first BZ looks the same for the ZZ-W3 GNR, ZZ-W4 GNR and the ZZ-W5 GNR, since all lattices are described by the same reciprocal superlattice vector $\boldsymbol{R}$ defined in Eq.(3.104).
Due to the fact that the reciprocal lattice of a zig-zag GNR is described by an armchair GNR lattice and vice versa [51] [52], there are again some points in the reciprocal superlattice BZ^{Λ}, which are of particular interest. They are denoted Γ and K in the following and are located at

$$\Gamma = \left\{ ..., 0, \frac{2\pi}{a}, \frac{4\pi}{a}, ... \right\} \qquad \boldsymbol{K} = \left\{ ..., \frac{2\pi}{3a}, \frac{4\pi}{3a}, \frac{8\pi}{3a}, \frac{10\pi}{3a}, ... \right\}. \tag{3.107}$$

The notation was chosen in this specific way, because the defined K-points in the zig-zag GNRs reciprocal superlattice BZ^{Λ} and the Dirac points of the whole reciprocal armchair lattice are located exactly at the same k_x coordinates. Therefore, the development of *Dirac-cone-like* dispersion relations is expected at exactly this reciprocal superlattice points. The k_x coordinates of the reciprocal superlattice Γ-points correspond to the k_x coordinates of the Γ-points in the reciprocal armchair lattice. A graphical description is provided in Fig. 3.10.

As in the case of the infinite graphene lattice (Sec. 3.2), the intra-cluster hoppings of the particular zig-zag GNR clusters are required to calculate the retarded cluster Green's function $\boldsymbol{G}_0^R(\omega)$. Since

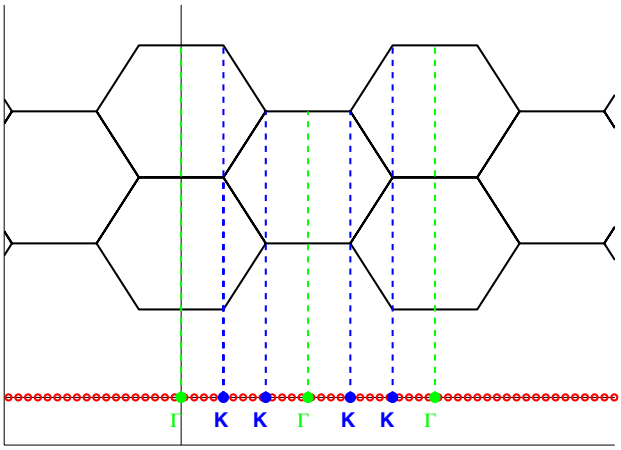

Figure 3.10: Above (black): Reciprocal lattice of a ZZ-W5 GNR. Below (red): Reciprocal superlattice Λ of all investigated zig-zag GNR structures. The distinguishing points Γ and K are indicated, with the k_x coordinates of the K-points corresponding to the k_x coordinates of the important Dirac points, as indicated by the blue dashed-lines.

all the investigated zig-zag structures basically consist of a graphene lattice, the nearest-neighbour hopping integrals t_{ij} are identical for all hopping processes:

$$t_{ij} = t \quad \forall\, i,j \mid |i-j| = 1 \tag{3.108}$$

Besides the cluster Green's function $\boldsymbol{G}_0^R(\omega)$, the hopping matrix $T(\boldsymbol{k})$ needs to be determined for all zig-zag GNR structures to calculate the retarded total lattice single-particle Green's function $\boldsymbol{G}^R(\omega)$ using Eq.(3.37). In the detailed views of the particular zig-zag GNR clusters in Fig. 3.9b (ZZ-W3 GNR), Fig. 3.9d (ZZ-W4 GNR) and Fig. 3.9f (ZZ-W5 GNR) the inter-cluster hoppings, which determine the matrix elements of the hopping matrices $T_{ZZ}^{2Ws}(\boldsymbol{k})$ according to Eq.(3.50), are plotted as black double-headed arrows. This leads to the following hopping matrices:

$$T_{ZZ}^{6s}(\boldsymbol{k}) = t \begin{pmatrix} 0 & e^{-i\boldsymbol{k}\boldsymbol{R}^\Lambda} & 0 & 0 & 0 & 0 \\ e^{i\boldsymbol{k}\boldsymbol{R}^\Lambda} & 0 & 0 & 0 & 0 & 0 \\ 0 & 0 & 0 & e^{i\boldsymbol{k}\boldsymbol{R}^\Lambda} & 0 & 0 \\ 0 & 0 & e^{-i\boldsymbol{k}\boldsymbol{R}^\Lambda} & 0 & 0 & 0 \\ 0 & 0 & 0 & 0 & 0 & e^{-i\boldsymbol{k}\boldsymbol{R}^\Lambda} \\ 0 & 0 & 0 & 0 & e^{i\boldsymbol{k}\boldsymbol{R}^\Lambda} & 0 \end{pmatrix} \tag{3.109}$$

$$T_{ZZ}^{8s}(\boldsymbol{k}) = t \begin{pmatrix} 0 & e^{-i\boldsymbol{k}\boldsymbol{R}^\Lambda} & 0 & 0 & 0 & 0 & 0 & 0 \\ e^{i\boldsymbol{k}\boldsymbol{R}^\Lambda} & 0 & 0 & 0 & 0 & 0 & 0 & 0 \\ 0 & 0 & 0 & e^{i\boldsymbol{k}\boldsymbol{R}^\Lambda} & 0 & 0 & 0 & 0 \\ 0 & 0 & e^{-i\boldsymbol{k}\boldsymbol{R}^\Lambda} & 0 & 0 & 0 & 0 & 0 \\ 0 & 0 & 0 & 0 & 0 & e^{-i\boldsymbol{k}\boldsymbol{R}^\Lambda} & 0 & 0 \\ 0 & 0 & 0 & 0 & e^{i\boldsymbol{k}\boldsymbol{R}^\Lambda} & 0 & 0 & 0 \\ 0 & 0 & 0 & 0 & 0 & 0 & 0 & e^{i\boldsymbol{k}\boldsymbol{R}^\Lambda} \\ 0 & 0 & 0 & 0 & 0 & 0 & e^{-i\boldsymbol{k}\boldsymbol{R}^\Lambda} & 0 \end{pmatrix} \tag{3.110}$$

$$T_{ZZ}^{10s}(\boldsymbol{k}) = t \begin{pmatrix} 0 & e^{-i\boldsymbol{k}\boldsymbol{R}^{\Lambda}} & 0 & 0 & 0 & 0 & 0 & 0 & 0 & 0 \\ e^{i\boldsymbol{k}\boldsymbol{R}^{\Lambda}} & 0 & 0 & 0 & 0 & 0 & 0 & 0 & 0 & 0 \\ 0 & 0 & 0 & e^{i\boldsymbol{k}\boldsymbol{R}^{\Lambda}} & 0 & 0 & 0 & 0 & 0 & 0 \\ 0 & 0 & e^{-i\boldsymbol{k}\boldsymbol{R}^{\Lambda}} & 0 & 0 & 0 & 0 & 0 & 0 & 0 \\ 0 & 0 & 0 & 0 & 0 & e^{-i\boldsymbol{k}\boldsymbol{R}^{\Lambda}} & 0 & 0 & 0 & 0 \\ 0 & 0 & 0 & 0 & e^{i\boldsymbol{k}\boldsymbol{R}^{\Lambda}} & 0 & 0 & 0 & 0 & 0 \\ 0 & 0 & 0 & 0 & 0 & 0 & 0 & e^{i\boldsymbol{k}\boldsymbol{R}^{\Lambda}} & 0 & 0 \\ 0 & 0 & 0 & 0 & 0 & 0 & e^{-i\boldsymbol{k}\boldsymbol{R}^{\Lambda}} & 0 & 0 & 0 \\ 0 & 0 & 0 & 0 & 0 & 0 & 0 & 0 & 0 & e^{-i\boldsymbol{k}\boldsymbol{R}^{\Lambda}} \\ 0 & 0 & 0 & 0 & 0 & 0 & 0 & 0 & e^{i\boldsymbol{k}\boldsymbol{R}^{\Lambda}} & 0 \end{pmatrix} \tag{3.111}$$

For the chosen cluster tilings no translationally equivalent sites occur within the zig-zag GNR clusters. Therefore, a periodization of the calculated Green's functions is not necessary, in contrast to the pristine graphene lattice. What follows is a presentation of the results of the equilibrium properties introduced in Sec. 3.1.2, which were calculated for different values of the on-site interaction U for the ZZ-W3, ZZ-W4 and ZZ-W5 GNR geometry.

3.3.2 Spectral function

The spectral function $A(\boldsymbol{k}, \omega)$ was calculated according to Eq.(3.68) for different values of the on-site interaction U, in order to achieve the desired energy-momentum dispersion relation $\omega(\boldsymbol{k})$. The resulting $\omega(\boldsymbol{k})$ curves of the particular zig-zag GNR structures are plotted in Fig. 3.11 (ZZ-W3 GNR), Fig. 3.12 (ZZ-W4 GNR) and Fig. 3.13 (ZZ-W5 GNR) for on-site interactions $U/t = \{0.0, 0.5, 1.0, 1.5, 2.0, 2.5, 3.0, 3.3, 4.0,$

Comparing the energy-momentum dispersion relations for the zig-zag GNRs to those of the infinite graphene lattice in Fig. 3.4, the occurence of more than two energy states per $\boldsymbol{k}$-value in the BZ is a first characteristic of the zig-zag GNR geometries. As outlined in Eq.(3.72), the number of expected energy bands in the first BZ is equal to the number of atoms in the physical unit cell. As for the case of the zig-zag GNRs investigated in this section the physical unit cell corresponds to the chosen clusters, the number of energy bands is given by the size of the particular clusters $N = 2W$. This is exactly what can be observed in the presented plots of the energy-momentum dispersion relations (as it is the case for all following plots of the GNRs' energy-momentum dispersion relations).
Another interesting difference of the zig-zag GNRs compared to the pristine graphene lattice is the lacking of the Dirac cones, i.e. the linear dispersion relation in the 2d plots, observable at the K-points in the energy-momentum plots of the pristine graphene lattice. The absence of Dirac cones can be explained due to a quantum size effect, since the width of the investigated structures is only a few nanometers. Comparing the $\omega(\boldsymbol{k})$ characteristics in the non-interacting $U = 0$ case in Fig. 3.11a (ZZ-W3 GNR), Fig. 3.12a (ZZ-W4 GNR) and Fig. 3.13a (ZZ-W5 GNR) with each other, the emergence of small cone-like features close to the K-points (highlighted with a red frame in the particular figures) is observable, which grow larger for increasing ribbon width. It will be shown later (Sec. 3.5) that for wider zig-zag GNR structures, Dirac cone-like features are regained at the K-points.

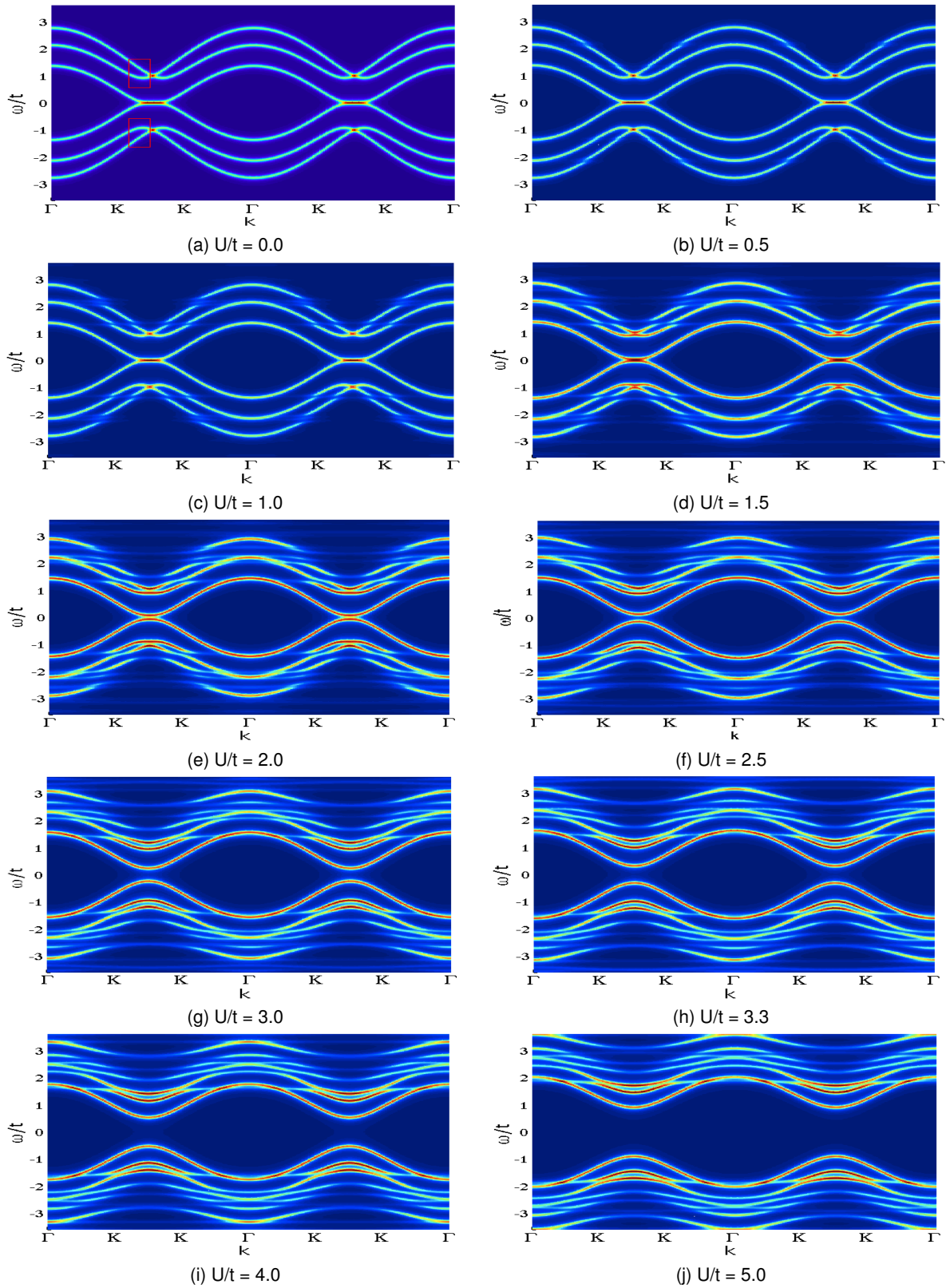

(a) U/t = 0.0 (b) U/t = 0.5

(c) U/t = 1.0 (d) U/t = 1.5

(e) U/t = 2.0 (f) U/t = 2.5

(g) U/t = 3.0 (h) U/t = 3.3

(i) U/t = 4.0 (j) U/t = 5.0

Figure 3.11: Energy-momentum dispersion relation $\omega(\boldsymbol{k})$ of a ZZ-W3 GNR for different on-site interactions $U/t = \{0.0, 0.5, 1.0, 1.5, 2.0, 2.5, 3.0, 3.3, 4.0, 5.0\}$, where the interaction strength (value of U) is labeled below each subplot. The energy ω is plotted in terms of the hopping integral t. The red frame in (a) highlights the appearing cone-like features. An on-site interaction value $U = 9.3eV \approx 3.3t$, which was found for graphene using cRPA [50], was used in subplot (h).

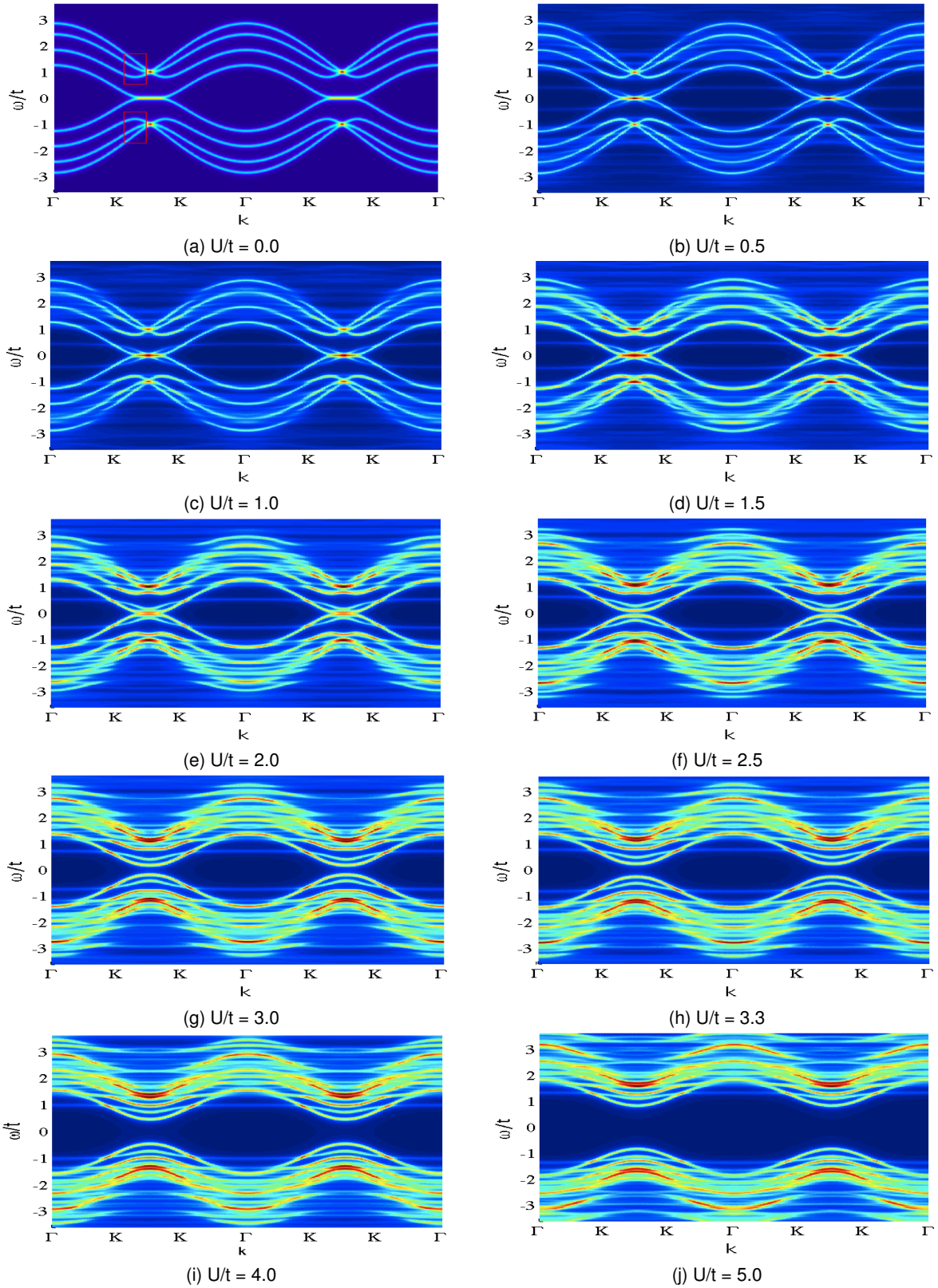

(a) U/t = 0.0

(b) U/t = 0.5

(c) U/t = 1.0

(d) U/t = 1.5

(e) U/t = 2.0

(f) U/t = 2.5

(g) U/t = 3.0

(h) U/t = 3.3

(i) U/t = 4.0

(j) U/t = 5.0

Figure 3.12: Same as Fig. 3.11, but for of a ZZ-W4 GNR.

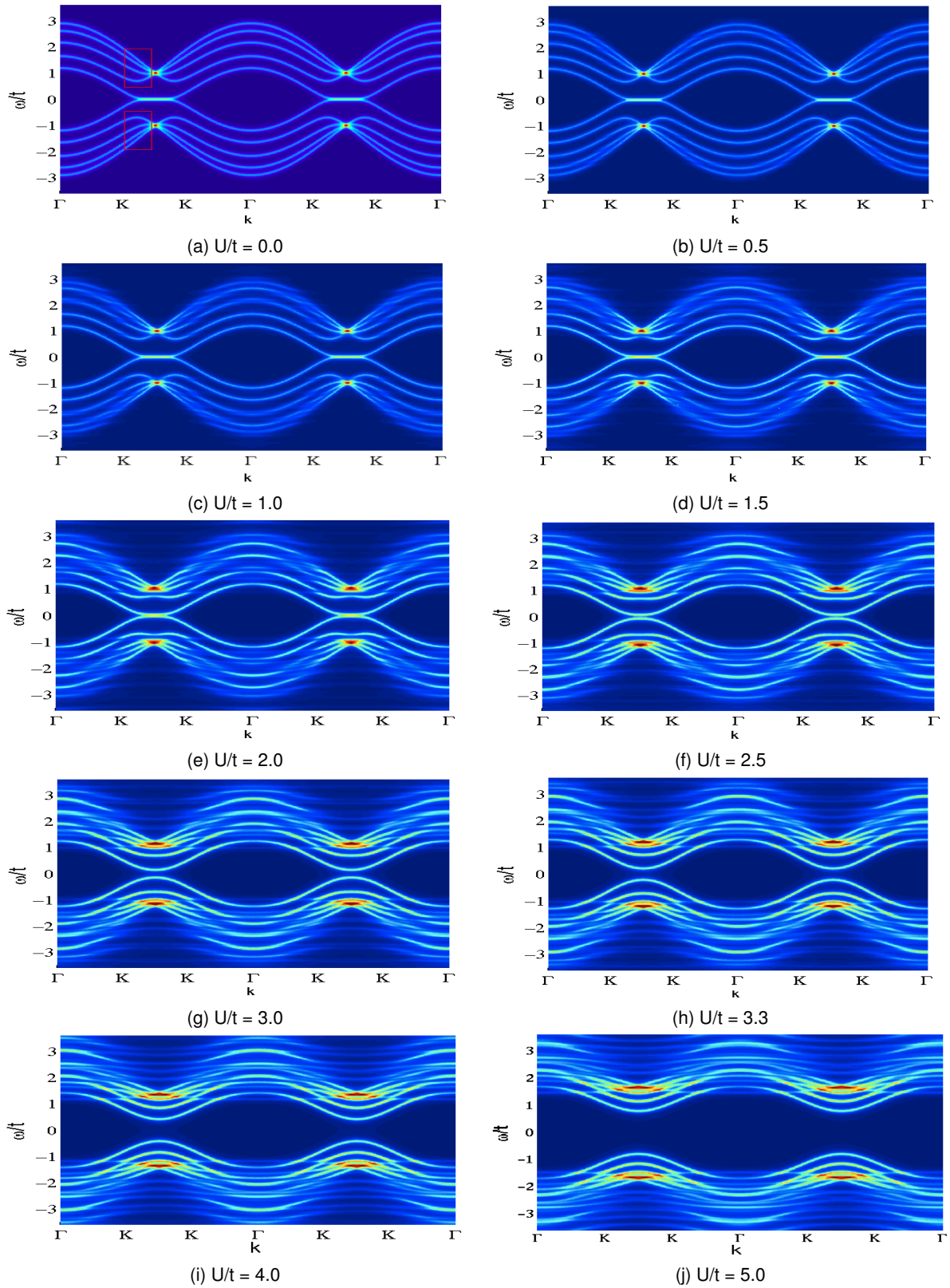

(a) U/t = 0.0

(b) U/t = 0.5

(c) U/t = 1.0

(d) U/t = 1.5

(e) U/t = 2.0

(f) U/t = 2.5

(g) U/t = 3.0

(h) U/t = 3.3

(i) U/t = 4.0

(j) U/t = 5.0

Figure 3.13: Same as Fig. 3.11, but for of a ZZ-W5 GNR.

Probably the most remarkable feature of the zig-zag GNR geometries is the appearance of conducting states at $\omega = 0$ in the non-interacting case, which can be seen clearly in Fig. 3.11a (ZZ-W3 GNR), Fig. 3.12a (ZZ-W4 GNR) and Fig. 3.13a (ZZ-W5 GNR). Due to the discovery of these states, the non-interacting zig-zag GNRs can be indeed described to behave in a *metallic* way, as predicted in the preliminary chapters.

Applying on-site interactions $U \neq 0$, a drastic change in the physical behaviour can be observed again, as it was the case for the infinite graphene lattice. As the on-site interaction increases, the number of conducting states at $\omega = 0$ decreases. Similar to the infinite graphene lattice, there exists some critical value for the on-site interaction U_{crit}, at which an energy gap appears. Comparing Fig. 3.11, Fig. 3.12 and Fig. 3.13 this critical values can be found to be

$$U_{crit}^{ZZ\text{-}W3} \approx 1.7t; \qquad U_{crit}^{ZZ\text{-}W4} \approx 2.0t; \qquad U_{crit}^{ZZ\text{-}W5} \approx 2.2t. \tag{3.112}$$

An accurate determination was rather difficult again due to the broadening of the energy bands. It is remarkable and also some kind of contradictory here that these critical on-site interaction values seem to increase with increasing ribbon width, since the value obtained for pristine graphene (see Eq.(3.99)), which should be the infinite width limit of the zig-zag GNRs, was found to be only $U_{crit} \approx 1.4t$. One reason for this arising contrariness could be the applied CPT method since it was shown that it overestimates the energy gap in graphene lattices compared to QMC calculations (see Fig. 3.5). But due to the fact that this overestimation would consequently also have to appear for the GNRs, the CPT formalism is not thought to be the reason for these large critical values. The real reason might rather be a divergence in the physical behaviour of wide zig-zag GNRs compared to that of wide armchair GNRs and pristine graphene, as will be shown in Sec. 3.5.
The described characteristics for increasing on-site interactions U are attended by a change of the physical behaviour from metallic to semiconducting. Since on-site interactions are not a theoretical artifact but rather real, this means that experimentally produced zig-zag GNRs are expected to behave like semiconductors.
A comparison of the increase of the energy gap Δ_{ZZ} depending on the value of U for the three zig-zag GNR geometries investigated in this section is presented in Fig. 3.14, with the particular energy gap calculated according to Eq.(3.74). The appearance of the critical interaction values U_{crit} can be discovered again. Remember its definition as the value of U where the energy gap Δ_{ZZ} exceeds the value of the broadening for the first time.
For the on-site interaction $U = 9.3eV \approx 3.3t$, which was found for graphene by cRPA [50], the energy gaps already reach a value of

$$\Delta_{ZZ\text{-}W3}|_{U_{graphene}} \approx 0.63t \approx 1.76\ eV; \quad \Delta_{ZZ\text{-}W4}|_{U_{graphene}} \approx 0.5t \approx 1.4\ eV; \quad \Delta_{ZZ\text{-}W5}|_{U_{graphene}} \approx 0.43t \approx 1.20\ eV \tag{3.113}$$

obviously characterizing the zig-zag GNRs as direct band gap semiconductors. Although the obtained energy gaps might be overestimated by the CPT method, there is no doubt about their opening in consequence of the applied electron-electron interactions.

Comparing the observed $\Delta_{ZZ}(U)$ characteristic to that of pristine graphene (see Fig. 3.5) it can be

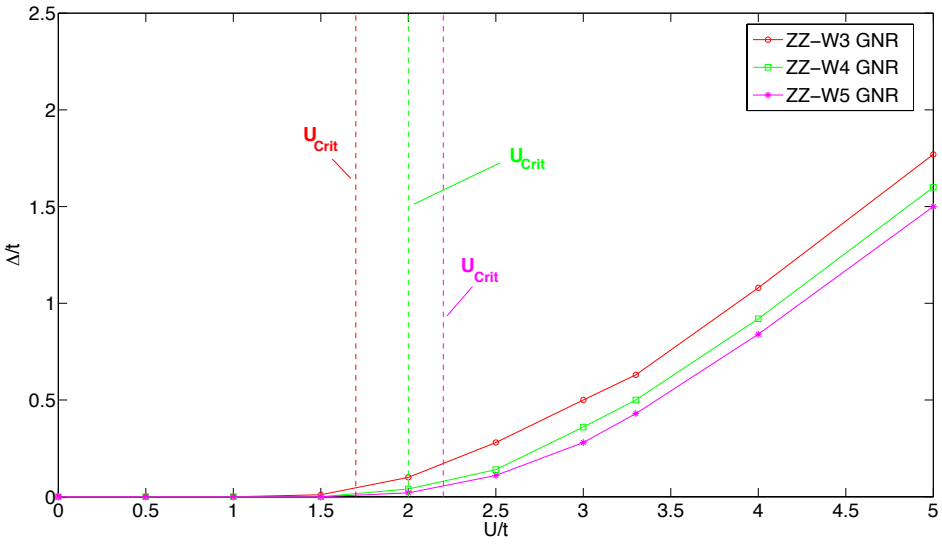

Figure 3.14: Energy gap $\Delta_{ZZ}(U)$ for a ZZ-W3 GNR, ZZ-W4 GNR and ZZ-W5 GNR as a function of the on-site interaction U, calculated according to Eq.(3.74). The critical values U_{crit}^{ZZ} where the energy gap opens up are indicated.

said that both the infinite structure and the GNR lattices show a similar behaviour, with slightly larger energy gaps in the infinite graphene lattice.
Since there are no literature values available for the width-dependence of the energy gap Δ_{ZZ} of zig-zag GNRs with applied on-site interactions, a comparison is not possible. However, for armchair GNRs the width-dependence of the energy gap Δ_{AC} in the non-interacting case was studied in detail [9] [53] and it shows precisely the same decreasing gap width for increasing ribbon width as observed for the zig-zag GNRs with applied on-site interactions.

As in the case of pristine graphene, the energy-momentum dispersion relation $\omega(\boldsymbol{k})$ of GNRs in the non-interacting case ($U = 0$), can also be obtained by Fourier transforming the whole problem into wavevector $\boldsymbol{k}$-space [9], which is possible due to the translational invariance in the longitudinal direction of the GNRs. Besides extended states zig-zag GNRs also feature one localized edge state, which causes the partially flat energy bands of zig-zag GNRs appearing in $\boldsymbol{k}$-space between every two contiguous K-points of the reciprocal superlattice BZ^{Λ} (shown in Fig. 3.10). Because of this localized state (which only occurs in the case of zig-zag GNRs) and the difference in the lattice geometries of zig-zag and armchair GNRs, two slightly different calculation formulas need to be derived. A comprehensive derivation is provided in [9]. The final analytical solution for $\omega(\boldsymbol{k})$ in the case of zig-zag GNR geometries is then given by

$$\omega(\boldsymbol{k}) = \pm t\sqrt{1 + {g_k}^2 + 2g_k cos(p)} \tag{3.114}$$

with $g_k = 2cos\,(k/2)$. $p = p(k, W)$ is the transverse wavenumber, which is given as the solution of

$$sin(pW) + g_k sin(pW + p) = 0. \tag{3.115}$$

The analytical description of the localized edge state is achieved by a similar formula:

$$\omega(\boldsymbol{k}) = \pm t\sqrt{1 + g_k{}^2 - 2|g_k|cosh(\eta)} \tag{3.116}$$

where η is given as the solution of

$$sin(\eta W) - |g_k|sin(\eta W + \eta) = 0. \tag{3.117}$$

The analytical solutions for the three zig-zag GNR geometries investigated in this section are plotted in Fig. 3.15 in order to prove the equivalence to the numerical solution of the non-interacting cases in Fig. 3.11a, Fig. 3.12a and Fig. 3.13a. The perfect accordance of the analytical and numerical solutions again corroborates that CPT is exact for $U = 0$.

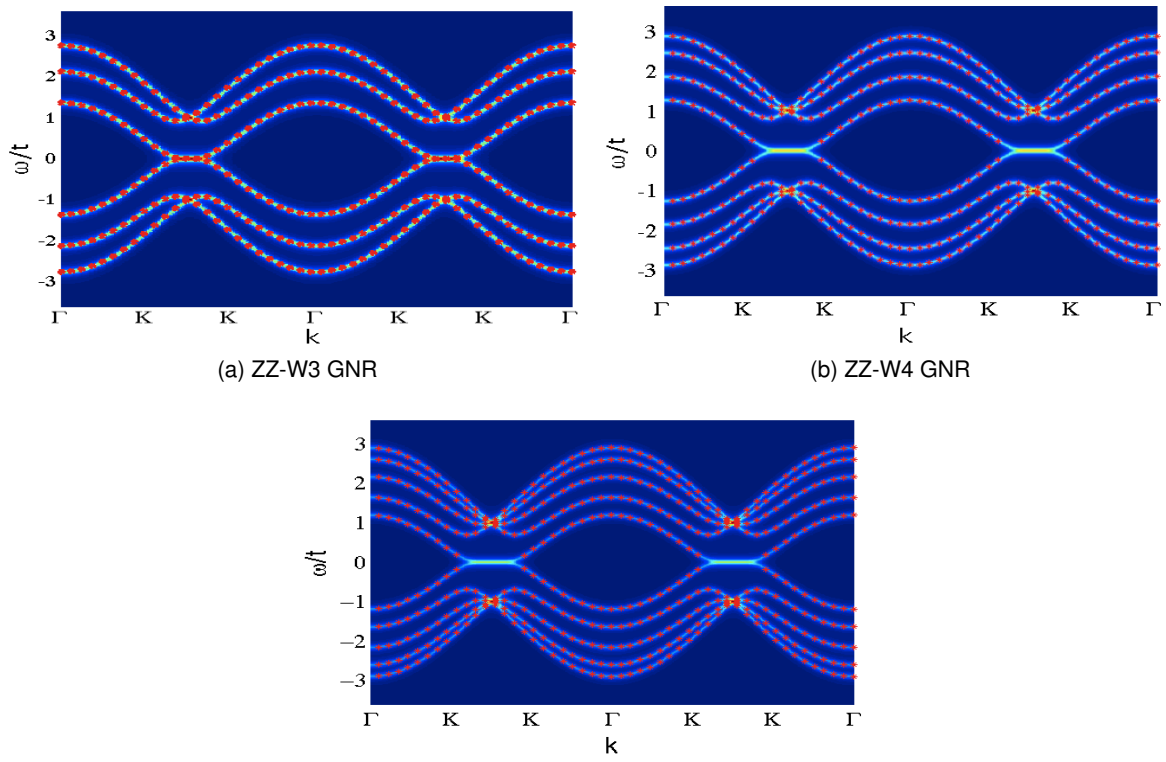

(a) ZZ-W3 GNR

(b) ZZ-W4 GNR

(c) ZZ-W5 GNR

Figure 3.15: Energy-momentum dispersion relation $\omega(\boldsymbol{k})$ of a ZZ-W3, ZZ-W4 and a ZZ-W5 GNR in the non-interacting $U = 0$ case (corresponding to Fig. 3.11a, Fig. 3.12a and Fig. 3.13a). The analytical solutions obtained by Eq.(3.114) and Eq.(3.116) are plotted in addttion (red markers) and show perfect agreement to the non-interacting numerical solutions.

3.3.3 (Local) electronic density of states

The energy-momentum dispersion relations $\omega(\boldsymbol{k})$ obtained in the last subsection delivered information wether the zig-zag GNRs behave like a metal, as predicted [24] [9], or not. Since the dispersion relation of a whole GNR provides no information about the cluster sites accountable for a possible metallic behaviour, it remains to investigate, which sites are providing the metallic states. To gain deeper insight into the distribution of the possible energy states on the different cluster sites, the DOS $\rho(\omega)$ and LDOS $\rho_i(\omega)$ of GNRs with a zig-zag edge orientation (calculated according to Eq.(3.76) and Eq.(3.78), respectively) are investigated in this section. In addition, by observing the changes in the DOS $\rho(\omega)$ and LDOS $\rho_i(\omega)$, caused by an applied on-site interaction U, a better understanding of the effect of the latter on the equilibrium properties of zig-zag GNRs can be gained.

The DOS and LDOS are plotted for different on-site interaction values $U/t = \{0.0, 0.5, 1.0, 1.5, 2.0, 2.5, 3.0, 3.3, 4.0, 5.0\}$ for the three investigated zig-zag GNR geometries. Fig. 3.16 and Fig. 3.17 illustrate the DOS and LDOS of the narrowest ZZ-W3 ribbon, while Fig. 3.18 and Fig. 3.19 show the DOS and LDOS of the ZZ-W4 ribbon. The results for the ZZ-W5 GNR are plotted in Fig. 3.20 and Fig. 3.21. To figure out, wether the metallic behaviour of the zig-zag GNRs, observed at least for the non-interacting $U = 0$ case in the previous subsection, can be attributed to localized edge states, as predicted in Ref. [11] or not, the LDOS of the outermost cluster site 1 and the first inner site 2 (see Fig. 3.9) is presented in the two top figures of every subplot.

A detailed investigation of the DOS and LDOS plots of the zig-zag GNRs reveals that the metallic states, observable in the energy-momentum dispersion relations (Fig. 3.11 - Fig. 3.13), occur indeed due to localized states at the edges of the ribbons. The LDOS $\rho_1(\omega)$ of the edge sites shows a sharp peak at $\omega = 0$ for on-site interaction values $U < U_{crit}^{ZZ}$, directly corresponding to these localized metallic edge states. As it was already described above, the metallic behaviour vanishes as the on-site interaction U gets larger than the critical value. The emergence of the energy gaps Δ_{ZZ} and the vanishing of the $\omega = 0$ peak can be clearly seen when comparing Fig. 3.16d and Fig. 3.16e for the ZZ-W3 GNR, Fig. 3.18e and Fig. 3.18f for the ZZ-W4 GNR and Fig. 3.20e and Fig. 3.20f for the ZZ-W5 GNR, respectively.
Furthermore, by investigating the top right plots of the LDOS $\rho_2(\omega)$ of the first inner sites, it can be observed that their shape hardly changes with increasing on-site interaction strength. Therefore, the on-site interaction U can be said to have the greatest effect on the outermost sites, which are exactly the sites, where the localized edge states occur.

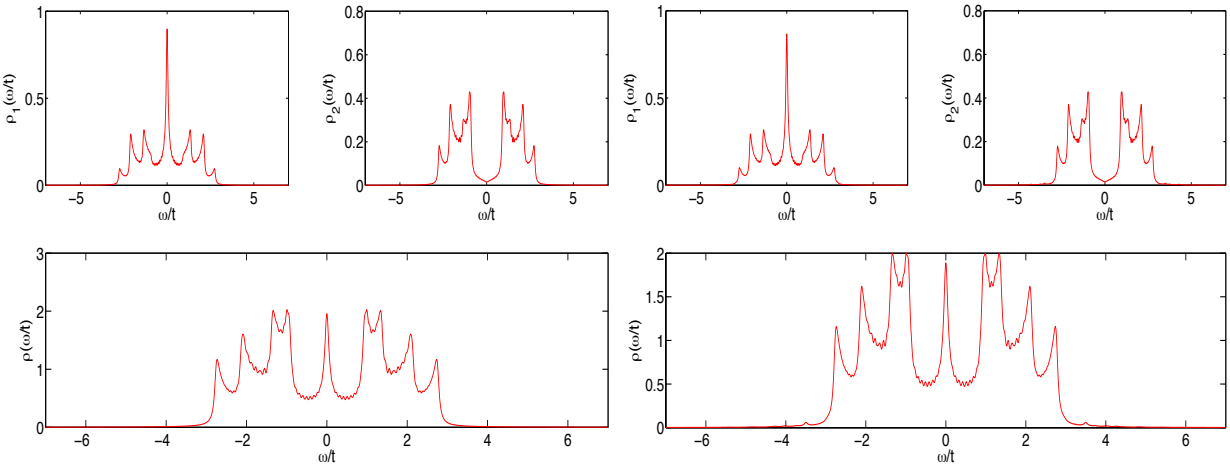

(a) U/t = 0.0

(b) U/t = 0.5

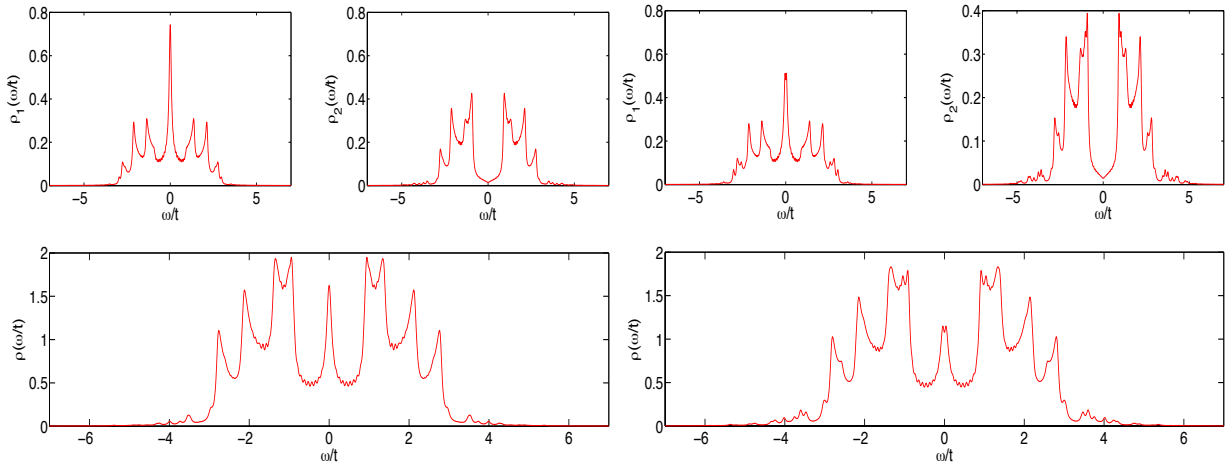

(c) U/t = 1.0

(d) U/t = 1.5

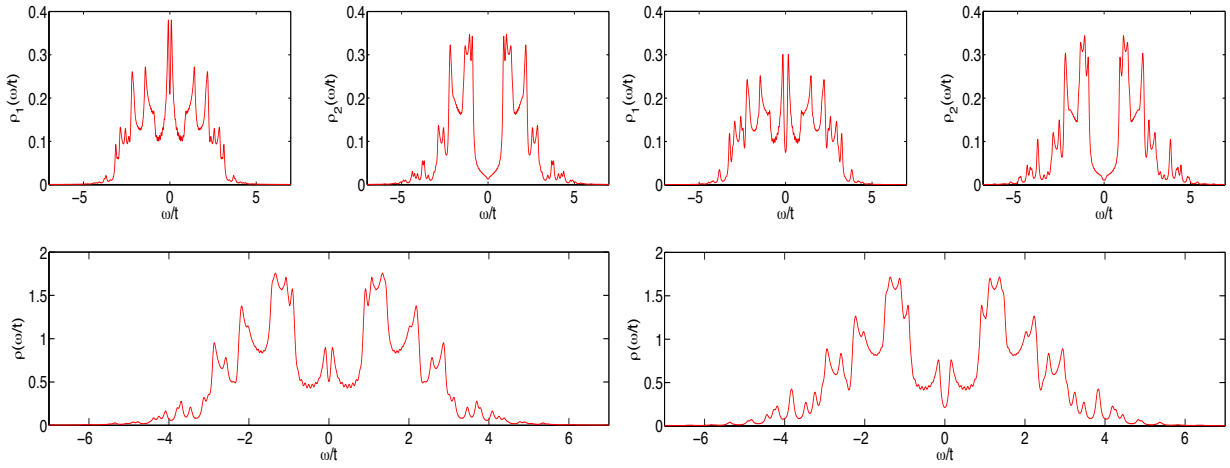

(e) U/t = 2.0

(f) U/t = 2.5

Figure 3.16: DOS $\rho(\omega)$ in the lattice of a ZZ-W3 GNR for different on-site interactions $U/t = \{0.0, 0.5, 1.0, 1.5, 2.0, 2.5\}$, where the interaction strength (value of U) is labeled below each subplot. Additionally the LDOS at the outermost site 1 (top left), which corresponds to the edge site, and at the first inner site 2 (top right) is presented in the two top figures of each subplot.

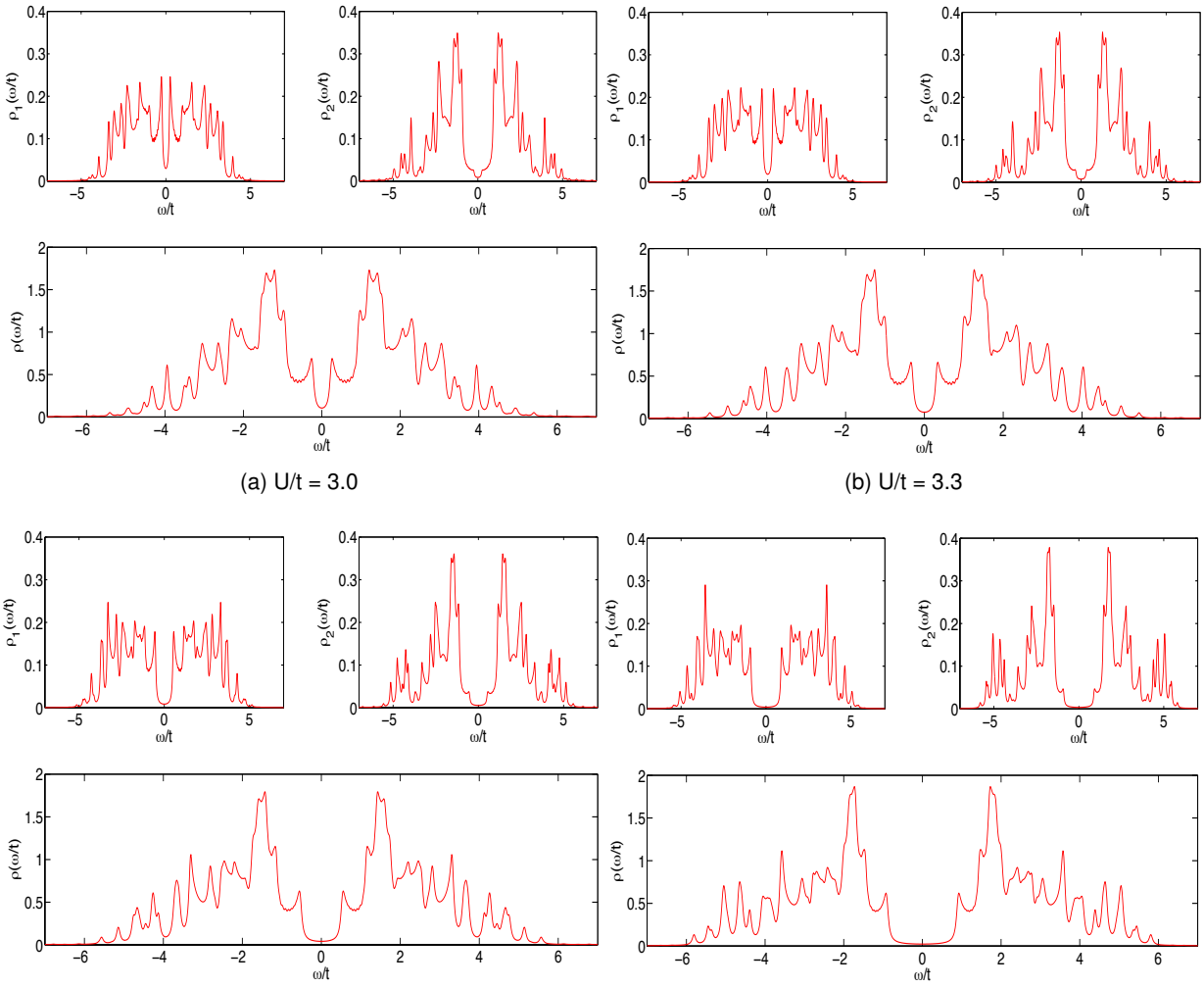

(a) U/t = 3.0

(b) U/t = 3.3

(c) U/t = 4.0

(d) U/t = 5.0

Figure 3.17: Same as Fig. 3.16, but for $U/t = \{3.0, 3.3, 4.0, 5.0\}$. The on-site interaction $U = 9.3eV \approx 3.3t$, which was found for graphene using cRPA [50], was used in subplot (b).

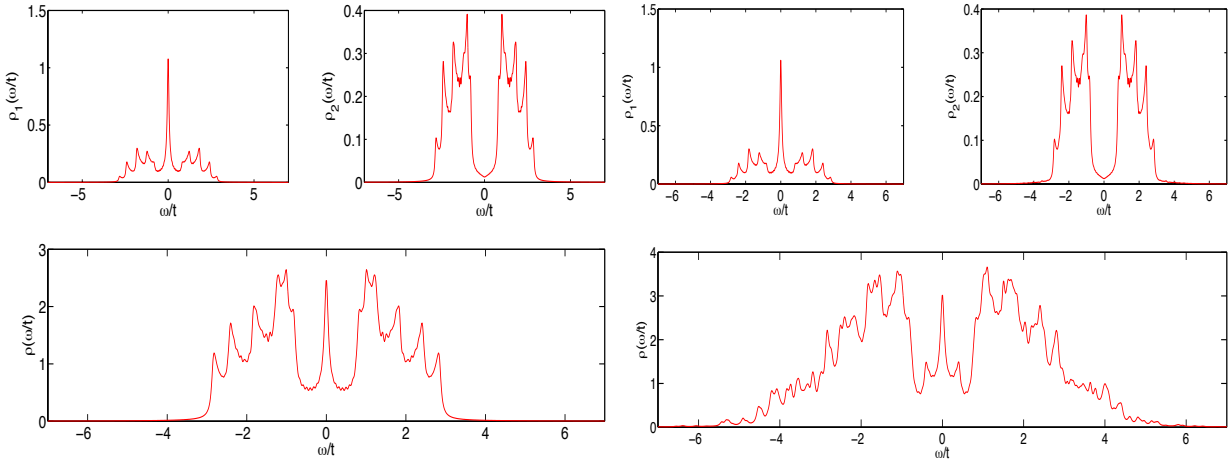

(a) U/t = 0.0

(b) U/t = 0.5

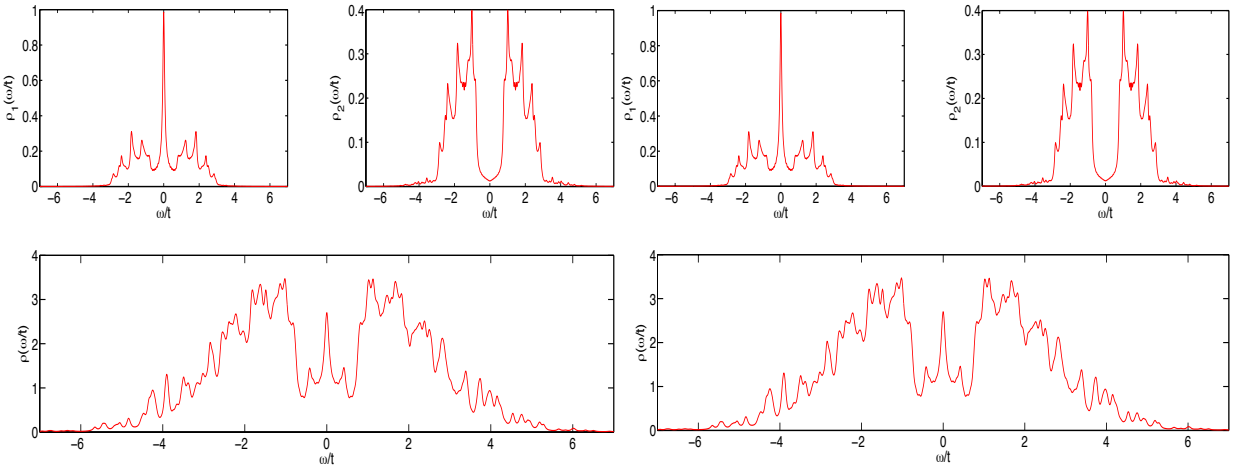

(c) U/t = 1.0

(d) U/t = 1.5

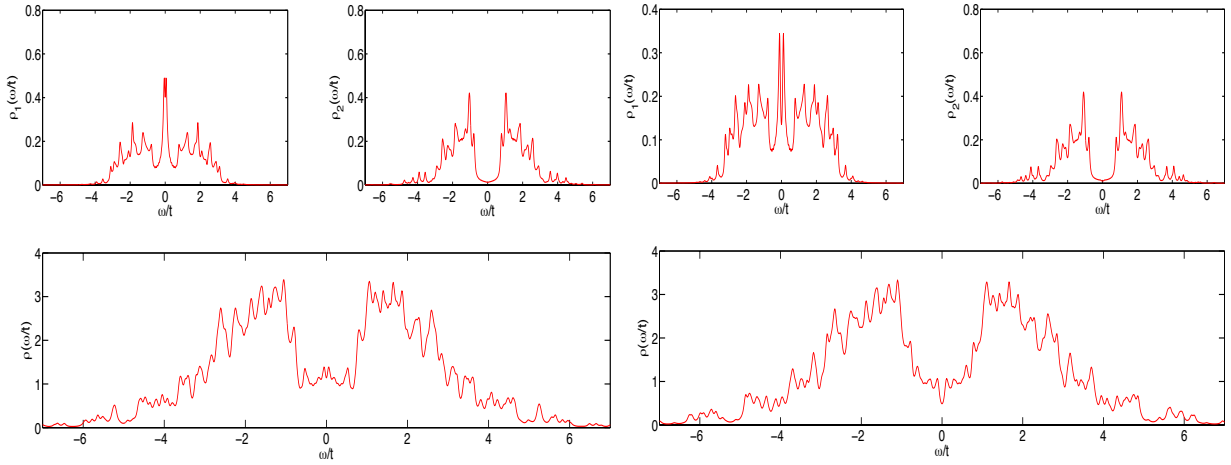

(e) U/t = 2.0

(f) U/t = 2.5

Figure 3.18: Same as Fig. 3.16, but for a ZZ-W4 GNR.

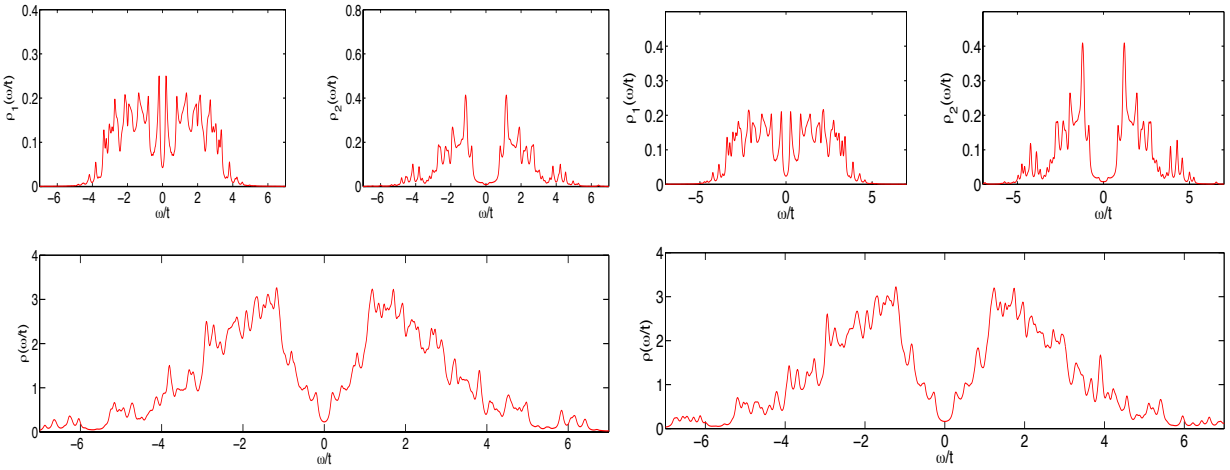

(a) U/t = 3.0 (b) U/t = 3.3

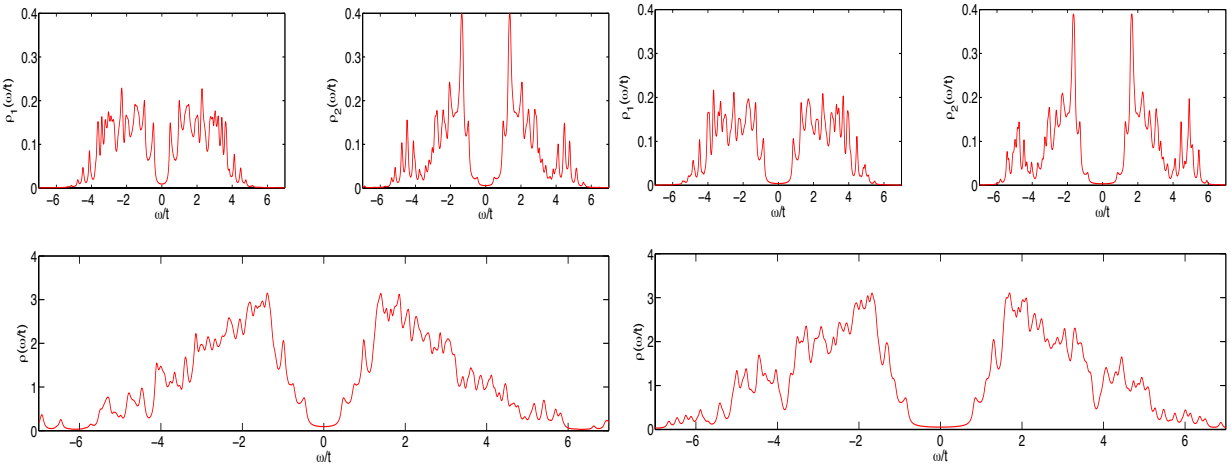

(c) U/t = 4.0 (d) U/t = 5.0

Figure 3.19: Same as Fig. 3.17, but for a ZZ-W4 GNR.

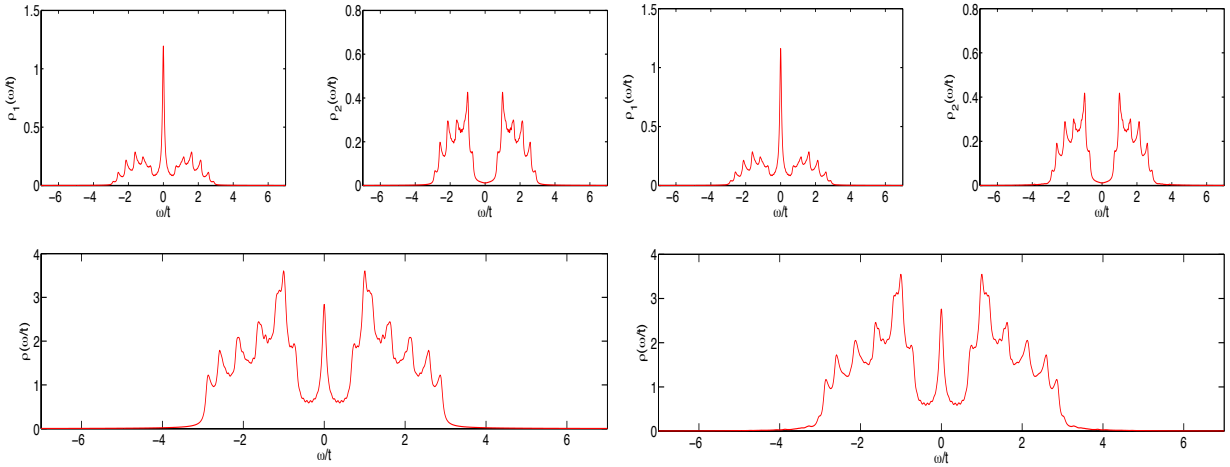

(a) U/t = 0.0

(b) U/t = 0.5

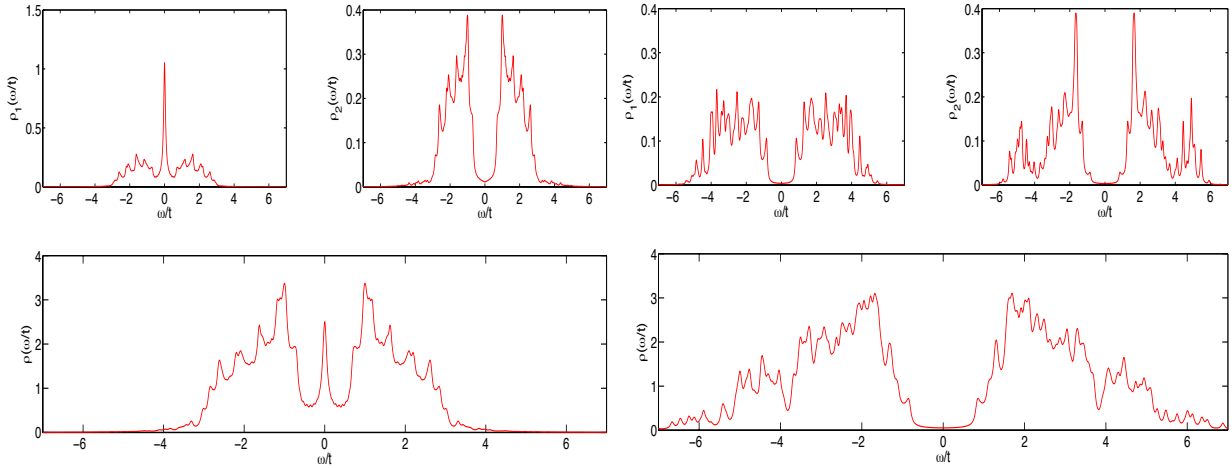

(c) U/t = 1.0

(d) U/t = 1.5

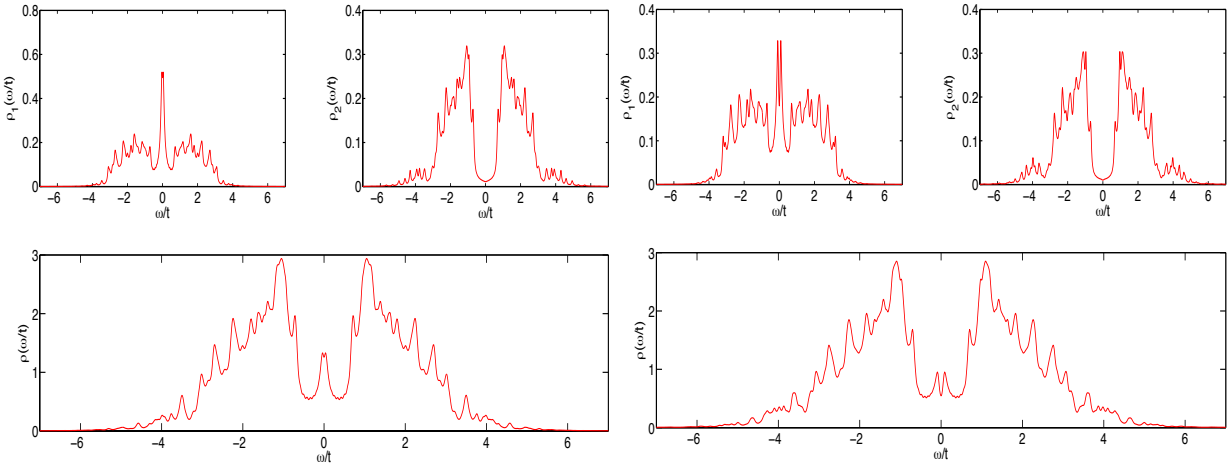

(e) U/t = 2.0

(f) U/t = 2.5

Figure 3.20: Same as Fig. 3.16, but for a ZZ-W5 GNR.

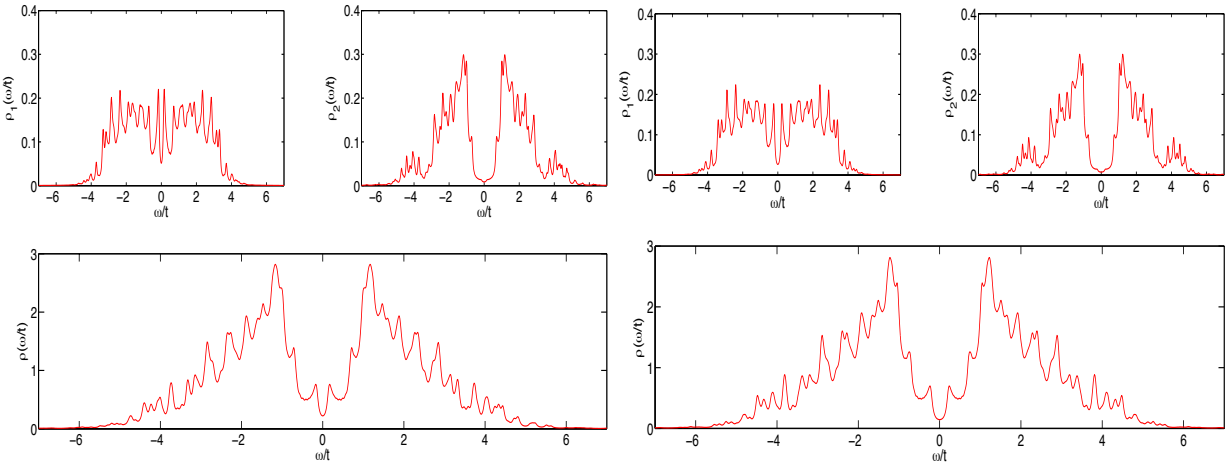

(a) U/t = 3.0

(b) U/t = 3.3

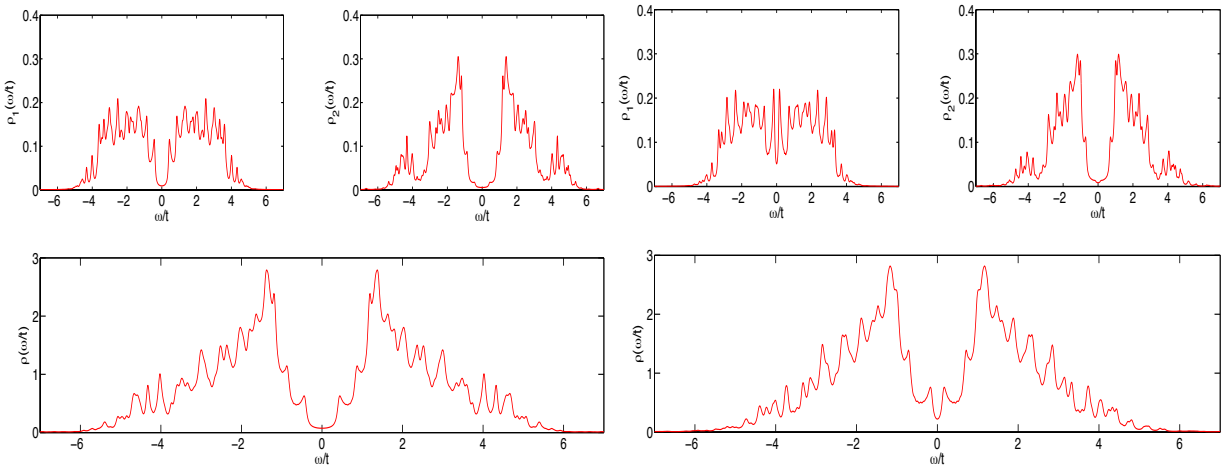

(c) U/t = 4.0

(d) U/t = 5.0

Figure 3.21: Same as Fig. 3.17, but for a ZZ-W5 GNR.

3.4 Armchair graphene nanoribbons with a width of four and five carbon atoms

After the investigation of narrow zig-zag GNR lattices in the previous section, the focus is now turned on armchair GNR geometries (see also Fig. 2.3b). As in the previous sections, a closer look on the lattice geometries of the treated structures is taken first, subsequently followed by a presentation of the gained results for the equilibrium properties, i.e. spectral function $A(\omega, \boldsymbol{k})$, energy gap Δ and the (L)DOS $\rho(\omega)$. Last but not least an interpretation of the results is provided, in terms of an explanation of the discovered behaviours.

3.4.1 Lattice geometry

Armchair GNRs with 4 and 5 C atoms along the width W are investigated in this section, where a $W = N$ ribbon is denoted *AC-WN* in the following. The geometry of the two investigated armchair GNRs is shown in Fig. 3.22a (AC-W4) and Fig. 3.22c (AC-W5).
As in the case of zig-zag GNRs, there remains only one lattice vector for armchair GNR geometries given by

$$\boldsymbol{r} = \frac{a}{\sqrt{3}} \begin{pmatrix} 3 \\ 0 \end{pmatrix}. \tag{3.118}$$

The chosen CPT clusters coincide again with the physical unit cell, resulting in a superlattice vector $\boldsymbol{R}$ equal to the lattice vector $\boldsymbol{r}$:

$$\boldsymbol{R} = \boldsymbol{r} = \frac{a}{\sqrt{3}} \begin{pmatrix} 3 \\ 0 \end{pmatrix}. \tag{3.119}$$

The lattice geometries of the two investigated armchair GNRs, the chosen cluster tiling and the resulting superlattice vector $\boldsymbol{R}$ are shown in Fig. 3.22, where it can be also observed that the above statements apply to both investigated armchair GNR geometries. The cluster tiling is represented by the green lines in Fig. 3.22a (AC-W4) and Fig. 3.22c (AC-W5). The corresponding superlattice vectors $\boldsymbol{R}$ are sketched as brown arrows. A detailed view of the used clusters, with all the possible inter-cluster hoppings indicated by black double-headed arrows, is presented in Fig. 3.22b (AC-W4) and Fig. 3.22d (AC-W5)

The locations of the atoms in the symmetrical 8-site cluster of the AC-W4 GNR are given by

$$\boldsymbol{c}_{1,8} = \tfrac{a}{\sqrt{3}} \begin{pmatrix} \mp 1 \\ \sqrt{3} \end{pmatrix}; \quad \boldsymbol{c}_{2,7} = \tfrac{a}{\sqrt{3}} \begin{pmatrix} \mp \frac{1}{2} \\ \frac{\sqrt{3}}{2} \end{pmatrix}; \quad \boldsymbol{c}_{3,6} = \tfrac{a}{\sqrt{3}} \begin{pmatrix} \mp 1 \\ 0 \end{pmatrix}; \quad \boldsymbol{c}_{4,5} = \tfrac{a}{\sqrt{3}} \begin{pmatrix} \mp \frac{1}{2} \\ -\frac{\sqrt{3}}{2} \end{pmatrix} \tag{3.120}$$

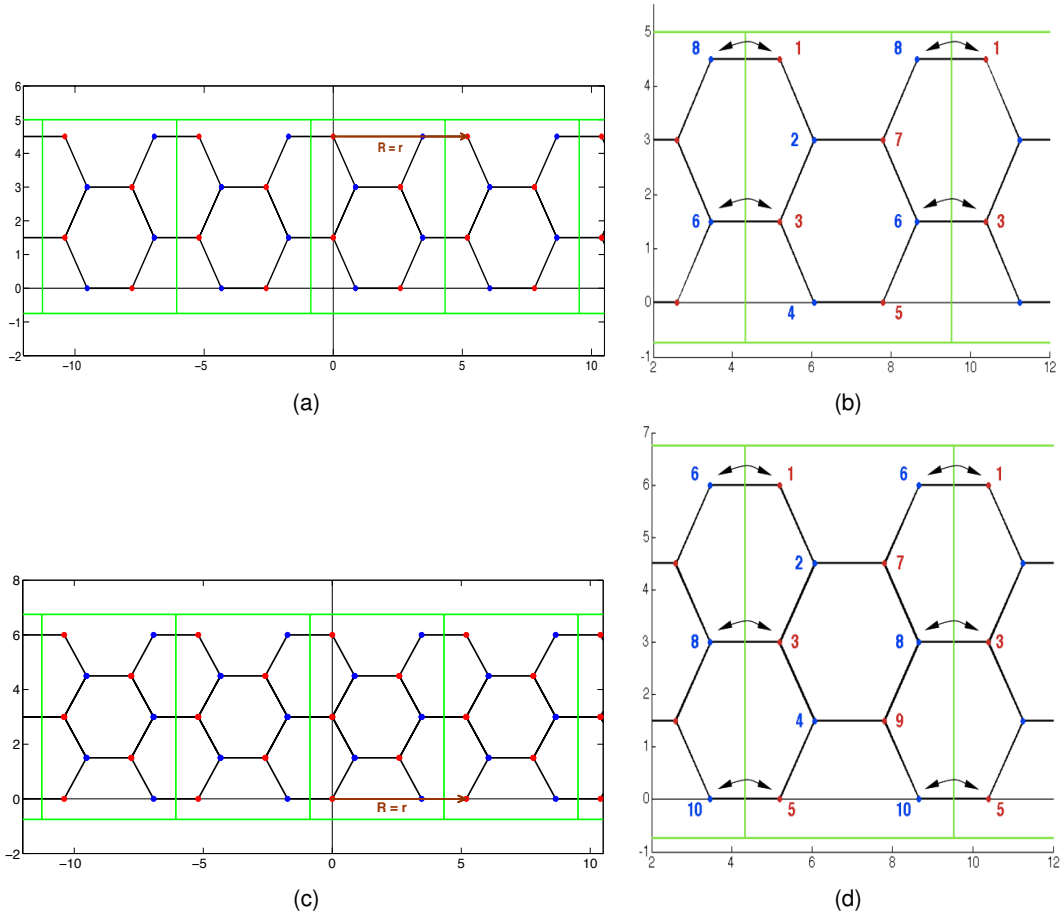

Figure 3.22: Geometry of the real-space lattice λ and the applied cluster tiling for an AC-W4 GNR (a) and an AC-W5 GNR (c). The red and blue dots mark the C atoms corresponding to the two different sublattices of the infinite graphene lattice. The lattice vector $\boldsymbol{r}$ and the superlattice vector $\boldsymbol{R}$ are represented by the brown arrows. (b) and (d): Detailed view of the corresponding $2W$-site clusters. The numbers label the $2W$ cluster sites, while the double-headed arrows indicate the possible inter-cluster hoppings.

while the atoms in 10-site cluster of the AC-W5 GNR are located at the following positions

$$\boldsymbol{c}_{1,6} = \frac{a}{\sqrt{3}}\begin{pmatrix}\mp 1\\ \sqrt{3}\end{pmatrix}; \quad \boldsymbol{c}_{2,7} = \frac{a}{\sqrt{3}}\begin{pmatrix}\mp\frac{1}{2}\\ \frac{\sqrt{3}}{2}\end{pmatrix}; \quad \boldsymbol{c}_{3,8} = \frac{a}{\sqrt{3}}\begin{pmatrix}\mp 1\\ 0\end{pmatrix}; \quad \boldsymbol{c}_{4,9} = \frac{a}{\sqrt{3}}\begin{pmatrix}\mp\frac{1}{2}\\ -\frac{\sqrt{3}}{2}\end{pmatrix}; \quad \boldsymbol{c}_{5,10} = \frac{a}{\sqrt{3}}\begin{pmatrix}\mp 1\\ -\sqrt{3}\end{pmatrix} \tag{3.121}$$

where the 10-site cluster is symmetric again.

The cluster tiling again introduces a superlattice Γ and a corresponding one-dimensional superlattice BZ^{Λ}, which is shown in Fig. 3.23. The resulting reciprocal superlattice vector $\boldsymbol{K}$ is given by

$$\boldsymbol{K} = \frac{2\pi}{\sqrt{3}a}\begin{pmatrix}1\\ 0\end{pmatrix}. \tag{3.122}$$

Obviously, the first BZ looks the same for the AC-W4 GNR and the AC-W5 GNR, since their lattices are described by the same superlattice vector $\boldsymbol{R}$ defined in Eq.(3.119).
Since the reciprocal lattice of an armchair GNR is described by a zig-zag GNR lattice, as already mentioned before, there are again some points in the reciprocal superlattice BZ^{Λ}, which are of particular interest. They are denoted M and K in the following and are located at the following reciprocal space coordinates k_x

$$M = \left\{..., \frac{\pi}{2\sqrt{3}a}, \frac{3\pi}{2\sqrt{3}a}, ...\right\} \quad ; \quad \boldsymbol{K} = \left\{..., 0, \frac{\pi}{\sqrt{3}a}, \frac{2\pi}{\sqrt{3}a}, ...\right\}. \tag{3.123}$$

The notation was chosen in this specific way again, because the defined K-points in the armchair GNRs reciprocal superlattice BZ^{Λ} and the Dirac points of the whole reciprocal zig-zag lattice are located exactly at the same k_x coordinates. Therefore, the development of *Dirac-cone-like* dispersion relations is expected at exactly these reciprocal superlattice points. The k_x coordinates of the reciprocal superlattice Γ-points correspond to the k_x coordinates of the Γ-points in the reciprocal zig-zag lattice. A graphical description is provided in Fig. 3.23.

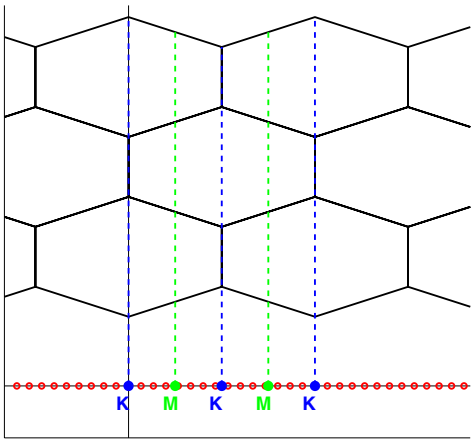

Figure 3.23: Above (black): Reciprocal lattice of an AC-W5 GNR. Below (red): Reciprocal superlattice Λ of all investigated armchair GNR structures. The distinguishing points M and K are indicated, with the k_x coordinates of the K-points corresponding to the k_x coordinates of the important Dirac points, as indicated by the blue dashed-lines.

The calculation of the retarded cluster Green's function $\boldsymbol{G}_0^R(\omega)$ requires the nearest-neighbour intra-cluster hoppings of the particular armchair GNR clusters again, which are described by the nearest-neighbour hopping integrals t_{ij} of graphene and are identical for all hoppings. In contrast to the zig-zag GNR geometries, care must be taken with the indices of the nearest-neighbours (according to the site labeling in Fig. 3.22):

$$t_{ij} = t \quad \forall \text{ nearest neighbours } i,j \text{ according to Fig. 3.22 .} \tag{3.124}$$

The detailed views of the particular armchair GNR clusters in Fig. 3.22b (AC-W4 GNR) and Fig. 3.22d (AC-W5 GNR) show the inter-cluster hoppings as black double-headed arrows, which determine the corresponding hopping matrices $T_{AC}^{2Ws}(\boldsymbol{k})$ according to Eq.(3.50):

$$T_{AC}^{8s}(\boldsymbol{k}) = t \begin{pmatrix} 0 & 0 & 0 & 0 & 0 & 0 & 0 & e^{-i\boldsymbol{k}\boldsymbol{R}^\Lambda} \\ 0 & 0 & 0 & 0 & 0 & 0 & 0 & 0 \\ 0 & 0 & 0 & 0 & 0 & e^{-i\boldsymbol{k}\boldsymbol{R}^\Lambda} & 0 & 0 \\ 0 & 0 & 0 & 0 & 0 & 0 & 0 & 0 \\ 0 & 0 & 0 & 0 & 0 & 0 & 0 & 0 \\ 0 & 0 & e^{i\boldsymbol{k}\boldsymbol{R}^\Lambda} & 0 & 0 & 0 & 0 & 0 \\ 0 & 0 & 0 & 0 & 0 & 0 & 0 & 0 \\ e^{i\boldsymbol{k}\boldsymbol{R}^\Lambda} & 0 & 0 & 0 & 0 & 0 & 0 & 0 \end{pmatrix} \tag{3.125}$$

$$T_{AC}^{10s}(\boldsymbol{k}) = t \begin{pmatrix} 0 & 0 & 0 & 0 & 0 & e^{-i\boldsymbol{k}\boldsymbol{R}^\Lambda} & 0 & 0 & 0 & 0 \\ 0 & 0 & 0 & 0 & 0 & 0 & 0 & 0 & 0 & 0 \\ 0 & 0 & 0 & 0 & 0 & 0 & 0 & e^{-i\boldsymbol{k}\boldsymbol{R}^\Lambda} & 0 & 0 \\ 0 & 0 & 0 & 0 & 0 & 0 & 0 & 0 & 0 & 0 \\ 0 & 0 & 0 & 0 & 0 & 0 & 0 & 0 & 0 & e^{-i\boldsymbol{k}\boldsymbol{R}^\Lambda} \\ e^{i\boldsymbol{k}\boldsymbol{R}^\Lambda} & 0 & 0 & 0 & 0 & 0 & 0 & 0 & 0 & 0 \\ 0 & 0 & 0 & 0 & 0 & 0 & 0 & 0 & 0 & 0 \\ 0 & 0 & e^{i\boldsymbol{k}\boldsymbol{R}^\Lambda} & 0 & 0 & 0 & 0 & 0 & 0 & 0 \\ 0 & 0 & 0 & 0 & 0 & 0 & 0 & 0 & 0 & 0 \\ 0 & 0 & 0 & 0 & e^{i\boldsymbol{k}\boldsymbol{R}^\Lambda} & 0 & 0 & 0 & 0 & 0 \end{pmatrix} \tag{3.126}$$

What follows is a presentation of the results of the equilibrium properties introduced in Sec. 3.1.2, which were calculated for different values of the on-site interaction U for the AC-W4 and AC-W5 GNR geometry.

3.4.2 Spectral function

The spectral function $A(\boldsymbol{k}, \omega)$ was calculated again according to Eq.(3.68) for on-site interactions $U/t = \{0.0, 0.5, 1.0, 1.5, 2.0, 2.5, 3.0, 3.3, 4.0, 5.0\}$. The resulting energy-momentum dispersion relation $\omega(\boldsymbol{k})$ of the particular armchair GNRs are plotted in Fig. 3.24 (AC-W4 GNR) and Fig. 3.25 (AC-W5 GNR)

It was outlined in Chapter 2 that armchair GNRs can behave in a semiconducting *or* (semi-)metallic way, depending on their particular width [25]. The necessary condition to be fulfilled for a (semi-)metallic behaviour, was a number of $N = 3M - 1$ C atoms along the ribbon width, where M is an integer. Now, this condition is obviously fulfilled for the AC-W5 GNR with $N = 5 = 3 \cdot 2 - 1$ atoms along the width of the ribbon. Therefore, the two investigated armchair structures are expected to exhibit completely different equilibrium properties.

Focusing on the narrower AC-W4 GNR first, the appearance of an energy gap Δ_{AC} can be observed already for the non-interacting $U = 0$ case in Fig. 3.24a, clearly approving the expected semiconducting behaviour. Similar to the zig-zag GNR geometries the emergence of cone-like features (highlighted with a red frame in the particular figure) precisely at the K-points - the reciprocal lattice points where the Dirac cones were observed in the energy-momentum plots of the pristine graphene lattice (see Fig. 3.4) - can be observed again. However, in contrast to the continuous disappearance of the Dirac cones (cone-like features) with increasing on-site interaction U in the case of pristine graphene (zig-zag GNRs), for the AC-W4 GNR geometry the energy gap first decreases with increasing on-site interaction U, which comes along with a transformation of the cone-like features to real Dirac cones. The described features are clearly observable in Fig. 3.24a - Fig. 3.24f. For an on-site interaction value $U = 2.5t$ the energy gap completely vanishes and the Dirac cones of the non-interacting pristine graphene lattice are completely reestablished, resulting in a semi-metallic physical behaviour. This absolutely striking and somehow paradoxical characteristic is shown in Fig. 3.24f. A similar behaviour was also reported for pristine graphene using Renormalization Group Theory (RGT) [54].
The energy gap increases again with increasing on-site interactions for $U > 2.5t$. The complete U-dependency of the energy gap $\Delta_{AC}(U)$ is presented in Fig. 3.26, which allows for a comprehensive analyzation of the physical changes in the AC-W4 GNR lattice due to applied on-site interactions.

Next, the focus is turned on the AC-W5 GNR geometry. As explained above, a semi-metallic behaviour is expected at least for the non-interacting case $U = 0$ [25] . Analyzing Fig. 3.25a - Fig. 3.25c, the appearance of linear dispersion relations, i.e. Dirac cones in three dimensions, at the reciprocal K-points can be obtained, approving the expected semi-metallic behaviour without ambiguity.
Similar to the pristine graphene lattice, the semi-metallic behaviour changes to a semiconducting one at some critical value for the on-site interaction U_{crit}. Inspecting Fig. 3.25d - Fig. 3.25j the emergence of an energy gap Δ_{AC}, which grows with increasing on-site interaction U, can be observed. This enhancement of the bandgap Δ_{AC} is directly related to the change from semi-metallic

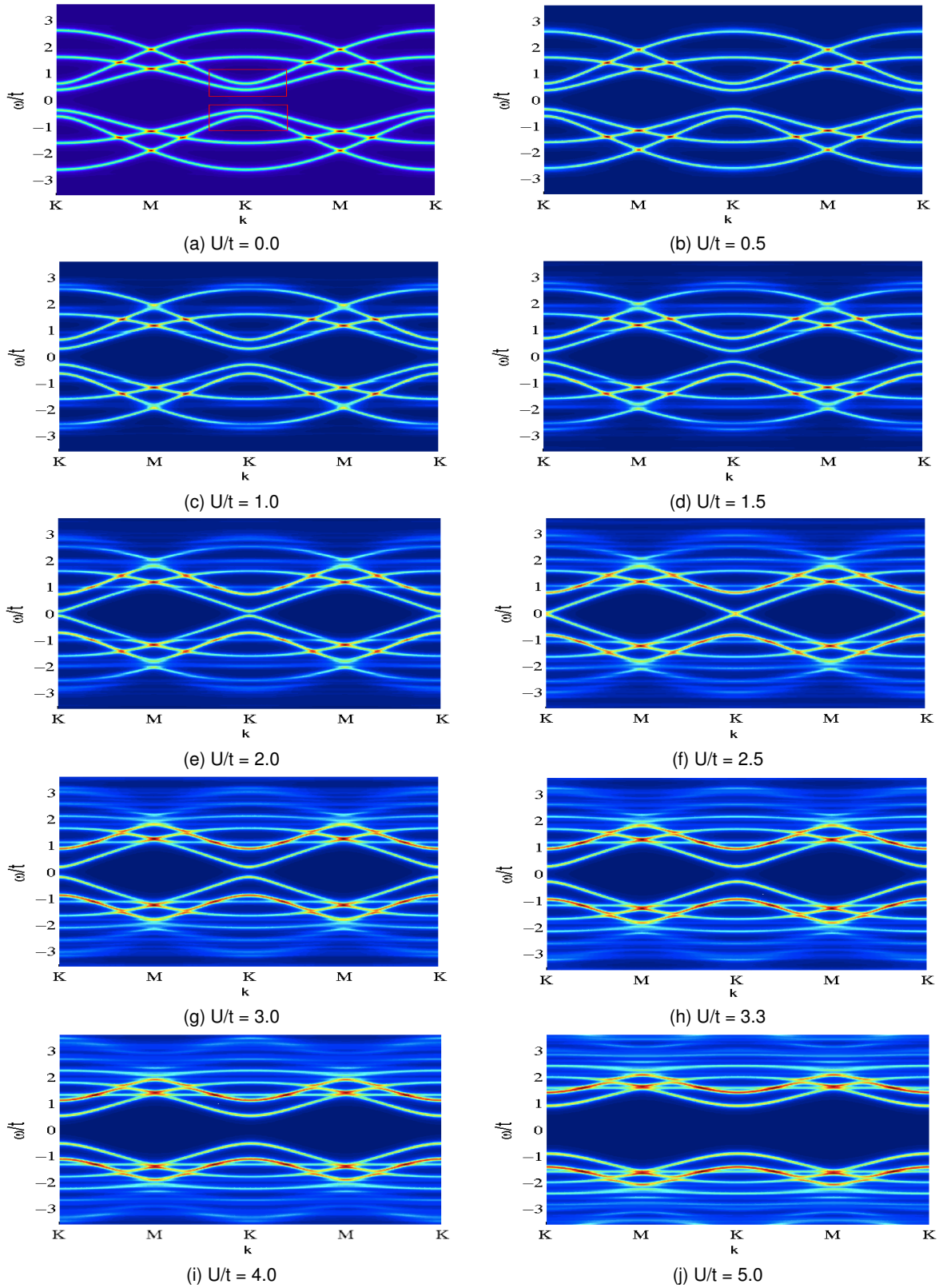

(a) U/t = 0.0 (b) U/t = 0.5

(c) U/t = 1.0 (d) U/t = 1.5

(e) U/t = 2.0 (f) U/t = 2.5

(g) U/t = 3.0 (h) U/t = 3.3

(i) U/t = 4.0 (j) U/t = 5.0

Figure 3.24: Energy-momentum dispersion relation $\omega(\boldsymbol{k})$ of an AC-W4 GNR for different on-site interactions $U/t = \{0.0, 0.5, 1.0, 1.5, 2.0, 2.5, 3.0, 3.3, 4.0, 5.0\}$, where the interaction strength (value of U) is labeled below each subplot. The energy ω is plotted in terms of the hopping integral t: $\omega = \omega/t$. The red frame in (a) highlights the appearing cone-like features. An on-site interaction value $U = 9.3eV \approx 3.3t$, which was found for graphene using cRPA [50], was used in subplot (h).

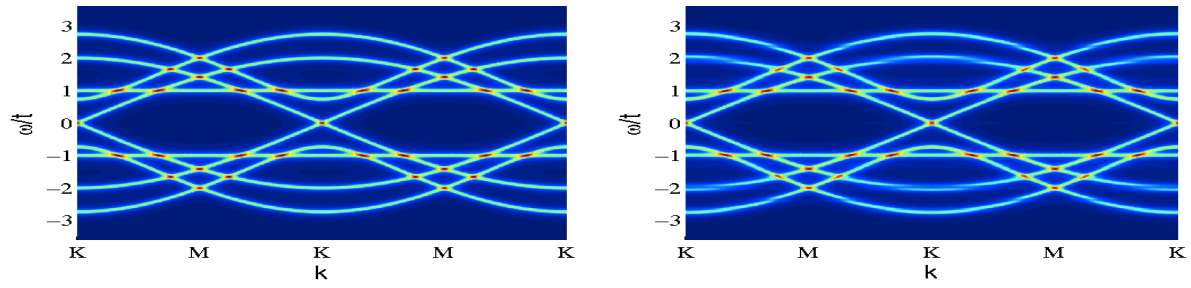

(a) U/t = 0.0

(b) U/t = 0.5

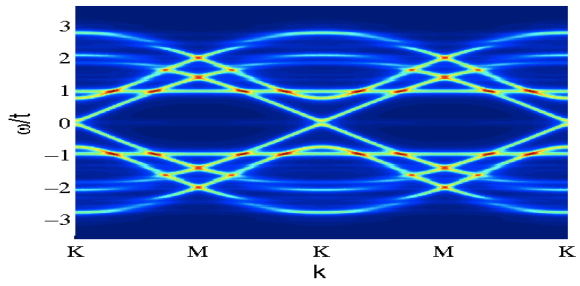

(c) U/t = 1.0

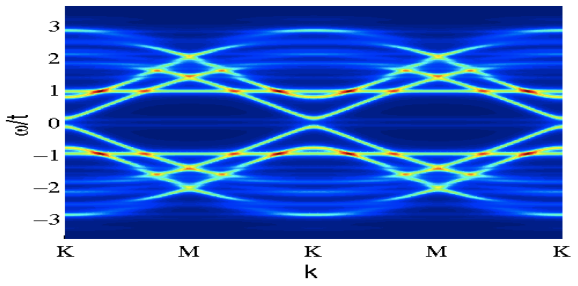

(d) U/t = 1.5

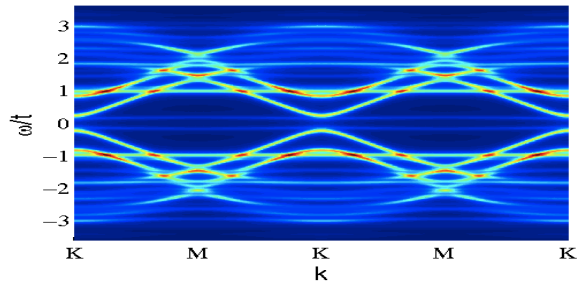

(e) U/t = 2.0

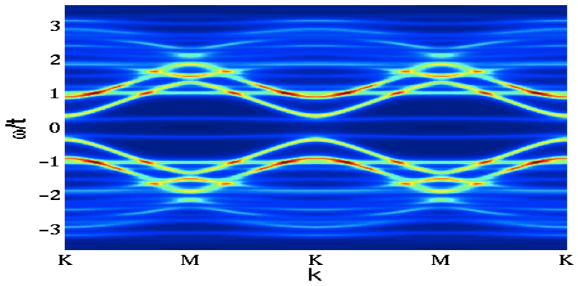

(f) U/t = 2.5

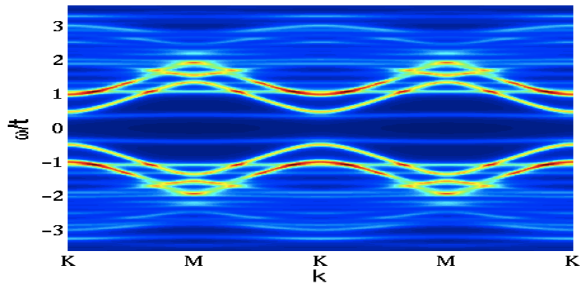

(g) U/t = 3.0

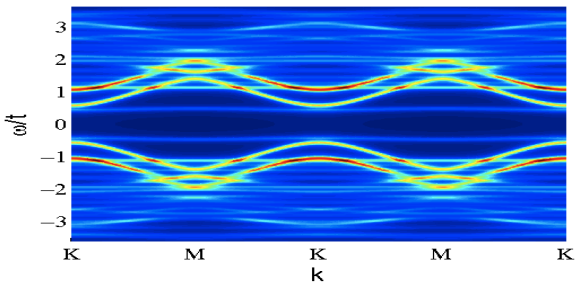

(h) U/t = 3.3

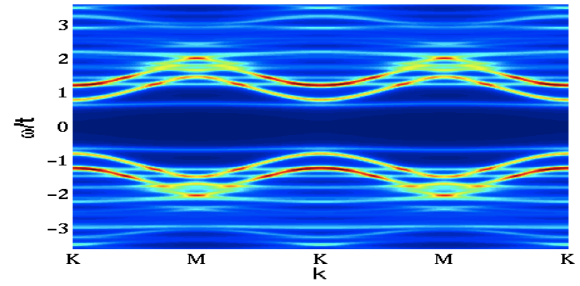

(i) U/t = 4.0

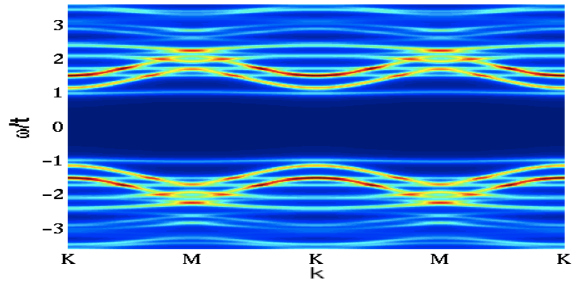

(j) U/t = 5.0

Figure 3.25: Same as Fig. 3.24, but for an AC-W5 GNR.

to semiconducting behaviour. Continuously comparing the subplots of Fig. 3.25 with each other, a critical value U_{crit} can be found:

$$U_{crit}^{AC\text{-}W5} \approx 1.2t \tag{3.127}$$

where the occurring broadening of the energy bands, which makes an accurate determination rather difficult, needs to be mentioned again.

The enhancement of the energy gap width Δ_{AC} of the AC-W5 GNR geometry with increasing on-site interaction U is also presented in Fig. 3.26, where the energy gap was calculated according to Eq.(3.74). The critical interaction value U_{crit} is indicated.

The described characteristics at increasing on-site interactions U are attended by a change of the physical behaviour from semi-metallic to semiconducting. This means that experimentally produced AC-W5 GNRs are expected to behave like semiconductors.

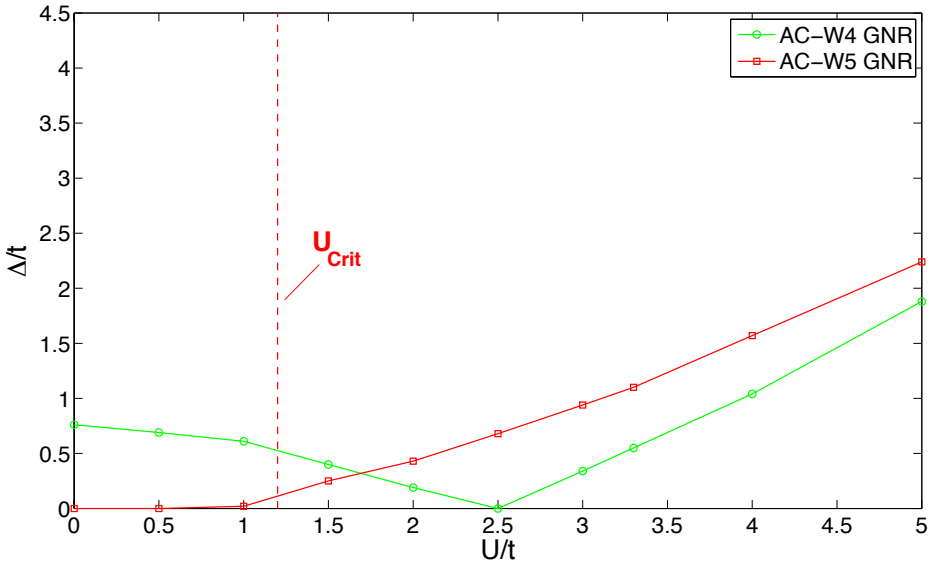

Figure 3.26: Energy gap $\Delta_{AC}(U)$ for an AC-W4 and AC-W5 GNR as a function of the on-site interaction U, calculated according to Eq.(3.74). The critical value U_{crit}^{AC} where the energy gap opens up in the AC-W5 GNR is indicated.

For the on-site interaction $U = 9.3eV \approx 3.3t$, which was found for graphene by cRPA [50], the energy gaps of the two investigated armchair GNR geometries are given by

$$\Delta_{AC\text{-}W4}|_{U_{graphene}} \approx 0.55t \approx 1.54\ eV; \quad \Delta_{AC\text{-}W5}|_{U_{graphene}} \approx 1.15t \approx 3.22\ eV \tag{3.128}$$

obviously distinguishing both armchair GNRs as direct band gap semiconductors. In this context the probably occurring overestimation of the energy gaps due to the applied CPT method should be remembered again.

Comparing the observed $\Delta_{AC}(U)$ characteristic of the AC-W5 GNR to that of pristine graphene (see Fig. 3.5) it can be said that both the infinite structure and the armchair GNR lattice show a similar behaviour, with comparatively larger energy gaps in the armchair GNR lattice.

For the energy gap Δ_{AC} of the AC-W4 GNR geometry in the non-interacting case $U = 0$ a value of $\Delta_{AC} \approx 0.77t \approx 2.15\ eV$ was found. This value is in perfect agreement with the values given in literature [9] [53].

As already stated in the previous section, the energy-momentum dispersion relation $\omega(\boldsymbol{k})$ of armchair GNRs in the non-interacting case ($U = 0$), can also be obtained by Fourier transforming the whole problem into wavevector $\boldsymbol{k}$-space. A comprehensive derivation (provided in [9]) yields the final analytical solution for $\omega(\boldsymbol{k})$ in the case of armchair GNR geometries

$$\omega(\boldsymbol{k}) = \pm t\sqrt{1 + \epsilon_p{}^2 + 2\epsilon_p cos\left(\frac{k}{2}\right)} \tag{3.129}$$

with $\epsilon_p = 2cos(p)$. $p = p(W)$ is the transverse wavenumber, which is determined through the edge boundary condition by

$$p = \frac{r}{W+1}\pi, \quad r = 1, 2, 3, ...W. \tag{3.130}$$

The analytical solutions for the two armchair GNR geometries investigated in this section are plotted in Fig. 3.27 in order to prove their equivalence to the numerical solutions of the non-interacting cases in Fig. 3.24a and Fig. 3.25a. The perfect accordance of both the analytical and numerical solution corroborates again that CPT is exact for $U = 0$.

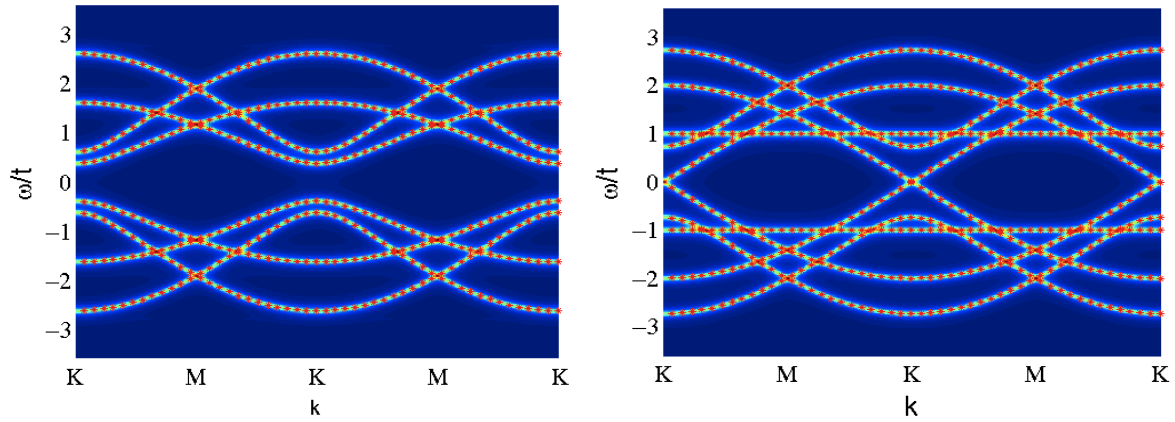

(a) AC-W4 GNR

(b) AC-W5 GNR

Figure 3.27: Energy-momentum dispersion relation $\omega(\boldsymbol{k})$ of an AC-W4 and an AC-W5 GNR in the non-interacting $U = 0$ case (corresponding to Fig. 3.24a and Fig. 3.25a). The analytical solutions obtained by Eq.(3.129) are plotted in addtion (red markers) and show perfect agreement to the non-interacting numerical solutions.

3.4.3 (Local) electronic density of states

The energy-momentum dispersion relations $\omega(\boldsymbol{k})$ obtained in the last subsection delivered information wether the armchair GNRs behave like a (semi -) metal, as predicted for AC-W5 GNRs, or like a semiconductor, as predicted for AC-W4 GNRs [9]. Since the dispersion relation of a whole GNR provides no information about the cluster sites accountable for a possible (semi-) metallic behaviour, the DOS $\rho(\omega)$ and LDOS $\rho_i(\omega)$ of the AC-W4 GNR and AC-W5 GNR (calculated according to Eq.(3.76) and Eq.(3.78), respectively) are investigated for different on-site interaction values $U/t = \{0.0, 0.5, 1.0, 1.5, 2.0, 2.5, 3.0, 3.3, 4.0, 5.0\}$ in this subsection. As it was the case also in the previous sections, the LDOS of the outermost cluster site 1 and the first inner site 2 (see Fig. 3.22) are presented in the two top figures of each subplot. In addition, the changes in the DOS and LDOS, caused by an applied on-site interaction U, provide a better understanding of the effect of the latter on the equilibrium properties of armchair GNRs.

Fig. 3.28 and Fig. 3.29 illustrate the DOS and LDOS of the AC-W4 GNR, while Fig. 3.30 and Fig. 3.31 show the DOS and LDOS of the AC-W5 GNR. Care has to be taken when analyzing the plots of $\rho(\omega)$, $\rho_1(\omega)$ and $\rho_2(\omega)$ in the particular cases, since there are different scalings applied in order to provide a suitable resolution of the curves.

Since the two investigated armchair GNR structures physically behave in a different way, where the AC-W4 GNR features semiconducting characteristics, due to its width $W = 4 \neq 3M - 1, \quad M \in \mathbb{N}$, in contrast to the semi-metalic AC-W5 GNR with a width $W = 5 = 3 \cdot 2 - 1$, a separate analyzation of the (L)DOS will be presented.

Starting out with the narrower AC-W4 GNR structure, Fig. 3.28a clearly shows an appearing bandgap Δ_{AC} in the non-interacting $U = 0$ case. Both, the outermost site 1 and the first inner site 2, contribute states to the overall DOS $\rho(\omega)$ in a similar way. The paradoxical closure of the energy gap for increasing on-site interactions can be clearly discovered in Fig. 3.28a - Fig. 3.28f. The gap has completely vanished in the latter, where an on-site interaction $U = 2.5t$ has been applied. Fig. 3.28f also reveals that the (semi -) metallic states are again located at the outermost site 1, as it was the case for the localized edge states in the zig-zag GNRs.

In contrast to this, investigating Fig. 3.30a - Fig. 3.30c yields that the (semi-) metallic states observed in the energy-momentum dispersion relation of the AC-W5 GNR in Fig. 3.25a - Fig. 3.25c, seem to be located at the outermost site 1 *and* the first inner site 2 in an equal number (notice the different scalings in the particular top plots here). Only the lowest states above and the highest states below the energy gap Δ_{AC} seem to be concentrated at the outermost site 1.
The appearance of an energy gap Δ_{AC} with increasing on-site interaction strength can be discovered here again, by taking a detailed look on Fig. 3.30d - Fig. 3.31d. The states for these values of the on-site interaction U are again contributed by site 1 and 2 in an equal amount.

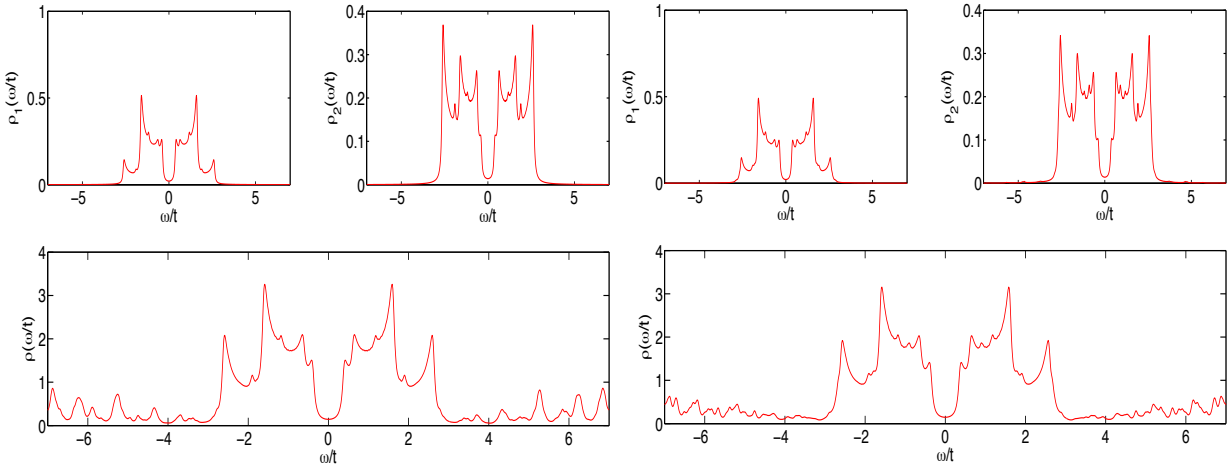

(a) U/t = 0.0

(b) U/t = 0.5

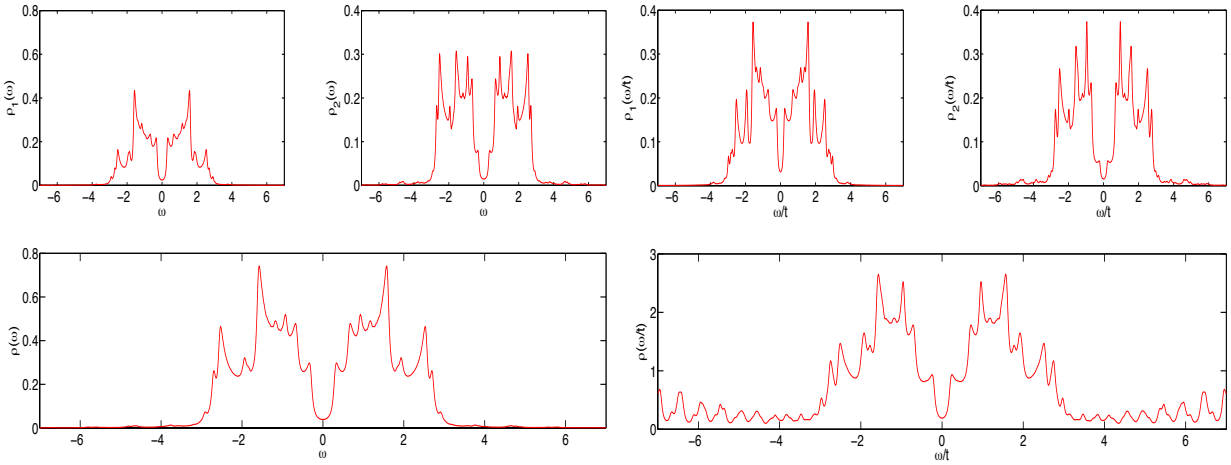

(c) U/t = 1.0

(d) U/t = 1.5

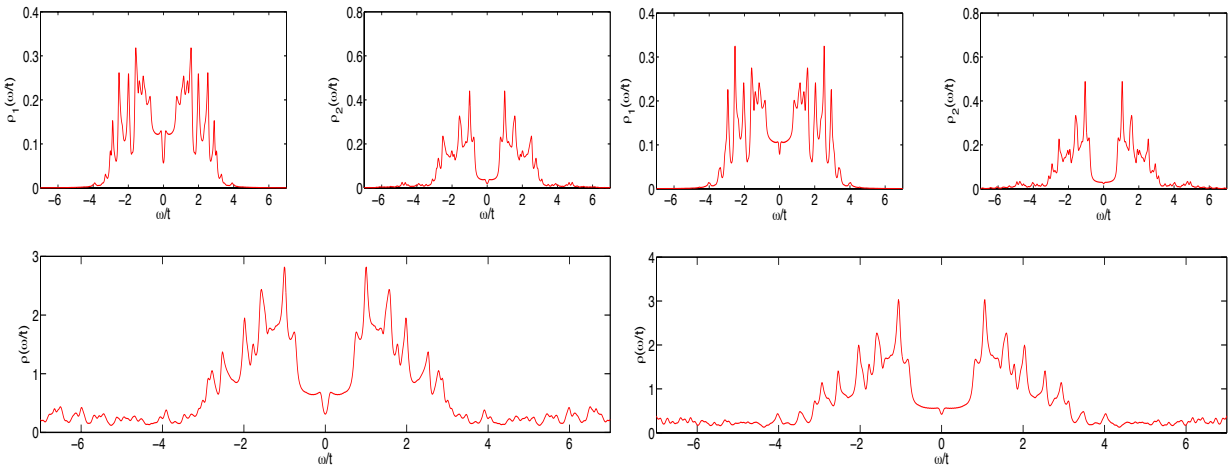

(e) U/t = 2.0

(f) U/t = 2.5

Figure 3.28: DOS $\rho(\omega)$ in the lattice of an AC-W4 GNR for different on-site interactions $U/t = \{0.0, 0.5, 1.0, 1.5, 2.0, 2.5\}$, where the interaction strength (value of U) is labeled below each subplot. Additionally the LDOS at the outermost site 1 (top left), which corresponds to the edge site, and at the first inner site 2 (top right) is presented in the two top figures of each subplot.

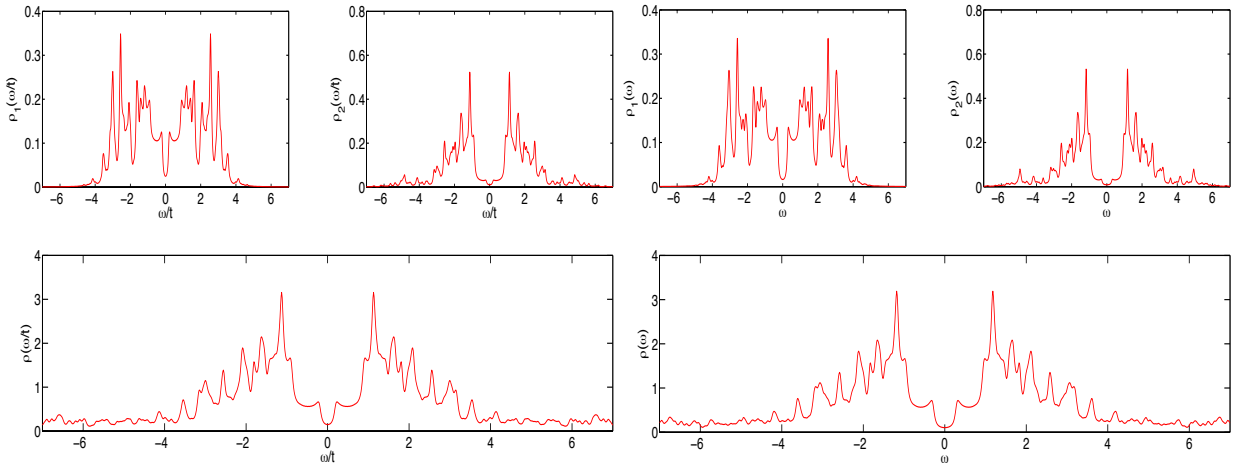

(a) U/t = 3.0

(b) U/t = 3.3

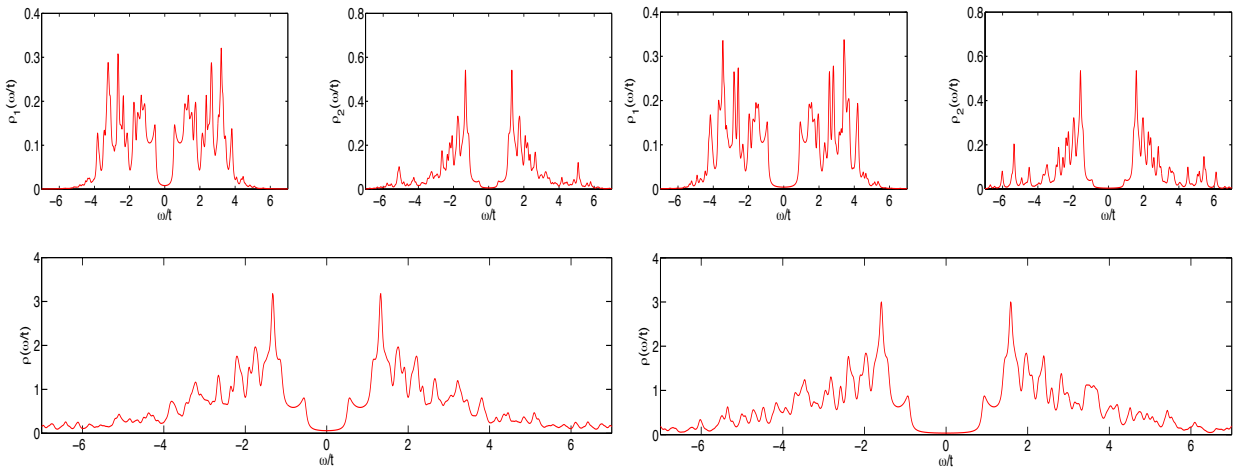

(c) U/t = 4.0

(d) U/t = 5.0

Figure 3.29: Same as Fig. 3.28, but for $U/t = \{3.0, 3.3, 4.0, 5.0\}$. The on-site interaction $U = 9.3eV \approx 3.3t$, which was found for graphene using cRPA [50], was used in subplot (b).

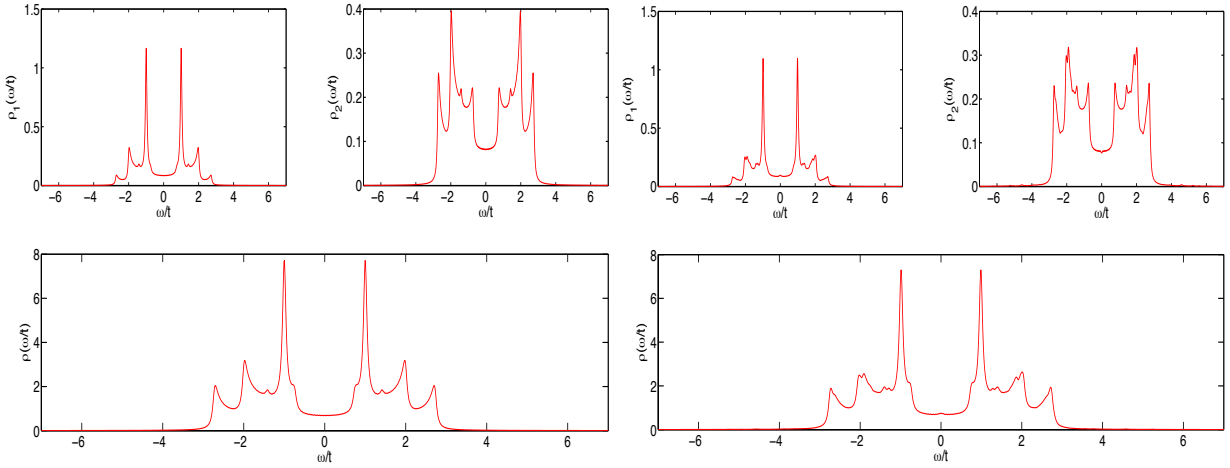

(a) U/t = 0.0

(b) U/t = 0.5

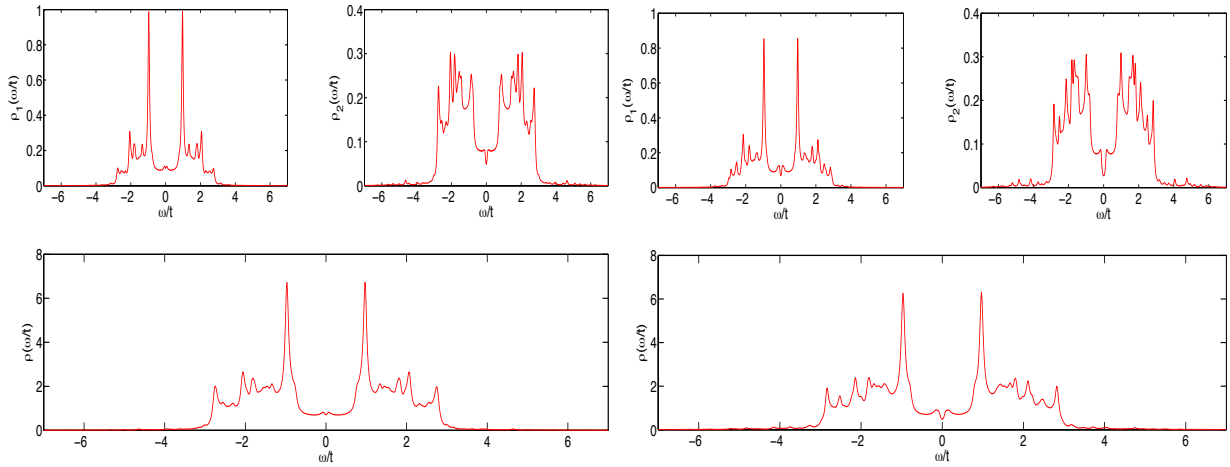

(c) U/t = 1.0

(d) U/t = 1.5

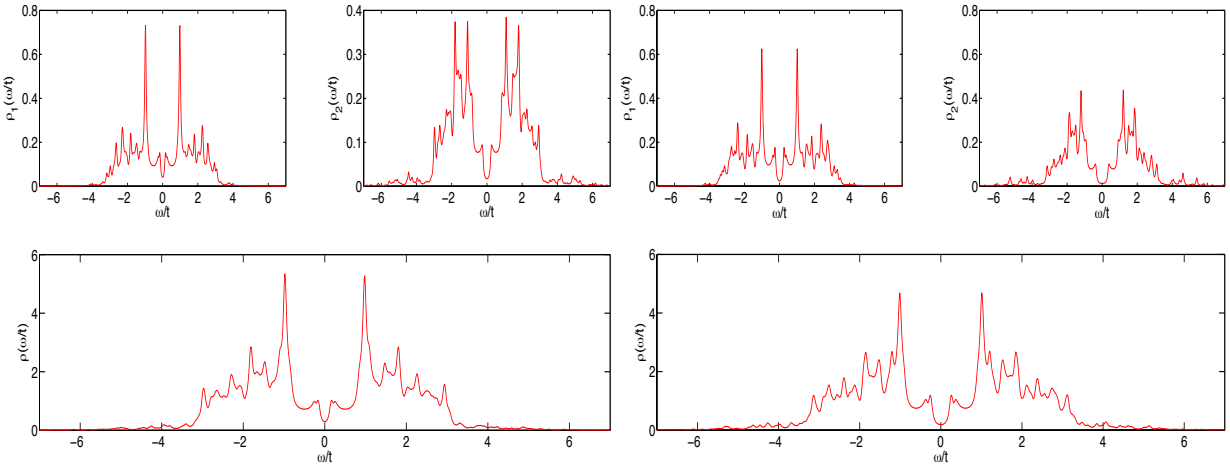

(e) U/t = 2.0

(f) U/t = 2.5

Figure 3.30: Same as Fig. 3.28, but for an AC-W5 GNR.

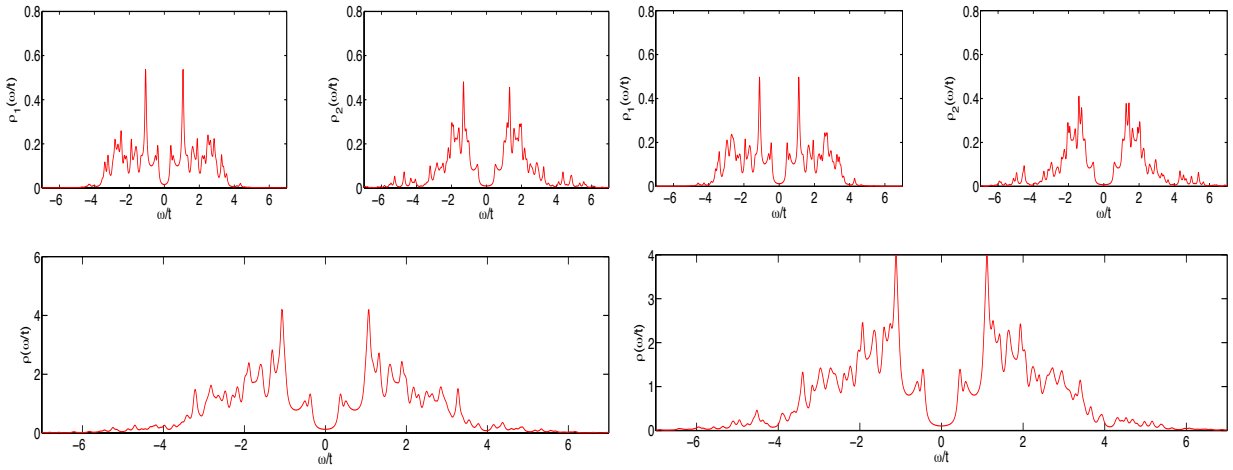

(a) U/t = 3.0

(b) U/t = 3.3

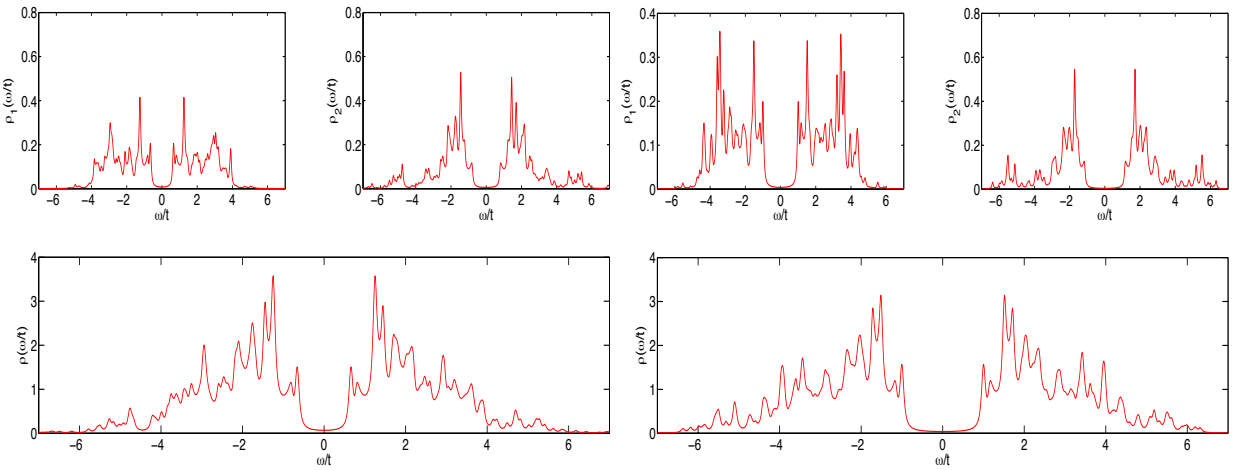

(c) U/t = 4.0

(d) U/t = 5.0

Figure 3.31: Same as Fig. 3.29, but for an AC-W5 GNR.

3.5 Zig-zag and armchair graphene nanoribbons with a width of thirty carbon atoms

After the detailed investigations of narrow zig-zag and armchair GNR structures in the previous sections the focus is turned on wider GNRs (i.e. with more C atoms along the width) now. Physical equilibrium properties similar to those found for the infinitely extended graphene lattice in Sec. 3.2 are expected.
A zig-zag GNR and an armchair GNR with 30 C atoms along the width, respectively, denoted as ZZ-W30 GNR and AC-W30 GNR in the following, are investigated concerning their equilibrium properties. A presentation of the results for the spectral function $A(\omega, \boldsymbol{k})$, the energy gap Δ(U) and the (L)DOS $\rho(\omega)$, as well as an interpretation of the results in terms of an explanation of the discovered behaviours, is provided in the next subsections.

3.5.1 Lattice geometry

The geometry of the two investigated GNRs is shown in Fig. 3.32a (ZZ-W30) and Fig. 3.32c (AC-W30), where the two sublattices of graphene are marked by the red and blue dots again.
For both structures, the introduced superlattices Λ, with the superlattice vectors $\boldsymbol{R}$, as well as the corresponding reciprocal superlattices, with the reciprocal superlattice vectors $\boldsymbol{K}$ are exactly the same, as for the narrow structures treated in the previous sections. The superlattice vectors $\boldsymbol{R}$ are given in Eq.(3.104) (ZZ-W30) and Eq.(3.119) (AC-W30), the introduced reciprocal superlattices are shown in Fig. 3.10 (ZZ-W30) and Fig. 3.23 (AC-W30) and the reciprocal superlattice vectors $\boldsymbol{K}$ are defined in Eq.(3.106) (ZZ-W30) and Eq.(3.122) (AC-W30).

Now, the physical unit cells, which spread out over the whole width of the ribbons as in the case of the narrow ribbons, contain 60 atoms. Such a size cannot be treated exactly in the interacting case, since a limit of approximately 20-site clusters appear for these kind of many-body calculations using state-of-the art numerics (see also: Introduction of Chapter 3). One therefore has to split the unit cell into smaller clusters, which can be solved exactly, and combine them via CPT. In consequence of this splitting, the superlattice vector $\boldsymbol{R}$ required for the calculation of the first BZ^{Λ} of the reciprocal superlattice *is not equal* to the superlattice vectors $\boldsymbol{R_1}$ and $\boldsymbol{R_2}$, which are needed to build up the physical unit cell with the chosen clusters. For the ZZ-W30 GNR structure these vectors are given by

$$\boldsymbol{R}_1^{ZZ} = \begin{pmatrix} a \\ 0 \end{pmatrix} \qquad \boldsymbol{R}_2^{ZZ} = \frac{a}{\sqrt{3}} \begin{pmatrix} 0 \\ 3 \end{pmatrix}. \tag{3.131}$$

while for the AC-W30 GNR geometry they are defined as

$$\boldsymbol{R}_1^{AC} = \frac{a}{\sqrt{3}} \begin{pmatrix} \frac{3}{2} \\ \frac{3\sqrt{3}}{2} \end{pmatrix} \qquad \boldsymbol{R}_2^{AC} = \frac{a}{\sqrt{3}} \begin{pmatrix} \frac{3}{2} \\ \frac{-3\sqrt{3}}{2} \end{pmatrix}. \tag{3.132}$$

which are identical to the superlattice vectors of the pristine graphene lattice.

The lattice geometries of the two investigated GNRs with the applied cluster tiling and the resulting superlattice vectors are shown in Fig. 3.32. The cluster tiling is represented by the green lines in Fig. 3.32a (ZZ-W30) and Fig. 3.32c (AC-W30). The superlattice vectors $\boldsymbol{R_1}$ and $\boldsymbol{R_2}$ needed to build up the physical unit cell are sketched as brown arrows. A detailed view of the used clusters, with all the possible inter-cluster hoppings indicated by black double-headed arrows, is presented in Fig. 3.32b (ZZ-W30) and Fig. 3.32d (AC-W30). The consecutive numbering of the sites in the different clusters should be noted, which appears due to the splitting of the unit cell into smaller clusters.

The locations of the atoms within the first 4-site cluster of the ZZ-W30 GNR (i.e. at the bottom of Fig. 3.32a) are given by

$$\boldsymbol{c}_1 = \tfrac{a}{\sqrt{3}} \begin{pmatrix} \frac{\sqrt{3}}{2} \\ 0 \end{pmatrix}; \quad \boldsymbol{c}_2 = \tfrac{a}{\sqrt{3}} \begin{pmatrix} 0 \\ 1 \end{pmatrix}; \quad \boldsymbol{c}_3 = \tfrac{a}{\sqrt{3}} \begin{pmatrix} 0 \\ 3 \end{pmatrix}; \quad \boldsymbol{c}_4 = \tfrac{a}{\sqrt{3}} \begin{pmatrix} \frac{\sqrt{3}}{2} \\ 4 \end{pmatrix} \tag{3.133}$$

while the positions of the atoms in the first 6-site cluster of the AC-W30 GNR (i.e. at the bottom of Fig. 3.32c) are the same as for the 6-site cluster used for the investigation of the infinitely extended graphene lattice (see Eq.(3.93)).

As in the previous sections the intra-cluster hoppings need to be defined for the calculation of the cluster Green's function $\boldsymbol{G}_0^R(\omega)$ (according to the site labeling in Fig. 3.32b). For the ZZ-W30 GNR they are given by

$$t_{ij} = t \quad \forall\, i,j \mid |i-j| = 1 \tag{3.134}$$

while the intra-cluster hoppings for the AC-W30 GNR structure are again equal to those of the cluster used for the description of the pristine graphene lattice (see Eq.(3.96)).

To enable a calculation of the retarded total lattice single-particle Green's function $\boldsymbol{G}^R(\omega)$ for the particular zig-zag and armchair GNR structures investigated in this section using Eq.(3.37), the Green's function for the whole physical unit cell $\boldsymbol{G}^R_{u.c.}(\omega)$ has to be constructed. In order to do so, a bulk diagonal $2W \times 2W = 60 \times 60$ matrix is constructed, by putting the cluster Green's function $\boldsymbol{G}_0^R(\omega)$ fifteen times (ZZ-W30) or ten times (AC-W30), respectively, along the diagonal:

$$\boldsymbol{G}^R_{u.c.}(\omega) = \begin{pmatrix} \boldsymbol{G}_0^R(\omega) & & & \\ & \boldsymbol{G}_0^R(\omega) & & \\ & & \boldsymbol{G}_0^R(\omega) & \\ & & & \ddots \end{pmatrix}. \tag{3.135}$$

The dimension $2W \times 2W$ of the constructed matrices originates from the size of the corresponding unit cells. A simple explanation for the matrix dimensions can be provided for the ZZ-W30 (AC-W30) GNR lattice:
Since there are fifteen 4-site clusters (ten 6-site clusters) needed to build up the whole width of the ribbon and every 4-site cluster (6-site cluster) has a dimension of 4×4 (6×6), the resulting dimension is $15 \cdot 4 \times 15 \cdot 4 = 60 \times 60$ ($10 \cdot 6 \times 10 \cdot 6 = 60 \times 60$). The electron spin, which would double the dimensions of all matrices described here, was neglected in this simplified explanation.

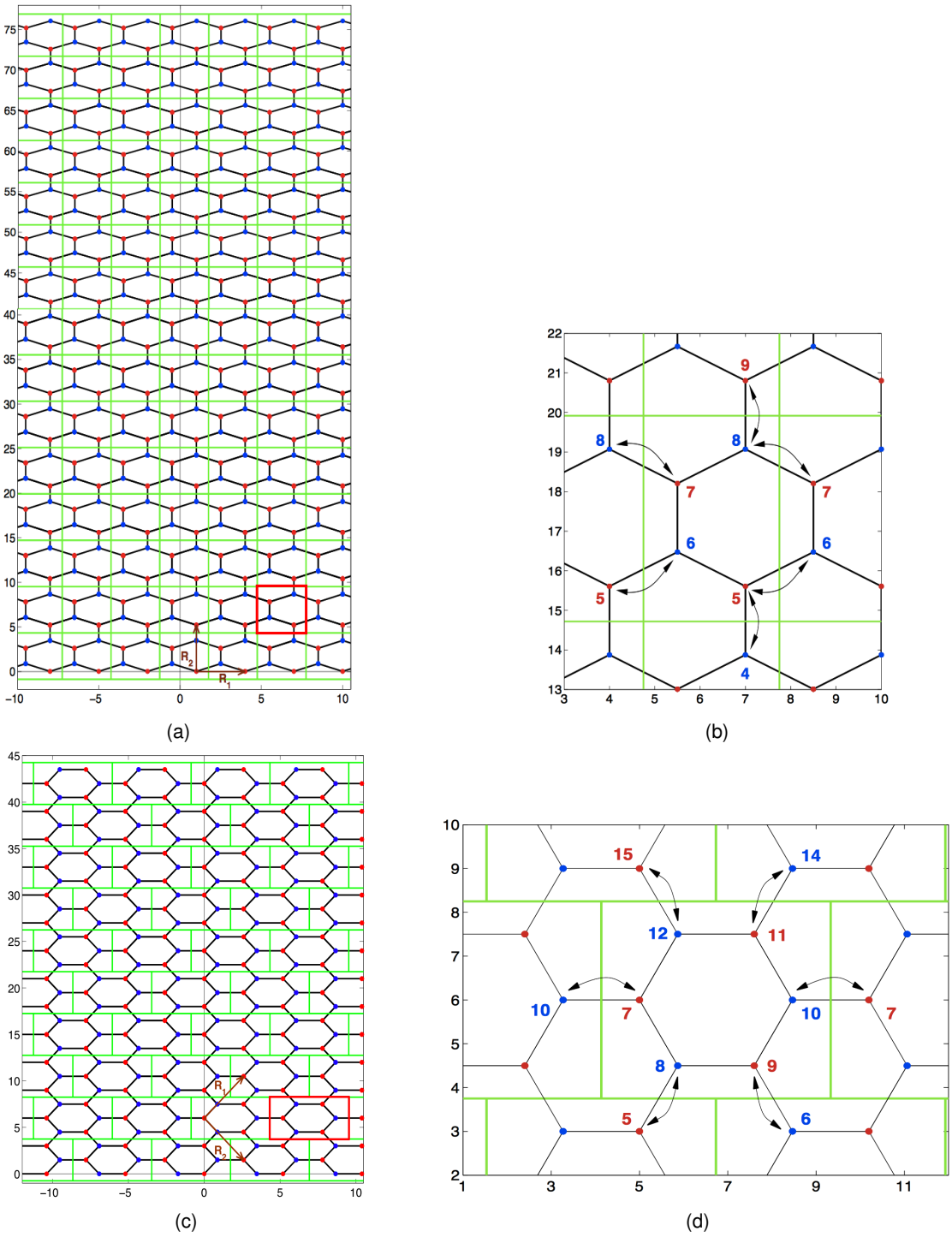

Figure 3.32: Real-space lattice λ and the applied cluster tiling for a ZZ-W30 GNR (a) and an AC-W30 GNR (c). The red and blue dots mark the C atoms corresponding to the two different sublattices of the infinite graphene lattice. The superlattice vectors $\boldsymbol{R_1}$ and $\boldsymbol{R_2}$ needed to build up the physical unit cell are represented by the brown arrows. The physical unit cells can be constructed by concetenate all clusters along the width of the ribbons. (b): Detailed view of the corresponding cluster chosen for the ZZ-W30 GNR geometry (highlighted with a red frame in (a)). (d): Detailed view of the corresponding cluster chosen for the AC-W30 GNR geometry (highlighted with a red frame in (c)). The numbers label the $2W$ cluster sites, while the double-headed arrows indicate the possible inter-cluster hoppings.

The required hopping matrices $T(\boldsymbol{k})$ need to be determined again. A difference to the investigation of the narrow GNRs arises in this context, since the clusters do not coincide with the physical unit cells, as stated above. In consequence to that, the clusters have to be connected not only along the longitudinal direction, but also along the transversal to build up the whole ribbon.

In the case of the ZZ-W30 geometry, a block-diagonal 60×60 matrix has to be constructed, with the 4×4 hopping matrices, which would be used if the clusters are only connected along the longitudinal axis, along the diagonal. The additional inter-cluster hopping terms for the transversal connections are added by hand afterwards, similar to a splitting of a Hamiltonian described in Eq.(3.34).
As explained above, for the ZZ-W30 GNR the hopping matrix of the 4-site cluster has to be put fifteen times along the diagonal to build up the overall hopping matrix. In the detailed view of the particular zig-zag cluster in Fig. 3.32b the inter-cluster hoppings, which determine the matrix elements of the 4×4 hopping matrix $T_{ZZ}^{4s}(\boldsymbol{k})$ according to Eq.(3.50), are plotted as black double-headed arrows. This leads to the following overall hopping matrix

$$T_{ZZ}^{W30}(\boldsymbol{k}) = t \begin{pmatrix} 0 & e^{i\boldsymbol{k}\boldsymbol{R_1}^{\Lambda}} & 0 & 0 & 0 & 0 & 0 & 0 & \dots \\ e^{-i\boldsymbol{k}\boldsymbol{R_1}^{\Lambda}} & 0 & 0 & 0 & 0 & 0 & 0 & 0 & \dots \\ 0 & 0 & 0 & e^{-i\boldsymbol{k}\boldsymbol{R_1}^{\Lambda}} & 0 & 0 & 0 & 0 & \dots \\ 0 & 0 & e^{i\boldsymbol{k}\boldsymbol{R_1}^{\Lambda}} & 0 & e^{i\boldsymbol{k}\boldsymbol{R_2}^{\Lambda}} & 0 & 0 & 0 & \dots \\ 0 & 0 & 0 & e^{-i\boldsymbol{k}\boldsymbol{R_2}^{\Lambda}} & 0 & e^{i\boldsymbol{k}\boldsymbol{R_1}^{\Lambda}} & 0 & 0 & \dots \\ 0 & 0 & 0 & 0 & e^{-i\boldsymbol{k}\boldsymbol{R_1}^{\Lambda}} & 0 & 0 & \dots & \\ 0 & 0 & 0 & 0 & 0 & 0 & 0 & e^{-i\boldsymbol{k}\boldsymbol{R_1}^{\Lambda}} & \dots \\ 0 & 0 & 0 & 0 & 0 & 0 & e^{i\boldsymbol{k}\boldsymbol{R_1}^{\Lambda}} & 0 & \dots \\ \vdots & \vdots & \vdots & \vdots & \vdots & \vdots & \vdots & \vdots & \ddots \end{pmatrix} \tag{3.136}$$

where the longitudinal inter-cluster hoppings of the 4-site clusters are highlighted in red, while the transversal inter-cluster hopping terms are indicated in blue. For a comprehensible understanding of the constructed matrix, the consecutive numbering of the cluster sites due to the splitting of the whole unit cell into smaller clusters has to be remembered (see Fig. 3.32b).

Setting up the hopping matrix $T_{AC}^{W30}(\boldsymbol{k})$ for the AC-W30 GNR is more complicated, since the clusters are not aligned above each other, but are also shifted in the longitudinal direction (see Fig. 3.32c). Therefore, the inter-cluster hoppings between the 6-site clusters, obtainable from the detailed view of the particular armchair cluster in Fig. 3.32d, have to be arranged properly in a 60×60 matrix. The resulting overall hopping matrix is given by

$$T_{AC}^{W30}(\boldsymbol{k}) = t \cdot$$

$$\begin{pmatrix}
0 & 0 & 0 & e^{-i\boldsymbol{k}(\boldsymbol{R}_1+\boldsymbol{R}_2)} & 0 & 0 & 0 & 0 & 0 & 0 & \dots \\
0 & 0 & 0 & 0 & 0 & 0 & 0 & 0 & 0 & 0 & \dots \\
0 & 0 & 0 & 0 & 0 & 0 & 0 & 0 & 0 & 0 & \dots \\
e^{-i\boldsymbol{k}(\boldsymbol{R}_1+\boldsymbol{R}_2)} & 0 & 0 & 0 & 0 & 0 & 0 & 0 & 0 & 0 & \dots \\
0 & 0 & 0 & 0 & 0 & 0 & 0 & e^{i\boldsymbol{k}\boldsymbol{R}_1} & 0 & 0 & \dots \\
0 & 0 & 0 & 0 & 0 & 0 & 0 & 0 & e^{-i\boldsymbol{k}\boldsymbol{R}_2} & 0 & \dots \\
0 & 0 & 0 & 0 & 0 & 0 & 0 & 0 & 0 & e^{-i\boldsymbol{k}(\boldsymbol{R}_1+\boldsymbol{R}_2)} & \dots \\
0 & 0 & 0 & 0 & e^{-i\boldsymbol{k}\boldsymbol{R}_1} & 0 & 0 & 0 & 0 & 0 & \dots \\
0 & 0 & 0 & 0 & 0 & e^{i\boldsymbol{k}\boldsymbol{R}_2} & 0 & 0 & 0 & 0 & \dots \\
0 & 0 & 0 & 0 & 0 & 0 & e^{i\boldsymbol{k}(\boldsymbol{R}_1+\boldsymbol{R}_2)} & 0 & 0 & 0 & \dots \\
0 & 0 & 0 & 0 & 0 & 0 & 0 & 0 & 0 & 0 & \dots \\
0 & 0 & 0 & 0 & 0 & 0 & 0 & 0 & 0 & 0 & \dots \\
\vdots & \vdots & \vdots & \vdots & \vdots & \vdots & \vdots & \vdots & \vdots & \vdots & \ddots
\end{pmatrix} \tag{3.137}$$

where the longitudinal inter-cluster hoppings are highlighted in red again, while the transversal inter-cluster hopping terms are indicated in blue. Note that the superscript $^{(\Lambda)}$ of the superlattice vectors was omitted here to afford better readability. Again, the consecutive numbering of the cluster sites shown in Fig. 3.32d has to be remembered to gain a comprehensible understanding of the constructed matrix.

The results of the equilibrium properties introduced in Sec. 3.1.2, which were calculated for different values of the on-site interaction U for the large ZZ-W30 and AC-W30 GNR geometries, are presented in the following subsection.

3.5.2 Spectral function

The spectral function $A(\boldsymbol{k}, \omega)$ was calculated according to Eq.(3.68) for different values of the on-site interaction $U/t = \{0.0, 0.5, 1.0, 1.5, 2.0, 2.5, 3.0, 3.3, 4.0, 5.0\}$. The resulting energy-momentum dispersion relations $\omega(\boldsymbol{k})$ are plotted in Fig. 3.33 (ZZ-W30 GNR) and Fig. 3.34 (AC-W30 GNR).

Fig. 3.33a shows the energy-momentum dispersion relation $\omega(\boldsymbol{k})$ for the ZZ-W30 GNR in the non-interacting case $U = 0$. The conducting states at $\omega = 0$ are observed again, determining the expected metallic behaviour. Similar to the narrow zig-zag GNR structures investigated in Sec. 3.3 the metallic behaviour is changed to a semiconducting one for on-site interaction strengths larger than the critical value U_{crit}. The appearance of an increasing energy gap Δ_{ZZ} for increasing on-site interaction strengths is also observed again in Fig. 3.33i and Fig. 3.33j. In comparison to the narrow GNR structures (see Fig. 3.11 - Fig. 3.13) the obtained critical value for the on-site interactions is rather large,

$$U_{crit}^{ZZ\text{-}W30} \approx 3.4t \tag{3.138}$$

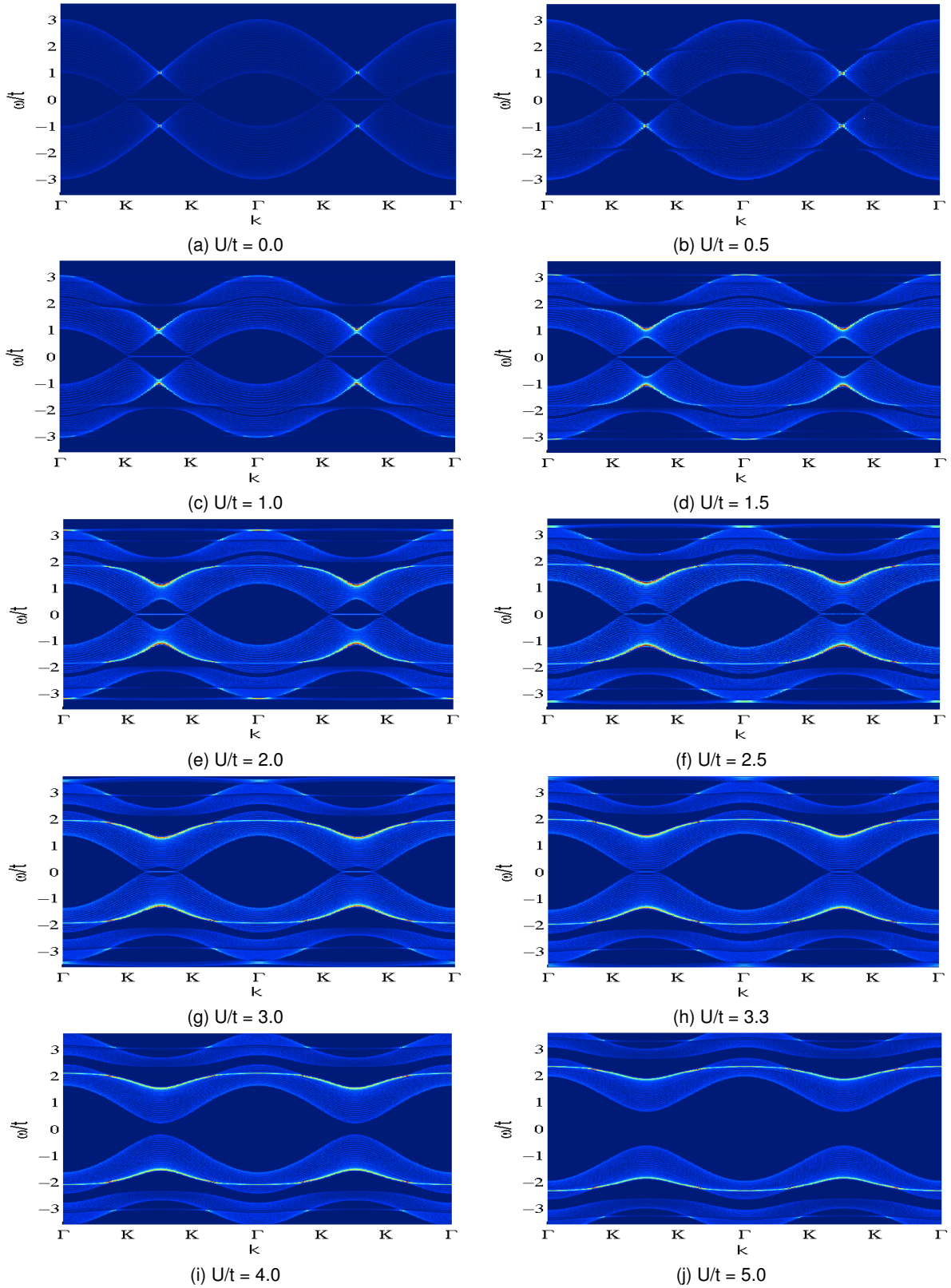

(a) U/t = 0.0 (b) U/t = 0.5

(c) U/t = 1.0 (d) U/t = 1.5

(e) U/t = 2.0 (f) U/t = 2.5

(g) U/t = 3.0 (h) U/t = 3.3

(i) U/t = 4.0 (j) U/t = 5.0

Figure 3.33: Energy-momentum dispersion relation $\omega(\boldsymbol{k})$ of a ZZ-W30 GNR for different on-site interactions $U/t = \{0.0, 0.5, 1.0, 1.5, 2.0, 2.5, 3.0, 3.3, 4.0, 5.0\}$, where the interaction strength (value of U) is labeled below each subplot. The energy ω is plotted in terms of the hopping integral t: $\omega = \omega/t$. The on-site interaction $U = 9.3eV \approx 3.3t$, which was found for graphene using cRPA [50], was used in subplot (h).

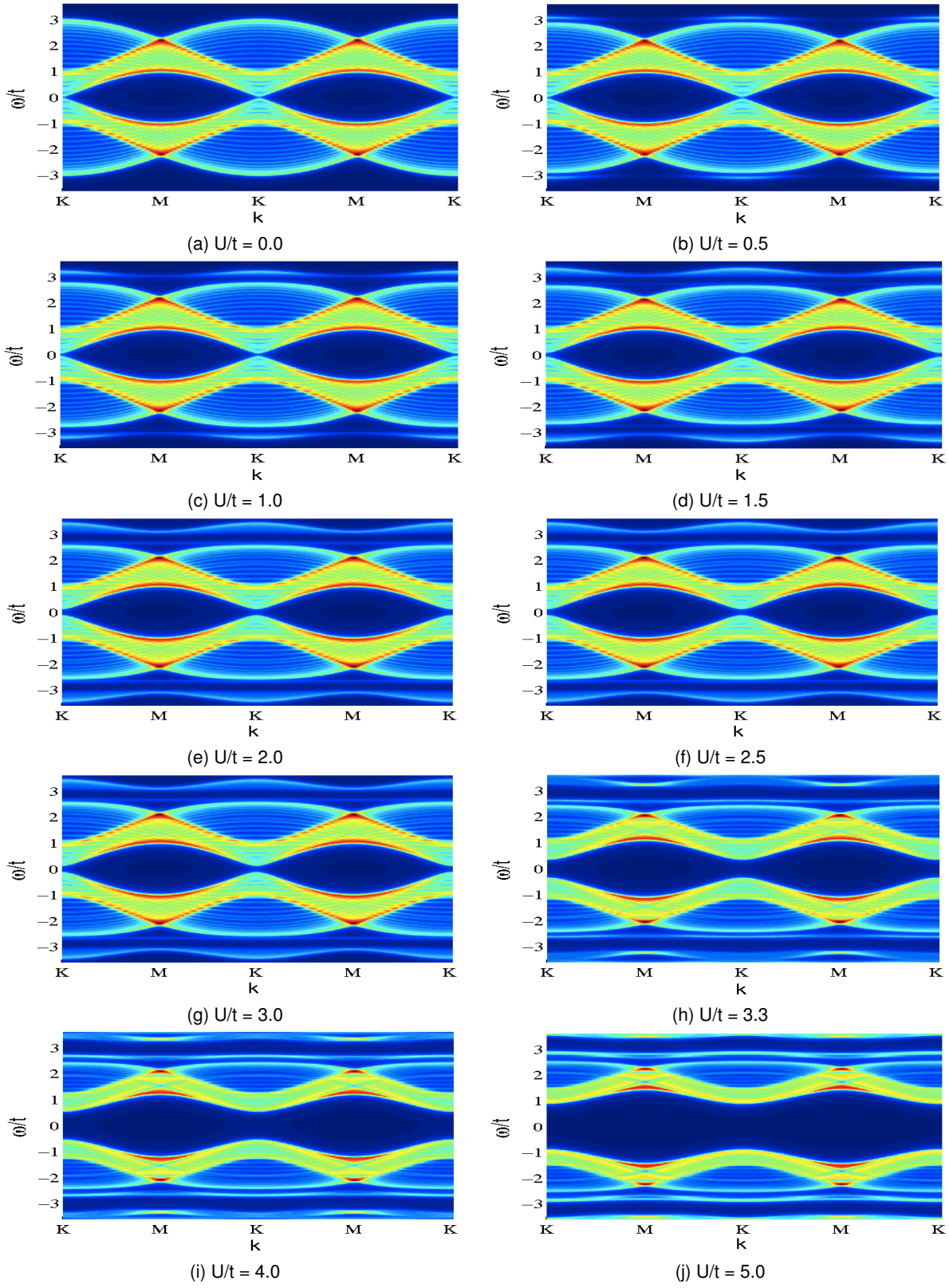

(a) U/t = 0.0 (b) U/t = 0.5

(c) U/t = 1.0 (d) U/t = 1.5

(e) U/t = 2.0 (f) U/t = 2.5

(g) U/t = 3.0 (h) U/t = 3.3

(i) U/t = 4.0 (j) U/t = 5.0

Figure 3.34: Same as Fig. 3.33, but for an AC-W30 GNR. The colormap has been changed in this plot to afford a better differentiation of the individual energy bands.

which is somehow paradoxical, since the large zig-zag GNR structure should be closer to the infinite limit of the pristine graphene lattice, where a much smaller critical value of $U_{crit}^{simple\ graphne} \approx 1.4t$ was obtained (see Eq.(3.99)). Since it is not believed that this behaviour is spuriously delivered by the applied CPT method, it seems like the mere existence of zig-zag edges is determining the equilibrium GNR properties in an impressive manner, *independent* of the ribbon width. Since the infinitely extended graphene lattice is treated as a periodic lattice *without* any edges, this would explain why there can be such a significant difference between the critical on-site interaction values U_{crit}.
A very interesting observation can be made in Fig. 3.33h. For the on-site interaction $U = 9.3eV \approx 3.3t$ (reported for pristine graphene [50]), the energy gap has not yet appeared, for the ZZ-W30 GNR geometry. Therefore, the metallic behaviour or at least a semi-metallic one is expected for these structure, which is a very interesting result, since it would charcterize the interacting model of the ZZ-W30 GNR as a metal. Therefore, the electrical conductivity within this wide ribbon should be much larger than the one of the narrow zig-zag GNRs.
Another important feature of this wide zig-zag GNR is the reestablishment of Dirac cone-like features at the reciprocal K-points of the first BZ, which can be discovered clearly in Fig. 3.33a - Fig. 3.33f.

Turning to the AC-W30 GNR lattice now, the almost perfect reestablishment of the Dirac cones is the first important feature observable in the plot of the non-interacting case $U = 0$ in Fig. 3.34a. Although there appears a very small gap at the K-points, the non-interaction AC-W30 GNR lattice can be said to exhibit almost a semi-metallic behaviour. These two properties discovered for the AC-W30 GNR are in perfect agreement with the equilibrium properties found for the non-interacting infinitely extended graphene lattice (see. Fig. 3.4a.). Moreover, when comparing the energy-dispersion relations $\omega(\boldsymbol{k})$ of the two non-interacting cases in Fig. 3.4a (pristine graphene) and Fig. 3.34a (AC-W30 GNR) respectively in detail, a perfect agreement between the energy bands of pristine graphene between the K- and M-point of the 1st BZ and the lowest (highest) energy band in the conduction (valence) band of the wide armchair structure can be obtained. In fact, this agreement proves the expected significance of the infinitely extended graphene lattice, as the asymptotic limit for GNRs structures with growing width dimensions.
The asymptotical convergence of the equilibrium properties of AC-W30 GNRs to the results found for pristine graphene, shown above for the non-interacting case, is also observed for non-zero on-site interactions $U \neq 0$. Fig. 3.34f - Fig. 3.34j show an enhancement of the energy gap Δ_{AC} similar to that found for pristine graphene in Fig. 3.4f - Fig. 3.4j. Furthermore, the progression of the $\Delta_{AC}(U)$ curve of AC-W30 GNRs plotted in Fig. 3.35 matches the one of $\Delta(U)$ for pristine graphene, which is also plotted, almost perfect. For the sake of completeness the energy gap $\Delta_{ZZ}(U)$ of the ZZ-W30 GNR is plotted in addition in Fig. 3.35. The large occurring critical on-site interaction value can be clearly discovered again.
For the on-site interaction $U = 9.3eV \approx 3.3t$, which was found for graphene by cRPA [50], the energy gap of the AC-W30 GNR geometry has already reached a value of

$$\Delta_{AC\text{-}W30}\big|_{U_{graphene}} \approx 0.65t \approx 1.82\ eV \tag{3.139}$$

which is close to the value found for pristine graphene in Eq.(3.100). This obviously distinguishes

AC-W30 GNRs as direct band gap semiconductors, as it was the case for the geometry of pristine graphene.

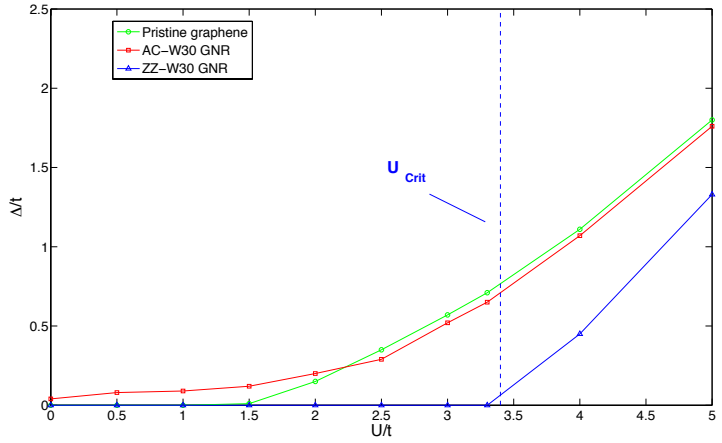

Figure 3.35: Energy gap $\Delta_{AC}(U)$ for an AC-W30 GNR as a function of the on-site interaction U, calculated according to Eq.(3.74). The energy gap $\Delta(U)$ of the infinitely extended graphene lattice is plotted in addition, to provide a comparison to the asymptotic limit $W \to \infty$. Additionally, the energy gap $\Delta_{ZZ}(U)$ of the ZZ-W30 GNR is shown, with the large occurring critical value U_{crit} indicated.

As explained in the previous two sections, analytical solutions for the dispersion relations in the non-interacting $U = 0$ case can be obtained by Fourier transformation. The calculations were performed according to Eq.(3.114) and Eq.(3.116) (ZZ-W30 GNR) and Eq.(3.129) and (AC-W30 GNR) and their results are plotted in Fig. 3.36 in order to prove the equivalence to the numerical solutions of the non-interacting cases in Fig. 3.33a and Fig. 3.34a.

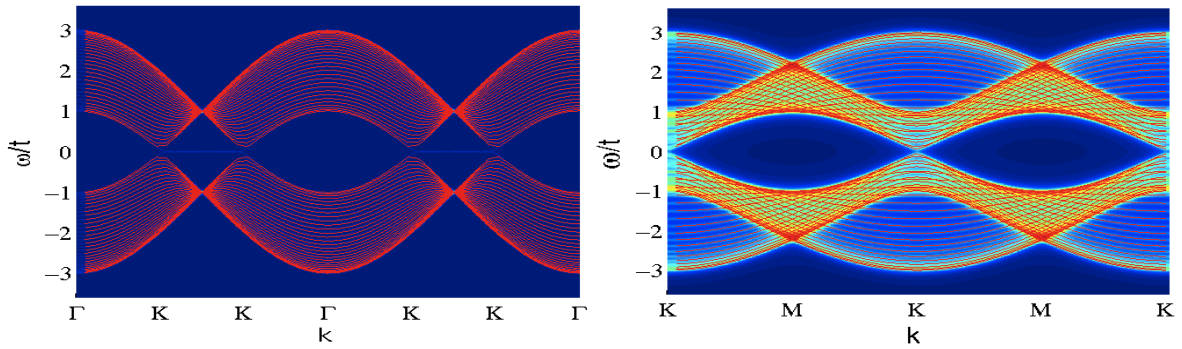

(a) ZZ-W30 GNR (b) AC-W30 GNR

Figure 3.36: Energy-momentum dispersion relation $\omega(\boldsymbol{k})$ of a ZZ-W30 (a) and an AC-W30 GNR (b) in the non-interacting $U = 0$ case (corresponding to Fig. 3.24a and Fig. 3.25a). The analytical solution for the ZZ-N30 GNR was obtained using Eq.(3.114) and Eq.(3.116) and is plotted in addition (red lines) in (a), while the analytical solution for the AC-N30 GNR was obtained using Eq.(3.129) and is plotted in addition (red lines) in (b). Both analytic solutions show perfect agreement to the non-interacting many-body problem.

3.5.3 (Local) electronic density of states

Last but not least the DOS $\rho(\omega)$ and LDOS $\rho_i(\omega)$ (calculated according to Eq.(3.76) and Eq.(3.78), respectively) of the ZZ-W30 GNR and AC-W30 GNR geometry are investigated in this subsection. Both quantities are plotted for different on-site interaction values $U/t = \{0.0, 0.5, 1.0, 1.5, 2.0, 2.5, 3.0, 3.3, 4.0, 5.0\}$ in Fig. 3.37 and Fig. 3.38 (ZZ-W30), and in Fig. 3.39 and Fig. 3.40 (AC-W30).
In the case of the ZZ-W30 GNR the (L)DOS results serve the task of proving wether the observed metallic states correspond to localized edge states, as it was predicted in in Ref. [11], and as it was the case for the narrow zig-zag GNR geometries in Sec. 3.3, or not.
For the AC-W30 GNR, the (L)DOS was calculated to check which states of the physical unit cell account for the physical behaviour that was found to be very similar to the one of infinitely extended graphene.

The presented results for the DOS plots of the ZZ-W30 GNR clearly show the predicted localized metallic edge states for all on-site interactions $U < U_{crit}$. In the top left plot of the LDOS $\rho_1(\omega)$ in all subplots of Fig. 3.37 a sharp peak precisely at $\omega = 0$ can be observed, determining that the metallic states are only located at the outermost sites of the ZZ-W30 GNR. The LDOS $\rho_2(\omega)$ of the first inner sites do not contribute to the metallic states, since they feature no states around $\omega = 0$. The decrease in the number of metallic states can be seen nicely by continuously analyzing Fig. 3.37a - 3.38b. Fig. 3.38c and Fig. 3.38d show the DOS for an interaction strength $U > U_{crit}$, where the disappearance of the metallic states at $\omega = 0$ and the enhancement of the energy gap Δ_{ZZ} can be observed.

Comparing the DOS plots of the AC-W30 GNR in Fig. 3.39 and Fig. 3.40 to those of the infinitely extended graphene lattice in Fig. 3.7 and Fig. 3.8, the equivalence in the shape of the plots of the overall DOS $\rho(\omega)$ can be observed at the first glance. It should be noted here that the broadening η was chosen slightly larger in case of the AC-W30 GNR. However, neither the LDOS $\rho_1(\omega)$ of the edge state 1, nor the LDOS $\rho_2(\omega)$ of the first inner site feature a progression, comparable with those of the infinitely extended graphene lattice in the top plots of each subplot in Fig. 3.7 and Fig. 3.8. It seems that it is rather the superposition of both LDOS curve progressions $\rho_1(\omega) + \rho_2(\omega)$ which delivers a curve in the shape of the LDOS functions found for the 2d graphene lattice. Therefore, it can be stated that due to the size confinement in the case of the AC-W30 GNR structure, the LDOS of neighbouring sites do not feature an equivalent behaviour, in contrast to the limiting case of the infinite graphene lattice, but the superposition of both LDOSs $\rho_1(\omega) + \rho_2(\omega)$ rather does.

A summary and a final interpretation of the gained results for all GNR geometries of this chapter is provided in the concluding Chapter 5.

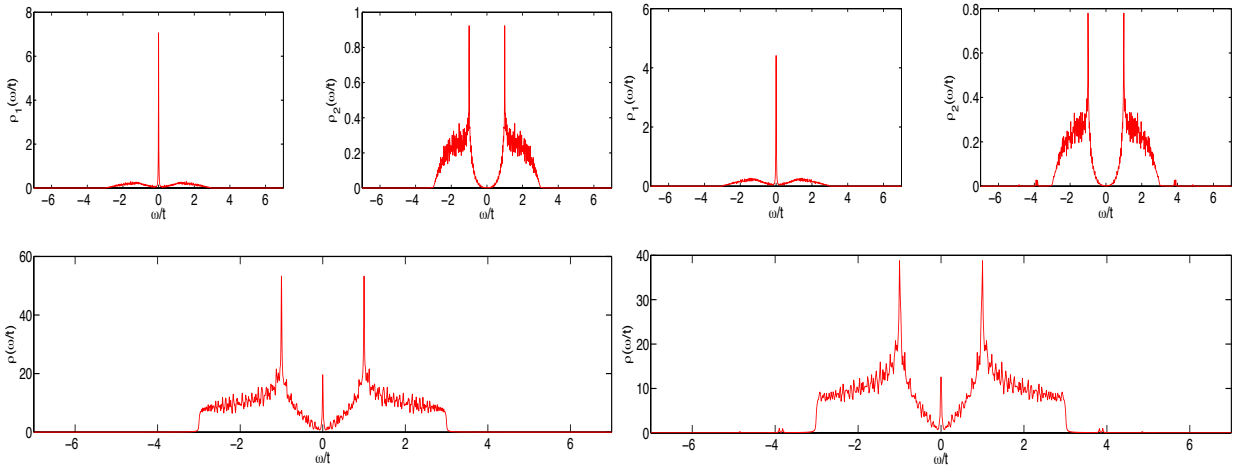

(a) U/t = 0.0

(b) U/t = 0.5

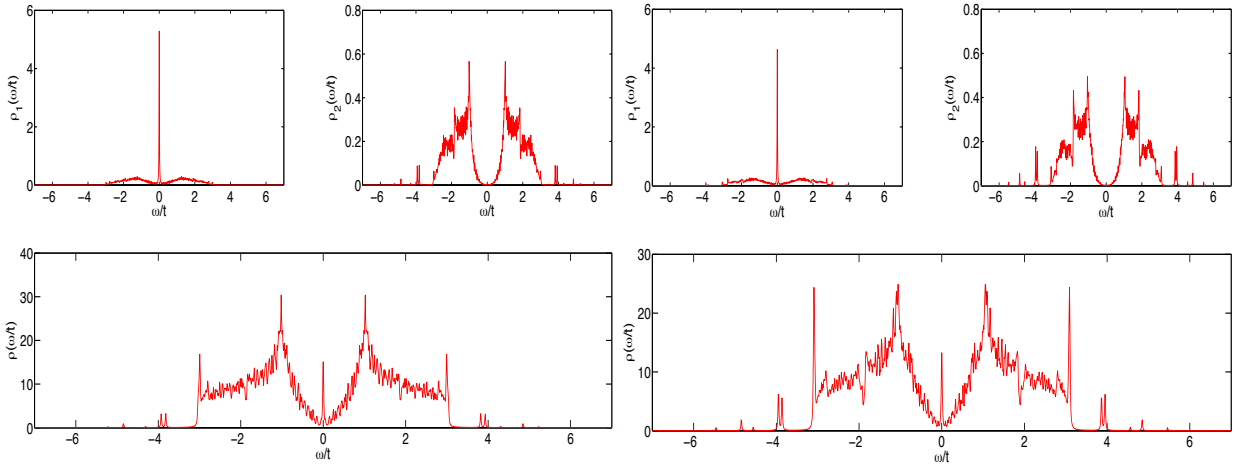

(c) U/t = 1.0

(d) U/t = 1.5

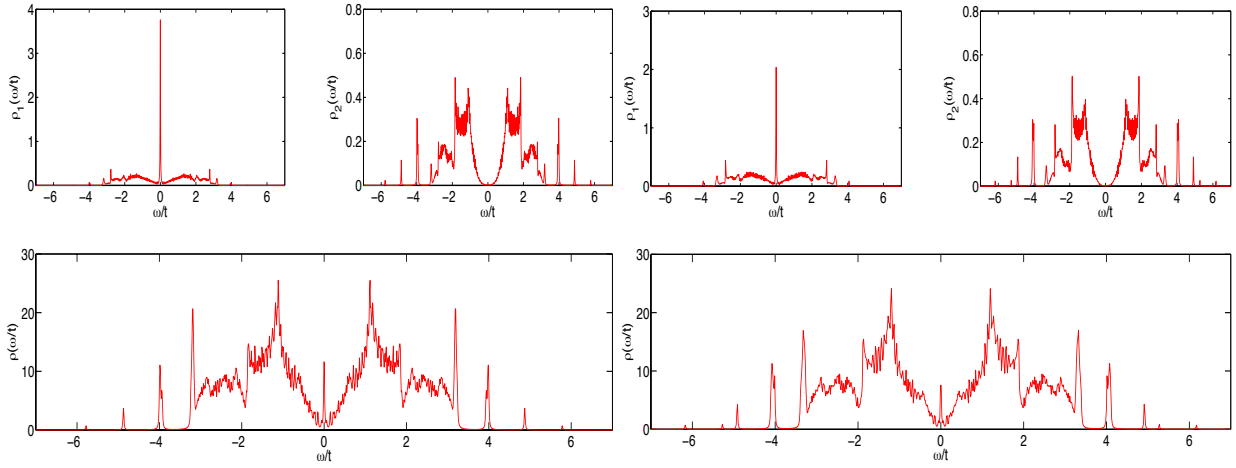

(e) U/t = 2.0

(f) U/t = 2.5

Figure 3.37: DOS $\rho(\omega)$ in the lattice of an ZZ-W30 GNR for different on-site interactions $U/t = \{0.0, 0.5, 1.0, 1.5, 2.0, 2.5\}$, where the interaction strength (value of U) is labeled below each subplot. Additionally the LDOS at the outermost site 1 (corresponds to the edge site) and at the first inner site 2 is presented in the two top figures of each subplot.

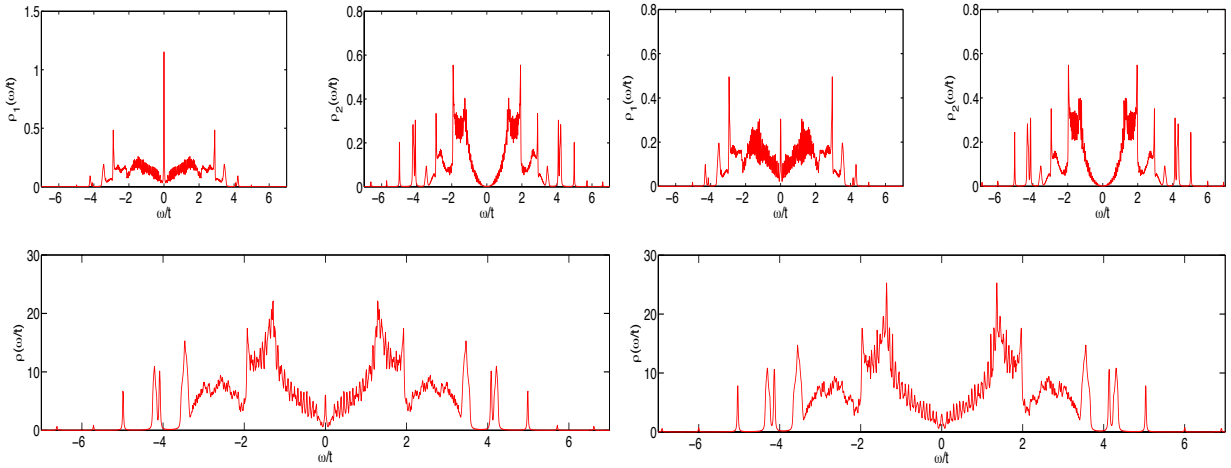

(a) U/t = 3.0 (b) U/t = 3.3

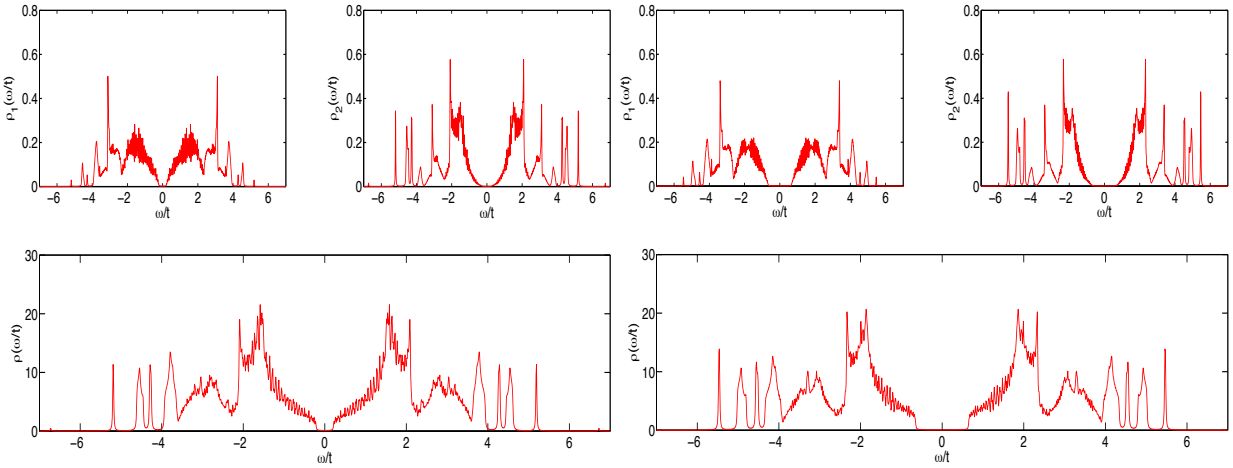

(c) U/t = 4.0 (d) U/t = 5.0

Figure 3.38: Same as Fig. 3.37, but for $U/t = \{3.0, 3.3, 4.0, 5.0\}$. The on-site interaction $U = 9.3eV \approx 3.3t$, which was found for graphene using cRPA [50], was used in subplot (b).

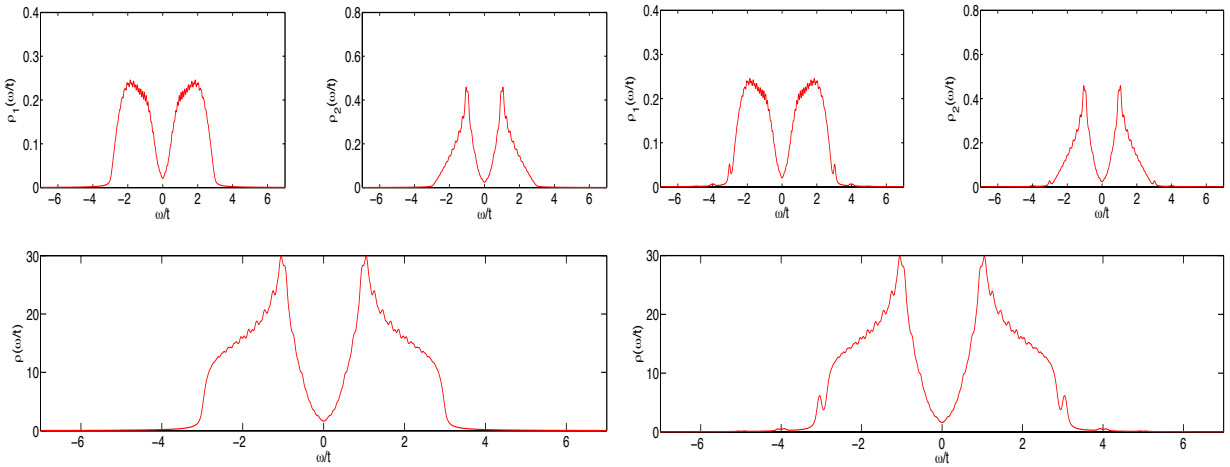

(a) U/t = 0.0

(b) U/t = 0.5

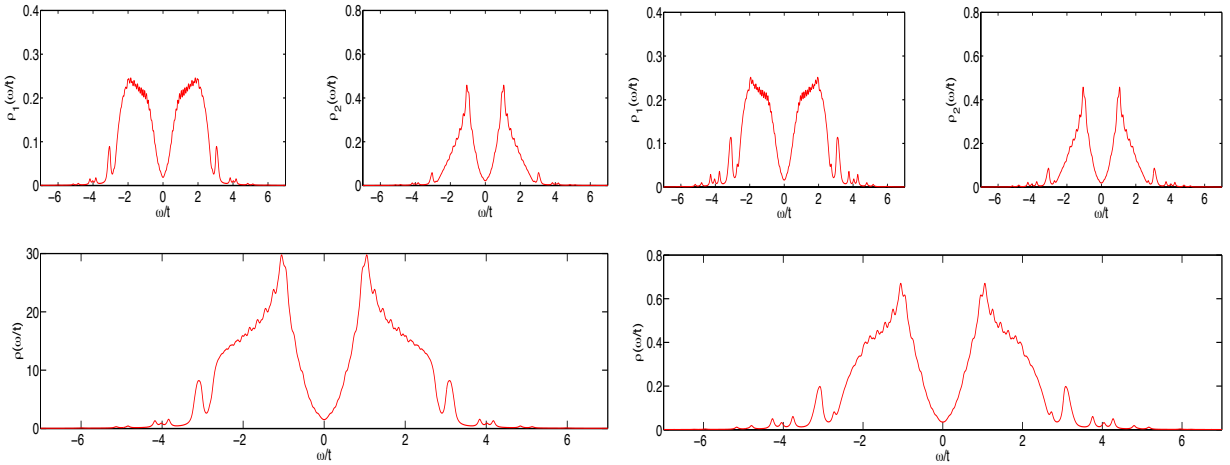

(c) U/t = 1.0

(d) U/t = 1.5

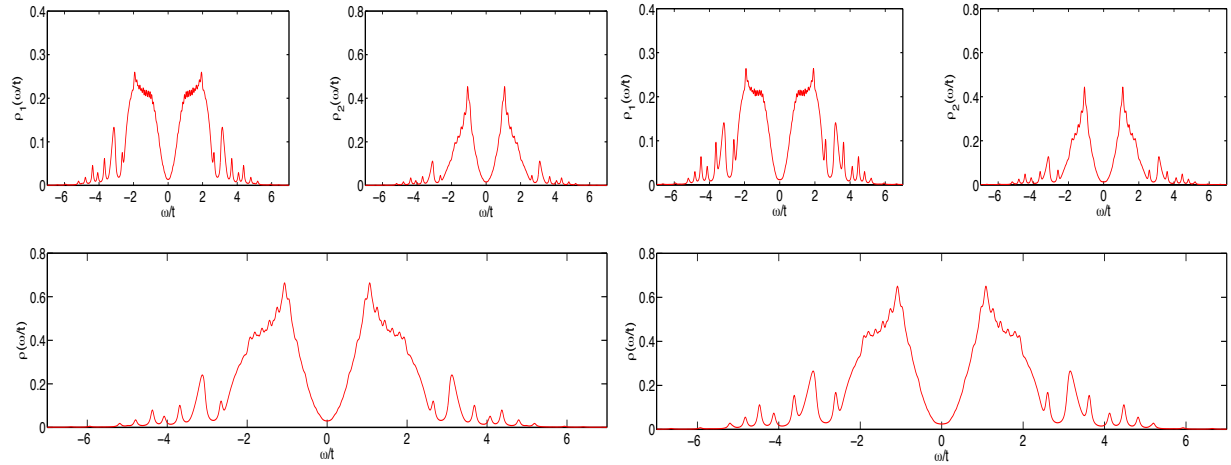

(e) U/t = 2.0

(f) U/t = 2.5

Figure 3.39: Same as Fig. 3.37, but for an AC-W30 GNR.

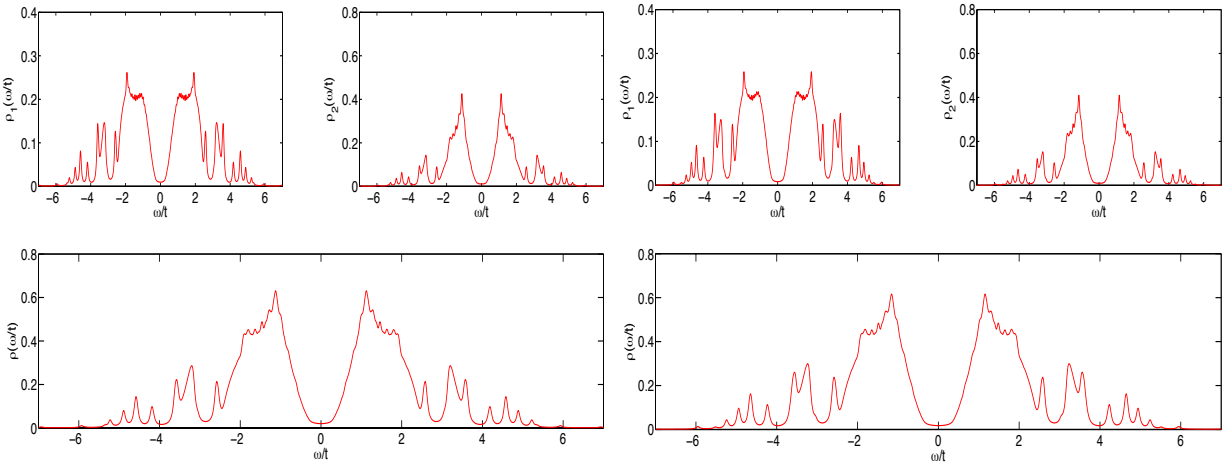

(a) U/t = 3.0

(b) U/t = 3.3

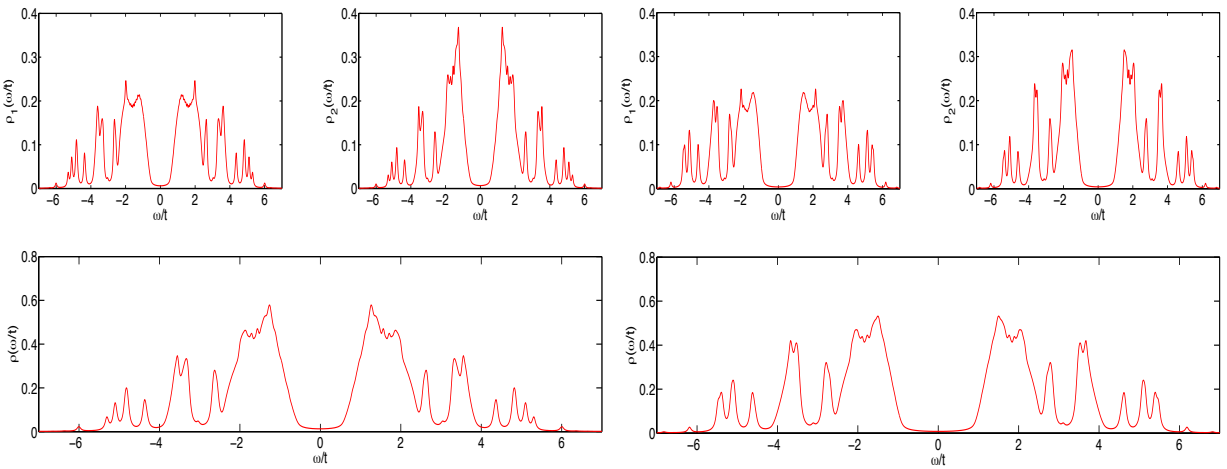

(c) U/t = 4.0

(d) U/t = 5.0

Figure 3.40: Same as Fig. 3.38, but for an AC-W30 GNR.

4 Electronic transport

After a detailed investigation of equilibrium properties of various GNR structures, the analyzation of electronic transport properties in GNR geometries is the final aim of the remaining chapter. Before the DC current characteristics of armchair and zig-zag GNRs are presented in Sec. 4.4, some preliminary cases have to be considered, to allow for a comprehensive and physically correct interpretation of the results gained for the GNR geometries.
Since the GNR geometries for the non-equilibrium calculations will be equivalent to those of the previous Chapter 3, i.e. GNRs with an infinite length, but finite widths, a special treatment of the energy dissipation within infinite structures is required. *Infinite* in this context means that *one* physical dimension is infinite. Therefore, an investigation of an infinite TB chain regarding its electronic transport properties is performed first. The results achieved for this rather simple geometry will represent an important support in the interpretation of the final results for armchair and zig-zag GNR geometries with 4 C atoms along the width.
Occurring Bloch Oscillations (BOs), preventing the flow of a constant DC current, are a challenging issue arising in infinite models without consideration of energy dissipation. However, this issue is of theoretical nature only, since BOs are hardly observable in real solids due to the presence of acoustic phonon and/or impurity scattering. For reasons of simplicity phonons and impurities are neglected in this work and therefore a dissipation mechanism has to be added to the physical system by hand. A detailed examination of BOs and an approach for solving the appearing dissipation problem by coupling artificial bath chains, are presented in Sec. 4.2, which is also where the applied model for the non-equilibrium investigations is explained. In this model a homogeneous DC electrical field is applied to the infinite structures to drive an electrical current to flow. It will be shown that the obtained results for the current density $j(E)$ as a function of the electrical field E exhibit an oscillatory behaviour. These oscillations occur due to *Wannier-Stark resonances* or *Wannier-Stark ladders of resonances*, which originate from the homogeneous electrical field that is applied in the particular model [55] [56] [57]. Therefore, the model for the electronic transport calculations is called *tight-binding Wannier-Stark model* in this work. A detailed discussion of the occurring Wannier-Stark oscillations and the associated theoretical background is provided in Sec. 4.3.
The numerical tools for the investigation of equilibrium properties presented in Sec. 3.1 need to be further developed to make a calculation of non-equilibrium properties possible. In other words, the Green's functions formalism used in the equilibrium case is expanded to the *Keldysh space*, where a calculation of electronic transport properties is feasible. This expansion and a brief derivation of the formulas of the non-equilibrium properties of interest are provided in the following Sec. 4.1.
While armchair GNRs feature a semiconducting behaviour for most considered values of the on-site interaction energy U in the equilibrium treatments in Sec. 3.4, zig-zag GNRs (considered in Sec. 3.3) mostly behave like metals (for small enough on-site interactions). To allow for the mentioned comprehensive and physically correct interpretation of the current characteristics gained for both GNR edge orientations, the infinite TB chain is investigated twice, where in the second case the natural metallic behaviour of a TB chain was tuned to a semiconducting one by an application of alternating on-site energies all along the chain. The DC electrical field driven current characteristics

$j(E)$ of the infinite TB chain coupled to semi-infinite bath chains in both, the metallic and the semiconducting cases, are presented in Sec. 4.3. Finally, the obtained electronic transport properties of GNRs are shown and discussed in Sec. 4.4.
The explicit numerical calculations of the electronic current densities performed in this work, with the approach of artificial fermion bath chains mimicking dissipation, deliver novel non-equilibrium results for the investigated infinite systems. For one-dimensional TB systems, the dynamics of BOs in consequence of an applied homogeneous electrical field have been studied in several reviews ([55] [56] [57], e.g.). The results obtained for the infinite TB chain in this work represent an extension to these previous research activities due to the considered dissipation mechanism. Within the scope of single-layer GNRs, occurring Wannier-Stark oscillations in the current densities have not been discussed before now, indicating the novelty of the results of this work. It has to be added here that BOs and Wannier-Stark states in the honeycomb lattice were studied recently [58]. Furthermore, the occurrence of Bloch-Zener oscillations at high bias for superlattices of GNRs was discussed in Ref. [59].

4.1 Numerical methods

The investigated structures in this chapter are treated within the same framework of numerical methods as already used for the investigation of equilibrium properties in Chapter 3. An additional expansion to these methods, which are described in detail in Sec. 3.1, has to be considered relating the used retarded Green's function $G(\omega, \boldsymbol{k})$. Since the retarded Green's function itself cannot be used to describe non-equilibrium transport properties like the steady-state current density j, an expansion to Keldysh-space has to be performed. A brief derivation and the numerical details of this expansion are provided in the following paragraphs, where additionally, the calculation formulas for the non-equilibrium properties of interest, e.g. the steady-state electrical current density j, are presented.
Dissipative bath chains are coupled to the physical system in order to provide a proper dissipation mechanism to prevent BOs. These additional couplings can be taken into account by a suitable form of Dyson's equation, already mentioned in conjunction with Eq.(3.38) in the derivation of CPT's central equation. Applying Dyson's equation to describe couplings of different 2d structures becomes rather non-trivial. As this is exactly what will be needed in the case of GNRs, the general calculation scheme applicable for different infinite geometries is presented in Sec. 4.2.

Keldysh non-equilibrium Green's functions formalism

An introduction to the Keldysh non-equilibrium Green's functions (KNEGF) formalism is topic of the present section. As already mentioned, the KNEGF are obtained by a generalization of the Green's functions discussed in Sec. 3.1.1 to Keldysh space. The KNEGF are also often referred to as *Contour Ordered Green's Functions*. Fortunately, some of the work has already been performed in Sec. 3.1.1, since the derivation of the KNEGF formalism agrees in large parts with the treatment of Green's functions in the equilibrium case.
The explanations of this section are widely based on the introductory lecture notes of *Jauho (2006)*

[60], where completive details were taken from more comprehensive reviews [61] [62] or books [63] [64]. A good overview of the topic is also presented in Ref. [43]. It is worth mentioning here that the Contour Ordered Green's Functions technique is named also Keldysh or KNEGF technique after the pioneering work by *Keldysh (1964)* [65].

As a starting point, the relationship for the zero-temperature single-particle Green's function obtained in Eq.(3.17) is considered again:

$$G^{(1)}\left(1|1'\right) := -i\left\langle T\left[\Psi(1)\Psi^{\dagger}(1')\right]\right\rangle = -i\frac{\langle\Psi_0|\ T\left[\Psi(1)\Psi^{\dagger}(1')\right]\ |\Psi_0\rangle}{\langle\Psi_0\ |\Psi_0\rangle} \tag{4.1}$$

with the time-ordering operator T defined in Eq.(3.7) and the angle brackets denoting an expectation value with respect to the ground state of the particular system. The number n was introduced as a shorthand notation of the space-time points $\{x_n t_n\}$. Since in the following derivation the explicit time-dependency is more important than space-dependency, the space-index x will be suppressed from now on.
The definition of the single-particle Green's function in Eq.(4.1) contains the ground state expectation value, which requires knowledge of the exact ground state $|\Psi_0\rangle$ of an interacting system. In the equilibrium case considered in Chapter 3 this requirement was met approximately by applying CPT, where the ground state of small enough clusters was obtainable using the Lanczos algorithm. A different approach to this property of Eq.(4.1) is to make use of the Gell-Mann and Low theorem [66] and express the unknown exact ground state $|\Psi_0\rangle$ in terms of the non-interacting ground state $|\Phi_0\rangle$

$$|\Psi_0\rangle = S(0,-\infty)\,|\Phi_0\rangle \tag{4.2}$$

The occurring $S(t,t')$-matrix is defined as

$$S(t,t') = U(t)U^{\dagger}(t'), \tag{4.3}$$

where U is the commonly used time-evolution operator in the interaction picture, and provides the time-dependent wavefunctions $\psi(t)$:

$$\psi(t) = S(t,t')\psi(t'). \tag{4.4}$$

It should be mentioned here that the S-Matrix can be expressed as a time-ordered product as well [67].
For the further derivation it is important to point out that the S-Matrix obeys the group property

$$S(t,t') = S(t,t'')S(t'',t'). \tag{4.5}$$

With the S-matrix defined, the expression for the ground state $|\Psi_0\rangle$ presented in Eq.(4.2) can be further analyzed: Since $S(0,-\infty)$ describes the time evolution of a wavefunction $\psi(t)$ from $t \to -\infty$ to $t = 0$, the ground state of the non-interacting system $|\Phi_0\rangle$ has to be obtained at $t \to -\infty$. This can be achieved in an elegant way by describing the systems general Hamiltonian as

$$H = H_0 + H_1(t) \tag{4.6}$$

where H_0 is the Hamiltonian of the non-interacting system. The interactions are switched on as in

$$H_1(t) = e^{-\eta|t|} V(t) \tag{4.7}$$

where η is a positive infinitesimal needed (which will be justified shortly), and $V(t)$ describes the perturbation of the system caused by interactions, similar as in Eq.(3.32), where V described the perturbation of a system caused by an applied cluster tiling. Eq.(4.7) implicates an adiabatic switching on of the interactions until the interactions full strength is attained at $t = 0$. The advantage of separating the total Hamiltonian in this way becomes obvious, when considering the limes $t \to -\infty$:

$$\lim_{t\to-\infty} H_1(t) = 0 \qquad \Rightarrow \qquad \lim_{t\to-\infty} H = H_0. \tag{4.8}$$

In consequence of this limiting behaviour the exact ground state of a particular system $|\Psi_0\rangle$ corresponds to the ground state of the non-interacting system $|\Phi_0\rangle$ in the limes $t \to -\infty$:

$$\lim_{t\to-\infty} |\Psi_0\rangle = |\Phi_0\rangle \tag{4.9}$$

which justifies the validity of Eq.(4.2) in a significant way.

Applying the expression for the ground state $|\Psi_0\rangle$ from Eq.(4.2) to the definition of the zero-temperature single-particle Green's function in Eq.(4.1) yields

$$G(t_1|t_2) = -i\frac{\langle\Phi_0| S(-\infty,0) T\left[\Psi(t_1)\Psi^\dagger(t_2)\right] S(0,-\infty)|\Phi_0\rangle}{\langle\Phi_0| S(-\infty,0) S(0,-\infty)|\Phi_0\rangle} \tag{4.10}$$

where the identity $\left(S(0,-\infty)|\Phi_0\rangle\right)^* \equiv \langle\Phi_0| S(-\infty,0)$ was used. Furthermore, the superscript $^{(1)}$ denoting the single-particle Green's function was dropped and the quantum number $n = 1'$ was replaced by $n = 2$ in order to afford better readability. Until now all wavefunctions and operators were expressed in the Heisenberg picture O^H. The next step is a transformation to the interaction representation with respect to H_0 according to [60]

$$\begin{aligned} \left|\Psi^{(I,H_0)}(t)\right\rangle &= S(t,-\infty)\left|\Psi^{(H)}(t)\right\rangle = S(t,-\infty)|\Phi_0\rangle \\ O^{(H)}(t) &= S(-\infty,t) O^{(I,H_0)}(t) S(t,-\infty). \end{aligned} \tag{4.11}$$

Remembering the group properties of the S-Matrix and applying the above transformation to Eq.(4.10) results in

$$G(t_1|t_2) = -i\frac{\langle\Phi_0| S(-\infty,t_1) T\left[S(t_1,-\infty)\Psi(t_1)\Psi^\dagger(t_2)\right]|\Phi_0\rangle}{\langle\Phi_0|\Phi_0\rangle} \tag{4.12}$$

where $S(t_1,-\infty)$ was pulled inside the argument of the time-ordering operator T. The term $S(-\infty,t_1)$ cannot be pulled inside T, because it do not feature the required time-order itself (check Eq.(4.3)), due to $t_1 > -\infty$. With the solution of this problem, a point has been reached where the equilibrium case starts deviating from the non-equilibrium case, which is the regime of interest in this chapter:

The above problem is solvable *in the equilibrium case* in a mathematically elegant way, by introduc-

ing the ground state in the distant future $|\Psi_0(t \to \infty)\rangle = S(\infty, -\infty)\,|\Phi_0\rangle$, to write

$$\langle\Phi_0|\, S(\infty, t_1) = \langle\Psi_0(t \to \infty)|\, S(\infty, -\infty)S(-\infty, t_1) = \langle\Psi_0(t \to \infty)|\, S(\infty, t_1). \tag{4.13}$$

which now allows to pull $S(\infty, t_1)$ into the time-ordering operator T in Eq.(4.12), due to $\infty > t_1$, leading to

$$G\,(t_1|t_2) = -i\frac{\langle\Psi_0(t \to \infty)|\, T\left[S(\infty, -\infty)\Psi(t_1)\Psi^\dagger(t_2)\right]|\Phi_0\rangle}{\langle\Psi_0(t \to \infty)|\, S(\infty, -\infty)\,|\Phi_0\rangle} \tag{4.14}$$

where $S(\infty, t_1)S(t_1, -\infty) = S(\infty, -\infty)$ was used. Finally, the obtained expression can be used as a starting point for perturbation theory by assuming the system to find its way back to the ground state $|\Phi_0\rangle$ of the non-interacting system in the distant future $t \to \infty$, i.e. replacing $|\Psi_0(t \to \infty)\rangle = e^{-i\Phi}\,|\Phi_0\rangle$ in Eq.(4.14). This assumption is justified by the Gell-Mann and Low theorem [66] again (see Eq.(4.2)), since the adiabatic behaviour of the interaction term $H_1(t)$ defined in Eq.(4.7) causes H_1 to vanish at times $t \to \infty$ as well, resulting in a systems Hamiltonian $H = H_0$. Eventually, the phase factor $e^{-i\Phi}$ occurring due to the final assumption shall be discussed. In fact, there appear phase factors in the enumerator *and* denominator of Eq.(4.14) making them both indeterminate. However, it can be shown that the quotient is well defined for *infinitely slow switch-on and switch-off characteristics of the interaction term* $H_1(t)$ in Eq.(4.6) [66], which explains the positive infinitesimal prefactor η in the exponent of Eq.(4.7).

Focusing on the *non-equilibrium case* now, the above assumption $|\Psi_0(t \to \infty)\rangle = e^{-i\Phi}\,|\Phi_0\rangle$ is no longer valid. Since the non-equilibrium situation is characterized by a flow of particles, energy, current, etc., a return of the system to its non-interacting ground state $|\Phi_0\rangle$ in consequence of adiabatically switching-off the interactions is not reasonable. Due to this deviation from the equilibrium case, a new approach for solving the problem defined below Eq.(4.12) has to be found. This approach is called *Contour Ordered Green's Function technique*.
Before the introduction of the required Keldysh contour, a slight manipulation has to be performed in Eq.(4.12) by inserting an identity operator $\mathbb{1} = S(t_1, \infty)S(\infty, t_1)$ in front of the time-ordering operator T:

$$G\,(t_1|t_2) = -i\frac{\langle\Phi_0|\, S(-\infty, \infty)T\left[S(\infty, -\infty)\Psi(t_1)\Psi^\dagger(t_2)\right]|\Phi_0\rangle}{\langle\Phi_0\,|\Phi_0\rangle}. \tag{4.15}$$

With this expression at hand, the troublesome term $S(-\infty, \infty)$ in the enumerator can be handled by introducing the closed-path or Keldysh contour illustrated in Fig. 4.1, which goes along with an additional contour dependency $C = \{+, -\}$ in the arguments of all objects in Eq.(4.15), i.e. $\Psi = \Psi(t, C)$. It has to be noted here that this particular contour is only valid for systems without initial correlations, since the information lost by an adiabatically switch-on and -off behaviour of the interactions is related to initial correlations [60]. However, in many physical situations, as in the case of steady-state transport e.g., this wash-out of the initial correlations by the interactions appears plausible.

The introduction of the Keldysh contour corresponds to an evolution of the system from $t \to -\infty$ to $t \to \infty$ in the forward time direction and then back again. Due to this closed time-path along different contour branches, the time-ordering operator T defined in Eq.(3.7) has to be extended to

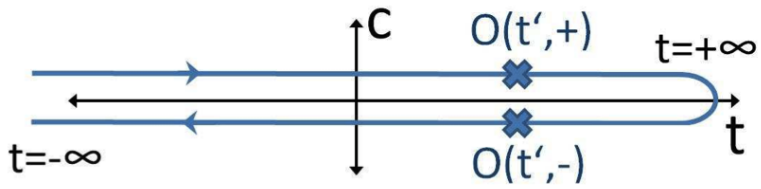

Figure 4.1: The Keldysh contour for Green's functions in non-equilibrium regimes. The upper branch of the contour is denoted by +, while a $-$ labels the lower one (adapted from Ref. [43]).

the contour-ordering operator T_C, according to

$$T_C\left[O_A(t_1,C_1)O_B(t_2,C_2)\right] = \begin{cases} O_A(t_1,C_1)O_B(t_2,C_2), & \text{for}\{t_1,C_1\} > \{t_2,C_2\} \\ O_B(t_2,C_2)O_A(t_1,C_1), & \text{for}\{t_2,C_2\} > \{t_1,C_1\} \end{cases} \tag{4.16}$$

where any time residing on the + branch in Fig. 4.1 appears earlier in sense of the Keldysh contour than any time residing on the $-$ branch.
The contour-ordering operator T_C allows to order all operators inside its argument along a particular contour, which makes it possible again to pull the $S(-\infty,-;\infty)$ term inside the ordering-operator:

$$G\left(t_1C_1|t_2C_2\right) = -i\frac{\langle\Phi_0|\ T_C\left[S(-\infty,-;\infty)S(\infty;-\infty,+)\Psi(t_1,C_1)\Psi^\dagger(t_2,C_2)\right]|\Phi_0\rangle}{\langle\Phi_0\ |\Phi_0\rangle}. \tag{4.17}$$

Remembering the relationship between field operators $\Psi\ \left(\Psi^\dagger\right)$ and annihilation (creation) operators $c\ \left(c^\dagger\right)$ (see Eq.(3.12)), the obtained expression defines the *contour-ordered single-particle Green's function in Keldysh space*, containing four different functions, corresponding to the four different possibilities for the contour variables $(C_1,C_2) = \{(+,+);(+,-);(-,+);(-,-)\}$:

$$G\left(t_1|t_2\right) = \begin{pmatrix} G\left(t_1+|t_2+\right) & G\left(t_1+|t_2-\right) \\ G\left(t_1-|t_2+\right) & G\left(t_1-|t_2-\right) \end{pmatrix} = \begin{pmatrix} G^T\left(t_1|t_2\right) & G^<\left(t_1|t_2\right) \\ G^>\left(t_1|t_2\right) & G^{\widetilde{T}}\left(t_1|t_2\right) \end{pmatrix} \tag{4.18}$$

where the following Green's functions have been introduced

$$\begin{aligned} G^T\left(1|2\right) &= -i\left\langle T\left[\Psi(1)\Psi^\dagger(2)\right]\right\rangle && \ldots \text{ time-ordered Green's function} \\ G^<\left(1|2\right) &= -i\zeta\left\langle\Psi^\dagger(1)\Psi(2)\right\rangle && \ldots \text{ lesser Green's function} \\ G^>\left(1|2\right) &= -i\left\langle\Psi(1)\Psi^\dagger(2)\right\rangle && \ldots \text{ greater Green's function} \\ G^{\widetilde{T}}\left(1|2\right) &= -i\left\langle\widetilde{T}\left[\Psi(1)\Psi^\dagger(2)\right]\right\rangle && \ldots \text{ antitime-ordered Green's function} \end{aligned} \tag{4.19}$$

where the quantum number n combining time-, space-, spin-, ... dependency has been re-introduced. The angle brackets are denoting an expectation value with respect to the ground state $|\Phi_0\rangle$ of the non-interacting system again and $\zeta = -1$ ($\zeta = 1$) for Fermions (Bosons) according to Eq.(3.8).

While the time-ordered and antitime-ordered Green's function G^T and $G^{\widetilde{T}}$, respectively, appear only due to the introduced Keldysh contour, one should be familiar to the lesser and greater Green's function $G^<$ and $G^>$, since they were already defined in Eq.(3.20) and Eq.(3.19) in the equilibrium case. According to Eq.(3.21) and Eq.(3.22) the latter ones can also be combined to the retarded

and advanced Green's functions G^R and G^A

$$\begin{aligned} G^R(1|2) &= \left(G^>(1|2) - G^<(1|2)\right)\theta(t_1 - t_1) \\ G^A(1|2) &= \left(G^<(1|2) - G^>(1|2)\right)\theta(t_2 - t_1). \end{aligned} \tag{4.20}$$

Furthermore, the four components of the contour-ordered single-particle Green's function are not linearly independent, since

$$G^T(1|2) + G^{\widetilde{T}}(1|2) = G^<(1|2) + G^>(1|2) := G^K(1|2) \tag{4.21}$$

where the Keldysh Green's function G^K has been introduced. In consequence of this linear dependence it is comprehensible to perform a rotation in Keldysh space:

$$G\,(1|2) = \begin{pmatrix} G^T\,(1|2) & G^<\,(1|2) \\ G^>\,(1|2) & G^{\widetilde{T}}\,(1|2) \end{pmatrix} \mapsto \begin{pmatrix} G^R\,(1|2) & G^K\,(1|2) \\ 0 & G^A\,(1|2) \end{pmatrix} := \widetilde{G}\,(1|2) \tag{4.22}$$

where the rotated Green's function $\widetilde{G}$ is used in the remaining parts of this work.

Quantities obtained by the Keldysh Non-Equilibrium Green's functions formalism

The non-equilibrium formalism presented here, based on the system's ground state in the remote (non-interacting) past ($t \to -\infty$), can be interpreted in the following way. In the distant past the central region (i.e. the geometry of which the non-equilibrium properties are under investigation) is decoupled from any current-driving contacts (leads), fields or baths and therefore considered to be in equilibrium. For this reason, the retarded component G^R of the Green's function $\widetilde{G}$ in Keldysh space is calculated exactly as in the equilibrium case (see Eq.(3.67)). The corresponding Keldysh Green's functions G^K of any regions, contacts or baths in equilibrium, i.e. before the coupling to the environment is considered, are characterized by their respective chemical potentials μ, according to

$$G^K(\omega, \mu) = \left(G^R(\omega) - G^A(\omega)\right)\left(2f_F(\omega, \mu, T) - 1\right) \tag{4.23}$$

where the equilibrium distribution function is described by the Fermi-Dirac distribution

$$f_F(\omega, \mu, T) = \left(e^{-\frac{\omega-\mu}{k_B T}} + 1\right)^{-1} \tag{4.24}$$

in which Boltzmann's constant k_B appears. It is taken as unity throughout the whole work.
It has to be noted here that these equilibrium distribution functions are the only quantities in which the particular chemical potential μ enters. At this point it is important to remember that the Hamiltonian H used in the equilibrium situation was transformed according to $H \to H - \mu N$ in Eq.(3.10), due to the description of the physical systems in the grand canonical ensemble. Since the chemical potential μ is explicitly entering the calculations in the non-equilibrium situation, it cannot be generally transformed into the Hamiltonian anymore.
Finally, the couplings of the different regions are re-established and treated via standard techniques

of perturbation theory, albeit some special treatment is necessary due to the introduced Keldysh contour.
In Sec. 4.2 the calculation of the contour-ordered single-particle Green's function $\widetilde{G}$ in Keldysh space is explained in detail for geometries under a driving DC electrical field with one infinitely extended dimension, where an iterative calculation scheme has to be used. In the following, the derivation of calculation formulas for the steady-state electrical current density j for interacting systems and for the effective local distribution function $f_{loc}(\omega)$ are schematically outlined. The interested reader is referred to Refs. [43] [60] or [63], where comprehensive derivations are provided.

Steady-state electrical current density for interacting systems

The final objective of this paragraph is to provide a calculation formula for the steady-state electrical current density j_{mn} between to neighbouring sites m, n in terms of the Keldysh Green's function G^K introduced in Eq.(4.21). *Steady-state* in this context means that one is interested in the long-time behaviour of the considered system, i.e. the physical situation where initial correlations have been entirely washed out by the interactions. Remember that the introduced Keldysh contour is valid only in exactly these cases.

Considering a linearly decreasing potential from left to right , the current density between a site m and its right nearest neighbouring site n - assuming an ensemble of Fermions (electrons) - is given by

$$j_{mn} = i\frac{e}{\hbar}t_{mn}\left\langle c_n^\dagger c_m - c_m^\dagger c_n\right\rangle \tag{4.25}$$

with e the charge of an electron and $\hbar$ the reduced Planck constant, which are both taken as unity in the remaining sections of this work. This expression is intuitive in a way, since the operator of which the expectation value is taken $\left\langle c_n^\dagger c_m - c_m^\dagger c_n\right\rangle$ describes the effective transition rates of electrons between site m and n.
Eq.(4.25) is derivable by describing the current density between site m and n as the time evolution of the occupation number operator $N_L(t)$ of all particles left to site m

$$j_{mn} = -\left\langle \dot{N_L}(t)\right\rangle = -\left\langle i\left[H, \sum_{i\leq m} n_m\right]\right\rangle \tag{4.26}$$

with the square brackets denoting the common commutator relation $[a, b] = ab - ba$. For a large part of the outlined derivation the explicit time dependency can be dropped, although it has to be kept in mind that all operators act at the same time t. Inserting the Hamiltonian of the 2d Hubbard model defined in Eq.(3.30) and evaluating all the occurring commutators the expression for the current stated in Eq.(4.25) can be obtained.

Continuing with Eq.(4.25), the elementary fermion commutation relation $[c_i, c_j^\dagger] = \delta_{ij}$ is used to to

symmetrize the operators according to

$$\begin{aligned} j_{mn} &= i t_{mn} \left\langle c_n^\dagger c_m - c_m^\dagger c_n \right\rangle \\ &= i \frac{t_{mn}}{2} \left\langle \left(c_n^\dagger c_m + c_n^\dagger c_m \right) - \left(c_m^\dagger c_n + c_m^\dagger c_n \right) \right\rangle \\ &= i \frac{t_{mn}}{2} \left\langle \left(c_n^\dagger c_m + c_m c_n^\dagger + \delta_{nm} \right) - \left(c_m^\dagger c_n + c_n c_m^\dagger + \delta_{mn} \right) \right\rangle \\ &= \frac{t_{mn}}{2} \left(i \left\langle c_n^\dagger c_m \right\rangle + i \left\langle c_m c_n^\dagger \right\rangle - i \left\langle c_m^\dagger c_n \right\rangle - i \left\langle c_n c_m^\dagger \right\rangle \right) \end{aligned} \tag{4.27}$$

where in the last line the additivity of the expectation value in the case of operators in the form $c_i c_j^\dagger$ $\left(c_i^\dagger c_j \right)$ was used and the two Kronecker deltas cancelled each other out.

At this point the definitions of the lesser and greater Green's function $G^<$ and $G^>$ in Eq.(3.20) and Eq.(3.19) can be used to replace the expectation values in Eq.(4.27), yielding

$$\begin{aligned} j_{mn} &= \frac{t_{mn}}{2} \left(G_{nm}^< - G_{mn}^> - G_{mn}^< + G_{nm}^> \right) \\ &= \frac{t_{mn}}{2} \left(G_{nm}^K - G_{mn}^K \right) \end{aligned} \tag{4.28}$$

where the definition of the Keldysh Green's function in Eq.(4.21) was used in the last line. The expression is further simplified by using the handy relationship of the Keldysh Green's function

$$G^K = - \left(G^K \right)^\dagger \tag{4.29}$$

providing a compact calculation formula for the current density in terms of the Keldysh Green's function:

$$\begin{aligned} j_{mn} &= \frac{t_{mn}}{2} \left[G_{nm}^K + \left(G_{nm}^K \right)^\dagger \right] \\ &= t_{mn} \, \Re \left\{ G_{nm}^K(t,t) \right\} \end{aligned} \tag{4.30}$$

where the explicit time dependency has been re-introduced in the last line. Similar to the equilibrium situation (see Eq.(3.27)), the final result is obtained by Fourier transforming the whole equation with respect to the only occurring time t into frequency space:

$$j_{mn} = \frac{t_{mn}}{2\pi} \int_{-\infty}^{\infty} d\omega \, \Re \left\{ G_{nm}^K(\omega) \right\} \tag{4.31}$$

which provides a convenient calculation formula in terms of the frequency dependent Keldysh Green's function $G^K(\omega)$, which remains to be calculated. A concluding explanation of the iterative calculation scheme applied for the investigation of (semi -) infinite structures, like the GNRs considered in this work, is provided in Sec. 4.2. What follows here, is a brief introduction of the effective local distribution function $f_{loc}(\omega)$.

Local distribution function

The definition of the Keldysh Green's function G^K in the case of equilibrium in Eq.(4.23) implicitly defines an effective local distribution function $f_{loc}(\omega)$. In the equilibrium situation it is given by the Fermi-Dirac distribution $f_F(\omega, \mu, T)$ defined in Eq.(4.24), while in the non-equilibrium case it is calculated according to

$$f_{loc}(\omega) = \frac{\Im\left\{G^K(\omega)\right\}}{G^R(\omega) - G^A(\omega)} + \frac{1}{2} = \frac{\Im\left\{G^K(\omega)\right\}}{2\Im\left\{G^R(\omega)\right\}} + \frac{1}{2} \tag{4.32}$$

which is obtainable by rearranging Eq.(4.23).
Furthermore, the results of $f_{loc}(\omega)$ in the non-equilibrium situation can be fitted by a Fermi-Dirac distribution with an effective temperature T_{eff}, although there is no particular reason to expect the non-equilibrium local distribution function to mimic the Fermi-Dirac distribution [68].

The presented formulas for the steady-state electrical current density j in Eq.(4.31) and for the effective local distribution function $f_{loc}(\omega)$ in Eq.(4.32) find their practical implementation in Sec. 4.3 and Sec. 4.4, where the DC electrical field driven current densities within an infinite TB chain and infinite GNRs are investigated. Introductory to these investigations, the special characteristics featured by (semi -) infinite structures in the case of non-equilibrium regimes are discussed in the following section.

4.2 Modeling energy dissipation in infinite structures

The particular situation of lattice geometries with one infinite dimension is considered in this section regarding their expected non-equilibrium behaviours. As already mentioned, dissipation in real solids is caused mainly by acoustic phonons. However, an approximate alternative way of mimicking dissipation by coupling fermion thermostats is used in this work, which allows for an exact solution in the non-interacting $U = 0$ case. The particular dissipation model is explained in Sec. 4.2.2 right after an introduction to the role of BOs in infinite geometries in Sec. 4.2.1. Furthermore, the applied model for the non-equilibrium investigations is outlined in Sec. 4.2.3 where the corresponding general calculation scheme is presented in addition. A detailed description of the iterative calculation scheme used for the determination of the Keldysh Green's function G^K, required to obtain the current characteristics, is provided as well.

4.2.1 The role of Bloch oscillations

The pioneering works of *Bloch (1928)* [69] and *Zener (1934)* [70] on the time evolution of electron wave packets captured in periodic potentials of crystal lattices led to the prediction that homogenous electrical fields will force electrons to oscillate around a certain central position rather than move uniformly against the direction of the electrical field. Intensive research activities followed the theoretical prediction of these *Bloch oscillations* (BOs), with the final aim of an experimental detec-

tion. However, it was only in the year 1992 that BOs were observed in semiconductor superlattices by optical investigations [71] [72], where the large spatial period of the superlattice in combination with very low temperatures was the key to success. The main problem in the experimental detection of BOs is the small scattering time of electrons in non-ideal crystal lattices, which is much shorter than the period of the BOs.

The occurrence of BOs, which is a pure quantum effect, can be explained considering an infinite one-dimensional model with a periodic potential $U(\boldsymbol{x}) = U_0 sin^2\left(\frac{\pi|\boldsymbol{x}|}{a}\right)$ [73]. The size of the physical unit cell a, i.e. the period of the lattice, defines the size of the first BZ in one dimension, according to

$$1^{st}\text{ BZ:} \qquad \left]-\frac{\pi}{a}, \frac{\pi}{a}\right]. \tag{4.33}$$

Due to the periodicity of the infinite lattice the well-known band structure of the energy spectrum (plotted in blue in Fig. 4.2) emerges. As a further consequence of the periodicity, the corresponding eigenenergies $E_n(q)$ and eigenstates $|n, \boldsymbol{q}\rangle$ (the so-called *Bloch states*) are periodic functions of the continuous quasimomentum $\boldsymbol{q}$ with a period $\frac{2\pi}{a}$.

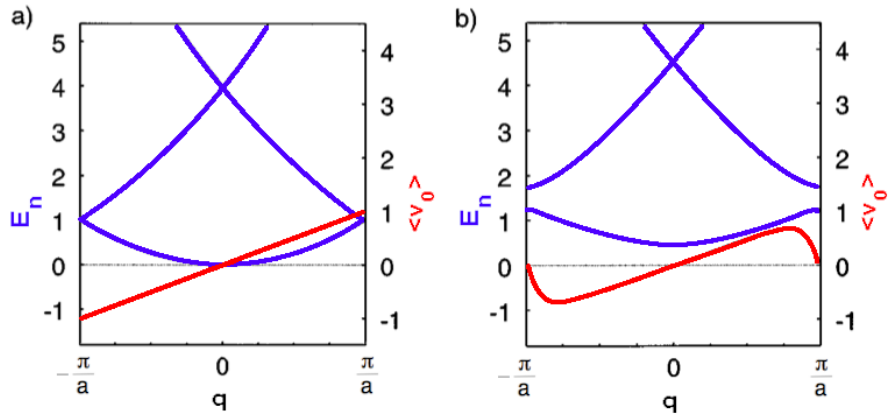

Figure 4.2: Energy-momentum dispersion relation $E(\boldsymbol{q})$ (blue line) and the average velocity $\langle \boldsymbol{v}_0 \rangle (\boldsymbol{q})$ in the lowest band (red line) of a free electron gas (a) and an electron captured in a periodic potential (b), (adapted from Ref. [73]).

By applying a homogeneous electrical field $\boldsymbol{F}$ along the infinite one-dimensional model which is weak enough not to induce transitions between different energy bands, the acceleration theorem $\hbar\dot{\boldsymbol{q}} = e\boldsymbol{F}$ [71] states that an initial Bloch state $|n, \boldsymbol{q}(0)\rangle$ evolves into a state $|n, \boldsymbol{q}(t)\rangle$ (neglecting a possible phase factor), with a quasimomentum $\boldsymbol{q}$ given by [73]

$$\boldsymbol{q}(t) = \boldsymbol{q}(0) + \frac{e\boldsymbol{F}t}{\hbar}. \tag{4.34}$$

The corresponding average velocity $\langle \boldsymbol{v} \rangle$ can be obtained by differentiating the energy-momentum dispersion relation $E(\boldsymbol{q})$ with respect to the quasimomentum $\boldsymbol{q}$, according to

$$\langle \boldsymbol{v}(\boldsymbol{q}) \rangle = \frac{1}{\hbar}\frac{dE(\boldsymbol{q})}{d\boldsymbol{q}}. \tag{4.35}$$

The energy-momentum dispersion relation $E_n(\boldsymbol{q})$ and the average velocity $\langle \boldsymbol{v}_0(\boldsymbol{q}) \rangle$ of a free electron gas under the force of an uniform electrical field $\boldsymbol{F}$, calculated according to the above formula, are plotted in Fig. 4.2a within the first BZ. For the dispersion relation of the free electron gas one finds the well-known expressions

$$E(\boldsymbol{q}) = \frac{\hbar^2 \boldsymbol{q}^2}{2m}; \qquad \boldsymbol{v}_0 = \frac{\hbar \boldsymbol{q}}{m} \tag{4.36}$$

with the electron mass m. The subscript in $\boldsymbol{v}_0$ indicates that the velocity is only plotted for the fundamental band. Obviously, a free electron gets accelerated to higher velocities steadily as its quasimomentum increases/decreases due to the electrical field. Since the particle is free and therefore not bound to any lattice potential, there appears no change in the behaviour when the border of the first BZ is reached.

In contrast to that, the occurrence of BOs of electrons captured in a periodic (lattice) potential under the influence of a weak uniform electrical field can be observed in Fig. 4.2b. Due to the periodic potential $U(\boldsymbol{x}) = U_0 sin^2\left(\frac{\pi|\boldsymbol{x}|}{a}\right)$ in the infinite lattice, the energy bands are flattened at the BZ boundaries (plotted in blue in Fig. 4.2b). In consequence of this band flattening, the electrons of the fundamental band are decelerated as they move closer to the BZ boundary, due to the electrical field driven increase of the quasimomentum. When the BZ boundary is reached the average electron velocity reaches a value of zero (plotted in red in Fig. 4.2b) and the electron gets accelerated into the opposite direction, i.e. the electron is Bragg reflected at the BZ boundary. Since the same Bragg reflection occurs to the electron at the other BZ boundary, an oscillatory motion of the electrons is induced. In fact, these oscillatory motions are indeed the pronounced BOs, which feature a constant time period τ depending on the strength of the electrical field $|\boldsymbol{F}| = F$ and the size of the physical unit cell a:

$$\tau_B = \frac{2\pi\hbar}{eFa}. \tag{4.37}$$

Alternatively, the occurrence of BOs can be explained in terms of the effective mass

$$m^* = \hbar^2 \left[\frac{d^2 E(\boldsymbol{q})}{d\boldsymbol{q}^2}\right]^{-1}. \tag{4.38}$$

Due to the flattened energy bands at the boundaries of the first BZ in Fig. 4.2b, the sign of the effective mass changes from positive to negative as the electron reaches the BZ boundary. The change of sign of the effective mass subsequently causes a change of sign in the kinetic energy $E = m^* v^2/2$, which results in a change of the moving direction and therefore leads to BOs as well.

4.2.2 Preventing Bloch oscillations by coupling fermion bath chains to the system

As already mentioned above, experimental observations of BOs in nature are a very challenging task, due to scattering processes in non-ideal crystal lattices. In the course of this master thesis investigations of infinite TB chains and infinite GNRs regarding their non-equilibrium properties are

performed and documented in the following Sec. 4.3 and Sec. 4.4. However, the applied model (introduced in the following subsection) *does not* include any scattering mediated by phonons, impurities or vacancies, and consequently enables the occurrence of BOs, which prevent the flow of a steady-state current.
Numerous methods have been developed for the investigation of non-equilibrium properties in strongly correlated systems. In optical lattices, isolated Hamiltonians suited for quench dynamics of cold atom systems were used [74], while periodical driven systems have been tried in strongly correlated electron systems [75]. Other basic dissipation models, like electron-phonon coupling [76] or fermion thermostats [77], were investigated as well.
In this work an approach of voltage probes is chosen, in which fermion bath chains are coupled to each site of the considered lattice geometry to allow for a proper dissipation mechanism. The non-equilibrium regime is generated by a constant electrical field, which is applied along the whole infinite structure and therefore drives a current to flow, in the case of a suitable dissipation mechanism. It has to be noted here that treating dissipation in a DC electrical field driven lattice by fermion baths is a commonly used approach [68] [77] [78] [79]. The collective conclusions in these reviews describe the fermion thermostat model as a good minimal setup to study strong correlation effects in driven lattice models, even though its modeling of a realistic dissipation mechanism is rather simple [78]. Since this is in nice agreement with the final objective of investigating infinite GNRs regarding their non-equilibrium properties, using strong-coupling many-body physics within the framework of CPT, this approach of fermion bath chains was chosen.
In the next subsection, the overall model (including ED for the particular equilibrium cluster solution as well as non-equilibrium transport forced by an electrical field and coupled bath chains) is outlined, with some important approaches, like the iterative calculation scheme for the Keldysh and retarded Green's functions, explained in detail.

4.2.3 Tight-binding Wannier-Stark model

The calculation of the non-equilibrium properties presented in Sec. 4.1 for infinite lattice geometries (TB chain and GNRs) in case of an applied DC electrical field requires a couple of subsequent steps. Both the numerical methods for the non-equilibrium situation, presented in the previous section, and the numerical methods used in case of an equilibrium regime, presented in Sec. 3.1, are included in the extensive computation scheme. What follows is an introduction to the overall model, with the important iterative calculation scheme for the Keldysh and retarded Green's functions $G^R(\omega)$ and $G^K(\omega)$ of an infinitely extended structure explained in detail.

Geometry

In Fig. 4.3 the investigated infinite lattice geometries are sketched, where Fig. 4.3a shows the infinite TB chain and Fig. 4.3b an AC-W5 GNR as an example of a GNR geometry. The fermion bath chains are Indicated by the green chains coupled to each site, while the direction of the *homogeneous* DC electrical field $\boldsymbol{E}$ is given by the black arrows. As a first step of the calculation scheme, the infinite

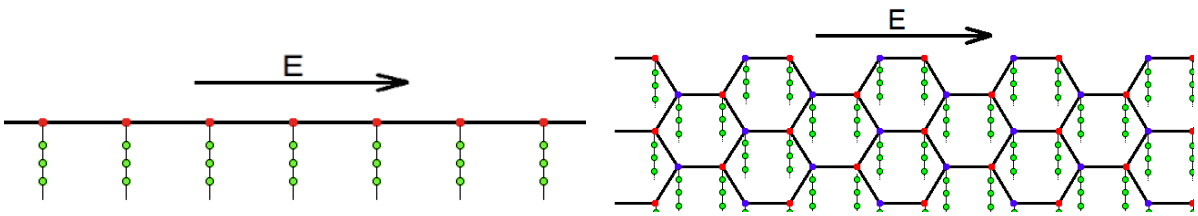

Figure 4.3: Infinite lattice geometries under investigation regarding their non-equilibrium properties. (a) infinite TB chain, (b) AC-W5 GNR as a representing example of an infinite GNR structure. The coupled fermion reservoir chains are indicated in green, the direction of the *homogeneous* DC electrical field ***E*** is given by the black arrow.

structures are split up into three parts:

1. A central part (cluster) right in the middle of the infinite chain, where *middle* means that the point of origin of the potential energy that result from the applied electrical field, is set exactly into the middle of this central part,

2. a semi-infinite chain (ribbon) on the left-hand side of the central part composed of coupled clusters, with every cluster equal to the central one, and

3. a semi-infinite chain (ribbon) on the right-hand side of the central part, again, composed of coupled clusters, where again every cluster is equal to the central one

These three parts are sketched in Fig. 4.4 for the case of an infinite TB chain as a representing example for all investigated structures. Furthermore, the (potential) on-site energies, which occur due to the applied DC electrical field at every particular site, are depicted. The parameter E_1 denotes the potential drop between two particular neighbouring sites of the TB chain. In the actual notation used in this work, E_1 also denotes the strength of the applied electrical field, since the lattice spacing is 1 in the units of this thesis.
It has to be mentioned here that the nomenclature *semi-infinite ribbon* is mathematically not entirely justifiable. However, it describes the particular geometry in a suitable way and is therefore used in the following.

When investigating infinite GNR geometries, the central part has to be replaced by the particular GNR clusters, which were introduced in the equilibrium situation in Chapter 3. For zig-zag edge orientation the particular cluster is plotted in Fig. 3.9d (ZZ-W4), while Fig. 3.22b (AC-W4) shows the cluster for the composition of an armchair GNR. It is important to notice here that the electrical field intensities at the particular sites of the infinite GNRs have to be adjusted to the geometries of every respective GNR. Fig. 4.19 in Sec. 4.4, where the results for the GNR geometries are presented, provide information on these on-site field intensities, in a similar way, as in Fig. 4.4 for the case of the infinite TB chain.

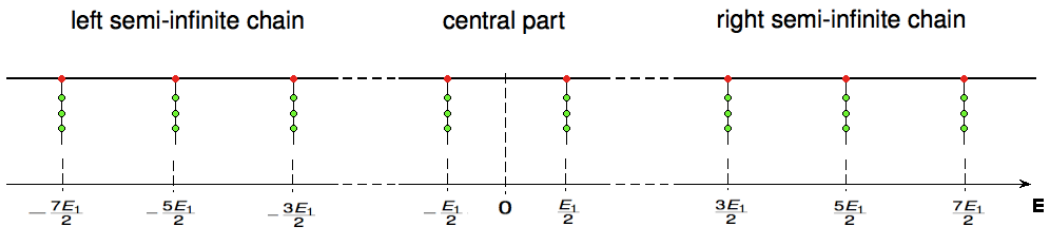

Figure 4.4: Composition of an infinite TB chain with coupled bath chains. Semi-infinite chains are coupled to a central part containing two sites, indicating the two-site cluster decomposition applied for the non-equilibrium investigations in case of the infinite TB chain. Furthermore, the electrical field intensities at every particular site are given, where E_1 is a constant determining the potential drop between two neighbouring sites, due to the applied homogeneous electrical field. The splitting into three parts applies also to the investigated GNR geometries, with the central two-site cluster replaced by the particular GNR clusters introduced in Chapter 3 and the semi-infinite chains replaced by semi-infinite ribbons.

General calculation scheme

The general calculation scheme for the non-equilibrium situation is outlined in the following:
First of all, the central cluster is solved by ED without considering the fermion bath chains required for dissipation. In consequence of the neglect of the bath chains, the situation corresponds exactly to the equilibrium case analyzed in detail in Chapter 3. The applied electrical field leads to occurring potential energies $\epsilon_i(E_1)$ at every site i along the infinite structures in the non-equilibrium case. These on-site energies can be considered by an additional correction to the equilibrium cluster Green's function, according to

$$\left[\boldsymbol{G}^0_{\text{non-equilibrium}}(\omega, E_1)\right]^{-1} = \left[\boldsymbol{G}^0_{\text{equilibrium}}(\omega)\right]^{-1} - \begin{pmatrix} \epsilon_1(E_1) & 0 & \dots & & \\ 0 & \epsilon_2(E_1) & 0 & \dots & \\ \dots & 0 & \epsilon_3(E_1) & 0 & \dots \\ & & & \ddots & \end{pmatrix}. \tag{4.39}$$

Therefore, the clusters are solved in exactly the same way as in the equilibrium case, described in Sec. 3.1.3, with an subsequent correction according to Eq.(4.39) in order to account for the effect of the applied electrical field.
The obtained retarded cluster Green's function $\boldsymbol{G}^0(\omega, E_1)$ is the basic ingredient for the composition of the right and left semi-infinite chains (ribbons), where Dyson's equation is used for the couplings between the chain (ribbon) clusters and between the chain (ribbon) and the reservoir chains. Since the semi-infinite structure cannot be constructed by coupling more and more clusters together, an iterative method is used to obtain the four-component Green's function $\widetilde{\boldsymbol{G}}(\omega, E_1)$ in Keldysh space (introduced in Eq. 4.22) of the respective first clusters in the semi-infinite chains (ribbons). In a final step, Dyson's equation is applied again to couple the left and right semi-infinite chains (ribbons) to the central cluster. At the very end, the non-equilibrium properties of interest, i.e. the steady-state

electrical current density $j(E_1)$ as a function of the electrical field intensity E_1 and the effective local distribution function $f_{loc}(\omega)|_{E_1}$ are calculated according to the derived formulas in Eq.(4.31) and Eq.(4.32).
A detailed description of the iterative method applied for the calculation of the four-component Green's function $\widetilde{\boldsymbol{G}}(\omega, E_1)$ in Keldysh space and of the final coupling of the three parts (see Fig. 4.4) is provided in the following paragraph.

Obtaining the four-component Green's function in Keldysh space for infinite lattice geometries by means of an iterative method

The derivation of a conditional equation for the four-component Green's function in Keldysh space in case of an infinite chain (GNR) is based on Dyson's equation. First of all, the central part of the TB chain in Fig. 4.4 is coupled to its fermion bath chains (the corresponding geometry plots for the GNRs are shown in Fig. 4.19). The right/left semi-infinite chain (ribbon) with coupled fermion bath chains is constructed afterwards by means of an iterative method. In a final step, the left and right semi-infinite chains (ribbons) are coupled to another central cluster, resulting in the desired infinite structure.
The outlined calculation scheme is applicable in case of an infinite TB chain *and* in case of infinite GNRs in a similar way, where the only difference arises in the coupling matrices $\widetilde{\boldsymbol{V}}$ and $\widetilde{\boldsymbol{T}}$.

Dyson's equation is used to couple the central part to its fermion bath chains in the following way (the explicit dependencies on ω and E_1 as well as the tilde denoting the four-component Keldysh space are omitted to ease the notation):

$$\boldsymbol{G}_{11} = \boldsymbol{g}_{11} + \boldsymbol{g}_{11}\boldsymbol{V}_{12}\boldsymbol{G}_{21} \tag{4.40}$$

$$\boldsymbol{G}_{21} = \boldsymbol{g}^{B}_{22}\boldsymbol{V}_{21}\boldsymbol{G}_{11}. \tag{4.41}$$

$\boldsymbol{G}_{11}$ denotes the desired Green's function of the central part coupled to fermion bath chains, $\boldsymbol{g}_{11}$ the Green's function of the uncoupled central part, $\boldsymbol{G}_{21}$ the Green's function between the central part and the coupled fermion bath chains and $\boldsymbol{g}^{B}_{22}$ the Green's function of the first sites of the uncoupled fermion bath chains. $\boldsymbol{V}_{12}$ and $\boldsymbol{V}_{21}$ are the respective coupling matrices. The matrix elements V_{ij} are either 0 or v, where v denotes the hopping integral between the first site of a bath chain and the site of the physical system which it is coupled to. The particular expressions for the coupling matrices are provided in Sec. 4.3 for the infinite TB chain and Sec. 4.4 for the GNRs.

The right/left semi-infinite chain in Fig. 4.4 (ribbon in Fig. 4.19) with coupled fermion bath chains is constructed in a similar way. The Dyson equations required in this situation are given by

$$\boldsymbol{G}^{L/R}_{11} = \boldsymbol{G}_{11} + \boldsymbol{G}_{11}\boldsymbol{T}^{L/R}_{12}\boldsymbol{G}^{L/R}_{21} \tag{4.42}$$

$$\boldsymbol{G}^{L/R}_{21} = \boldsymbol{g}^{L/R}_{22}\boldsymbol{T}^{L/R}_{21}\boldsymbol{G}^{L/R}_{11} \tag{4.43}$$

with $\boldsymbol{G}^{L/R}_{11}$ denoting the desired Green's function of the central part coupled to the left/right semi-infinite chain (ribbon), $\boldsymbol{G}^{L/R}_{21}$ the Green's function between the central part and the left/right semi-

infinite chain (ribbon) and $\boldsymbol{g}_{22}^{L/R}$ the Green's function of the boundary site of the left/right semi-infinite chain in Fig. 4.4. $\boldsymbol{G}_{11}$ is given by Eq.(4.40). The matrix elements T_{ij} of the coupling matrices $\boldsymbol{T}_{12}^{L/R}$ and $\boldsymbol{T}_{21}^{L/R}$ are either 0 or t, where t is the hopping integral between two neighbouring sites in the TB chain (GNR). Again, the particular expressions for the coupling matrices are provided in Sec. 4.3 for the infinite TB chain and Sec. 4.4 for the GNRs. All matrices in Eq.(4.40), Eq.(4.41), Eq.(4.42) and Eq.(4.43) are of dimension $L \times L$, with L the number of sites in the central part.

Eq.(4.40), Eq.(4.41), Eq.(4.42) and Eq.(4.43) can be combined into one expression. After some trivial analysis the final form of Dyson's equation, used to obtain the four-component Green's function of the central part coupled to the left/right chain (ribbon) $\boldsymbol{G}^{L/R}(\omega, E_1)$, is given by the following expression:

$$\left[\boldsymbol{G}^{L/R}(\omega, E_1)\right]^{-1} = \left[\boldsymbol{G}^{0}(\omega, E_1)\right]^{-1} - \Sigma(\omega, E_1) \tag{4.44}$$

$$\Sigma(\omega, E_1) = \underbrace{\boldsymbol{V}_{12}\boldsymbol{G}^{B}(\omega, E_1)\,\boldsymbol{V}_{21}}_{\text{fermion bath chains}} + \underbrace{\boldsymbol{T}_{12}^{L/R}\boldsymbol{g}_{22}^{L/R}(\omega, E_1)\,\boldsymbol{T}_{21}^{L/R}}_{\text{semi-infinite chain (ribbon)}} \tag{4.45}$$

where the explicit dependencies on ω and E_1 were re-introduced and $\Sigma(\omega, E_1)$ denotes the self-energy. The Green's function of the uncoupled central part $\boldsymbol{g}_{11}$ was replaced by the cluster Green's function $\boldsymbol{G}^0(\omega, E_1)$ in Keldysh-space and $\boldsymbol{G}^B(\omega, E_1)$ is written for the Green's function $\boldsymbol{g}_{22}^B$ of the first sites in the bath chains.

At this point, the iteration scheme has to be explained in detail: Starting out with the four components of the inverted equilibrium cluster Green's function $\left[\boldsymbol{G}^0(\omega, E_1)\right]^{-1}$ it is important that the resulting Keldysh component can be set to zero. Considering the definition of the Keldysh Green's function in Eq.(4.23), this is comprehensible at least in the non-interacting case, where

$$\left[G_0^R(\omega, E_1)\right]^{-1} = \omega + i\eta - H - \epsilon(E_1) \quad \Rightarrow \quad \left[G_0^R(\omega, E_1)\right]^{-1} - \left[G_0^A(\omega, E_1)\right]^{-1} = 2i\eta \approx 0 \tag{4.46}$$

where ω was written explicitly as $\omega + i\eta$, with η a positive infinitesimal (which is omitted again in the following) and $\epsilon(E_1)$ is the correction matrix of Eq.(4.39). Therefore, the four-component inverted equilibrium cluster Green's function is given by

$$\left[\boldsymbol{G}^0(\omega, E_1)\right]^{-1} = \begin{pmatrix} \left[G_0^R(\omega, E_1)\right]^{-1} & \mathbf{0} \\ \mathbf{0} & \left[G_0^A(\omega, E_1)\right]^{-1} \end{pmatrix} \tag{4.47}$$

where the dimension of the retarded/advanced cluster Green's function $G_0^{R/A}(\omega, E_1)$ is $(L \times L)$ with L denoting the size of the chosen central cluster (e.g. $L = 2$ for the infinite TB chain).

Next, the two components of the self-energy Σ are considered, where the first term of its definition in Eq.(4.45) makes the start. The four-component bath Green's function $\boldsymbol{G}^B(\omega, E_1)$ contains the retarded, advanced and Keldysh components of the Green's functions of the first sites of every semi-infinite fermion bath chain within a particular central cluster. Fortunately, all bath chains are equivalent to each other, apart from a shift of the on-site energy $\omega \to \omega \pm \epsilon_i(E_1) = \omega + i \cdot E_i$ at site i,

depending on the particular value of the electrical field (note that this simple relation does not hold anymore in case of the GNR geometries). Therefore, the Green's function of a fermion bath chain has to be calculated only once. Basically, two different approaches for this Green's function $G^B(\omega)$ of one single reservoir chain appear in the present work:

$$G_B^R(\omega) = \frac{\omega}{2t_B^2} \pm \frac{1}{t_B}\sqrt{\left(\frac{\omega}{2t_B}\right)^2 - 1} \qquad \text{semi-infinite TB chain} \tag{4.48}$$

$$G_B^R(\omega) = i\Gamma \qquad \text{wide-band limit.} \tag{4.49}$$

For every result presented in the following sections, the chosen approach will be indicated. In case of semi-infinite TB reservoir chains t_B denotes the nearest-neighbour hopping integral inside the bath chain, while Γ, occurring in the wide-band limit approach, is called the *damping parameter*.
The advanced Green's function $G_B^A(\omega)$ of one single reservoir chain is then given by the hermitian conjugate of the retarded component, while the Keldysh component $G_B^K(\omega)$ is calculated according to Eq.(4.23). One should remember in this context, that the Keldysh components of the bath Green's functions are the only quantities in which the chemical potential μ enters. In this work, the particular value of μ was chosen in a way to describe the 2d Hubbard model at half filling.
Since all the individual bath chains are decoupled by construction, the resulting matrix of the retarded/advanced/Keldysh component of the whole bath Green's function for a particular central cluster is a diagonal ($L \times L$) matrix, with the respective (energy-shifted) retarded/ advanced/Keldysh Green's function $G_B^{R/A/K}(\omega, E_1)$ of one single reservoir chain one every place along the diagonal:

$$\boldsymbol{G}^B(\omega) = \begin{pmatrix} \begin{pmatrix} G_B^R(\omega-\epsilon_1(E_1)) & 0 & \dots \\ 0 & G_B^R(\omega-\epsilon_2(E_1)) & \dots \\ \vdots & & \ddots \end{pmatrix} & \begin{pmatrix} G_B^K(\omega-\epsilon_1(E_1)) & 0 & \dots \\ 0 & G_B^K(\omega-\epsilon_2(E_1)) & \dots \\ \vdots & 0 & \ddots \end{pmatrix} \\ \begin{pmatrix} G_B^A(\omega-\epsilon_1(E_1)) & 0 & \dots \\ 0 & G_B^A(\omega-\epsilon_2(E_1)) & \dots \\ \vdots & 0 & \ddots \end{pmatrix} & \begin{pmatrix} 0 & 0 & \dots \\ 0 & 0 & \dots \\ \vdots & 0 & \ddots \end{pmatrix} \end{pmatrix}. \tag{4.50}$$

The proper energy-shift at site i is given by $\epsilon_i(E_1)$ in this expression. Due to the particular diagonal form of the bath Green's function $\boldsymbol{G}^B(\omega)$, the coupling matrices $\boldsymbol{V}_{12} = \boldsymbol{V}_{21} = \boldsymbol{V}$ are identical and also diagonal, where every matrix element along the diagonal is given by the hopping integral v. For the practical implementation of the non-equilibrium calculation scheme the coupling constant was set to a value $v = 1$ throughout the entire work.

As already mentioned before, the construction of the left or right semi-infinite chain/ribbon using Eq.(4.44) requires an iterative method. The used approach is simple but powerful: By coupling the Green's function of an additional central cluster to the Green's function of an existing semi-infinite chain/ribbon, one should end up with the Green's function of a semi-infinite chain/ribbon again. Considering the geometry splitting of the applied model for the TB chain in Fig. 4.4 this approach is realized by taking the left/right semi-infinite chain *shifted by an energy* $\omega_{shift} = 2E_1$, coupling it to a central cluster again, and demanding that the resulting Green's function should be equal to that of the *unshifted* left/right semi-infinite chain (the respective energy shift ω_{shift} for the GNRs is provided

in Sec. 4.4). Mathematically, this can be formulated as

$$\left[\boldsymbol{G}^{L/R}(\omega, E_1)\right]^{-1} = \left[\boldsymbol{G}^{0}(\omega, E_1)\right]^{-1} - \boldsymbol{V}_{12}\boldsymbol{G}^{B}(\omega, E_1)\,\boldsymbol{V}_{21} + \boldsymbol{T}_{12}^{L/R}\boldsymbol{G}^{L/R}(\omega \mp \omega_{shift}, E_1)\,\boldsymbol{T}_{21}^{L/R} \quad (4.51)$$

where the crucial energy shift ω_{shift} is indicated in red. The above equation can be iterated straight forwardly, beginning from any starting value, and converges to the correct Green's function $\boldsymbol{G}^{L/R}$ of the left/right semi-infinite chain.

In order to achieve the desired infinite structure, the constructed left and right semi-infinite chains/ribbons have to coupled to another central cluster in a final step. Eq.(4.44) is used for this coupling, where the second term of Eq.(4.45) has to be added twice, because both the left *and* right semi-infinite chain/ribbon have to be coupled to the central cluster. The mathematical formulation of the final coupling is given by

$$\begin{aligned}[\boldsymbol{G}(\omega, E_1)]^{-1} \;=\; & \left[\boldsymbol{G}^{0}(\omega, E_1)\right]^{-1} - \boldsymbol{V}_{12}\boldsymbol{G}^{B}(\omega, E_1)\,\boldsymbol{V}_{21} - \boldsymbol{T}_{12}^{L}\boldsymbol{G}^{L}(\omega + \omega_{shift}, E_1)\,\boldsymbol{T}_{21}^{L} - \\ & - \boldsymbol{T}_{12}^{R}\boldsymbol{G}^{R}(\omega - \omega_{shift}, E_1)\,\boldsymbol{T}_{21}^{R}\end{aligned} \quad (4.52)$$

which can be calculated straight forwardly since all required variables are known at this point. Again, in the case of the GNR geometries, only the energy shift ω_{shift} and the coupling matrices $\boldsymbol{V}_{12}$, $\boldsymbol{V}_{21}$, $\boldsymbol{T}_{12}^{L/R}$ and $\boldsymbol{T}_{21}^{L/R}$, have to be adapted to the GNR geometries.

It has to be mentioned here that the iterative method for the determination of the Green's functions of the semi-infinite chains/ribbons can be dramatically speeded up, by splitting the whole iteration scheme into two part iterations; one for the retarded and one for the Keldysh component of the four-component Green's function in Keldysh space, respectively. This is possible due to the analytical form of the inverse four-component Green's function in Keldysh space, which is given by

$$[\boldsymbol{G}(\omega)]^{-1} = \begin{pmatrix} \boldsymbol{G}^{R}(\omega) & \boldsymbol{G}^{K}(\omega) \\ \boldsymbol{0} & \boldsymbol{G}^{A}(\omega) \end{pmatrix}^{-1} = \begin{pmatrix} \left[\boldsymbol{G}^{R}(\omega)\right]^{-1} & \left[\boldsymbol{G}^{R}(\omega)\right]^{-1}\boldsymbol{G}^{K}(\omega)\left[\boldsymbol{G}^{A}(\omega)\right]^{-1} \\ \boldsymbol{0} & \left[\boldsymbol{G}^{A}(\omega)\right]^{-1} \end{pmatrix}. \quad (4.53)$$

Before the results of the non-equilibrium investigations are presented in the next sections, it should be mentioned here that Dyson's equation, in a form similar to that of Eq.(4.44) and Eq.(4.45), is also used to calculate the current densities between the lattice geometry under investigation and the coupled fermion bath chains.

4.3 Electrical field driven current through an infinite tight-binding chain

After the presentation of the numerical methods required for the non-equilibrium calculations in Sec. 4.1 and the given introduction to electronic transport in infinite structure in Sec. 4.2, the results gained by an non-equilibrium investigation of an infinite TB chain are presented in this section. It should be noted here that all energy values (ω, E, E_1, U, etc.) are given in units of the nearest

neighbour hopping integral t, i.e $t = 1$ was used in the particular calculations, except for Sec. 4.3.2, where $t = 0.5$ was chosen.
It was already mentioned in the introductory paragraphs of the current chapter that the results gained for the electronic current transport in an infinite TB chain geometry should essentially support and allow for a comprehensive and physically correct interpretation of the obtained non-equilibrium characteristics of armchair and zig-zag GNRs. To cover both the semiconducting armchair and the metallic zig-zag edge orientation, the infinite TB chain, basically featuring a metallic behaviour, was additionally tuned to behave in a semiconducting way, by applying on-site energies with an alternating sign to the whole chain. Based on the knowledge gained from the equilibrium treatment of the infinitely extended graphene lattice in Sec. 3.2, a change of the physical behaviour of the infinite TB chain from metallic to semiconducting should also be observable when including electron-electron on-site interactions. Therefore, the interacting case $U \neq 0$ is considered and investigated as well, regarding its non-equilibrium properties. The results for the metallic infinite TB chain are presented in the following Sec. 4.3.1, while Sec. 4.3.2 provides the important results for the semiconducting TB chain.
In both the metallic and the semiconducting case, the steady-state electronic current density $j(E_1)$ was calculated as a function of the electrical field intensity E_1, for various sets of parameters. Furthermore, the introduced effective local distribution function $f_{loc}(\omega)$ was computed for different electrical field intensities.
Besides its task of serving as a support for interpreting the electron transport characteristics of GNRs, the results of the metallic and semiconducting infinite TB chain are interesting themselves. Although the considered lattice geometry seems to be rather unspectacular at first sight, it features some quite unexpected behaviours and provides a good amount of information on the applicability of the applied model, with a driving DC electrical field and a dissipation mechanism mimicked by artificial fermion bath chains, for infinite structures.
For the particular case of a metallic non-interacting infinite TB chain there are some reference solutions available [68] [78] [77], which are compared to the gained results in this section. It is worth noting here that the reference solutions were achieved by different approaches than the one chosen in the present work, namely, time-dependent perturbation theory with a temporal gauge [68] [78] and DMFT [77] in combination with the KNEGF technique in each case. However, an equivalence between the time-dependent theory and the scattering state formalism used in this thesis can be shown [68].

The coupling matrices required for the non-equilibrium calculations in case of the infinite TB chain (introduced in Sec. 4.2.3) are given by

$$\boldsymbol{T}^L_{12} = \begin{pmatrix} t & 0 \\ 0 & 0 \end{pmatrix} = \boldsymbol{T}^R_{21} \qquad \boldsymbol{T}^L_{21} = \left(\boldsymbol{T}^L_{12}\right)' = \boldsymbol{T}^R_{12} \tag{4.54}$$

indicating that the Green's function at the left/right site of the central cluster (corresponding to site number 1/2) is coupled to the first site of the left/right semi-infinite chain (corresponding to site 2/1). It has to be noted here that the matrices *are not* given in Keldysh-space, since the actual iteration was performed in two separate steps to save computation time (as already explained above).

4.3.1 Metallic tight-binding chains

The model used for the non-equilibrium investigation of a metallic infinite TB chain was already introduced in Sec. 4.2.3, where the particular geometry was shown in Fig. 4.4 and the general calculation scheme was explained. The results for the non-interacting case $U = 0$ are presented in the following, while the question, wether the physical behaviour changes from metallic to semiconducting by applying a non-zero on-site interaction U, is answered afterwards.

Non-interacting case

First of all the equilibrium DOS $\rho(\omega)|_{E_1=0}$ (calculated according to Eq.(3.76) for zero electrical field) is plotted in Fig. 4.5 in order to prove the metallic behaviour of the infinite TB chain in the non-interacting case. A wide-band limit approach was used for the retarded Green's functions of the bath chains $G_B^R(\omega)$ in Fig. 4.5a according to Eq.(4.48). The corresponding values for the damping Γ are indicated in the legend of the plot.
In Fig. 4.5b semi-infinite TB chains were used as bath chains, according to Eq.(4.49), with the respective hopping integral t_B inside the bath chains indicated in the legend of the plot as well. It should be remembered here that the coupling constant v describing the coupling between the bath chains and the infinite TB chain is taken as unity throughout the entire work.

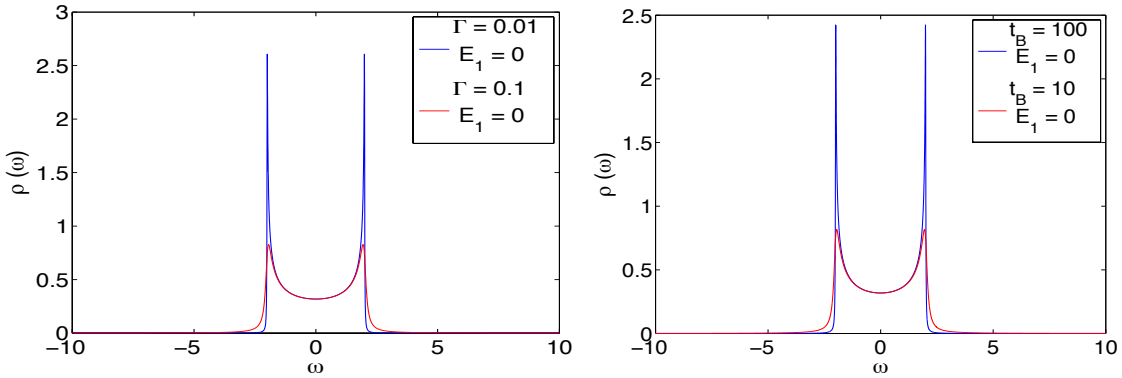

Figure 4.5: DOS $\rho(\omega)$ of the infinite TB chain with coupled bath chains. (a): bath chains described by a wide-band limit approach with different values for the damping parameter Γ, which are indicated in the respective legends. (b): bath chains described by semi-infinite TB chains with different values for the hopping integral inside the bath chains t_B, which are indicated again in the respective legends. The non-zero values at $\omega = 0$ and in its close vicinity proof the metallic behaviour in a significant way.

Due to the occurring non-zero DOS $\rho(\omega)$ at the point of origin $\omega = 0$ and in its close vicinity in both Fig. 4.5a and Fig. 4.5b, the metallic behaviour of the non-interacting infinite TB chain with coupled fermion bath chains is demonstrated in a significant way.
Comparing the particular plots of Fig. 4.5a, where the wide-band limit approach for the retarded component of the bath Green's function was chosen, a considerable broadening for the larger value

of the damping $\Gamma = 0.1$ can be manifested in comparison to the smaller value $\Gamma = 0.01$. *Broadening* in this context means that the peaks of the spectral function $A(\omega, \boldsymbol{k})$ (see Sec. 3.1.2 for a detailed explanation) are broadened, which smoothes the peaks in the corresponding DOS out in further consequence.
The same broadening is also observable in Fig. 4.5b, where semi-infinite TB chains were taken as bath chains. Here the *smaller* value of the hopping t_B inside the bath chain leads to a larger broadening, i.e. smoother peaks, in the plot of the DOS, which can be explained by the following relationship

$$\max_{\omega} \Im\left\{G_B^R(\omega)\right\} = \begin{cases} \frac{v^2}{t_B}, & \text{semi-infinite TB chain} \\ \Gamma, & \text{wide-band limit} \end{cases} \quad \Rightarrow \quad \Gamma = \frac{v^2}{t_B}. \tag{4.55}$$

Eq.(4.55) also states that a wide-band limit approach for the bath Green's function with a damping value of $\Gamma = 0.1$ (0.01) should cause a similar broadening effect as an approach where semi-infinite TB bath chains with a hopping paramter $t_B = 10$ (100) are coupled to the system. This predicted agreement is exactly what can be observed by comparing these two cases, indicated in red (blue), in Fig. 4.5a and Fig. 4.5b.

As the metallic behaviour is proved now, the results for the steady-state electric current density $j(E_1)$ along the infinite TB chain as a function of the electrical field intensity E_1 are presented next for different approaches and parameters of the fermion bath chains. The particular current densities were calculated between the two sites of the central cluster (see Fig. 4.4) according to Eq.(4.31). Since the lattice spacing is 1 in the units of this work, E_1 also denotes the potential drop between these two sites, as already explained when introducing the applied model for the non-equilibrium calculations in Sec. 4.2.3.
Fig. 4.6a shows the steady-state current density $j(E_1)$ along the infinite TB chain for the wide-band limit approach of the bath Green's functions. The respective damping parameters Γ are indicated again in the legend of the plots.
The steady-state current density $j(E_1)$ between the two sites of the central cluster with coupled semi-infinite TB bath chains, is plotted in Fig. 4.6b in comparison. The particular hopping parameters t_B inside the chain were chosen suitable to end up with the same values for the damping Γ, according to Eq.(4.55), as in Fig. 4.6a.
In the strong-coupling limit $t >> E_1, t >> \Gamma$ an approximative analytical expression for the current density within the infinite TB chain can be found by time-dependent perturbation theory [78]:

$$j_{approx}(E_1) \approx \frac{4t\,\Gamma E_1}{\pi\left(E_1^2 + 4\Gamma^2\right)} \tag{4.56}$$

which is plotted in Fig. 4.6 as dashed line in addition to the results of the numerical non-equilibrium calculations (solid lines) for all different approaches and parameters.

Comparing the gained results in Fig. 4.6a and Fig. 4.6b the first important observation states that the current densities $j(E_1)$ in the non-interacting infinite TB chain feature exactly the same progression, independently of the chosen approach for the bath chains Green's function. Therefore, the following

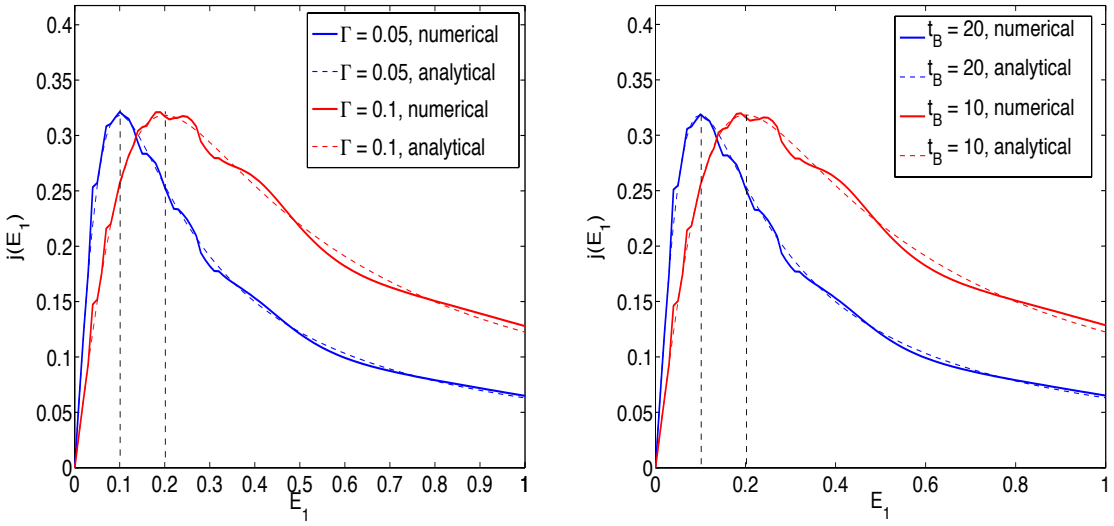

(a) (b)

Figure 4.6: Steady-state current density $j(E_1)$ along an infinite TB chain coupled to bath chains as a function of the electrical field intensity E_1. (a): bath chains described by a wide-band limit approach with different values for the damping parameter Γ, which are indicated in the respective legends. (b): bath chains described by semi-infinite TB chains with different values for the hopping integral inside the bath chains t_B, which are chosen suitable to result in the same values for the damping Γ as in (a), and are indicated again in the respective legends. In addition the strong-coupling approximations for the current density, given by Eq.(4.56), are shown as coloured dashed lines in (a) and (b), while the field intensities corresponding to a maximum current density are marked with black dashed lines.

interpretation is valid for both approaches. Since the realization of fermion reservoir chains by semi-infinite TB chains seems to be closer to reality than the corresponding wide-band limit approach, the former approach will be used in the remainder of the present work.

Interpreting the current density progressions for the two different damping values $\Gamma = 0.05$ and $\Gamma = 0.1$ in Fig. 4.6, the field intensity E_1, where the maximum current density occurs, is approximately given by

$$E_1\big|_{j(E_1)=j_{max}} \approx 2\,\Gamma \tag{4.57}$$

which is in perfect agreement with the field intensity at the maximum current density of the approximative analytic expression, obtainable by differentiating Eq.(4.56) with respect to the electrical field E_1. Eq.(4.57) points out the important role of the fermion bath chains to allow for a non-zero current again. Without bath chains the damping parameter Γ would be zero, resulting in

$$\lim_{\Gamma\to 0} E_1\big|_{j(E_1)=j_{max}} \approx 0 \tag{4.58}$$

which is equivalent to

$$\lim_{\Gamma\to 0} j \approx 0 \tag{4.59}$$

since the occurrence of a non-zero current density is coupled to a non-zero electrical field E_1.

Eq.(4.59) implies again the occurrence of BOs in infinite structures without a proper dissipation mechanism considered.
Continuing with the comparison of the numerically obtained current densities and the approximative analytic solutions in Eq.(4.56), a remarkable agreement between both solutions for all values of E_1 and a chain-hopping parameter $t = 1$ is found, although the analytical approximation is rigorously valid only in the strong-coupling limit $t >> E_1, \Gamma$.
Due to this fact, the maximum value for the steady-state current density $j(E_1)$ can be approximated by the maximum value of the approximative analytical solution, obtainable by substituting $E_1 = 2\Gamma$ in Eq.(4.56):

$$j_{max} \approx j(E_1 = 2\,\Gamma) \approx \frac{t}{\pi} \tag{4.60}$$

which pronounces the striking feature of an absolute maximum current density j_{max} independent of the damping Γ at $E_1 = 2\Gamma$.
Furthermore, the particular progression of the $j(E_1)$ curve can be explained as follows: For weak electrical fields, i.e. the first part of the $j(E_1)$ curves in Fig. 4.6, a linear relationship $j(E_1) \propto E_1$ is found, corresponding to Ohm's Law. This initial linear region would also be obtainable by means of linear response theory [80]. The occurrence of a maximum value for the current density in combination with a subsequent negative differential conductivity, i.e. a decreasing curve progression, can be explained due to the increasing relevance of BOs at larger electrical field intensities:
While the energy *gain* of an electron hopping from one site of the chain to a neighbouring one is proportional to the electrical field intensity E_1, the corresponding energy *dissipation* is given in terms of the damping Γ. For $E_1 >> \Gamma$ the dissipation mechanism is simply too weak to dissipate enough energy and consequently prevent the occurrence of BOs, which results in a continuously decreasing current density for $E_1 >> \Gamma$.

The dependence of the steady-state current density j within the TB chain on both the electrical field intensity E_1 and the damping Γ induced by the coupling of fermion bath chains is shown in Fig. 4.7, where the current density is plotted for the whole parameter space (E_1, Γ). The contour plot again proves the relationship found for the electrical field of the maximum occurring current density j_{max} in Eq.(4.60) in a very demonstrative way. Moreover, it clearly shows that the same values of the current density j are obtained for any damping Γ, where only the scaling on the E_1-axis changes. The next interesting feature in Fig. 4.7 arises when comparing the explicit current density dependencies on Γ for a fixed value of E_1 and on E_1 for a fixed value of Γ. It can be observed that both the $j\,(\Gamma)|_{E_1}$ - and the $j\,(E_1)|_{\Gamma}$ - curve exhibit a similar form, where again the same values for the steady-state current density are found and only the scaling of the particular axis varies.

The presented results found for the steady-state electronic current density j by means of many-body non-equilibrium calculations are in good agreement with reference values found by time-dependent perturbation theory with a temporal gauge [78]. After the treatment of the current density, the effective local distribution function $f_{loc}(\omega)$ is under investigation in the following for different values of the electrical field intensity E_1 and the damping parameter Γ. It should be noted first that the local distribution function was calculated for the right site in the central cluster of the infinite TB chain (see Fig. 4.4 for the particular geometry).

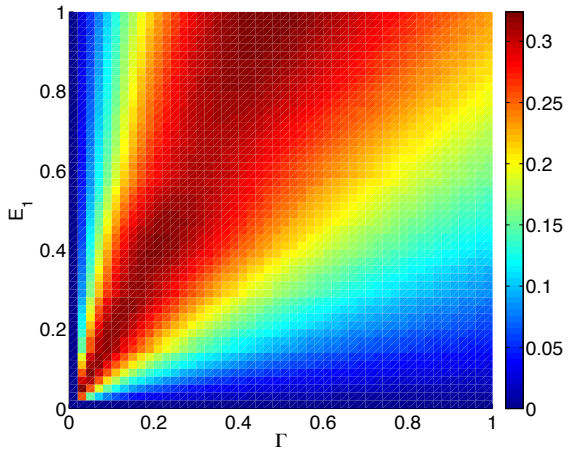

Figure 4.7: Contour plot of the steady-state current density $j(E_1, \Gamma)$ along the infinite TB chain for the whole parameter space (E_1, Γ).

The results for the effective local distribution function $f_{loc}(\omega)$ were gained by applying Eq.(4.32) to the four-component Green's function in Keldysh space found for the infinite TB chain coupled to fermion bath chains by means of the iterative method introduced in Sec. 4.2.3.
In the equilibrium situation (corresponds to $E_1 = 0$ in the non-equilibrium framework) the local distribution function $f_{loc}(\omega)$ is expected to be given by the Fermi-Dirac distribution, according to Eq.(4.23), which is proved in Fig. 4.8c (blue line).
Turning to the non-equilibrium situation now, Fig. 4.8a shows the numerical results of the local distribution function $f_{loc}(\omega)$ for a weak electrical field E_1 and different values of the damping Γ. In the strong-coupling limit $t >> E_1, t >> \Gamma$ (which is satisfied for all sets of parameters in Fig. 4.8a) the local distribution function features a superposition of small steps and oscillations, which are occurring due to the superposition of the Fermi-Dirac distributions $f_F\left(\omega \pm \frac{2n+1}{2}E_1\right)$ of the coupled bath chains Keldysh Green's functions at every site n of the infinite TB chain (see Eq.(4.23) also). A detailed investigation of the obtained step-like behaviour shows that the energy spacing between the occurring steps is approximately $\Delta_{steps} \approx 0.05$, which corresponds exactly to the induced potential drop between two neighbouring sites $E_1 = 0.05$. Moreover, this important relationship holds for *all* sets of parameters applied for the three plots in Fig. 4.8, (which can be seen in the most obvious way in Fig. 4.8b).

As E_1 and Γ are increased to values on the order of the hopping integral t (i.e. O(1) in this chapter) the correspondence of the energy width of the occurring steps in $f_{loc}(\omega)$ to the potential difference between neighbouring sites E_1 becomes more and more evident. Analyzing the local distribution functions $f_{loc}(\omega)$ plotted in Fig. 4.8b (blue and red line), this conclusion is achievable. In this picture, the saturation of the steady-state current density $j(E_1)$ to a value of zero for very large electrical field intensities E_1 becomes reasonable, since the width of the steps in the local distribution function is larger than the bandwidth of the system $\Delta_{BW} \approx 4t$.
One can clearly see that the origin of the local distribution functions in Fig. 4.8b is shifted by $\omega_{shift} = -0.5 = -\frac{E_1}{2}$ on the frequency axis. Remembering that the presented $f_{loc}(\omega)$-curves were calculated for the right central cluster site of the infinite TB chain, this shift becomes apparent, since the on-site

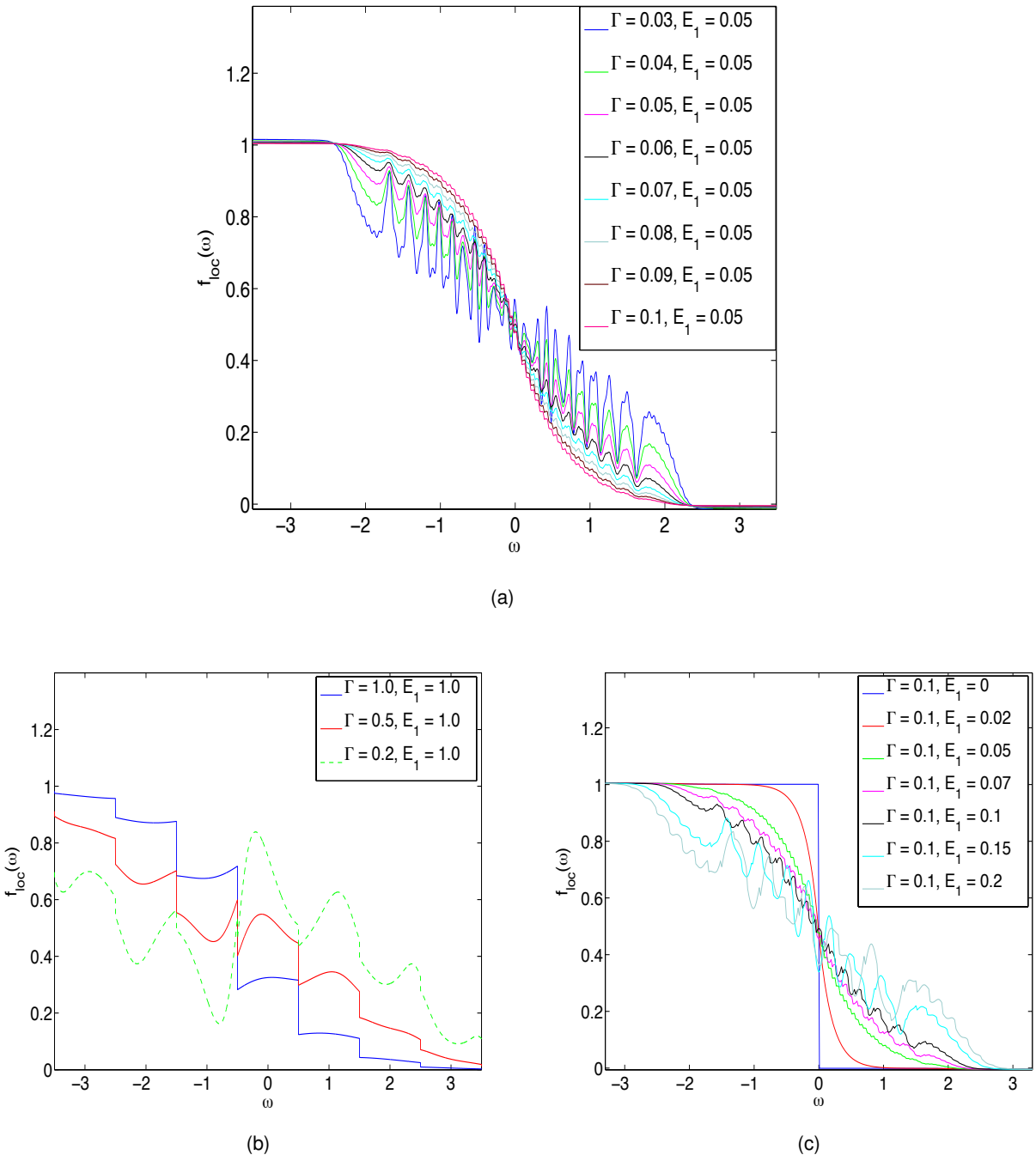

Figure 4.8: Effective local distribution function $f_{loc}(\omega)$ of the right central cluster site (see Fig. 4.4 for the particular geometry) of the electrical field driven infinite TB chain for various sets of parameters (E_1, Γ). (a): $f_{loc}(\omega)$ for a weak electrical field $E_1 = 0.05$ and different parameters of the damping Γ. (b): $f_{loc}(\omega)$ for a strong electrical field $E_1 = 1.0$ and several parameters of the damping Γ. (b): $f_{loc}(\omega)$ for a comparable large damping $\Gamma = 0.1$ and weak electrical fields E_1 between neighbouring site, where also the equilibrium case $E_1 = 0$ is plotted, which features the well-known form of the Fermi-Dirac distribution.

energy at this particular site is given by $\epsilon = \frac{E_1}{2}$. Further on, an interesting behaviour is observable in the $\Gamma = 0.2$ case for the comparatively strong electrical field $E_1 = 1.0$ (green dashed line in Fig. 4.8b), where a population inversion in $f_{loc}(\omega)$ occurs. Similar population inversions are observable for very small values of the parameters (E_1, Γ) in Fig. 4.8a, though on a much smaller scale.
Finally, Fig. 4.8c shows the change of the functional form of $f_{loc}(\omega)$ with increasing electrical field intensity for a constant value of the damping parameter $\Gamma = 0.1$. Starting from the equilibrium situation ($E = 0$), where the Fermi-Dirac distribution $f_F(\omega)$ is regained, more and more electrons located just below the Fermi level $\omega_F = 0$ get excited to states right above ω_F as the electrical field gets increased. Additionally, the steps and oscillations in the local distribution function are amplified, with the energy spacing increasing corresponding to the relationship $\Delta_{steps} \approx \frac{E_1}{2}$ found above.
In the context of analyzing this local distribution functions $f_{loc}(\omega)$ one could put the question, why there appears no significance in the functional forms of $f_{loc}(\omega)$ for the paticular case $E_1 = 2\Gamma$, which was found as the condition to be met for the maximum current density j_{max}. Remembering the interpretations given above for the particular form of the $j(E_1)$-curve, the occurrence of a maximum in the current density curves was argued due to the increasing relevance of BOs at larger electrical fields. Therefore, the rise of a maximum condition for the applied electrical field is explainable rather in terms of the ratio of gained to dissipated energy, than in terms of the particular number of electrons above the Fermi level ω_F (which is determined by the local distribution function $f_{loc}(\omega)|_{E_1=2\Gamma}$),

The presented results for the local distribution function $f_{loc}(\omega)$ are in good agreement with results reported for time-dependent perturbation theory calculations [68] and DMFT [77]. After this comprehensive investigation of the non-interacting case, the effects of non-zero repulsive on-site interactions $U \neq 0$ on the steady-state current densities are presented in the next paragraph.

Interacting case

As already mentioned in the introduction of the present chapter, the non-equilibrium investigations on the infinite TB chain were performed to allow for a comprehensive and physically correct interpretation of the results gained for the electronic transport properties of GNR geometries, which are presented in Sec. 4.4. The different physical behaviours depending on the edge geometry, where zig-zag GNRs feature a metallic behaviour in contrast to the semiconducting (or semi-metallic) of armchair GNRs, were already discussed in Chapter 3. Since the non-interacting infinite TB chain features a metallic behaviour (proved in Fig. 4.5 in the former paragraph), an investigation of a non-troublesome semiconducting geometry with one infinite dimension has to be performed as well. For the metallic zig-zag GNR geometries (investigated regarding their equilibrium properties in Sec. 3.3) a change in the physical behaviour from metallic to semiconducting is observable when the repulsive Coulomb on-site interactions are increased above a critical value U_{crit}. Since a similar effect is also expected for an one-dimensional structure, the non-equilibrium treatment of the infinite TB chain is repeated for different values of the on-site interaction U. The gained results are presented in the following, where the focus is turned on the equilibrium DOS $\rho(\omega)$ at first to verify wether the structure behaves in a semiconducting way or not, for a particular value of U. The corresponding steady-state current densities $j(E_1)$ of the respective interacting infinite TB chains are presented and interpreted

subsequently in the next subsection.

Fig. 4.9 shows the DOS $\rho(\omega)$ for the infinite TB chain in the equilibrium situation ($E = 0$) for different parameters of the on-site interaction $U = \{0.0, 1.0, 2.0, 3.0, 4.0, 5.0\}$. The chosen value for the damping is given by $\Gamma = 0.1$. The opening of an energy gap Δ, which increases with increasing U, is clearly observable. The metallic behaviour is indeed changed to a semiconducting one, at least for on-site interactions $U > 3.0$. Therefore, the steady-state current density $j(E_1)$ within the infinite TB chain for non-zero on-site interactions $U \neq 0$ is part of the investigations in the following subsection about semiconducting TB chains.

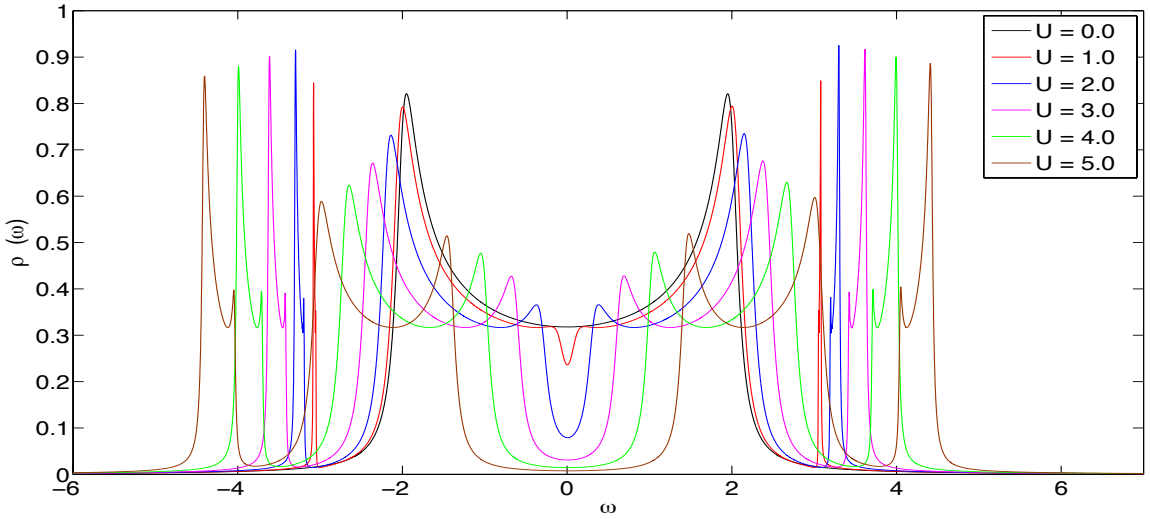

(a)

Figure 4.9: DOS $\rho(\omega)$ of the infinite TB chain with coupled bath chains for different on-site interactions $U = \{0.0, 1.0, 2.0, 3.0, 4.0, 5.0\}$. The particular interaction strengths (values of U) are labeled in the legend. The damping parameter is given by $\Gamma = 0.1$.

In course of the non-equilibrium investigations of the GNR geometries in Sec. 4.4 an upper limit for the damping Γ, induced by the coupled bath chains, appears, since it causes a respective level broadening. Due to this broadening, the fine structure of the GNRs' energy momentum dispersion relation $\omega(\boldsymbol{k})$ and DOS $\rho(\omega)$ is badly smeared out for large dampings Γ, which prevents a proper description of the detailed physical behaviour of those structures. To check if the obtained DOS of the infinite TB chain in Fig. 4.9 is representing all fine-structured details, it was calculated again for a smaller value of the damping $\Gamma = 0.01$ and is plotted in Fig. 4.10. Comparing this plot to the DOS-plot for the larger damping $\Gamma = 0.1$ in Fig. 4.9, it is observable that the energy gap Δ is larger for every particular value of the on-site interaction U in this case. Furthermore, the occurring peaks are thinner and the peak-height is larger. Since the damping Γ is only a side effect of the *artificial* TB bath chains, which were coupled to the system for reasons of providing a proper dissipation mechanism, its effect on the physical non-equilibrium properties of the investigated system has to be minimized. In the present situation a damping of $\Gamma = 0.1$ is simply to large to resolve the fine-structure of the DOS of the interacting infinite TB chain. Therefore, the investigation of the steady-state current density $j(E_1)$ within the infinite TB chain for non-zero on-site interactions U in the following section is restricted to the smaller damping parameter $\Gamma = 0.01$. As mentioned above, a similar problem

emerges also in the non-equilibrium investigations of zig-zag and armchair GNRs in Sec. 4.4.

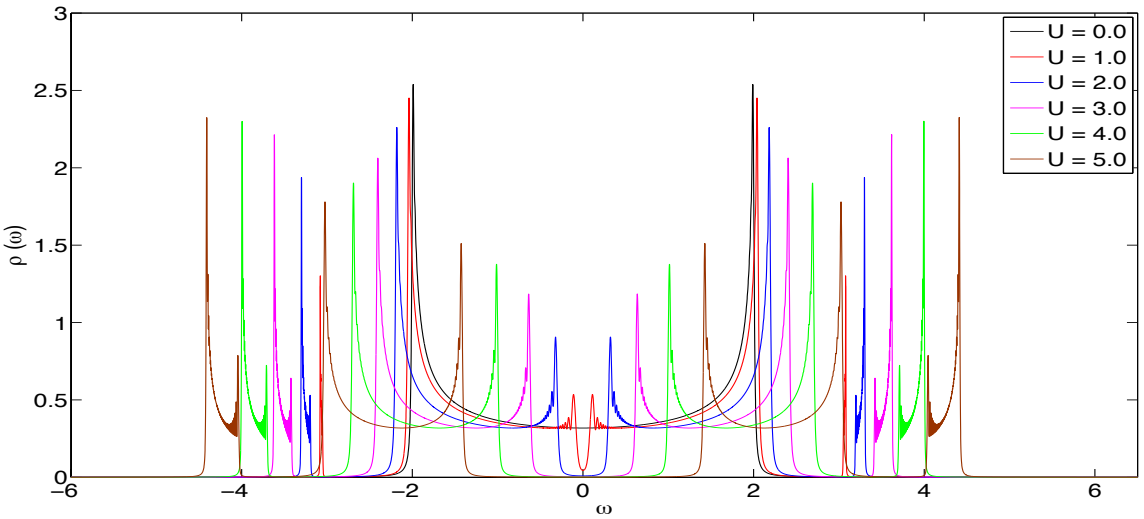

(a)

Figure 4.10: Same as Fig. 4.9, but for $\Gamma = 0.01$.

4.3.2 Semiconducting tight-binding chains

The physical behaviour of infinite TB chains is changed from metallic to semiconducting when non-zero on-site interactions U are applied, as shown in the previous subsection. A simpler approach to the realization of a semiconducting infinite TB chain using alternating on-site energies $\pm\epsilon$, is considered first, since it comes along with a tunable energy gap. Due to the fact that in both approaches the resulting current densities are determined by occurring tunneling resonances (Wannier-Stark resonances), a comprehensible explanation and interpretation is demanded. It is provided subsequently to the presentation of the particular current characteristics.

The equilibrium DOS $\rho(\omega)$ and the steady-state current density $j(E_1)$ for $U = \{1.0, 2.0\}$ are presented in Fig. 4.11 as representing examples for infinite TB chains featuring a semiconducting behaviour due to non-zero on-site interactions. The damping was set to $\Gamma = 0.01$ and the hopping integral between neighbouring sites of the infinite TB chain was set to $t = 0.5$ in this special case.

The oscillatory behaviour of the current densities observable in Fig. 4.11c and Fig. 4.11d appears puzzling at the first sight. In the classical picture zero current would have been expected in an one-dimensional semiconductor for electrical field induced electron energies smaller than the energy gap [81]. As the electron energy exceeds the energy gap one would expect a similar current-density progression as for the non-interacting $U = 0$ case (red dashed line in Fig. 4.11c), i.e. a continuously increasing current-density, with an appearing maximum and a subsequent decrease due to increasing BOs. Apparently, such a behaviour cannot be observed in Fig. 4.11c and Fig. 4.11d. The reason for the occurring oscillations in the current densities lies in the actual Wannier-Stark model used for the non-equilibrium investigations in this work, where a homogeneous electrical field is applied in order to force an electronic current to flow (see. Sec. 4.2.3). In consequence of this homogeneous

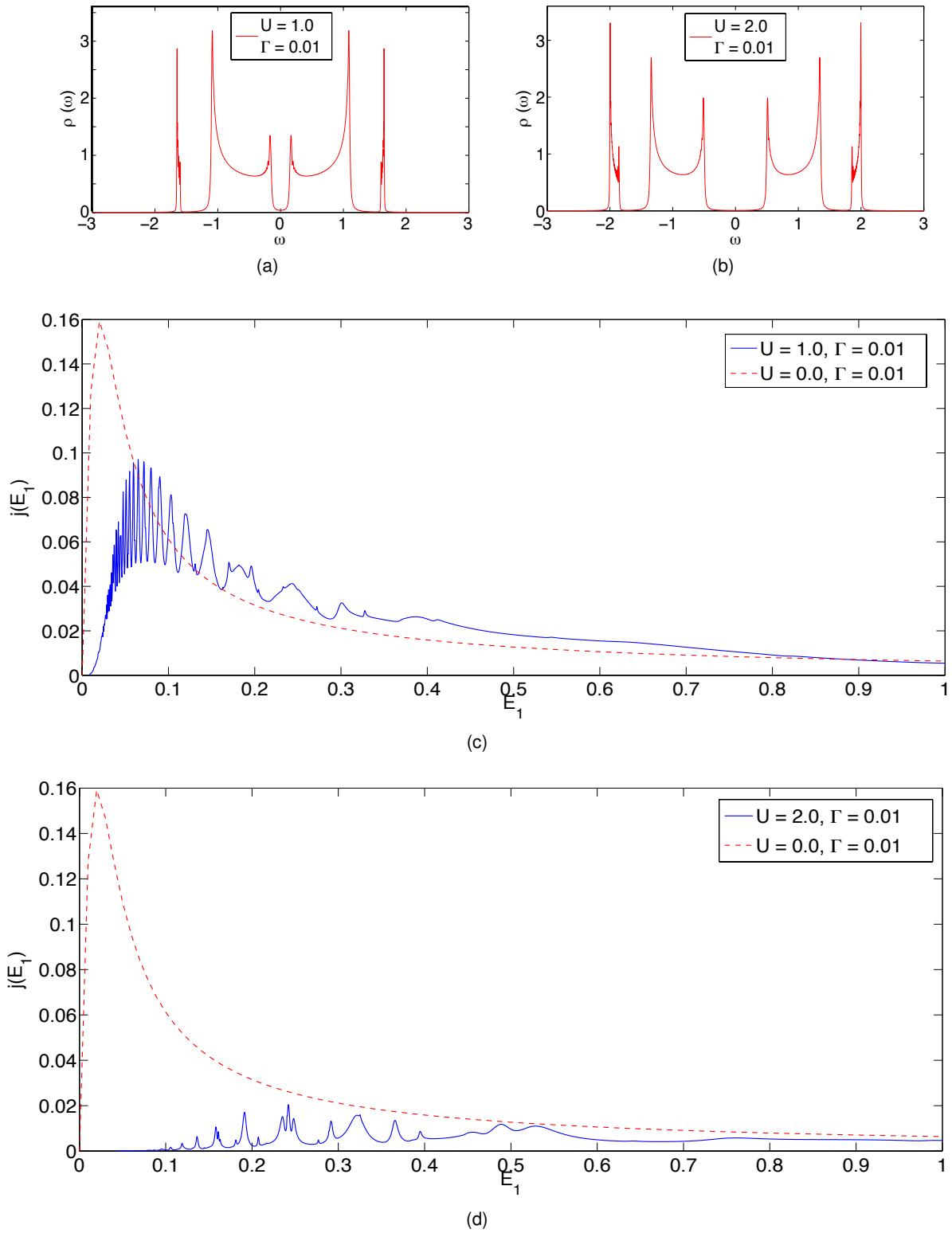

Figure 4.11: Equilibrium DOS $\rho(\omega)$ of the infinite TB chain with coupled bath chains for a small damping parameter $\Gamma = 0.01$ and on-site interactions $U = 1.0$ (a) and $U = 2.0$ (b). The corresponding steady-state electronic current densities $j(E_1)$ are presented in (c) and (d), where the non-interacting $U = 0$ reference solution is plotted in addition. The occurrence of Wannier-Stark resonances can be observed.

electrical field a step-like potential is established (see Fig. 4.15d), which in combination with the appearing energy gap in the interacting situation leads to *resonant tunneling processes* for particular values of the electrical field. The observable peaks in the current densities in Fig. 4.11c and Fig. 4.11d correspond exactly to those tunneling processes called *Wannier-Stark resonances*.
To make a theoretical description of the observed transport characteristics easier, a simplified non-interacting "version" of a semiconducting infinite TB chain is constructed in the following, where the appearing energy gap originates from alternating on-site energies $\pm\epsilon$ along the chain instead of applied on-site interactions U.

Construction of a non-interacting semiconducting TB chain

Considering a particle (electron) within a non-interacting one-dimensional TB chain with a suitable dissipation mechanism, a homogeneous electrical field will force the particle to move along the chain, resulting in a finite electrical current (see Sec. 4.3). The situation changes significantly when on-site energies ϵ with an alternating sign are applied to all sites along the chain. The difference $\Delta = \epsilon - (-\epsilon) = 2\epsilon$ in the on-site energies between two neighbouring sites of the chain corresponds to an arising energy barrier, which hinders the particle in its movement along the chain as long as its particular kinetic energy is smaller than the barrier. More precisely, alternating on-site energies $\pm\epsilon$ along the infinite TB chain cause an energy gap

$$\Delta = 2\epsilon \tag{4.61}$$

to appear in the chain's equilibrium dispersion relation. As a consequence, the physical behaviour of the TB chain is changed from metallic to semiconducting as requested. It should be noted that the energy gap appears symmetrically around $\omega = 0$ as long as the absolute values of the on-site energies are identical.
The equilibrium DOS $\rho(\omega)$ of the infinite TB chain, plotted in Fig. 4.12 for different values of the on-site energy ϵ, clearly exhibit the expected energy gap. The size of the particular energy gaps in Fig. 4.12 is indeed given by Eq.(4.61). Since the introduced model is used for the electronic transport calculations, the semi-infinite bath chains are still coupled to the physical system. Therefore, the energy levels are broadened again due to the damping Γ, which occurs in connection with the coupled bath chains. The same value $\Gamma = 0.01$ as in the interacting model (see Fig. 4.10 and above) was used again.

The plots for the DOS $\rho(\omega)$ of the non-interacting semiconducting TB chain show good agreement with those obtained for the interacting TB chain in Fig. 4.10. In the former ones, the energy gap Δ increases with increasing on-site *energy* ϵ, while in the latter ones, the value of the on-site *interaction* U determines the size of Δ.

Due to the shown equivalence of the equilibrium properties, the observed current densities $j(E_1)$ in Fig. 4.11 can be physically interpreted by means of the non-interacting approach for the semiconducting TB chain. Therefore, the steady-state current densities $j(E_1)$ for the non-interacting semiconducting model are presented in Fig. 4.13 and Fig. 4.14 for the same values of ϵ as in the

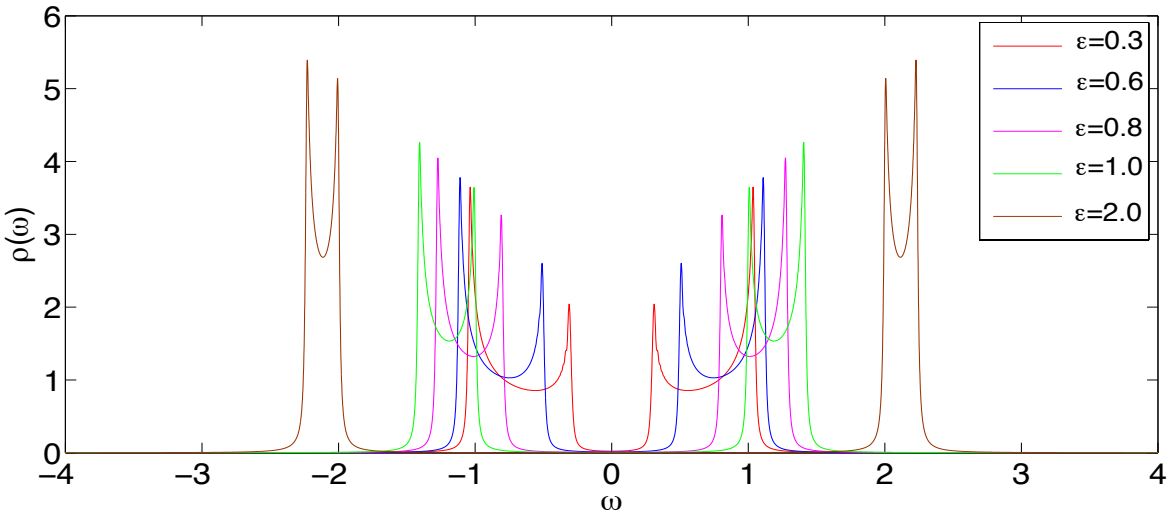

(a)

Figure 4.12: DOS $\rho(\omega)$ of the infinite TB chain with coupled bath chains and alternating on-site energies $\pm\epsilon$ along the chain, for different values of $\epsilon = \{0.0, 1.0, 2.0, 3.0, 4.0, 5.0\}$. The particular values are labeled in the legend. A value of $\Gamma = 0.01$ was used for the damping parameter.

corresponding DOS plots in Fig. 4.12. For the damping parameter and the hopping integral between neighbouring sites of the infinite TB chain, the same values as in Fig. 4.11 ($\Gamma = 0.01$; $t = 0.5$) were used.

The current densities in Fig. 4.13 and Fig. 4.14 again exhibit an oscillatory progression, similar to the current densities for the interacting TB chain in Fig. 4.11. The peaks of these oscillations correspond again to Wannier-Stark resonances that occur in the used Wannier-Stark model (see Sec. 4.2.3). Comparing the particular subplots of Fig. 4.13 and Fig. 4.14 with each other, it is striking that the number of occurring resonances decreases with increasing energy gap $\Delta = 2\epsilon$. The figures also indicate an increasing energy interval between the current peaks. It should be mentioned as well that for the smallest on-site energy value $\epsilon = 0.3$ and therefore for the smallest energy gap, the current density curve of the metallic TB chain is enveloping the actual current density of the semiconducting chain.

What follows is a comprehensible explanation of the apparent physical non-equilibrium properties of infinite one-dimensional semiconducting TB chains in terms of occurring Wannier-Stark resonances.

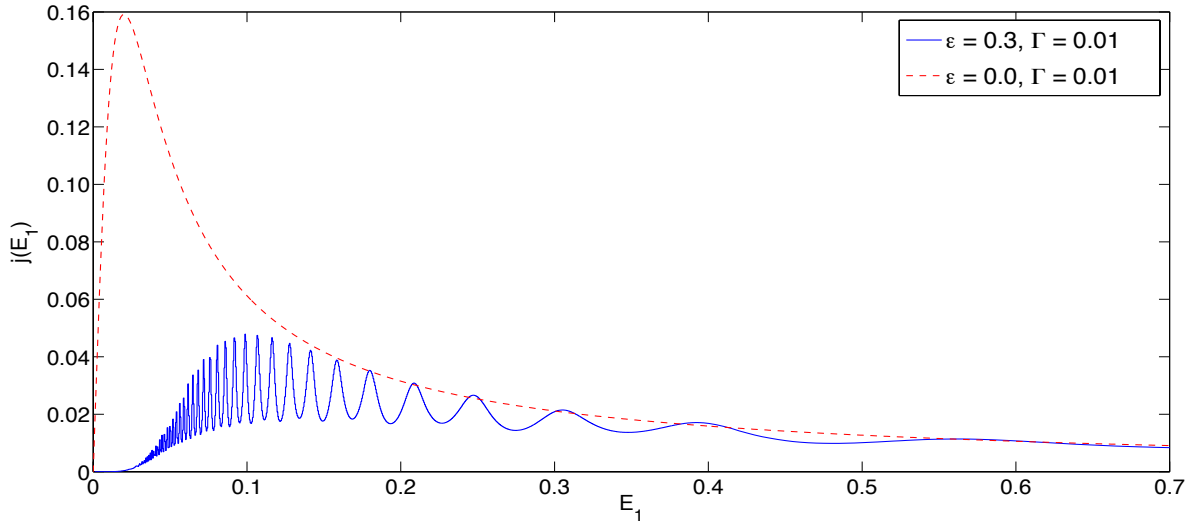

(a)

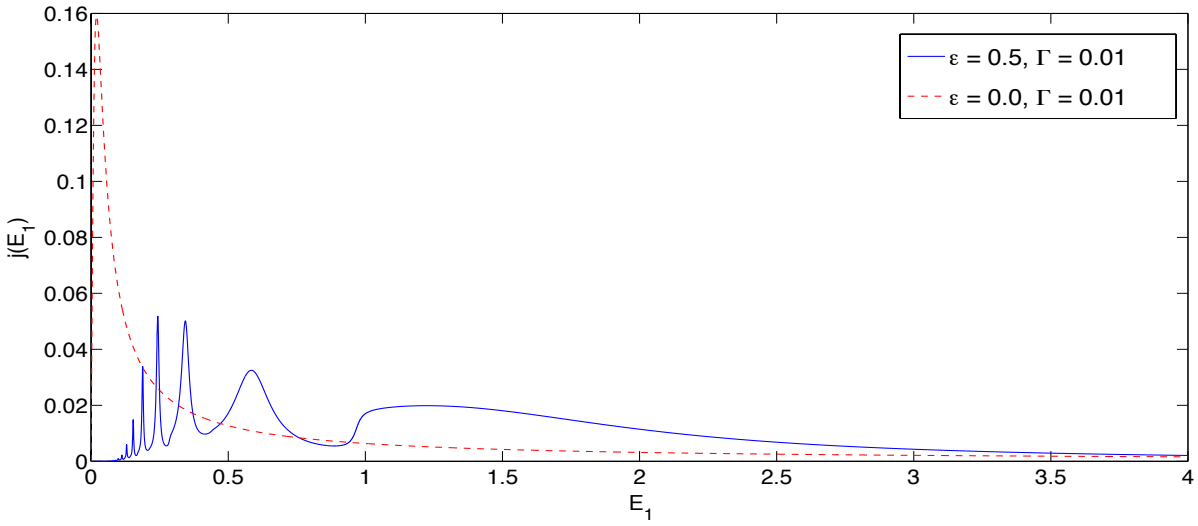

(b)

Figure 4.13: Steady-state current density $j(E_1)$ within the infinite TB chain coupled to fermion bath chains, with alternating on-site energies $\pm\epsilon$ applied along the chain, for different values of $\epsilon = \{0.3, 0.5\}$. The particular values of ϵ are indicated in the legends. Additionally, the current density of the metallic infinite TB chain, i.e. for zero on-site interaction $\epsilon = 0$, is plotted as a reference in both subplots. A value of $\Gamma = 0.01$ was chosen for the damping parameter. The occurrence of Wannier-Stark resonances can be observed again.

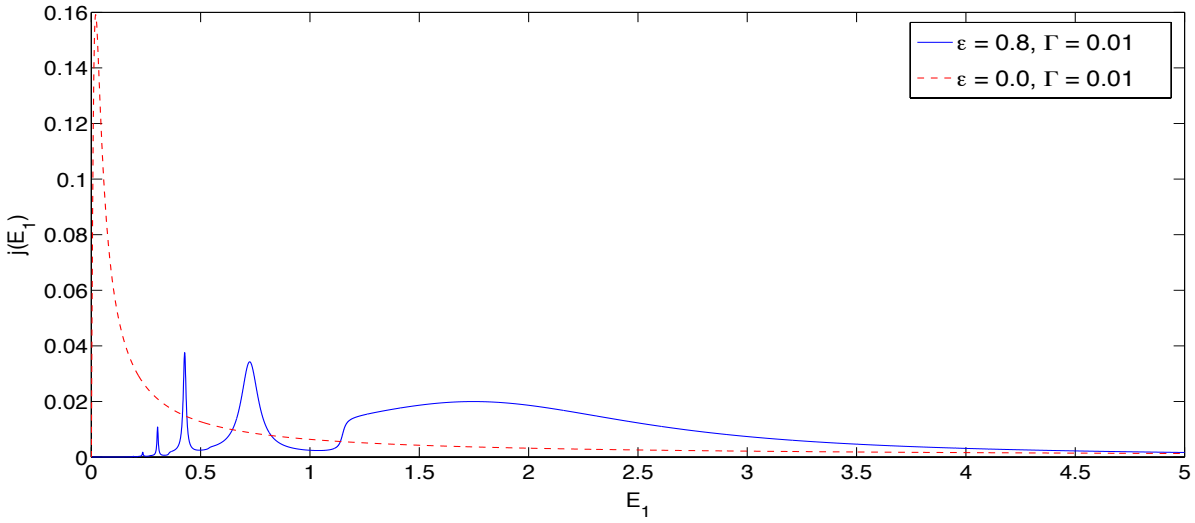

(a)

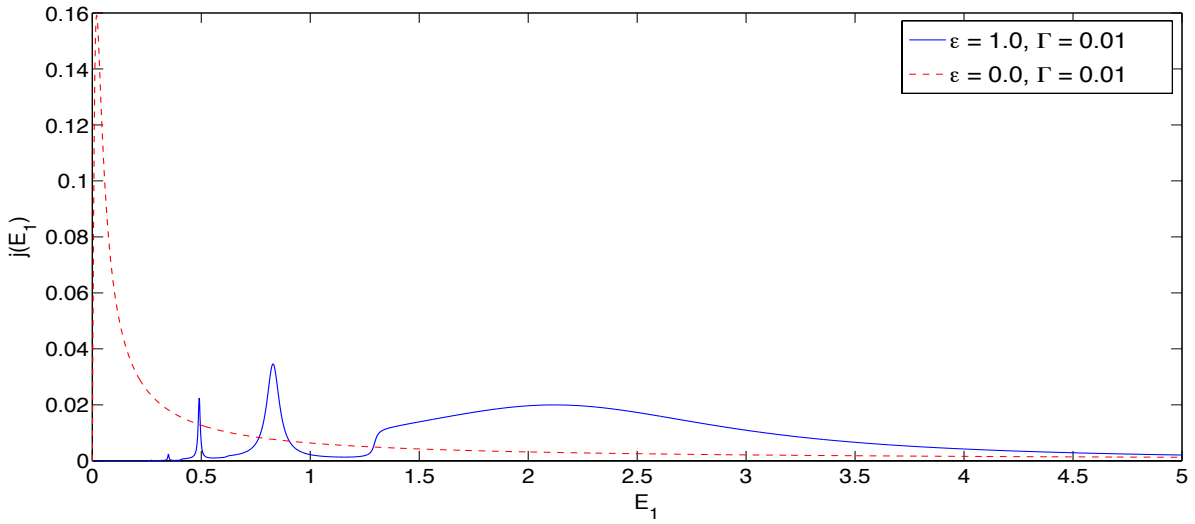

(b)

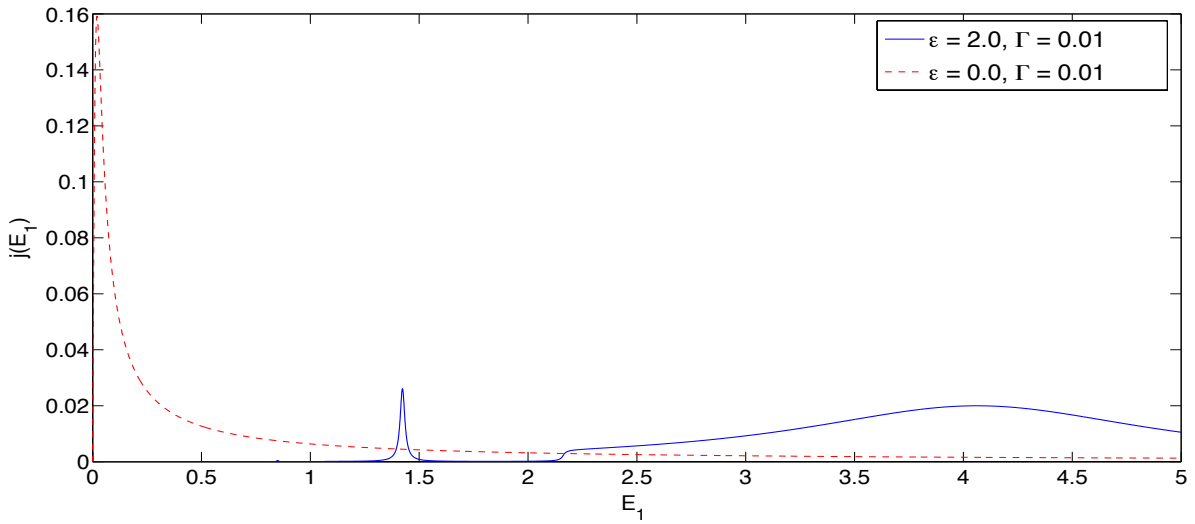

(c)

Figure 4.14: Same as Fig. 4.13, but for $\epsilon = \{0.8, 1.0, 2.0\}$

Wannier-Stark resonances in the one-dimensional semiconducting TB model

Until now the particular profile of the potential energy V, which arises due to the applied homogeneous electrical field, was not discussed since the results for the non-interacting metallic TB chain did not demand it. To provide a suitable physically motivated reasoning of the observed current densities in Fig. 4.13 and Fig. 4.14, the particular potential energy V_m at every site m of the infinite chain is plotted for the non-interacting semiconducting TB chain with alternating on-site energies in Fig. 4.15b and Fig. 4.15d. Additionally, Fig. 4.15 a and Fig. 4.15c show the potential curves for the interacting model of a semiconducting TB chain, to point out the difference between these two introduced models.

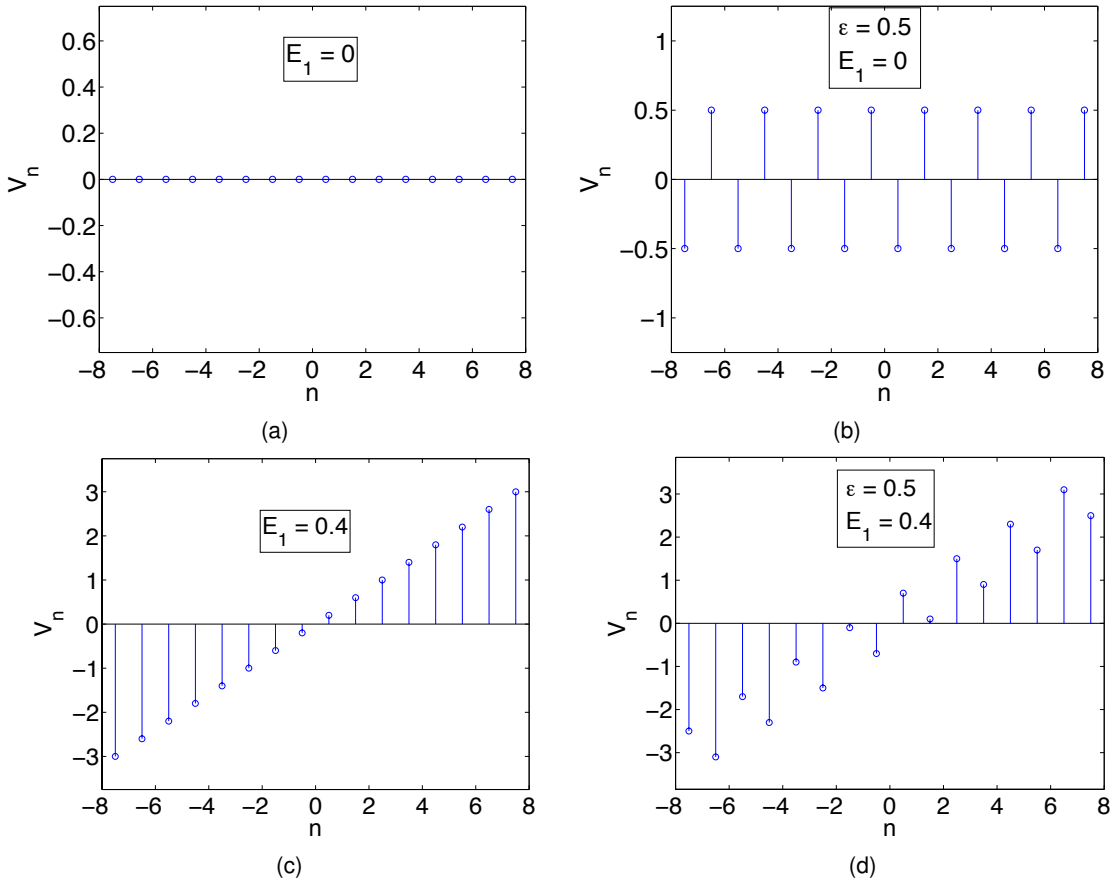

Figure 4.15: Potential energy profiles for the two different models of a semiconducting infinite TB chain. The potentials V_m at sites m are shown in particular for the interacting model ($U \neq 0$) in the equilibrium $E_1 = 0$ (a) and non-equilibrium $E_1 \neq 0$ (b) situation. Note that the actual effect of U on the potential energy has been neglected. For the non-interacting model with alternating on-site energies the potential profile is shown as well in case of equilibrium (c) and non-equilibrium (d).

The equilibrium situation ($E_1 = 0$) for the interacting model is shown in Fig. 4.15a. Due to the lack of any electrical field or on-site energies the potential energy is equal to zero at every site. Fig. 4.15c shows the non-equilibrium situation where a non-zero electrical field $E_1 \neq 0$ causes a linearly increasing potential energy according to $V_m = eE_1 m$, with the electron charge e (which is still taken as unity). Applying alternating on-site energies $\pm\epsilon$ at all sites m along the overall infinite chain

changes the potential energy V_m significantly, which is illustrated in Fig. 4.15c. One can clearly see the alternating on-site potential energies. For a non-zero electrical field $E_1 \neq 0$ the potential energy is modified in the same way as in case of the interacting model, i.e. a linear increase is superposed to the alternating potential energy profile. The resulting potential curve, plotted in Fig. 4.15d, is the starting point for a physically motivated reasoning of the observed current densities in Fig. 4.13 and Fig. 4.14.

As already mentioned, the Wannier-Stark model used in this Chapter enables resonant tunneling processes [55] [56] [57]. Three conditions need to be satisfied for the formation of an observable Wannier-Stark resonance:

1. The total potential drop across the semiconducting chain has to exceed the zero-field energy gap Δ. Obviously, in case of an infinite structure this condition is always met.

2. At least *two* sites of the infinite chain have to possess the same potential energy V_m. As a consequence of the applied model, an infinite number of pairs of sites with aligned potential energies occurs if the former condition is satisfied (illustrated in Fig. 4.16)

3. The spatial wavefunctions of the localized Wannier-Stark resonace states need to exhibit a finite overlap, since the tunneling probability is proportional to this overlap.

As the first condition is trivially fulfilled in an infinite structure with an homogeneous electrical field, only the remaining two are discussed here:
Fig. 4.15d shows the potential energies V_m at the central sites m of the TB chain for a particular set of parameters (ϵ, E_1). The second condition is definitely not satisfied in the depicted situation, since there appear no aligned potentials. The potential profile is plotted again in Fig. 4.16 for slightly different values of the potential drop E_1 between two particular neighbouring sites of the TB chain.

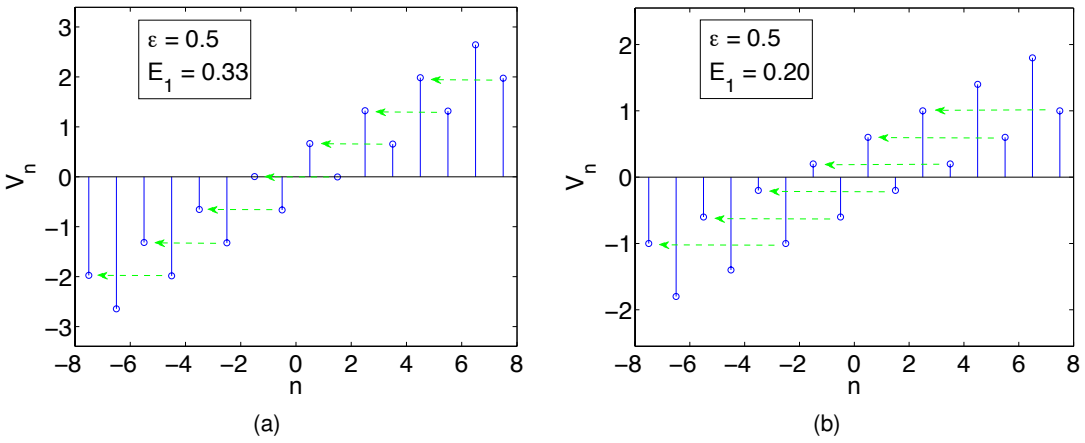

Figure 4.16: Potential energy profiles along the semiconducting TB chain in the case of resonace. (a): Wannier-Stark resonances induced by aligned potentials V_m at sites m and $m+3$. (b): Wannier-Stark resonances induced by aligned potentials V_m at sites m and $m+5$. The resonant tunneling processes are indicated by the green arrows, which form the resulting Wannier-Stark ladder of resonances.

One can clearly see that for these particular parameters the second resonance condition is fully met. Furthermore, Fig. 4.16 indicates that the alignment of the potential energies at two different sites in the chain consequently leads to a whole *ladder* of pairs of resonant states. Due to the name of the applied model this ladder is called *Wannier-Stark ladder of resonances*. As a consequence of the formation of resonant pairs within the chain, electrons can surmount the arising potential barriers by resonant tunneling processes (illustrated by the green arrows in Fig. 4.16).
Focusing on the ratio of the particular values for the on-site energy ϵ and the electrical field E_1 now, it can be observed that equal potential energies V_m appear at the states m and $m+3$ in Fig. 4.16a ($E_1 = 0.33$). In case of a slightly weaker electrical field $E_1 = 0.20$ in Fig. 4.16b, identical values for the potential energies occur at the states m and $m+5$. Due to the alternating on-site energies there appear no Wannier-Stark resonances for values of the electrical field $0.20 < E_1 < 0.33$, which is also observable by a conscientious comparison of the two subplots in Fig. 4.16. Therefore, the second resonance condition can be formulated in the following mathematical way:

$$\frac{\Delta}{E_1} \stackrel{!}{=} 2n+1, \quad n \in \mathbb{N}^+. \tag{4.62}$$

The third resonance condition demands a finite overlap of the wavefunctions of the respective resonant pairs of states. It is important in this context that the eigenstates of the Hamiltonian H^{WS} in the Wannier-Stark model become localized, whenever the first resonance condition is satisfied [55]. The corresponding spatial wavefunctions at the particular sites of the chain can be described by exponentially decreasing functions, according to

$$\psi(r) \propto exp\left(-\frac{|r|}{L}\right) \tag{4.63}$$

where r is the spatial coordinate in units of the lattice spacing and has its origin at the respective site m. The quantity L describes a coherence length, which determines the spatial extent of the wavefunction. Since the wavefunction describes a localized state it has to be normalized. The normalization constant Z is determined using

$$\frac{1}{Z}\int_{-\infty}^{\infty}\psi(r) = \frac{1}{Z}\int_{-\infty}^{\infty} exp\left(-\frac{|r|}{L}\right) \stackrel{!}{=} 1 \qquad \Rightarrow \qquad Z = 2L \tag{4.64}$$

According to Eq.(4.63) and Eq.(4.64), the overlap $O\left(\frac{\Delta}{E_1}\right)$ of two wavefunctions, which correspond to a pair of resonant states ψ_1 and ψ_2 centered at $r = 0$ and $r = \Delta r$, respectively, is given by

$$\begin{aligned} O\left(\frac{\Delta}{E_1}\right) &= \int_{-\infty}^{\frac{\Delta r}{2}} \psi_2(r-\Delta r)dr + \int_{\frac{\Delta r}{2}}^{\infty}\psi_1(r)dr \\ &= \int_{-\infty}^{\frac{2n+1}{2}} \psi_2(r-2n+1)dr + \int_{\frac{2n+1}{2}}^{\infty}\psi_1(r)dr \\ &= \int_{-\infty}^{\frac{\Delta}{2E_1}} \psi_2\left(r-\frac{\Delta}{E_1}\right)dr + \int_{\frac{\Delta}{2E_1}}^{\infty}\psi_1(r)dr \end{aligned} \tag{4.65}$$

$$
\begin{aligned}
&= \int_{-\infty}^{\frac{\Delta}{2E_1}} \frac{1}{Z} \cdot exp\left(-\frac{\left|r-\frac{\Delta}{E_1}\right|}{L}\right) dr + \int_{\frac{\Delta}{2E_1}}^{\infty} \frac{1}{Z} \cdot exp\left(-\frac{|r|}{L}\right) dr \\
&= \int_{-\infty}^{\frac{\Delta}{2E_1}} \frac{1}{Z} \cdot exp\left(\frac{r-\frac{\Delta}{E_1}}{L}\right) dr + \int_{\frac{\Delta}{2E_1}}^{\infty} \frac{1}{Z} \cdot exp\left(-\frac{r}{L}\right) dr \\
&= \frac{1}{Z}\left\{L \cdot exp\left(-\frac{\frac{\Delta}{E_1}}{L}\right) \cdot exp\left(\frac{\frac{\Delta}{2E_1}}{L}\right) dr + L \cdot exp\left(-\frac{\frac{\Delta}{2E_1}}{L}\right)\right\} dr \\
&= \frac{1}{Z} \cdot 2L \cdot exp\left(-\frac{\Delta}{E_1 \cdot 2L}\right) \\
&= exp\left(-\frac{\Delta}{E_1 \cdot 2L}\right).
\end{aligned}
$$

The definition of $O\left(\frac{\Delta}{E_1}\right)$ in the first line is based on the symmetry of the overlap area, with the symmetry axis located at $r = \frac{\Delta r}{2}$. Line two fulfills the second resonance condition given in Eq.(4.62), which is used afterwards to obtain line three. In the fourth line the wavefunctions $\psi(r)$ were replaced by Eq.(4.63). The absolute values $\left|r-\frac{\Delta}{E_1}\right|$ and $|r|$ were replaced in the fifth line, which is possible due to the particular integration limits. Subsequently, some trivial analysis was performed leading to the final result, which fulfills the essential condition

$$\lim_{\Delta \to 0} O\left(\frac{\Delta}{E_1}\right) = 1. \tag{4.66}$$

In the resonant tunneling regime the overlap of two wavefunctions belonging to a pair of resonant states determines the tunneling probability of an electron faced with an energy barrier [82], which leads to the resulting tunnel current density

$$j(E_1) \propto O\left(\frac{\Delta}{E_1}\right) = C \cdot exp\left(-\frac{\Delta}{E_1 \cdot 2L}\right) \tag{4.67}$$

with a proportionality constant C .

It should be clear now that signatures of Wannier-Stark resonances in the resulting current densities $j(E_1)$ only appear in case of a finite overlap of the wavefunctions of the resonant Wannier-Stark states.

With Eq.(4.62) and Eq.(4.67) at hand, the gained current densities $j(E_1)$ in Fig. 4.13 and Fig. 4.14 can be analyzed again, in terms of occurring resonant tunneling processes. In order to do so, the maxima of the current oscillations in the weak electrical field regime are fitted by Eq.(4.67) to verify that Wannier-Stark resonances appear solely in cases where the third resonance condition is fulfilled. It is important to note here that the derived formula for the tunnel current density is only valid in the weak electrical field regime, since it does not take into account any decrease or saturation due to an increasing relevance of BOs at larger fields. The second resonance condition is checked as well by comparing the positions (electrical fields) where the maxima appear with the theoretical values according to Eq.(4.62).

The regions of the current densities $j(E_1)$ where Wannier-Stark resonances appear are plotted again in the left subplots of Fig. 4.17 and Fig. 4.18, where the occurring current maxima in the weak electrical field regime are marked and fitted by Eq.(4.67). The fitting function describes the values of the current maxima almost perfect for all considered on-site energies, which indeed identifies the appearing maxima as Wannier-Stark resonances. Furthermore, the obtained values for the coherence length L (which are given in the particular subplots) feature an increasing behaviour with decreasing energy gap Δ, respectively. Bearing in mind that wavefunctions in metallic systems are typically delocalized, i.e. their coherence length converges to infinity, the observed behaviour again confirms the physical correctness of the resonant tunneling approach, since the infinite TB chain features metallic properties for vanishing on-site energies.
The fits of the current maxima verify the resonant tunneling approach in the weak electrical field. To prove if this approach is also consistent for lager electrical fields, the positions (values of the electrical field E_1) of the occurring current maxima were investigated in terms of their correspondence to the second resonance condition. The right subplots of Fig. 4.17 and Fig. 4.18 show the theoretical positions of the Wannier-Stark resonances (magenta markers), which were calculated according to the mathematical description of the second resonance condition in Eq.(4.62). The actual electrical fields E_1 at the occurring current maxima in the corresponding plots of the current densities $j(E_1)$ in Fig. 4.13 and Fig. 4.14 or in the left subplots of Fig. 4.17 and Fig. 4.18, respectively, are plotted for comparison (blue markers). It should be noted that for the actual position values the index n indicates the n^{th} largest electrical field where a maximum appears. Starting out with the case of the largest energy gap $\Delta = 4.0$ in Fig. 4.18f one can clearly see that the current maxima almost exactly appear at the theoretically predicted values of the electrical field. Good agreement with the theoretical values is also found for $\Delta = 2.0$ (Fig. 4.18d), $\Delta = 1.6$ (Fig. 4.18b) and $\Delta = 1.0$ (Fig. 4.17d) where it shows up that the agreement is slightly better for larger values of n. This observed characteristic is reasonable in two ways:
First of all, due the fact that a small value of n corresponds to a large electrical field, the positions of the current maxima are also affected by the occurring current decrease and saturation.
Further on, a small value of n corresponds to few energy barriers for the electron to tunnel through. In this case the actual ratio of the hopping integral t within the chain and the energy gap Δ plays an important role, since the approach of electrons which can overcome energy barriers by tunneling processes only, increasingly fails for $\frac{t}{\Delta} \approx O(1)$ and few energy barriers. The fail of the approach for $\frac{t}{\Delta} \approx O(1)$ is quite reasonable, since the electrons can simply surmount the arising energy barrier without any additional tunneling processes because of the comparatively large hopping integral $t \approx \Delta$. This effect is most clearly observable for the smallest energy barrier $\Delta = 0.6$ in Fig. 4.17b, where $\frac{t}{\Delta} \approx 1$.
Summing up, the second resonance condition is satisfied for most of the occurring maxima in the current densities with some reasonable deviations for small energy gaps and/or large electrical fields. This result points out again that the observed current maxima correspond to Wannier-Stark resonances.

The detailed investigation of the non-interacting semiconducting TB chain with alternating on-site energies yielded a comprehensible physically motivated interpretation of the obtained oscillations in

the current densities $j(E_1)$. The presented explanation also holds in case of the interacting semiconducting TB chain (see Fig. 4.11 for the particular current densities), since non-zero interactions U change the potential energy profile (plotted without considering the effect of U in Fig. 4.15c) in a similar way as the on-site energies ϵ in Fig. 4.15d.

In the next section the electronic transport properties of an armchair and a zig-zag GNR are presented. The detailed interpretation of the obtained results for the infinite TB chain in the present section will allow for a comprehensive and physically correct interpretation of the gained results for the GNRs.

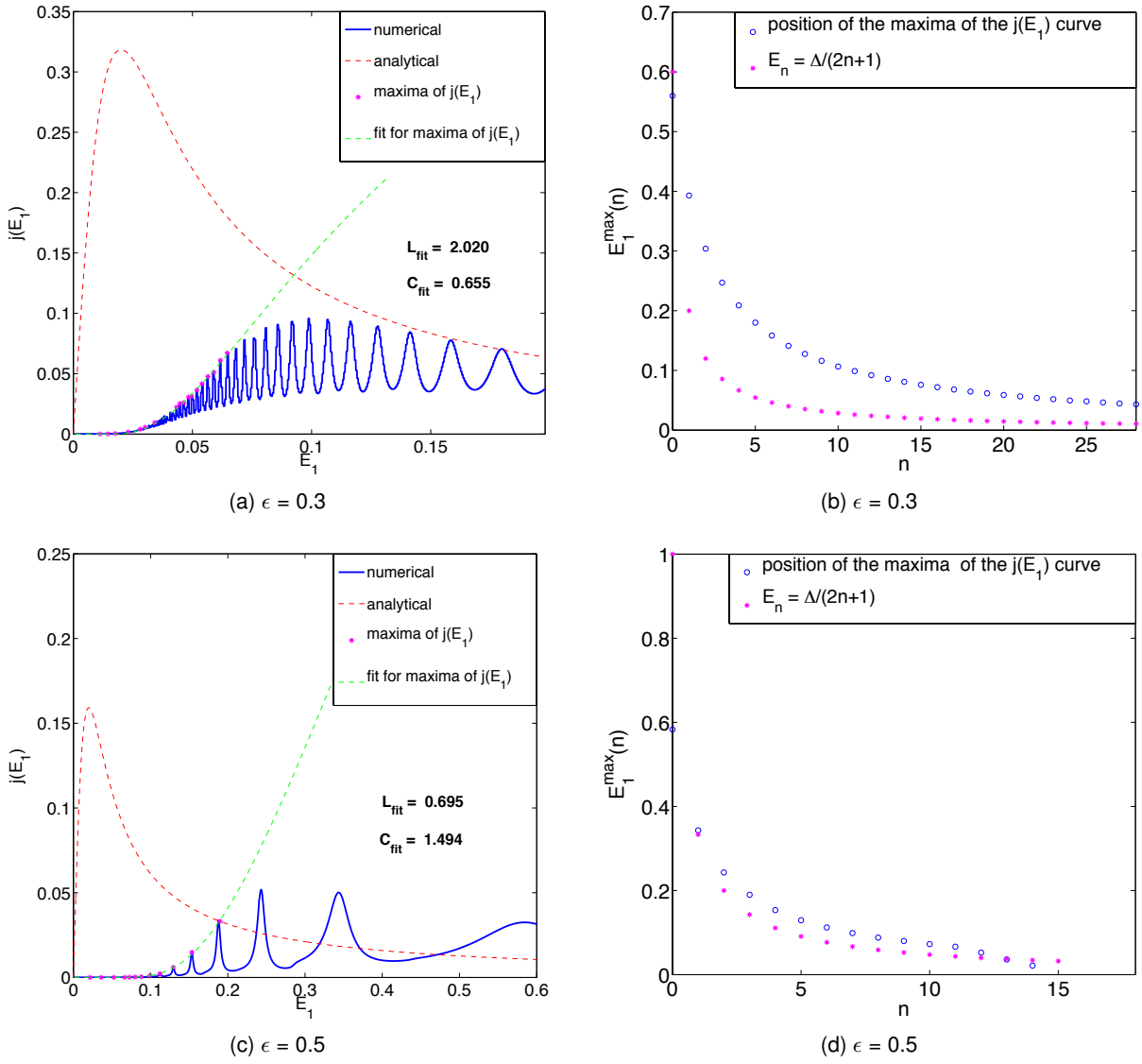

(a) $\epsilon = 0.3$ (b) $\epsilon = 0.3$

(c) $\epsilon = 0.5$ (d) $\epsilon = 0.5$

Figure 4.17: (a),(c): Zoomed-in plots of the steady-state current densities $j(E_1)$ within the infinite TB chain in Fig. 4.13. The observed maxima are highlighted (magenta markers) and fitted according to Eq.(4.67) (green dashed lines), with the fitting parameters L_{fit}, C_{fit} given. (b), (d): Respective positions E_1 of the occurring maxima (blue markers) in comparison to the theoretical values (magenta markers) calculated according to Eq.(4.62). The particular values of the on-site energies ϵ are given below each subplot.

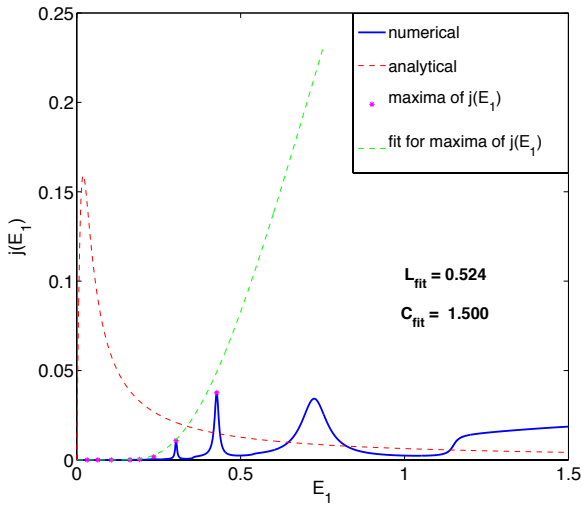

(a) ϵ = 0.8

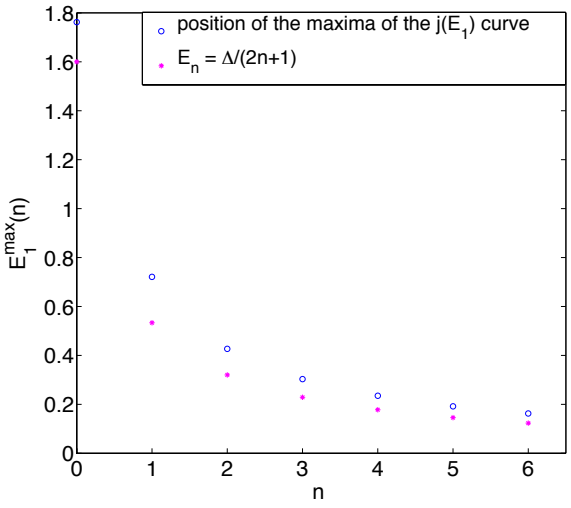

(b) ϵ = 0.8

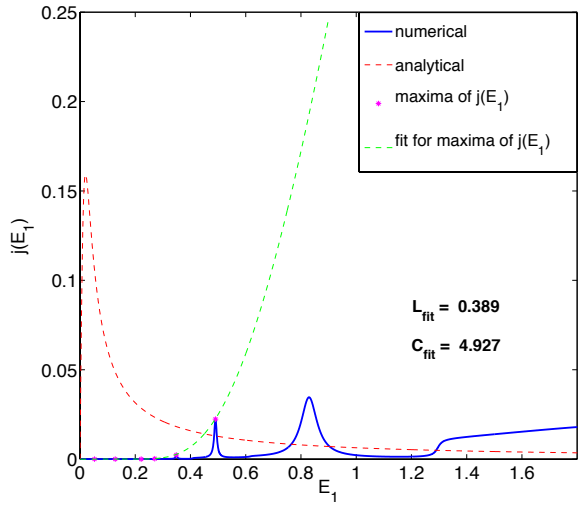

(c) ϵ = 1.0

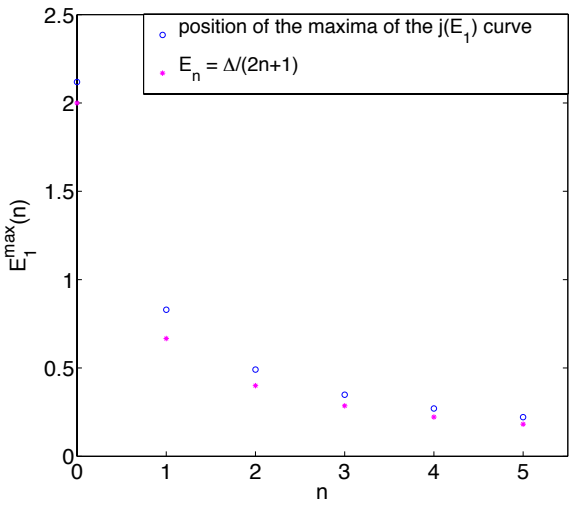

(d) ϵ = 1.0

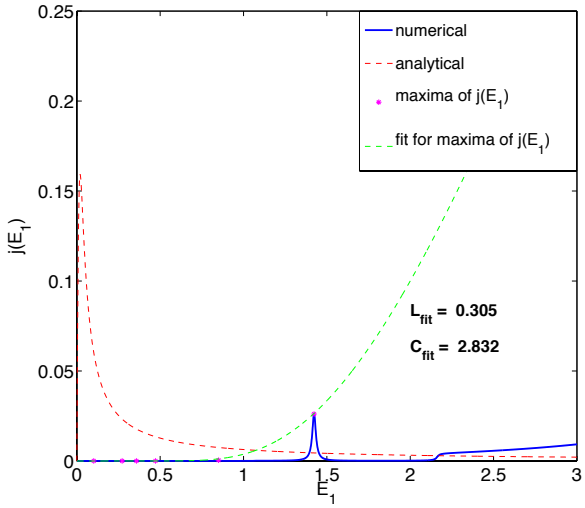

(e) ϵ = 2.0

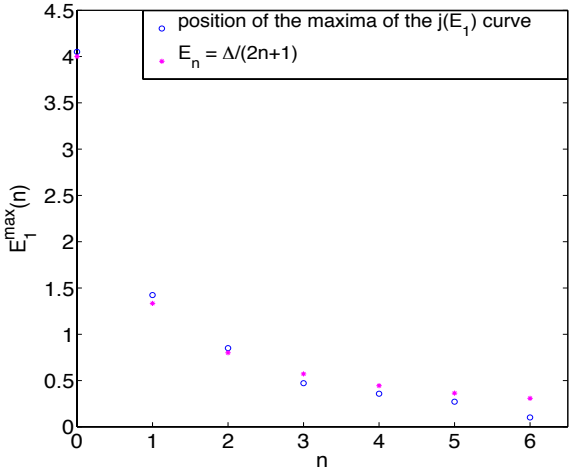

(f) ϵ = 2.0

Figure 4.18: Same as Fig. 4.17, but for the steady-state current densities $j(E_1)$ of Fig. 4.14.

4.4 Non-equilibrium electronic transport properties of graphene nanoribbons

Finally, the results of the electronic transport properties of an armchair and a zig-zag GNR with four C atoms along the width (corresponding to the AC-W4 and ZZ-W4 GNR in Chapter 3) are presented in this section. The Wannier-Stark model introduced in Sec. 4.2.3 for the infinite TB chain is used for the GNRs as well, since it is not restricted to strictly one-dimensional geometries. As it was pointed out already during the introduction of the Wannier-Stark model, the only differences in the calculations appear in the particular on-site energies ϵ (due to the 2d spatial extent of the central cluster) and in the coupling matrices $\boldsymbol{T}^{L/R}$.
The infinite GNRs are again split up into three parts: a central part (cluster) and two semi-infinite ribbons on the right- and left-hand side of the central part. The particular splitting is shown in Fig. 4.19, where the respective values of the on-site energies ϵ, which arise due to the applied homogeneous electrical field $\boldsymbol{E}$, are indicated as well. It has to be mentioned here that a slightly different notation is used in this section, where the absolute value of the electrical field is denoted as E (in contrast to E_1 in the previous sections). Again, the values for the electrical field E and the repulsive on-site interaction U are given in terms of the nearest neighbour hopping integral t.

While the construction of the coupling matrices for the infinite TB chain was rather simple, it becomes more complicated in case of the GNRs due to there 2d geometry. The detailed plot of the central cluster for the AC-W4 GNR in Fig. 3.22b or Fig. 4.20a with the indicated site labeling leads to the following coupling matrices for the armchair GNR

$$\boldsymbol{T}^{L}_{12} = \begin{pmatrix} 0 & 0 & 0 & 0 & 0 & 0 & 0 & t \\ 0 & 0 & 0 & 0 & 0 & 0 & 0 & 0 \\ 0 & 0 & 0 & 0 & 0 & t & 0 & 0 \\ 0 & 0 & 0 & 0 & 0 & 0 & 0 & 0 \\ 0 & 0 & 0 & 0 & 0 & 0 & 0 & 0 \\ 0 & 0 & 0 & 0 & 0 & 0 & 0 & 0 \\ 0 & 0 & 0 & 0 & 0 & 0 & 0 & 0 \\ 0 & 0 & 0 & 0 & 0 & 0 & 0 & 0 \end{pmatrix} = \boldsymbol{T}^{R}_{21} \qquad \boldsymbol{T}^{L}_{21} = \left(\boldsymbol{T}^{L}_{12}\right)' = \boldsymbol{T}^{R}_{12} \tag{4.68}$$

with the hopping integral t inside the graphene structure given by Eq.(2.5).

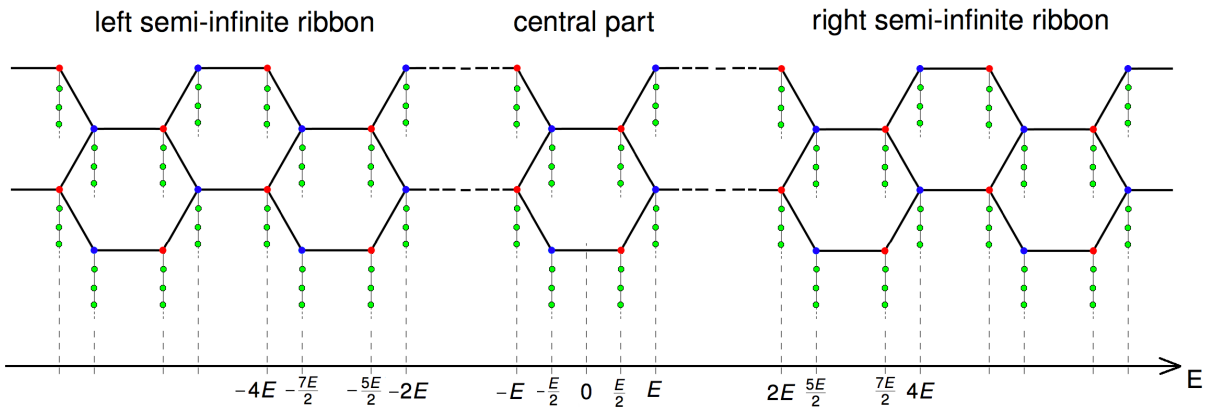

(a) AC-W4 GNR

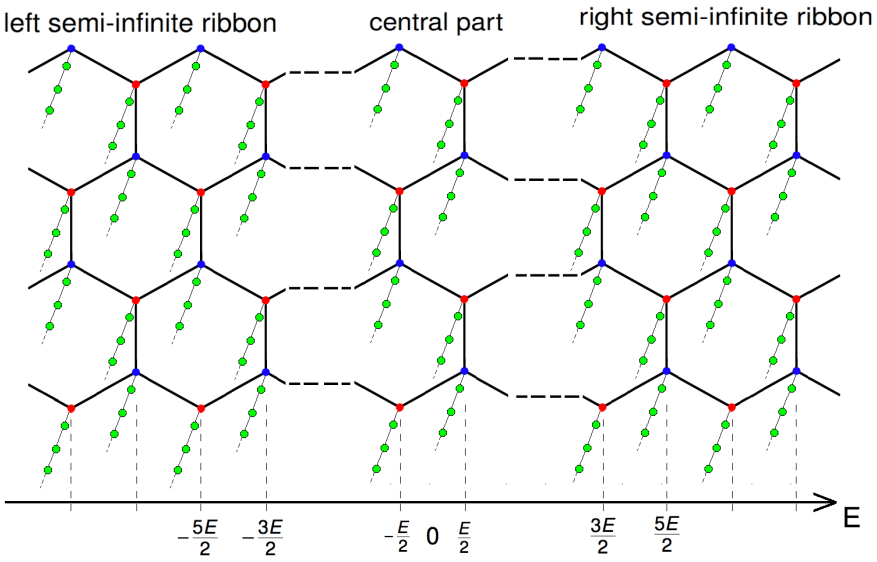

(b) ZZ-W4 GNR

Figure 4.19: Composition of an AC-W4 GNR (a) and a ZZ-W4 GNR (b) with coupled bath chains. Semi-infinite ribbons are coupled to a central part containing eight sites, indicating the eight-site cluster decomposition applied for the non-equilibrium investigations in case of these GNR lattices. Furthermore, the electrical field intensities at every particular site are given, where E is a constant determining the potential drop between two neighbouring sites, due to the applied homogeneous electrical field.

Similarly, Fig. 3.9d or Fig. 4.20b provide a detailed view of the central cluster used in case of the ZZ-W4 GNR. The indicated site labeling determines the particular form of the coupling matrices for the zig-zag GNR:

$$\boldsymbol{T}_{12}^{L} = \begin{pmatrix} 0 & t & 0 & 0 & 0 & 0 & 0 & 0 \\ 0 & 0 & 0 & 0 & 0 & 0 & 0 & 0 \\ 0 & 0 & 0 & 0 & 0 & 0 & 0 & 0 \\ 0 & 0 & t & 0 & 0 & 0 & 0 & 0 \\ 0 & 0 & 0 & 0 & 0 & t & 0 & 0 \\ 0 & 0 & 0 & 0 & 0 & 0 & 0 & 0 \\ 0 & 0 & 0 & 0 & 0 & 0 & 0 & 0 \\ 0 & 0 & 0 & 0 & 0 & 0 & t & 0 \end{pmatrix} = \boldsymbol{T}_{21}^{R} \qquad \boldsymbol{T}_{21}^{L} = \left(\boldsymbol{T}_{12}^{L}\right)' = \boldsymbol{T}_{12}^{R}. \tag{4.69}$$

In contrast to the infinite TB chain, where the current density is equivalent between all neighbouring sites, the situation is more complicated for the GNRs. Due to their 2d geometries there appear different currents between the eight C atoms of the central clusters. To allow for a comprehensive interpretation of the results for the current densities within the AC-W4 and ZZ-W4 GNR (which are presented in the following) a detailed view of the central clusters with all flowing currents indicated is provided in Fig. 4.20.

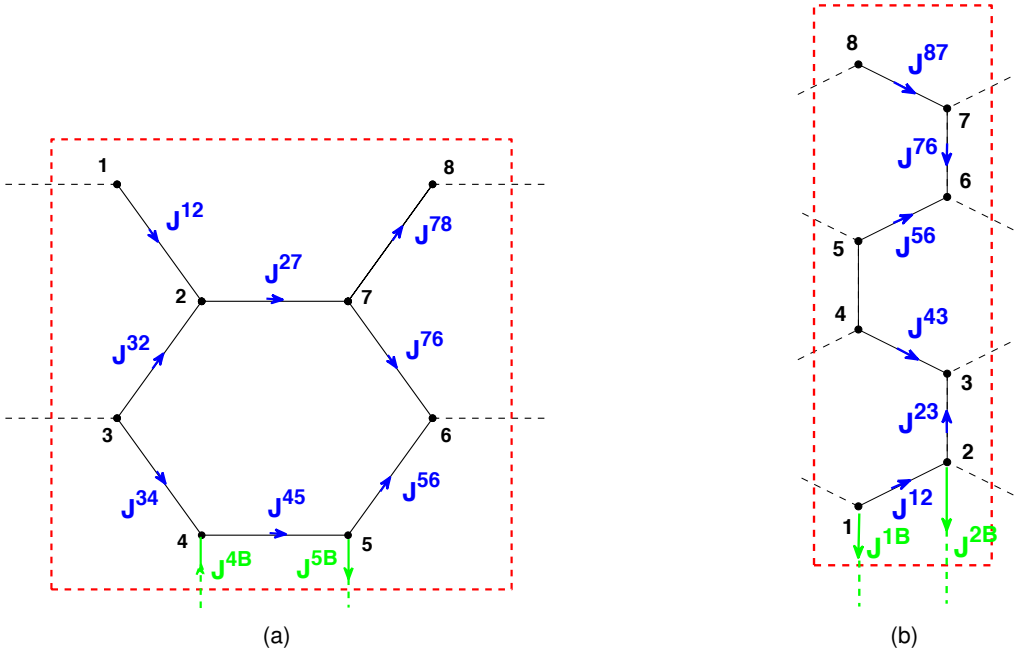

Figure 4.20: Central clusters of the investigated AC-W4 GNR (a) and ZZ-W4 GNR (b) with the different flowing currents indicated. Currents between a site m and a site n within the GNRs are denoted as J^{mn}, while the quantity J^{mB} corresponds to a current between site m of the physical system and the coupled artificial bath chain. These bath currents should be orders of magnitudes smaller than the currents within the GNRs to ensure physically correctness of the used model.

One needs to distinguish between currents flowing within the GNRs and currents flowing into the

artificial bath chains. A current between a site m and a site n within the GNRs is denoted as J^{mn}, while J^{mB} corresponds to a current flowing between a site m of the GNR and its coupled fermion bath chain. The intention of coupling fermion bath chains to the physical system was, to allow for a proper dissipation mechanism. It is desired to have an energy current into the baths, i.e. a dissipation of the Joule heat from the physical system. In contrast to that, any particle current flow from the physical system to a coupled bath chain or from a coupled bath chain to the physical system, respectively, would be non-physical.

4.4.1 Armchair graphene nanoribbon with four carbon atoms along the width

The obtained results for the steady-state electronic current densities $j(E)$ within an AC-W4 GNR under the influence of a homogeneous electrical field E are plotted in Fig. 4.21 and Fig. 4.22 for different values of the repulsive on-site interactions U. The particular values of U and the used parameters for the fermion bath chains are indicated top right in each subplot.

The current densities in Fig. 4.21 and Fig. 4.22 clearly show an oscillatory behaviour, as it was the case for the infinite TB chain (see Fig. 4.11 e.g.). Before the particular plots are analyzed and compared to each other, some general properties, valid for all current density plots of the AC-W4 GNR are given:

First of all, the total current density $j^{tot}(E)$ is given by $j^{tot}(E) = J^{27}(E) + J^{45}(E)$ due to the geometry of the central cluster depicted in Fig. 4.20a.
Next, the particular currents $J^{12}(E)$ and $J^{78}(E)$ are identical in all subplots, as well as $J^{34}(E)$ and $J^{56}(E)$, which appears due to symmetries of the central cluster.
Furthermore, it is observable that Kirchhoff's laws [83] are satisfied within the central part, since $J^{34}(E) = J^{45}(E) = J^{56}(E)$, $J^{12}(E) + J^{32}(E) = J^{27}(E)$ and $J^{27}(E) = J^{76}(E) + J^{78}(E)$ holds in all plotted current densities. It is important here that Kirchhoff's laws within the cluster can only be fulfilled if the bath currents J^{mB} within the fermion bath chains at every site m are approximately zero. This condition has also to be met to ensure physically correctness of the used model. Since the fermion bath chains were added to the system strictly artificially to enable a proper dissipation mechanism, any particle transfer from the sites of the AC-W4 GNR to the reservoirs would be unphysical. It should be clear that exactly the same condition applies to the ZZ-W4 GNR. It is observable in all plots of the current densities in the AC-W4 GNR that the condition of approximately zero bath currents J^{mB} (bold dashed lines in the particular plots) is fulfilled for almost every set of parameters (U,E). There appear some small deviations for large electrical fields, which however do not greatly matter, since the interesting region where the Wannier-Stark resonances can be observed corresponds to the weak electrical field regime.
Omitting the occurring oscillations for a moment, the general behaviour of the total current density $j^{tot}(E)$ along the AC-W4 GNR is very similar to the one found for the metallic infinite TB chain: Initially, the current increases with increasing electrical field until a maximum value is reached. Subsequently,

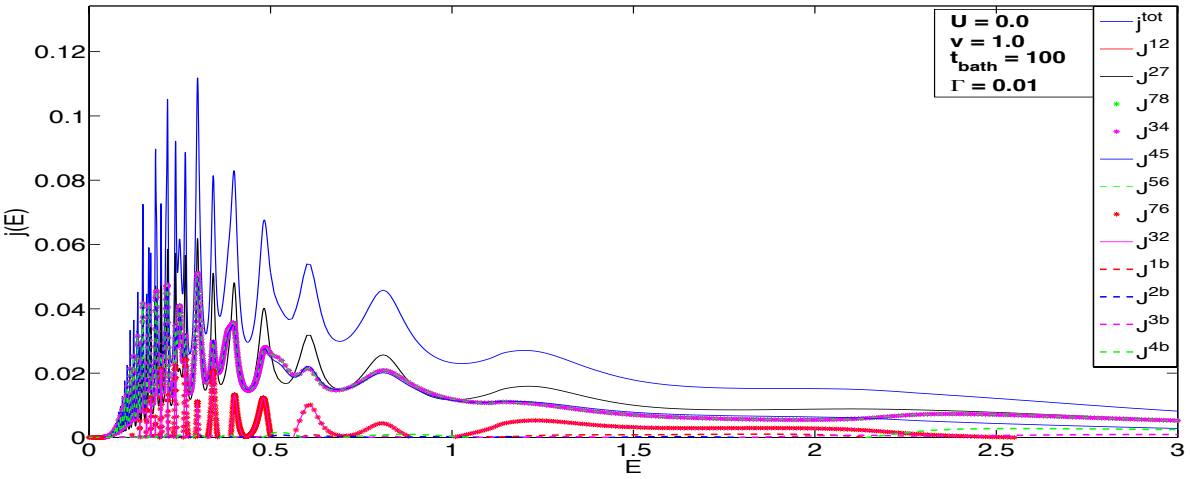

(a) U=0.0

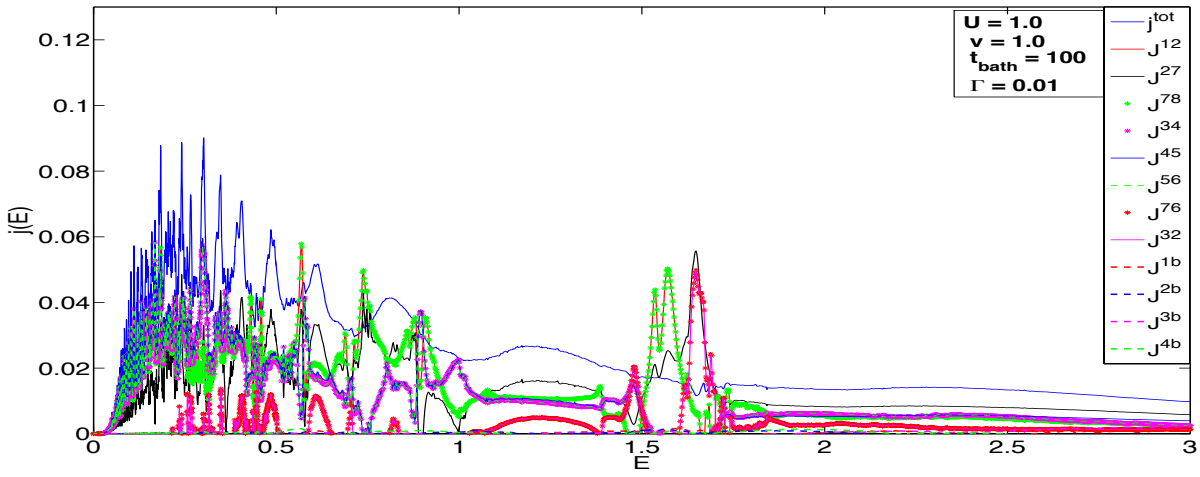

(b) U=1.0

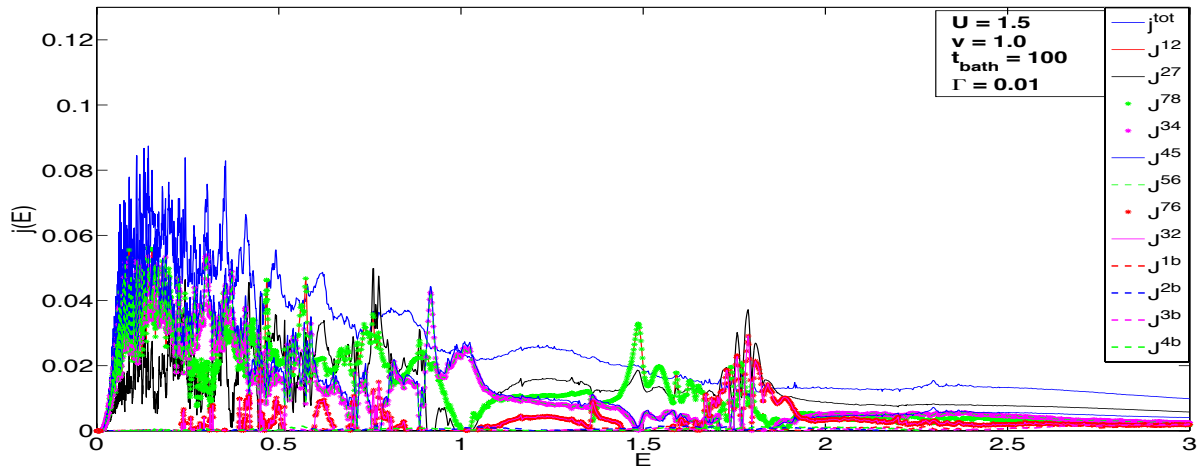

(c) U=1.5

Figure 4.21: Steady-state current densities $j(E)$ within an AC-W4 GNR coupled to fermion bath chains, for different values of the on-site interaction $U = \{0.0, 1.0, 1.5\}$. The particular values of U are indicated below each subplot. The sites between which the respective currents flow are depicted in the detailed plot of the central cluster in Fig. 4.20a. The parameters of the fermion bath chains are indicated in each subplot.

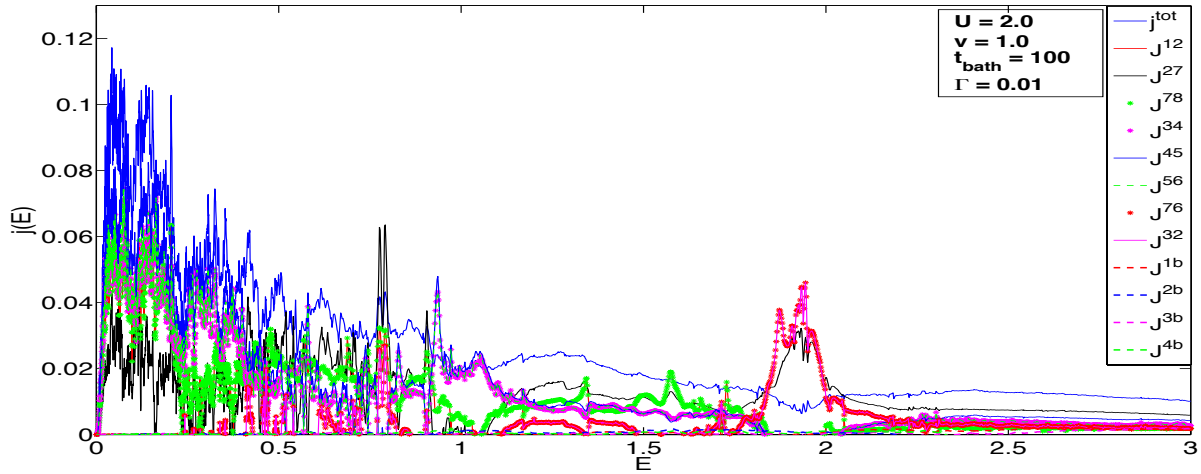

(a) U=2.0

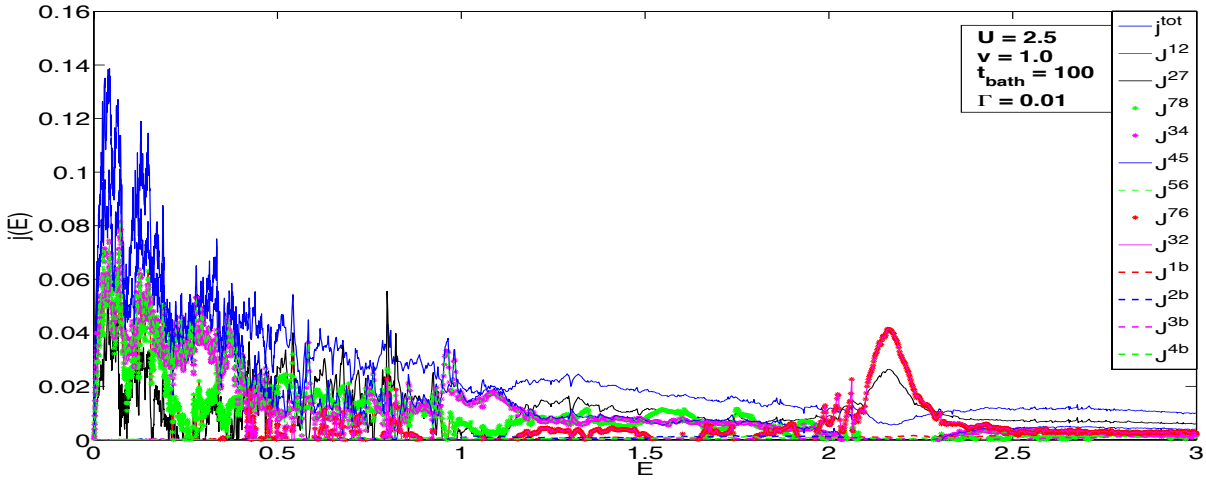

(b) U=2.5

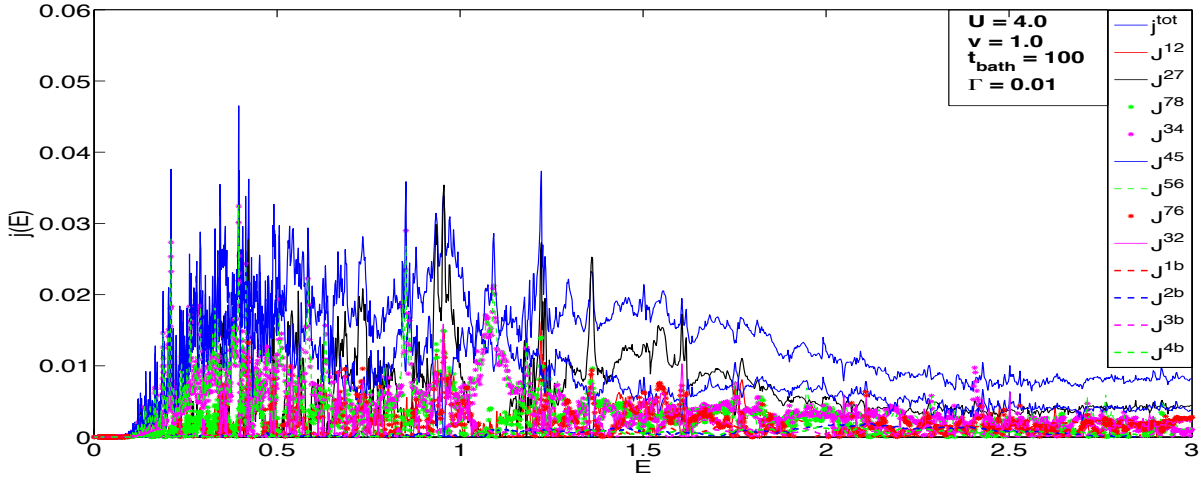

(c) U=4.0

Figure 4.22: Same as Fig. 4.21, but for $U = \{2.0, 2.5, 4.0\}$.

a decrease and saturation of the current for larger electrical fields can be observed, which is again a result of increasing BOs in consequence of a too weak dissipation mechanism.

Focusing on the particular current densities in the different subplots now, Fig. 4.21a, representing the non-interacting case, indicates that the distance (in terms of the electrical field E) between the occurring current maxima is very small for the weakest electrical fields and increases steadily with increasing electrical fields. This behaviour corresponds mainly to the second resonance condition formulated for the one-dimensional model in Eq.(4.62), albeit, an exact mathematical form is inapproachable here due to the 2d geometry of the GNRs. For non-zero interactions (Fig. 4.21b - Fig. 4.22c) the electrical fields where the current maxima occur stay almost the same, which indicates again an appearance of resonant tunneling processes.
Since the progression of the current density curve in the weak electrical field regime in Fig. 4.21a is also very similar to the one found for the semiconducting infinite TB chain (see Fig. 4.11a e.g.), the appearing oscillations in the current densities can indeed be attributed again to occurring Wannier-Stark resonances. Due to the fact that there appear more than one conduction band in the first BZ of an AC-W4 GNR (see Fig. 3.24), resonant tunneling processes between a filled valence band and any empty conduction band are thought to occur for many different values of the electrical fields. This corresponds to an establishment of several Wannier-Stark ladders of resonances, in contrast to the infinite TB chain, where only one Wannier-Stark ladder appeared (see Fig. 4.16). Therefore, simple mathematical forms of the resonance conditions, as in Eq.(4.62) and Eq.(4.67) for the one-dimensional model, can not be provided.

Although the presented current densities are dominated by Wannier-Stark resonances, the semiconducting behaviour of the AC-W4 GNR in the non-interacting case is clearly observable in Fig. 4.21a, due to the appearing energy gap. Certainly, nothing else than a semiconducting behaviour was expected in consequence of the performed equilibrium investigations. It should be noted here that the *non-equilibrium* energy gap *does not* coincide with the equilibrium energy gap Δ_{AC} which was found in Sec. 3.4 due to the presence of Wannier-Stark resonances. Comparing the current density of the non-interacting $U = 0$ case to the current densities for increasing values of U, it is observable that the small appearing energy gap decreases until it has totally vanished in Fig. 4.22b ($U = 2.5$). Actually a linear current-electrical field characteristic is found in Fig. 4.22b, which corresponds to Ohm's law and therefore identifies the AC-W4 GNR with $U = 2.5$ as a (semi -) metal. For an even larger value of the on-site interaction $U = 4.0$ the energy gap appears again, which can be seen in Fig. 4.22c. This effect of the on-site interactions U on the energy gap (and therefore on the semiconducting behaviour) is observable in a much more definite way in Fig. 4.23, which shows zoomed-in plots of the weak electrical field region of all the current densities plotted in Fig. 4.21 and Fig. 4.22. The observed non-equilibrium behaviour is in perfect agreement with the one found in the equilibrium situation, where it was shown for the particular AC-W4 GNR that the initial semiconducting behaviour for $U = 0$ changes to a semi-metallic one for $U = 2.5$ and again to a semiconducting one for $U > 2.5$ (see Fig. 3.24 or Fig. 3.26).

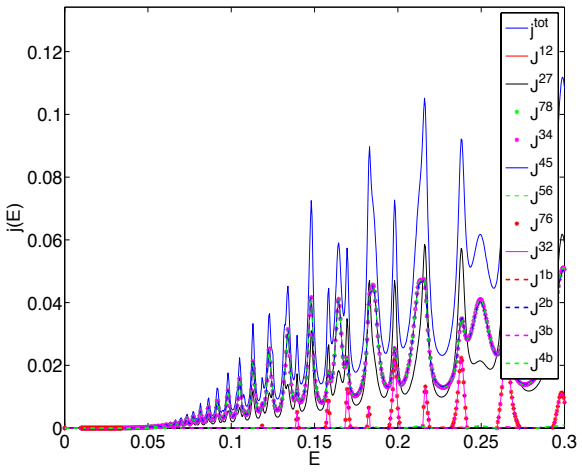

(a) U=0.0

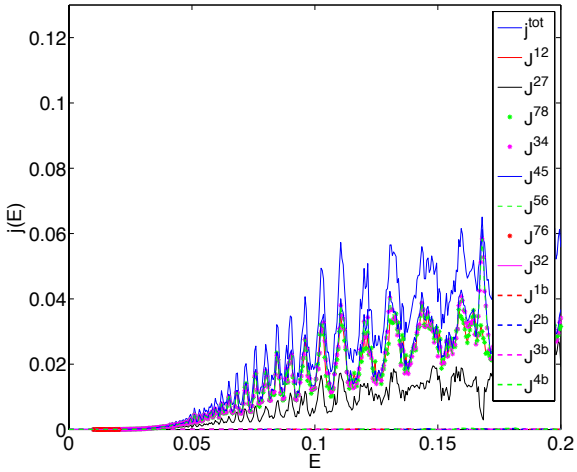

(b) U=1.0

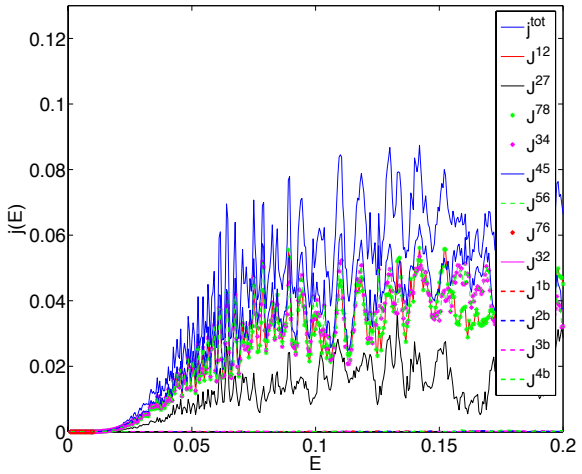

(c) U=1.5

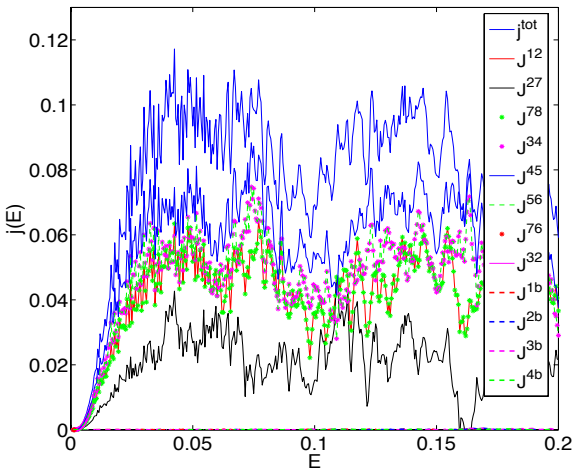

(d) U=2.0

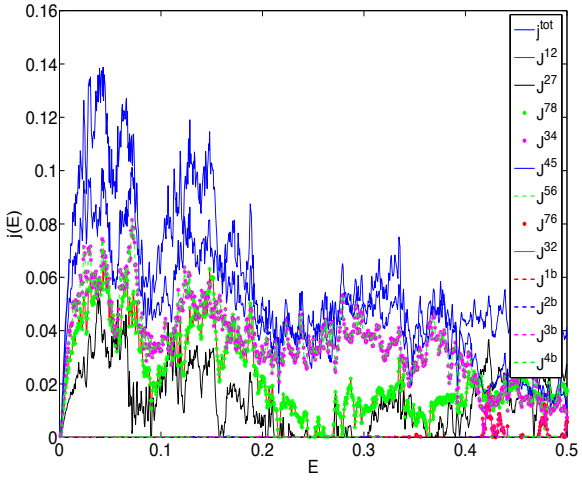

(e) U=2.5

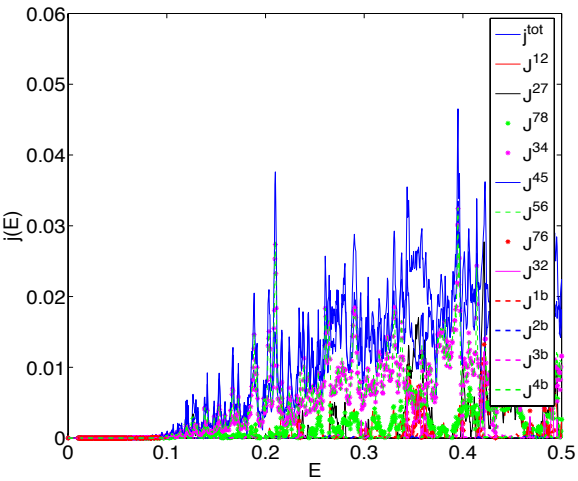

(f) U=4.0

Figure 4.23: Zoomed-in plots of the steady-state current densities within the AC-W4 GNR presented in Fig. 4.21 and Fig. 4.22.

4.4.2 Zig-zag graphene nanoribbon with four carbon atoms along the width

Turning to the zig-zag GNR geometry now, the results for the steady-state electronic current densities $j(E)$ within a ZZ-W4 GNR as a function of the homogeneous electrical field E are plotted in Fig. 4.24 and Fig. 4.25 for different values of the repulsive on-site interactions U. Again, the particular values of U and the used parameters for the fermion bath chains are indicated top right in each subplot.

First of all, similar as for the AC-W4 GNR, general properties, valid for all current density plots in Fig. 4.24 and Fig. 4.25 are given:
The total current density $j^{tot}(E)$ within the ZZ-W4 GNR is given by $j^{tot}(E) = J^{12}(E) + J^{43}(E) + J^{56}(E) + J^{87}(E)$ due to the geometry of the central cluster depicted in Fig. 4.20b.
Due to the fact that the central cluster is symmetric with respect to the longitudinal axis, $J^{12}(E) = J^{87}(E)$ and $J^{43}(E) = J^{56}(E)$ can be observed in all plots. As a consequence of this symmetry, the observable relation $J^{23}(E) = J^{54}(E) = J^{76}(E) \approx 0$ can be explained by Kirchhoff's laws.
Furthermore, it is observable in all plots of the current densities in the ZZ-W4 GNR that all bath currents J^{mB} (bold dashed lines in the particular plots) are approximately zero for almost every set of parameters (U,E). As it was the case for the AC-W4 GNR, this verifies the physical correctness of the applied model.
The general behaviour (i.e. omitting the oscillations) of the total current density $j^{tot}(E)$ along the ZZ-W4 GNR is again very similar to the one found for the infinite TB chain.

The current densities in Fig. 4.24 and Fig. 4.25a in general exhibit a linear current-electrical field relation in the weak electrical field regime, which corresponds to Ohm's law and therefore identifies the ZZ-W4 GNR for $U < 2.5$ as a metallic conductor. For $U > 2.5$ the current densities feature an energy gap, corresponding to a semiconducting transport behaviour. Fig. 4.26 again shows zoomed-in plots of the weak electrical field region of all the current densities plotted in Fig. 4.24 and Fig. 4.25 to allow for a better observability. Again, the observed transport behaviours perfectly agree to the equilibrium properties observed for the particular ZZ-W4 GNR geometry (see Fig. 3.12 or Fig. 3.14).

The most striking feature of the presented current densities is obviously the oscillatory behaviour, which is observable within the approximate range $0.1 < E < 1.0$ both for the metallic cases in Fig. 4.24a - Fig. 4.25a and the semiconducting ones in Fig. 4.25b and Fig. 4.25c. Due to the fact that the metallic TB chain *do not* features any Wannier-Stark resonances (as shown in Sec. 4.3.1), this deserves a particular explanation here:
As it was the case for the AC-W4 GNR, more than one conduction band appears in the first BZ of the ZZ-W4 GNR (see Fig. 3.12). Although there are no energy barriers arising for the electrons in metallic structures, the multiplicity of unoccupied conduction bands allows for resonant tunneling processes between an occupied valence band of a site m and an unoccupied higher conduction band at a site n in the used Wannier-Stark model. Therefore, the occurring Wannier-Stark resonances do

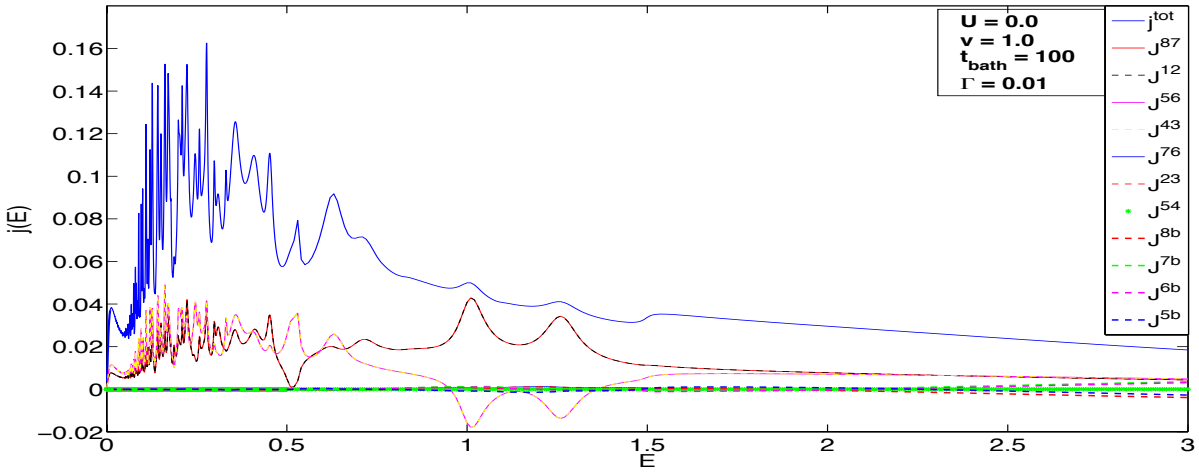

(a) U=0.0

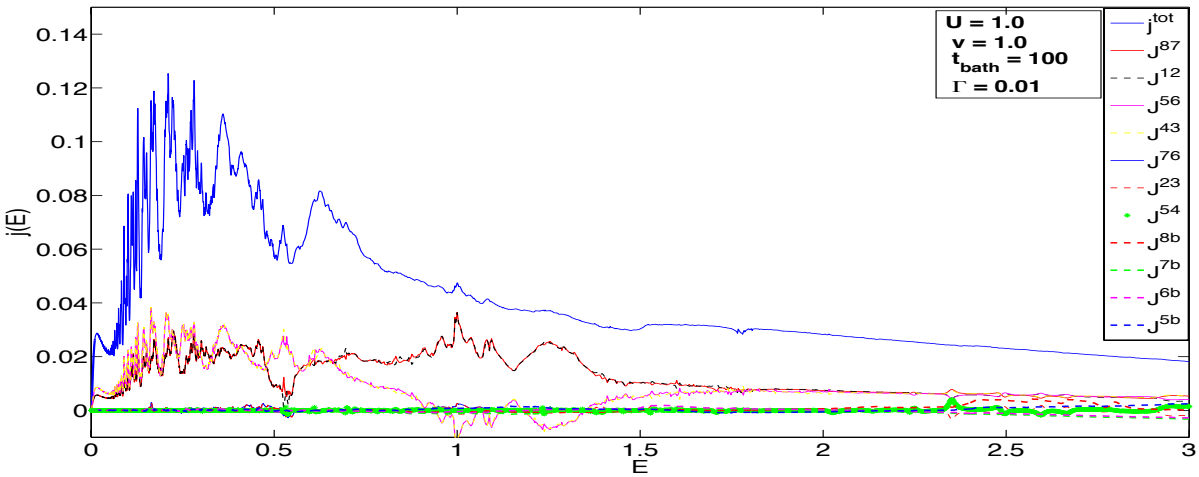

(b) U=1.0

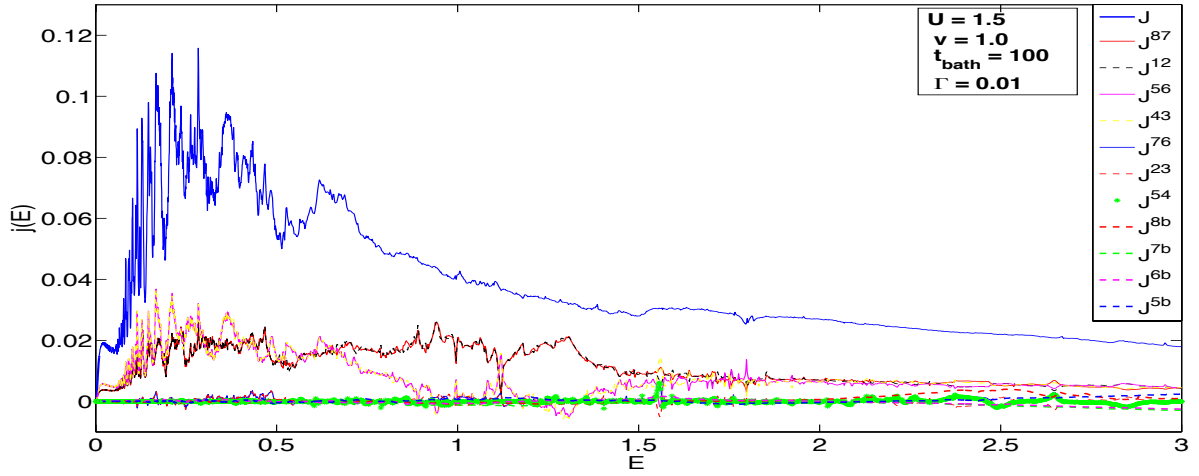

(c) U=1.5

Figure 4.24: Same as Fig. 4.21, but for a ZZ-W4 GNR.

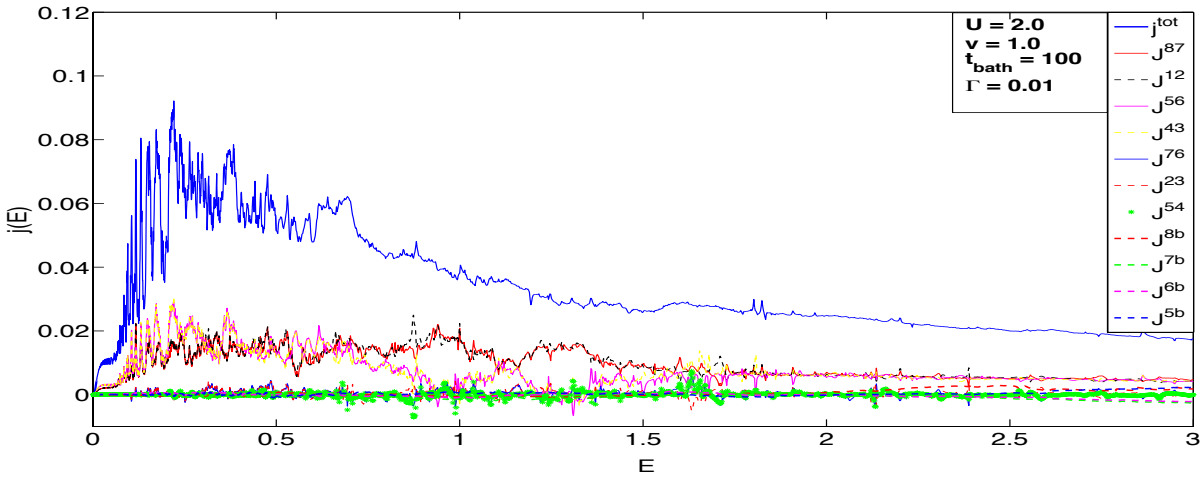

(a) U=2.0

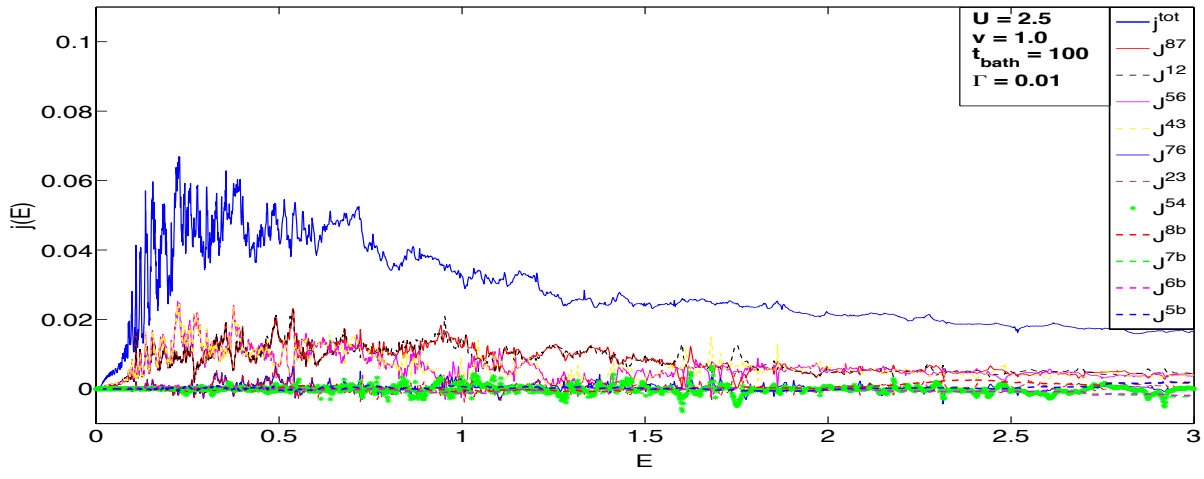

(b) U=2.5

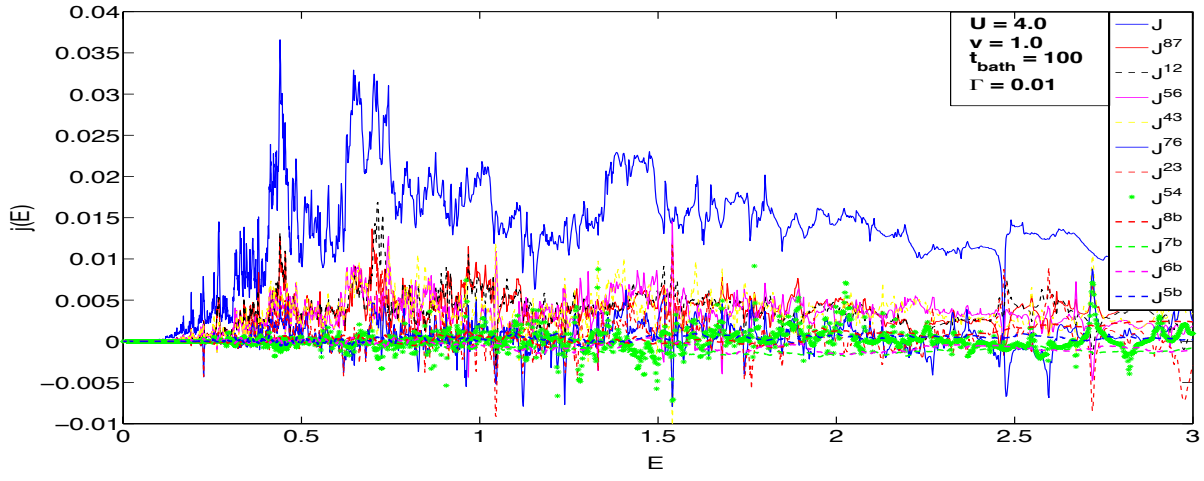

(c) U=4.0

Figure 4.25: Same as Fig. 4.22, but for a ZZ-W4 GNR.

not originate from an appearing energy gap in case of the ZZ-W4 GNR, but are a consequence of the formation of Wannier-Stark ladders of resonances due to the multiplicity of unoccupied conduction bands.

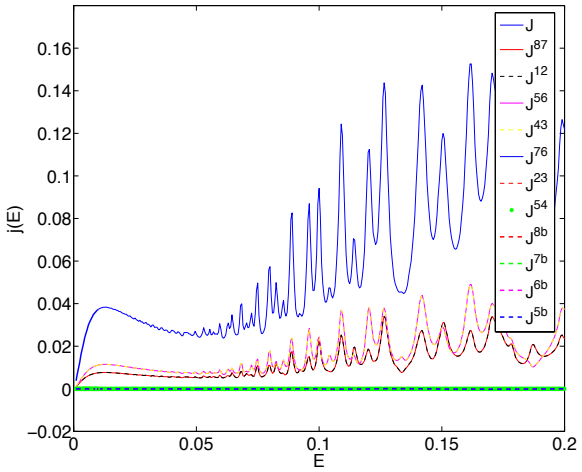

(a) U=0.0

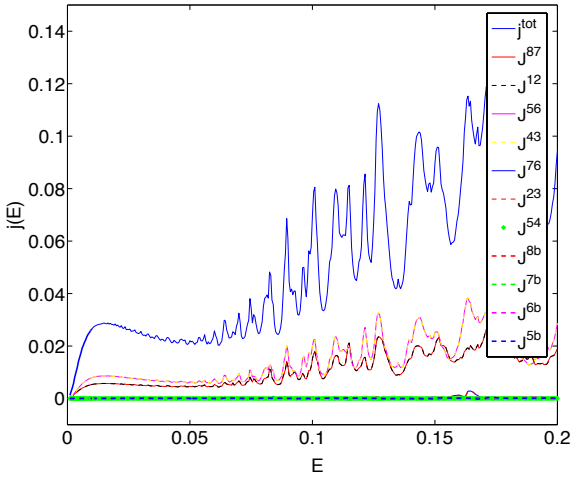

(b) U=1.0

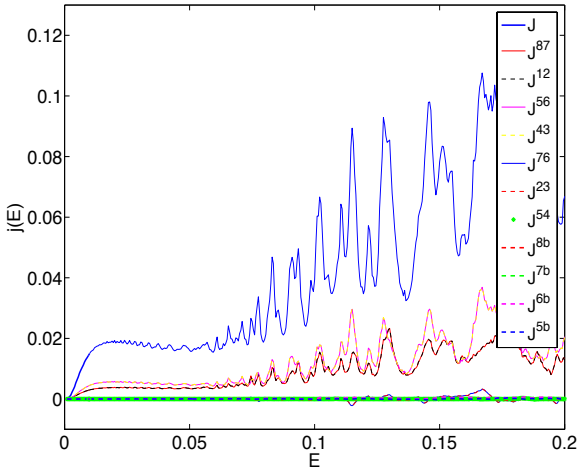

(c) U=1.5

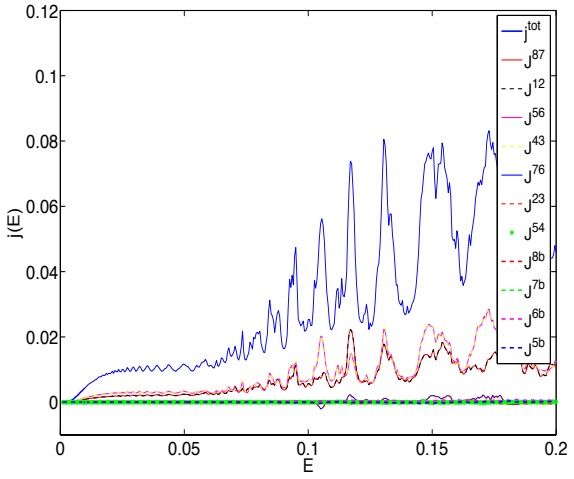

(d) U=2.0

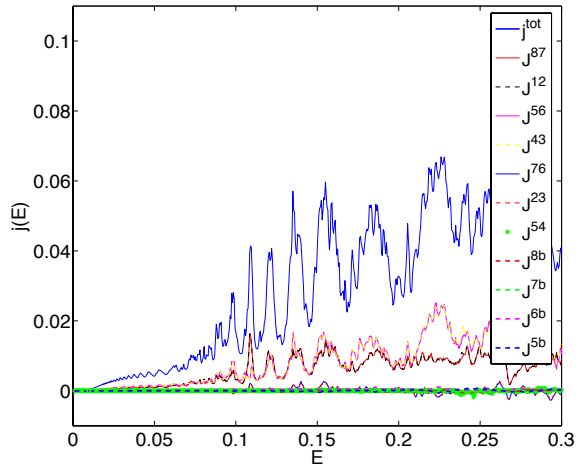

(e) U=2.5

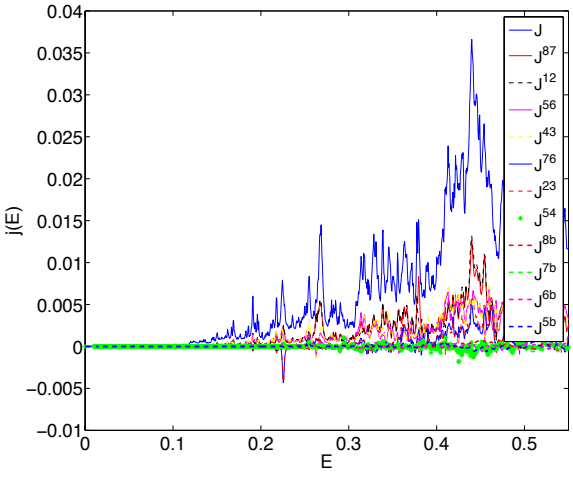

(f) U=4.0

Figure 4.26: Zoomed-in plots of the steady-state current densities within the ZZ-W4 GNR presented in Fig. 4.24 and Fig. 4.25.

5 Conclusions

In the present thesis equilibrium and electronic transport properties of single-layer GNRs were investigated. To allow for an accessible and effective inclusion of electron-electron interactions into the calculations, the 2d Hubbard model was used and treated within CPT.
Infinite armchair and zig-zag GNRs with various finite widths were investigated in the equilibrium case, as well as an infinitely extended layer of pristine graphene. The DOS and the energy-momentum dispersion relations were calculated in order to allow for a comprehensive interpretation of the physical characteristics. For the zig-zag GNRs the metallic behaviour predicted by several review articles was observed for small enough values of the on-site electron-electron interaction $U < U_{crit}$. It appears that the metallic states within the zig-zag GNRs indeed correspond to localized states at the very edges of the ribbons. As the on-site interactions exceeded a critical value U_{crit} a change to a semiconducting behaviour was observed. Similar metal-semiconductor transitions were found independent of the particular width. In case of an armchair edge orientation a width-dependent physical behaviour was observed in the non-interacting case. While an armchair GNR with four C atoms along the width yielded a semiconducting behaviour, a width of five C atoms resulted in a semi-metallic dispersion relation, in agreement with literature. An inclusion of the electron-electron interactions into the calculations showed the predicted metal-semiconductor transition for the case of five C atoms along the width as U increases. An unexpected contrary result was obtained for the armchair GNRs with a width of four C atoms, where the energy gap of the non-interacting case closes with increasing U, before it opens up again for stronger interactions. It is thought that this behaviour originates from a quantum size effect. A comparison of the equilibrium properties of comparatively large GNRs to the ones of pristine graphene showed that only the armchair GNR geometry exhibits a DOS and energy-momentum dispersion relation similar to that of pristine graphene. Furthermore, a reduced energy gap was observed for the wider armchair GNR, which is in good agreement with reference solutions. For the zig-zag GNR with thirty C atoms along the width a similar metallic behaviour and metal-semiconductor transition as for the narrow zig-zag GNRs was found. It appears that the bare existence of zig-zag edges causes metallic equilibrium properties, which is an interesting fact, since in reality every experimental probe is obviously finite and therefore always feature some kind of edges.
The non-equilibrium investigations of the infinite GNRs within the Wannier-Stark model, with additionally fermion bath chains coupled to the physical system in order to provide a proper dissipation mechanism, yielded oscillatory current-electrical field relations. In order to provide a comprehensive and physically correct interpretation of the gained electronic transport properties, the Wannier-Stark model was also applied to one-dimensional infinite TB chains. The obtained results for a metallic TB chain are in good agreement with results obtained by time-dependent perturbation theory, but do not feature any current oscillations. In contrast to that, the observed current density within a semiconducting TB chain indeed exhibits oscillations. It was shown that these oscillations correspond to occurring Wannier-Stark resonances, which originate from induced resonant tunneling processes. Finally, it was shown that the appearance of oscillations in the current characteristics of the GNRs can be explained in terms of resonant tunneling processes and corresponding Wannier-Stark reso-

nances as well. Moreover, the effect of electron-electron interactions on the transport characteristics was investigated. Although the current densities within the GNRs are primarily determined by resonant tunneling process, metal-semiconductor transitions were observed again for particular values of U, in perfect agreement with the equilibrium investigations. An occurrence of edge currents within the zig-zag GNR, as predicted in some review articles, was not observed in this work.

6 Bibliography

[1] K.S. Novoselov, A.K. Geim, S.V. Morozov, D. Jiang, Y. Zhang, S.V. Dubonos, I.V. Grigorieva, and A.A. Firsov, "*Electric Field Effect in Atomically Thin Carbon Films*," Science **306**, 666 (2004)

[2] S. Das Sarma, S. Adam, E.H. Hwang, and E. Rossi, "*Electronic transport in two-dimensional graphene*," Reviews of modern physics **83**, 407–469 (2011)

[3] P. Avouris, Z.H. Chen, and V. Perebeinos, "*Carbon-based electronics*," Nature Nanotech **2**, 605 (2004)

[4] J.S. Bunch, A.M. van der Zande, S.S. Verbridge, I.W. Frank, D.M. Tanenbaum, J.M. Parpia, H.G. Craighead, and P.L. McEuen, "*Electromechanical Resonators from Graphene Sheets*," Science **315**, 490 (2007)

[5] C. Lee, X. Wei, J.W. Kysar, and J. Hone, "*Measurement of the Elastic Properties and Intrinsic Strength of Monolayer Graphene*," Science **321**, 385 (2008)

[6] S. Iijima, "*Helical microtubules of graphitic carbon*," Nature **354**, 56–58 (1991)

[7] M.S. Dresselhaus, G. Dresselhaus, and P.C. Eklund, *"Science of Fullerenes and Carbon Nanotubes - Their Properties and Applications,"* (Academic Press, Amsterdam, Boston, 1996) ISBN 978-0-080-54077-1

[8] D.V. Kosynkin, A.L. Higginbotham, A. Sinitskii, J.R. Lomeda, A. Dimiev, B.K. Price, and J.M. Tour, "*Longitudinal unzipping of carbon nanotubes to form graphene nanoribbons*," Nature **458**, 872–876 (2009)

[9] K. Wakabayashi, K. Sasaki, T. Nakanishi, and T. Enoki, "*Electronic states of graphene nanoribbons and analytical solutions*," Science and Technology of Advanced Materials **11**, 054504–054522 (2010)

[10] S. Reich, J. Maultzsch, and C. Thomsen, "*Tight-binding description of graphene*," Physical Review B **66**, 035412 (2002)

[11] H. Feldner, Z.Y. Meng, A. Honecker, D. Cabra, S. Wessel, and F.F. Assaad, "*Magnetism of Finite Graphene Samples: Mean-Field Theory compared with Exact Diagonalization and Quantum Monte Carlo Simulation*," Physical Review B **81**, 115416 (2010)

[12] O. Hod, J.E. Peralta, and G.E. Scuseria, "*Edge effects in finite elongated graphene nanoribbons*," Physical Review B **76**, 233401 (2007)

[13] S. Ihnatsenka and G. Kirczenow, "*Effect of edge reconstruction and electron-electron interactions on quantum transport in graphene nanoribbons*," Physical Review B **88**, 125430 (2013)

[14] E. Schrödinger, "*An undulatory theory of the mechanics of atoms and molecules*," The Physical Review **28**, 1049–1070 (1926)

[15] A.H. Castro Neto, F. Guinea, N.M.R. Peres, K.S. Novoselov, and A.K. Geim, "*Electronic properties of graphene*," Reviews of modern physics **81**, 109–162 (2009)

[16] D.C. Elias, R.R. Nair, T.M.G. Mohiuddin, S.V. Morozov, P.Blake, M.P. Halsall, A.C. Ferrari, D.W. Boukhvalov, M.I. Katsnelson, K.S. Novoselov, and A.K. Geim, "*Control of graphene's properties by reversible hydrogenation: evidence for graphane*," Science **323**, 610–613 (2009)

[17] K.S. Novoselov, A.K. Geim, S.V. Morozov, D. Jiang, M.I. Katsnelson, I.V. Grigorieva, S.V. Dubonos, and A.A. Firsov, "*Two-dimensional gas of massless Dirac fermions in graphene*," Nature **438**, 197–200 (2005)

[18] V.M. Pereira, F. Guinea, J.M.B. Lopes dos Santos, N.M.R. Peres, and A.H. Castro Neto, "*Disorder Induced Localized States in Graphene*," Physical Review Letters **96**, 036801 (2006)

[19] X. Yang, X. Dou, A. Rouhanipour, L. Zhi, H.J. Räder, and K. Müllen, "*Two-Dimensional Graphene Nanoribbons*," Journal of the American Chemical Society **130**, 4216–4217 (2007)

[20] M.Y. Han, B. Özyilmaz, Y. Zhang, and P. Kim, "*Energy Band-Gap Engineering of Graphene Nanoribbons*," Physical Review Letters **98**, 206805 (2007)

[21] Z. Chen, Y. Lin, M.J. Rooks, and P. Avouris, "*Graphene nano-ribbon electronics*," Physica E **40**, 228–232 (2007)

[22] H.C. Schniepp, J. Li, M.J. McAllister, H. Sai, M. Herrera-Alonso, D.H. Adamson, R.K. Prud'homme, R. Car, D.A. Saville, and I.A. Aksay, "*Functionalized Single Graphene Sheets Derived from Splitting Graphite Oxide*," The Journal of Physical Chemistry B **110**, 8535–8539 (2006)

[23] X. Li, X. Wang, L. Zhang, S. Lee, and H. Dai, "*Chemically Derived, Ultrasmooth Graphene Nanoribbon Semiconductors*," Science **319**, 1229–1232 (2008)

[24] K.L.Ma, X.H.Yan, Y.Xiao, and Y.P.Chen, "*Electronic transport properties of metallic graphene nanoribbons with two vacancies*," Solid State Communications **150**, 1308 (2010)

[25] K. Wakabayashi, K. Sasaki, T. Nakanishi, and T. Enoki, "*Electronic states of graphene nanoribbons and analytical solutions*," Science and Technology of Advanced Materials **11**, 054054 (2010)

[26] S. Pairault, D. Sénéchal, and A.-M.S. Tremblay, "*Strong-Coupling Expansion for the Hubbard Model*," Physical Review Letters **80**, 5389 (1998)

[27] V.N. Kotov, B. Uchoa, V.M. Pereira, F. Guinea, and A.H. Castro Neto, "*Electron-Electron Interactions in Graphene: Current Status and Perspectives*," arXiv:1012.3484v2 (2012)

[28] Y. Son, M.L. Cohen, and S.G. Louie, "*Half-Metallic Graphene Nanoribbons*," Nature **444**, 347–349 (2006)

[29] H. Huang, D. Wei, J. Sun, S.L. Wong, Y.P. Feng, A.H. Castro Neto, and A.T.S. Wee, "*Spatially Resolved Electronic Structures of Atomically Precise Armchair Graphene Nanoribbons*," Scientific Reports **2**, 983 (2012)

[30] L. Jiang, Y. Zheng, C. Yi, H. Li, and T. Lu, "*Analytical study of edge states in a semi-infinite graphene nanoribbon*," Physical Review B **80**, 155454 (2009)

[31] MATLAB, *version 7.10.0 (R2012a)* (The MathWorks Inc., Natick, Massachusetts, 2012)

[32] J.O. Fjærestad (2013), "*Introduction to Green functions and many-body perturbation theory*," [PDF document], lecture notes retrieved from http://www.nt.ntnu.no/users/johnof/green-2013.pdf on November 8th 2013.

[33] J.W. Negele and H. Orland, *"Quantum Many-particle Systems,"* (Westview Press, New York, 1998) ISBN 0-7382-0052-2

[34] H. Lehmann, "*Über Eigenschaften von Ausbreitungsfunktionen und Renormierungskonstanten quantisierter Felder*," Nuovo Cimento **11**, 342 (1954)

[35] H.G. Evertz (2007), "*Quantenmechanik*," [PDF document], lecture notes retrieved from http://itp.tugraz.at/LV/evertz/QM_Skript/qm_skript_2007.pdf on November 11th 2013.

[36] D. Sénéchal, "*An introduction to quantum cluster methods*," arXiv:0806.2690 (2008)

[37] D. Sénéchal, D. Perez, and M. Pioro-Ladrière, "*Spectral Weight of the Hubbard Model through Cluster Perturbation Theory*," Physical Review Letters **84** , 522–525 (2000)

[38] C. Gros and R. Valentí, "*Cluster expansion for the self-energy: A simple many-body method for interpreting the photoemission spectra of correlated Fermi systems*," Physical Review B **48**, 418 (1993)

[39] M. Takahashi and J. Paldus, "*Bond length alternation in cyclic polyenes. VI. Coupled cluster approach with wannier orbital basis*," International Journal of Quantum Chemistry **28** , 459–479 (1985)

[40] M. Aichhorn, "*Ordering Phenomena in Strongly-Correlated Systems: Cluster Perturbation Theory Approaches*," Ph.D. thesis (2004)

[41] A.L. Fetter and J.D. Walecka, *"Quantum Theory of Many-Particle Systems,"* (Dover Publications, New York, 2003) ISBN 0-486-42827-5

[42] D. Sénéchal, D. Perez, and M. Pioro-Ladrière, "*Spectral Weight of the Hubbard Model through Cluster Perturbation Theory*," Physical Review Letters **84**, 522 (2000)

[43] M. Nuss, "*A cluster many-body approach to quantum impurity models*," Master thesis (2012)

[44] M. Aichhorn, E. Arrigoni, M. Potthoff, and W. Hanke, "*Variational cluster approach to the Hubbard model: Phase-separation tendency and finite-size effects*," Physical Review B **74** , 235117 (2006)

[45] P. Hadley (2012), "*Molecular and Solid State Physics - Lectures Winter Semester 2012*," [PowerPoint Slides], lecture notes retrieved from http://lamp.tu-graz.ac.at/ hadley/ss1/lectures12/dec10/slide5.html on November 21th 2013.

[46] J.M. Zhang and R.X. Dong, "*Exact diagonalization: the Bose-Hubbard model as an example*," European Journal of Physics **31**, 591 (2010)

[47] R.P. Feynman, R.B. Leighton, and M.Sands, *"The Feynman Lectures on Physics includeing*

Feynman's Tips On Physics: The Definitive and Extended Edition,", 2nd ed. (Addison Wesley, 2005) ISBN 0-805-39045-6

[48] C. Lanczos, "*An Iteration Method for the Solution of the Eigenvalue Problem of Linear Differential and Integral Operators*," Journal of Research of the National Bureau of Standards **45**, 255 (1950)

[49] Z. Bai, J. Demmel, J. Dongarra, A. Ruhe, and H. van der Vorst, "*Templates for the Solution of Algebraic Eigenvalue Problems: A Practical Guide*," SIAM, Philadelphia (2000)

[50] T.O. Wehling, E. Şaşoğlu, C. Friedrich, A.I. Lichtenstein, M.I. Katsnelson, and S.Blügle, "*Strength of Effective Coulomb Interactions in Graphene and Graphite*," Physical Review B **106**, 236805 (2011)

[51] D.L. Nika and A.A. Balandin, "*Two-dimensional phonon transport in graphene*," Journal of Physics: Condensed Matter **24**, 233203 (2012)

[52] J.A. Baimova, S.V. Dmitriev, and K. Zhou, "*Discrete breather clusters in strained graphene*," Europhysics Letters **100**, 36005 (2012)

[53] Y.-W. Son, M.L. Cohen, and S.G. Louie, "*Energy Gaps in Graphene Nanoribbons*," Physical Review Letters **97**, 216803 (2006)

[54] D.C. Elias, R.V. Gorbachev, A.S. Mayorov, S.V. Morozov, A.A. Zhukov, P. Blake, L.A. Ponomarenko, I.V. Grigorieva, K.S. Novoselov, F.Guinea, and A.K. Geim, "*Dirac cones reshaped by interaction effects in suspended graphene*," Nature Physics Letters **7**, 701 (2011)

[55] A. Di Carlo and P. Vogl, "*Theory of Zener tunneling and Wannier-Stark states in semiconductors*," Physical Review B **50**, 8358 (1994)

[56] M. Glueck, A.R. Kolovsky, and H.J. Korsch, "*Wannier-Stark resonances in optical and semiconductor superlattices*," Physics Reports **366**, 103 (2002)

[57] T. Hartmann, F. Keck, H.J. Korsch, and S. Mossmann, "*Dynamics of Bloch Oszillations*," New Journal of Physics **6**, 2 (2004)

[58] A.R. Kolovsky and E.N.Bulgakov, "*Wannier-Stark states and Bloch oscillations in the honeycomb lattice*," arXiv:1210.7406v1(2012)

[59] V. Krueckel and K. Richter, "*Bloch-Zener Oscillations in Graphene and Topological Insulators*," Physical Review B **85**, 115433 (2012)

[60] A.P. Jauho (2006), "*Introduction to Keldysh nonequilibrium Green function technique*," [PDF document], lecture notes retrieved from http://nanohub.org/resources/1878/download/jauho_negf.pdf on December 21st 2013.

[61] J. Rammer and H. Smith, "*Quantum field-theoretical methods in transport theory of metals*," Reviews of Modern Physics, **58**, 323 (1986)

[62] A. Kamenev, "*An introduction to quantum cluster methods*," arXiv:0412296v2 (2005)

[63] H. Haug and A.P. Jauho, *"Quantum Kinetics in Transport and Optics of Semiconductors,"* (Springer Verlag, Heidelberg, 1998) ISBN 3-540-61602-0

[64] A.A. Abrikosov, L.P. Gorkov, and I.E. Dzyaloshinski, *"Methods of quantum field theory in statistical physics,"* (Dover Publications, New York, 1975) ISBN 0-486-63228-8

[65] L.V. Keldysh, "*Diagram technique for nonequilibrium processes*," Journal of Experimental and Theoretical Physics, **47**, 1515 (1964)

[66] M. Gell-Mann and F. Low, "*Bound States in Quantum Field Theorys*," Physical Review, **84**, 350 (1951)

[67] G.D. Mahan, *"Many particle physics,"*, 3rd ed. (Springer Verlag, New York, 2000) ISBN 0-306-46338-5

[68] J.E. Han and J. Li, "*Energy dissipation in DC-field driven electron lattice coupled to fermion baths*," arXiv:1304.4269v1(2013)

[69] F. Bloch, "*Über die Quantenmechanik der Elektronen in Kristallgittern*," Zeitschrift für Physik, **52**, 555 (1928)

[70] C. Zener, "*A Theory of the Electrical Breakdown of Solid Dielectrics*," Proceedings of the Royal Society of London A, **145**, 523 (1934)

[71] J. Feldmann, K. Leo, J. Shah, D.A.B. Miller, J.E. Cunningham, T. Meier, G. von Plessen, A. Schulze, P. Thomas, and S. Schmitt-Rink, "*Optical investigation of Bloch oscillations in a semiconductor superlattice*," Physical Review B, **46**, 7252 (1992)

[72] K. Leo, P.H. Bolivar, F. Brüggemann, and R. Schwedler, "*Observation of Bloch oscillations in a semiconductor superlattice*," Solid State Communications, **84**, 943 (1992)

[73] M.B. Dahan, E. Peik, J. Reichel, Y. Castin, and C. Salomon, "*Bloch Oscillations of Atoms in an Optical Potential*," Physical Review Letters, **76**, 4508 (1996)

[74] V. Turkowski and J.K. Freericks, "*Nonlinear response of Bloch electrons in infinite dimensions*," Physical Review B, **71**, 085104 (2005)

[75] N. Tsuji, T. Oka, and H. Aoki, "*Nonequilibrium Steady State of Photoexcited Correlated Electrons in the Presence of Dissipation*," Physical Review Letters, **103**, 047403 (2009)

[76] L. Vidmar, J. Bonca, T. Tohyama, and S. Maekawa, "*Quantum Dynamics of a Driven Correlated System Coupled to Phonons*," Physical Review Letters, **107**, 246404 (2011)

[77] C. Aron, G. Kotliar, and C. Weber, "*Dimensional Crossover Driven by an Electric Field*," Physical Review Letters, **108**, 086401 (2012)

[78] J.E. Han, "*Solution of electric-field-driven tight-binding lattice coupled to fermion reservoirs*," Physical Review B, **87**, 085119 (2013)

[79] V. Turkowski and J.K. Freericks, "*Quenching Bloch oscillations in a strongly correlated material: Nonequilibrium dynamical mean-field theory*," Physical Review B, **71**, 075109 (2008)

[80] R. Kubo, "*Statistical-Mechanical Theory of Irreversible Processes. I. General Theory and Simple Applications to Magnetic and Conduction Problems*," Journal of the Physical Society of Japan, **12**, 570 (1957)

[81] I. Lokteva, S. Thiemann, F. Gannott, and J. Zaumseil, "*Ambipolar, low-voltage and low-hysteresis PbSe nanowire field-effect transistors by electrolyte gating*," Nanoscale, **5**, 4230 (2013)

[82] S. Hunklinger, *"Festkörperphysik,"* (Oldenbourg Verlag, München, 2009) ISBN 978-3-486-59045-6

[83] S. Kirchhoff, "*Ueber den Durchgang eines elektrischen Stromes durch eine Ebene, insbesondere durch eine kreisförmige*," Annalen der Physik, **140**, 497 (1845)